OCS Study
BOEM 2013-0119

Beaufort and Chukchi Seas Mesoscale Meteorology Modeling Study

Final Report

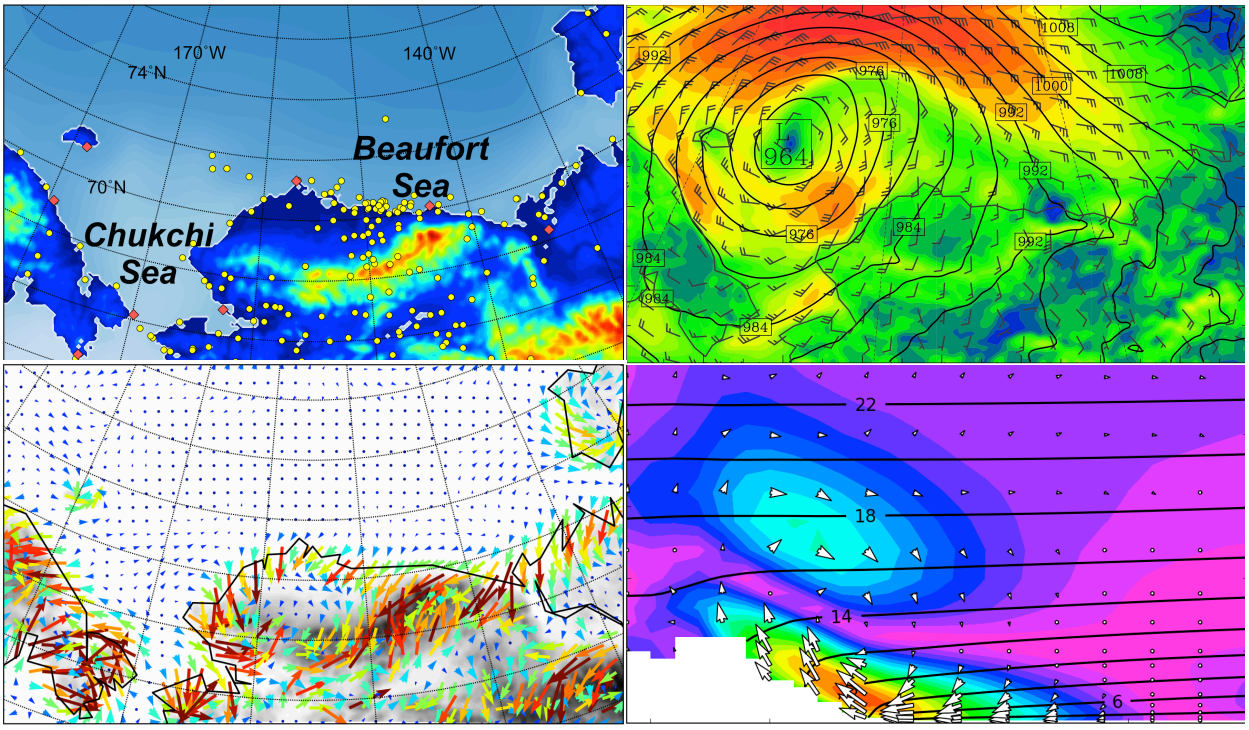

U.S. Department of the Interior
Bureau of Ocean Energy Management
Alaska OCS Region
www.BOEM.gov

BOEM
Bureau of Ocean Energy Management

OCS Study
BOEM 2013-0119

Beaufort and Chukchi Seas Mesoscale Meteorology Modeling Study

Final Report

Authors

Xiangdong Zhang and Jeremy Krieger
University of Alaska Fairbanks

Jing Zhang, Fuhong Liu, Steve Stegall, and Wei Tao
North Carolina A&T State University

Martha Shulski, Jinsheng You, William Baule, and Brittany Potter
University of Nebraska–Lincoln

Prepared under BOEM Contract
M06PC00018
by
University of Alaska Systems
P.O. Box 757880
Fairbanks, AK 99775-7880

Published by
U.S. Department of the Interior
Bureau of Ocean Energy Management **Alaska OCS Region**

DISCLAIMER

This report was prepared under contract between the Bureau of Ocean Energy Management (BOEM) and the University of Alaska Systems. This report has been technically reviewed by BOEM, and it has been approved for publication. Approval does not signify that the contents necessarily reflect the views and policies of BOEM, nor does mention of trade names or commercial products constitute endorsement or recommendation for use. It is, however, exempt from review and compliance with BOEM editorial standards.

REPORT AVAILABILITY

The report may be downloaded from the boem.gov website through the Environmental Studies Program Information System (ESPIS). You will be able to obtain this report also from the National Technical Information Service in the near future. Here are the addresses. You may also inspect copies at selected Federal Depository Libraries.

U.S. Department of the Interior
Bureau of Ocean Energy Management
Alaska OCS Region
3801 Centerpoint Drive
Suite 500
Anchorage, Alaska
99503-5823
Telephone requests may be placed at
(907) 334-5208

U.S. Department of Commerce
National Technical Information Service
5285 Port Royal Road
Springfield, Virginia 22161
Phone: (703) 605-6040
Fax: (703) 605-6900

Email: bookstore@ntis.gov

CITATION

Zhang, X., J. Zhang, J. Krieger, M. Shulski, F. Liu, S. Stegall, W. Tao, J. You, W. Baule, and B. Potter, 2013: Beaufort and Chukchi Seas Mesoscale Meteorology Modeling Study, Final Report. U.S. Dept. of the Interior, Bureau of Ocean Energy Management, Alaska OCS Region, Anchorage, AK. OCS Study BOEM 2013-0119. 204 pp.

Acknowledgments

This study was funded by the U.S. Department of the Interior, Bureau of Ocean Energy Management, Alaska Outer Continental Shelf Region, Anchorage, Alaska, under Contract No. M06PC00018 as part of the BOEM Alaska Environmental Studies Program.

The Arctic Region Supercomputing Center at the University of Alaska Fairbanks (UAF) provided significant computing and storage resources, without which this project would not have been possible.

Special thanks go to Robert Pickart of the Woods Hole Oceanographic Institution (WHOI) for his great help in deploying our meteorological buoy in the Chukchi–Beaufort Seas in 2009 and 2011, which facilitated the collection of high-quality offshore data. We also thank Jennifer Hutchings of the International Arctic Research Center, Jun Inoue of the Japan Agency for Marine-Earth Science and Technology, Robert Raye of the Shell Oil Company, Frank Urban of the United States Geological Survey, Herman Wong of the U.S. Environmental Protection Agency (EPA), and Chris Yetsko of the ConocoPhillips Company for providing observational data that greatly benefited this study.

The project team is grateful for the efforts of Deanna Huff of the Alaska Department of Environmental Conservation, Walter Johnson and his group at BOEM, Robert Pickart and his group at WHOI, Tom Weingartner and his group at UAF, and Herman Wong of the EPA for graciously examining and testing our interim products in their applications, and for their feedback which assisted in optimizing the final reanalysis product.

Most of all, the team members would like to express our sincere appreciation to our project manager at BOEM, Warren Horowitz, who offered us invaluable assistance over the years in all facets of the project, and without whom the resultant products would have been greatly diminished. In addition, we thank Ron Lai, Heather Crowley, and Caryn Smith of BOEM, who provided excellent recommendations and feedback as to the course of our research, as well as the members of the project's Scientific Review Board—Keith Hines, Peter Olsson, Igor Polyakov, and Tom Weingartner—whose guidance throughout the course of this study has served to greatly enhance the quality and success of our research efforts.

TABLE OF CONTENTS

List of Figures

List of Tables

Partial List of Acronyms Used in This Report

AKST	Alaska Standard Time
ARM	Atmospheric Radiation Measurement
AVHRR	Advanced Very High Resolution Radiometer
BE	(Model) Background Error
BOEM	Bureau of Ocean Energy Management
CAI	Cyclone Activity Index
CAM	Community Atmosphere Model
CBHAR	Chukchi–Beaufort High-Resolution Atmospheric Reanalysis
CFSR	Climate Forecast System Reanalysis
CMC	Canadian Meteorological Centre
COSMIC	Constellation Observing System for Meteorology, Ionosphere, and Climate
CRN	Climate Reference Network
ECMWF	European Centre for Medium-Range Weather Forecasts
ERA-40	ECMWF 40-Year Re-analysis
ERA-I	ECMWF Interim Reanalysis
GCM	General Circulation Model
GFS	Global Forecast System
ISH	Integrated Surface Hourly (database)
JAMSTEC	Japan Agency for Marine-Earth Science and Technology
JRA-25	Japanese 25-Year Reanalysis
LSM	Land-Surface Model
LTER	(Arctic) Long Term Ecological Research
LW	Longwave (radiation)
MODIS	Moderate Resolution Imaging Spectroradiometer
NARR	North American Regional Reanalysis
NASA	National Aeronautics and Space Administration
NCAR	National Center for Atmospheric Research
NCDC	National Climatic Data Center
NCEP	National Centers for Environmental Prediction
NSIDC	National Snow and Ice Data Center
OCS	Outer Continental Shelf
OSU	Ohio State University
PBL	Planetary Boundary Layer
PDF	Probability Density Function
QA	Quality Assurance
QC	Quality Control
QuikSCAT	Quick Scatterometer
RAWS	Remote Automated Weather Station
RMSE	Root-Mean-Square Error
RRTM	Rapid Radiative Transfer Model
RRTMG	Rapid Radiative Transfer Model for GCMs
SEDNA	Sea Ice Experiment: Dynamic Nature of the Arctic
SHEBA	Surface Heat Budget of the Arctic
SIC	Sea Ice Concentration

SIT	Sea Ice Thickness
SLP	Sea Level Pressure
SST	Sea Surface Temperature
SW	Shortwave (radiation)
SWE	Snow Water Equivalent
UAF	University of Alaska Fairbanks
USGS	United States Geological Survey
UTC	Coordinated Universal Time
WERC	Water and Environmental Research Center
WHOI	Woods Hole Oceanographic Institution
WRF	Weather Research and Forecasting (model)
WRFDA	WRF Data Assimilation (system)

Abstract

The Chukchi–Beaufort Seas Alaska OCS region has experienced drastic changes over recent decades, as evidenced by a rapid sea ice reduction and more frequent extreme weather events. These changes may increase threats to the environment, given the potential for oil spills related to offshore drilling. Should an oil spill occur, the surface wind field is a crucial parameter for accurately predicting spill transport. As such, a mesoscale meteorological modeling study over the Chukchi–Beaufort Seas region has been conducted under support from the U.S. Department of the Interior, Bureau of Ocean Energy Management. A physically-optimized, Arctic-processes-enhanced Weather Forecasting and Research (WRF) model and WRF-based data assimilation system have been established; a meteorological buoy was successfully deployed over the highly sea-ice-dynamic Beaufort Sea; a quality-controlled observational database was developed from available sources; and, finally, the high-resolution Chukchi–Beaufort Seas High-Resolution Atmospheric Reanalysis (CBHAR) was constructed for the period 1979–2009 with the optimized model and quality-controlled observations. CBHAR represents an improved estimate of the regional atmospheric state throughout the study area. CBHAR surface wind fields reveal that winds, particularly extreme winds, have strengthened over the Chukchi–Beaufort Seas in the autumn. Intensified onshore winds occur during summer due to combined sea and mountain breezes along the eastern Brooks Range and Chukotka Mountains. During winter, the mesoscale cold-air damming effect diverts the synoptic northeasterly winds to the southeast along the northern slope of the Chukotka Mountains. In the Brooks Range, downslope winds are the predominant driver of the surface wind field.

1 Introduction

The Chukchi–Beaufort Seas region is currently undergoing significant environmental changes, including the fastest rate of decline and maximum observed interannual variance of sea ice anywhere in the Arctic (Comiso 2012), along with increased surface wind speeds over recent decades as the sea ice retreats (Stegall and Zhang 2012). In addition to natural changes, the potential for further offshore development by the oil industry also exists in the area (Figure 1.1.1). With oil extraction comes the threat of oil spills, which can have serious environmental consequences, leading to increasing attention from the government, scientific community, and general public (e.g., Gundlach and Hayes 1978; Picou et al. 2009; Webler and Lord 2010). Oil spills may impact not only the immediate area, but also remote regions due to transport via ocean currents and drifting sea ice. Given that the Chukchi–Beaufort coastal areas comprise a particularly vulnerable and fragile region, with an ecosystem and environment that are especially sensitive to human impacts (Ford and Pearce 2010; Doney et al. 2012), it is therefore of critical importance to be able to accurately predict the dispersal and movement of oil spills in the region, and to assess the potential environmental impacts should a spill occur. Doing so requires a good understanding of surface wind, a crucial parameter for assessing and predicting oil spill transport (Reed et al. 1999).

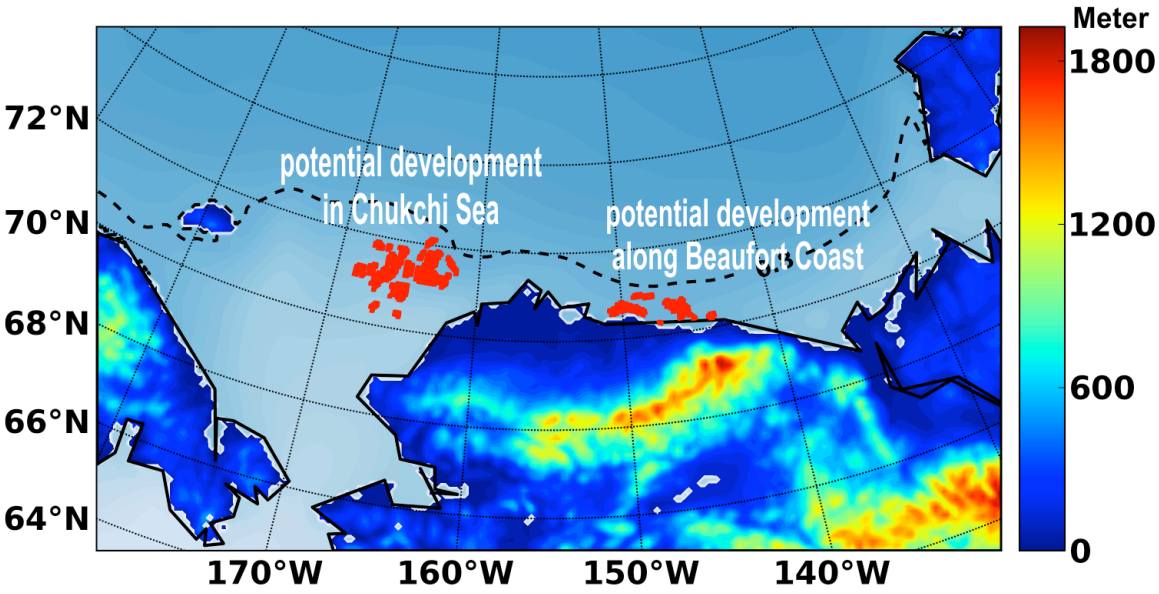

Figure 1.1.1. Potential locations of offshore oil development in the Chukchi–Beaufort Seas as indicated by the red shaded areas offshore (Source: BOEM leasing data provided by Warren Horowitz)

Surface wind is primarily determined by the interaction of prevailing synoptic weather patterns with prominent underlying geographic features; many studies of such factors impacting local wind regimes have been conducted for various regions around the world (e.g., Kozo 1979, 1980; Schwerdtfeger 1974; Parish and Bromwich 1987, 1991;

Bromwich 1989; Olsson and Harrington 2000; Parish and Cassano 2003; Liu et al. 2008; Moore and Pickart 2012). In the Chukchi–Beaufort Seas region, including across the Arctic Slope (known colloquially as the North Slope), the Beaufort High and Aleutian Low are the two dominant synoptic-scale weather patterns that most heavily influence surface winds (Shulski and Wendler 2007; Overland 2009; Moore 2012); when the intensity and location of these systems change, the surface winds over the study area vary in response (Lynch et al. 2004; Stegall and Zhang 2012). The prevailing synoptic circulations are modified by local geographic features, resulting in the generation of mesoscale circulations (e.g., Dickey 1961; Lynch et al. 2001; Moore and Pickart 2012). The geography in the study area is characterized by seasonally ice-covered ocean, along with the Brooks Range in northern Alaska and the Chukotka Mountains in eastern Siberia (Figure 1.1.2). In addition to the influence of topography, the presence of little-to-no sunlight during the winter months can cause the surface to become extremely cold, resulting in frequent temperature inversions throughout the area. Each of these local geographic features interacts with the prevailing synoptic weather systems to generate characteristic mesoscale atmospheric circulations that correspondingly influence the associated surface winds in the region.

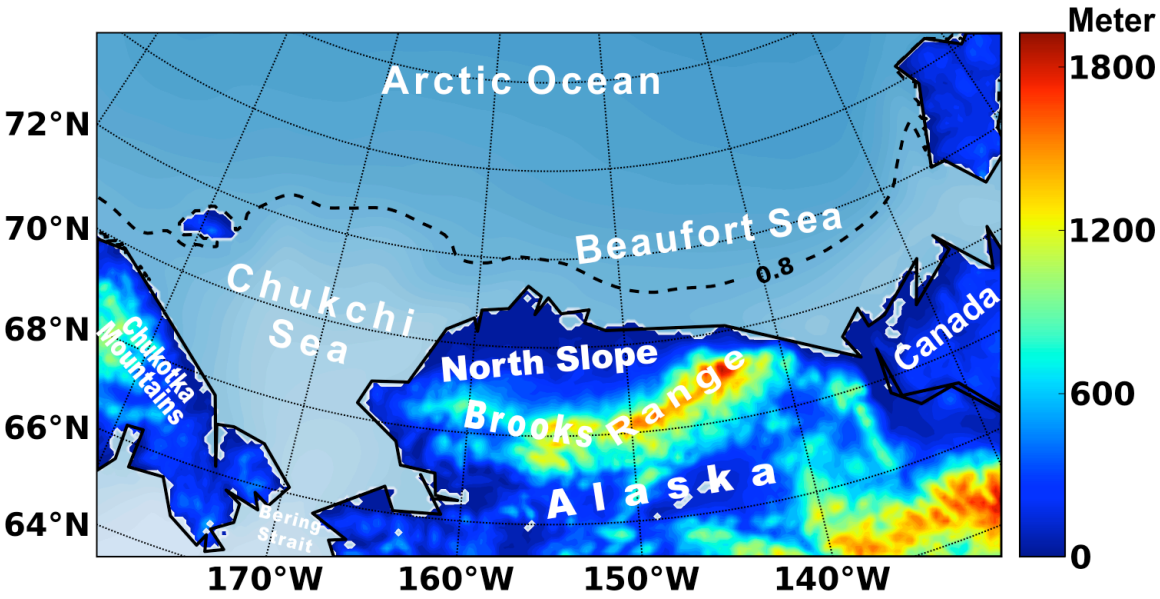

Figure 1.1.2. Study area, encompassing the Chukchi and Beaufort Seas, Chukotka Mountains, Arctic (North) Slope, Brooks Range, and parts of Interior Alaska and the Canadian Yukon. The mean climatological extent of 80% sea ice concentration is highlighted by the dashed line; topographic height (m) over land is shaded.

Due to the complexity of its predominant weather and climate systems, accurate numerical modeling of the study area poses a great challenge. To improve the performance of modeling the Arctic atmosphere, significant modeling and data analysis efforts have been made with the use of the state-of-the-art Weather Research and Forecasting (WRF) model (Skamarock et al. 2008). These have included the evaluation of WRF performance over a large pan-Arctic model domain (Cassano et al. 2011; Porter

et al. 2011), as well as the development of Polar WRF (Hines and Bromwich 2008; Bromwich et al. 2009; Hines et al. 2011), in which the model's Arctic land-surface processes and representation of sea ice have been improved. Most of these studies have focused on the Arctic as a whole, in contrast to the more regional interest of the current study. In order to better understand how the changing climate interacts with local finer-scale processes, and how these in turn impact the surface wind field over the Chukchi–Beaufort Seas and Arctic Slope, a comprehensive study of the region's mesoscale meteorology has been conducted and detailed herein. To achieve the best possible surface wind field climatology for the study area, two concurrent approaches have been adopted:

1) *Retrospective collection and climatological analysis of historical surface observations over the period 1979–2009 at a total of 262 sites throughout the study area.*
2) *Construction of a high-resolution regional reanalysis for the entire 31-year period through the synthesis of numerical simulations, in situ measurements, and satellite retrievals in support of climatological studies of the area's surface wind field.*

To implement the second approach, the WRF model and its data assimilation system WRFDA (WRF Data Assimilation) (Huang et al. 2009; Barker et al. 2012) have been applied to the study area (Figure 1.1.2) to generate the 31-year Chukchi–Beaufort High-Resolution Atmospheric Reanalysis (CBHAR) at a grid spacing of 10 km, with the goal to more accurately capture the finer-scale processes of the region's surface wind field than has been possible in prior larger-scale reanalyses. Based on the results of CBHAR, a comprehensive climatological analysis of the surface wind field over the Chukchi–Beaufort Seas and Arctic Slope has been carried out. In the following sections of this report, the detailed efforts conducted in this study and the resultant scientific findings are documented. The report is arranged as follows: observational data collection and analysis are summarized in Section 2; sensitivity tests conducted to physically optimize the model configuration for producing CBHAR are given in Section 3; detailed verification of CBHAR against the collected observations is described in Section 4; and a climatological analysis of CBHAR is detailed in Section 5.

2 Development and Analysis of the Chukchi–Beaufort Region Meteorological Database

2.1 Introduction

The study domain encompassed by this project spans from the Russian Chukchi Peninsula, including Wrangell Island, eastward to the northern Yukon and Northwest Territories of Canada, including Banks Island. Within this domain lie the Arctic Slope, Brooks Range, and northern Alaskan interior, as well as the Chukchi and Beaufort Seas (Figure 1.1.2). Geographically, the Arctic Slope is bounded to the south by the Brooks Range and to the north by the Arctic Ocean. The mountains provide a natural barrier separating this region, climatically, from the rest of Alaska. The ridgeline of the Brooks Range is somewhat curved and not precisely oriented along an east-west axis; in the east,

the mountains are situated much closer to the shoreline than in the west. This topographic feature has been shown to significantly influence the region's synoptic meteorological conditions (Dickey 1961; Kozo 1980; Kozo and Robe 1986).

Mean annual temperatures in the Arctic are well below freezing, being around −12°C along the northern Alaskan coast (Shulski and Wendler 2007). The winters are long and cold and the summers are cool and short; only 3–4 months have mean temperatures above freezing. No month reaches a mean temperature of 10°C on the coast, a condition necessary for tree growth. Precipitation is quite light at about 1000 mm annually, 75% of which falls as snow, which covers the ground for about nine months of the year. The Kuparuk weather station, located at the base camp of the Kuparuk oil field and close to the Beaufort Sea coast, has the lowest observed mean precipitation in Alaska, receiving only 92 mm annually (Shulski and Wendler 2007). However, precipitation in the region is normally underreported, due to the collection inefficiency of measuring gauges (termed "undercatch"). This is a well-known phenomenon and was first reported for the Arctic Slope by Black (1954). Further inland, the climate becomes more continental, with warmer summers, colder winters, and higher precipitation amounts.

The exact dividing line between the Alaskan coastal and continental climate regimes is not easily discernable. The most recent review of climate divisions for Alaska denotes that the climate from the Brooks Range northward encompasses the "North Slope" region (Bieniek et al. 2012). This paper utilized a cluster analysis technique using data from Barrow, Umiat, Barter Island, and Prudhoe Bay. For the current Bureau of Ocean Energy Management (BOEM) project described herein, it's noted that distinctions exist between the climate of locations along the coast and of those stations situated farther inland. Umiat, Alaska and Inuvik, Yukon Territory are positioned 115 km and 80 km from the coast, respectively. These stations provide a perspective of the inland climatology, which sometimes differs from the coastal perspective, represented by stations such as Barrow and Barter Island. This division will be discussed below as part of the climatological analysis (Section 2.4.1).

Along the coast, winds are persistent, with calm conditions prevailing only about 1% of the time. During the cold season, easterly winds generally predominate as a result of the Beaufort High, a semi-permanent feature in the pressure field centered offshore to the north of the coast. This high-pressure system produces the Beaufort Gyre, a characteristic anti-cyclonic flow in the oceanic surface waters. During the short summer season, a more local-scale phenomenon in the wind has also been observed. After the snow cover on land melts, a noticeable gradient in surface temperature arises from north to south as the land warms. This thermal gradient is enhanced by the constant daylight present at this time of year, inducing a sea breeze circulation that has been documented for the Alaskan Beaufort Sea coast (Kozo 1982a, 1982b).

Three additional major pressure patterns exist across the Arctic and sub-Arctic regions: the Aleutian Low, Icelandic Low, and Siberian High. The Aleutian Low, as the name implies, is located in the North Pacific in the area of the Aleutian Island chain. This semi-permanent pressure pattern is only evident during the cold season, from roughly October

through March. This region represents an area through which storm systems tend to track (from west to east) and intensify. These systems primarily affect the western and southern coasts of Alaska. During summer, the pressure increases, making wind and storm systems much less prevalent. In the North Atlantic, meanwhile, prevails the counterpart to the Aleutian Low: the Icelandic Low. It possesses quite similar characteristics and predominates over the winter pressure regime in the opposite hemisphere. The third primary pressure pattern, the Siberian High, is also a cold-season phenomenon that is established over the Eurasian continent, primarily over Russia. This pattern is regionally induced due to the large snow-covered landmass and results in relatively light winds across the continental interior and very low temperatures. A similar, but smaller-scale phenomenon occurs in sheltered and low-lying portions of Interior Alaska and Canada with the simultaneous occurrence of high pressure, low temperatures, and light winds.

The seasonal distribution of sea ice in the Beaufort and Chukchi Sea regions has garnered a great deal of attention in recent years. There exists a documented thinning and reduction in areal extent of the perennial ice pack that is most prevalent in this portion of the Arctic. The rate of change in sea ice cover has been found to be occurring faster here than in model projections (Stroeve et al. 2012), and, particularly during September (the time of year when minimum ice extent occurs), the Chukchi and Beaufort Seas have experienced a significant retreat in sea ice extent.

In the north-south direction, the study domain includes observations from 65°N to about 75°N latitude. The majority of surface stations in the domain are located in Alaska, while offshore in situ data come primarily from oil exploration well sites and buoys, primarily located in the shallow near-shore areas of the Chukchi and Beaufort Seas. It is from these meteorological stations (as described in the metadata accompanying the database) that the climatology described herein has been developed. Data from these observations were originally reported in various text-based formats, and were thus reformatted as part of this study in order to obtain uniformity in the data records and for inclusion in the final observational database. The processed and quality-controlled (as described below in Section 2.3) observational records were ultimately imported into an Oracle database platform for distribution to the general public. In addition to the in situ surface observations, QuikSCAT satellite-retrieved ocean-surface winds (described in more detail in Section 3.4) were also collected and incorporated into the observational database. See Appendix A for the database entity relationship diagram and a description of the tables included.

As described in the metadata report accompanying the database, the stations used for this study have widely varying periods of record; some, such as the exploration well sites, span only a few months, while others, such as the Barrow airport, have a complete 31-year record. Traditionally, international guidelines for producing a climatology require 30 years of data. For this study region, a 30-year data record is quite limiting and decreases the total number of available station locations to eight (Table 2.1.1 and Figure 2.2.1). A detailed climatological analysis will be discussed for these eight stations. However, in some cases the spatial detail provided by shorter-term stations warrants their inclusion. A

subset of these stations will accordingly be used to discuss spatial patterns and analysis, particularly for offshore areas.

Table 2.1.1. Long-term surface stations in the climatological database

Station	Latitude (°N)	Longitude (°E)	Elevation (m)
Barrow	71.300	−156.783	1.2
Bettles	66.916	−151.509	196.0
Deadhorse	70.192	−148.477	18.3
Inuvik	68.300	−133.483	68.0
Kotzebue	66.885	−162.579	4.9
Mys Shmidta	68.900	−179.367	4.0
Mys Uelen	66.150	−169.833	3.0
Ostrov Vrangelja	70.983	−178.483	5.0

Summary statistics have been calculated for the entire database on both a monthly and an annual basis, and are included with its distribution. Variables included in the summaries are surface air temperature, relative humidity, sea level pressure, and wind speed. The summarized fields for these variables include the monthly and annual average values (based on the individual hourly data points), monthly absolute maximum and minimum values, and the standard deviation of the monthly values. The statistics were computed based on the less-strict quality control measures ($f = 3$, detailed in Section 2.3). These summaries were calculated for all stations in the database as a means of comparison among stations. Note, however, that many locations have a short period of record. Therefore, a direct comparison of statistics from such stations with those from longer-term sites, such as those listed in Table 2.1.1, is not advised. In this report, however, statistics from shorter-term stations are given in order to provide some additional characterization of the data-sparse areas of the domain. In addition, summary data for the transient sites, such as ships (Ship_Obs-1, Ship_Obs-2, JAMSTEC, and Conoco_Ship), were calculated over the entire record and range of locations and should be treated as such. As these are not stationary sites, their summary statistics should not be compared with the other fixed stations.

2.2 Meteorological Observing Stations

2.2.1 Land-Based Measurements

Surface meteorological data from 262 stations, maintained by a variety of observing networks and various stand-alone projects, were obtained for this study, incorporating all available in situ meteorological data located in the domain for the period 1 January 1979 to 31 December 2009. Only a subset of these stations report for this entire time period and many stations have a relatively short period of record (i.e., less than 5 years). The following meteorological variables, where available, are included in the database: surface air temperature (°C), dew point temperature (°C), relative humidity (%), wind speed ($m\ s^{-1}$), wind direction (degrees), station pressure (hPa), sea level pressure (hPa), altimeter (in Hg), shortwave radiation ($W\ m^{-2}$), longwave radiation ($W\ m^{-2}$), 1-hr accumulated precipitation (mm), 6-hr precipitation (mm), 24-hr precipitation (mm), and snow depth (cm). Because the file format for each of the various datasets was not initially homogenous, the collected data files were standardized into a common format prior to quality control. All timestamps were transformed into Coordinated Universal Time (UTC) and missing observations identified as –999.0. Metadata for each observation include the year, month, day, hour, minute, latitude, longitude, and elevation at which the observation was made. A description of the various stations in the database, grouped by network, is given below. Since surface wind information is of particular importance to this study, relevant wind observation metadata are also included in the report (as well as in the metadata file accompanying the database).

A large portion of the stations in the database are represented in the Integrated Surface Hourly (ISH) database obtained from the National Climatic Data Center (NCDC), available at http://lwf.ncdc.noaa.gov/oa/climate/climatedata.html. Within the study domain, there are a total of 54 ISH stations in Alaska, United States, 14 in Chukotka, Russia, and 35 in Yukon and Northwest Territories, Canada (Figure 2.2.1) that reported observations during the study period. Elevation for the stations ranges from sea level up to 991 m, with an average of 153 m. In the U.S. and Canada, the anemometer height is standardized at 10 meters, though this does not necessarily hold true for all Automated Surface Observing System (ASOS) locations in the U.S. ISH stations are primarily located at airports across the region and are distributed fairly evenly throughout the domain. In Alaska, the stations within this network are most sparse in the region between the Brooks Range and Arctic coast. Also available from the NCDC are station observations of snowfall and snow depth, measured once-daily at a total of 49 stations in the study domain (Figure 2.2.2). These stations are often co-located with the hourly observing stations described above and shown in Figure 2.2.1.

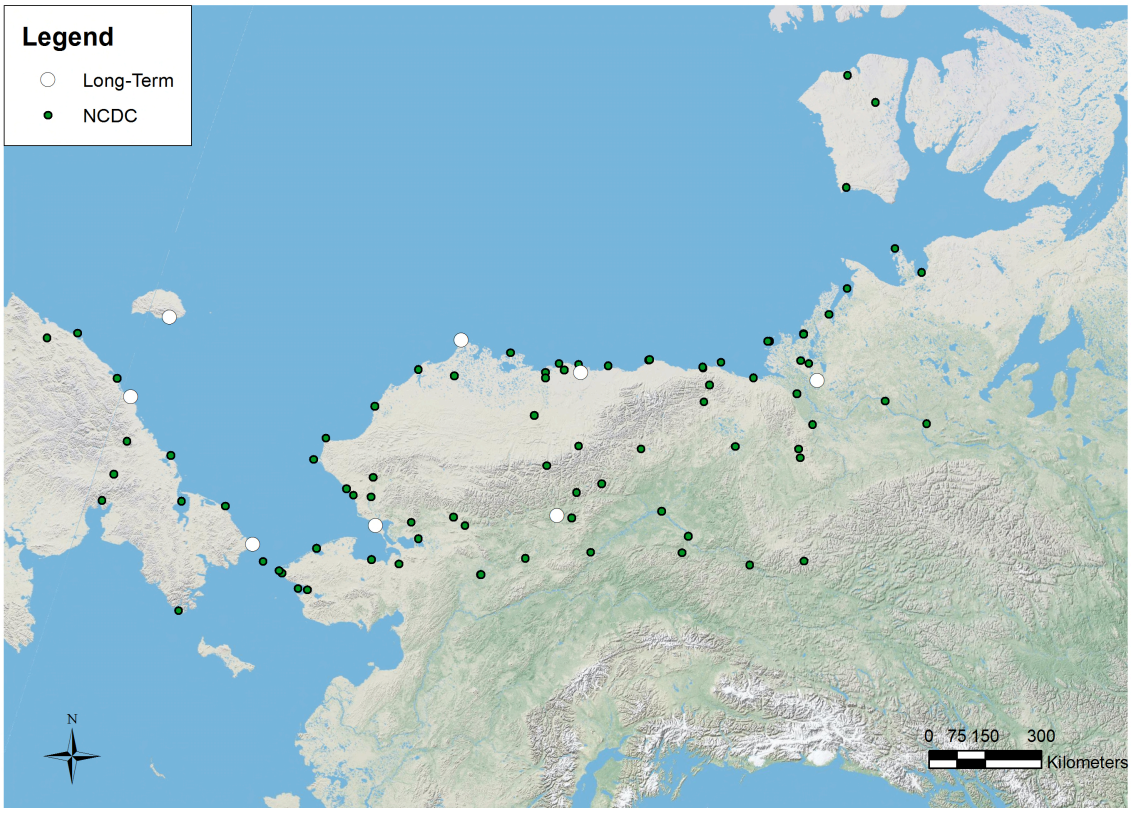

Figure 2.2.1. Locations of the 103 stations obtained from the National Climatic Data Center (NCDC). Stations denoted with a white circle indicate the long-term NCDC stations used for the climatology.

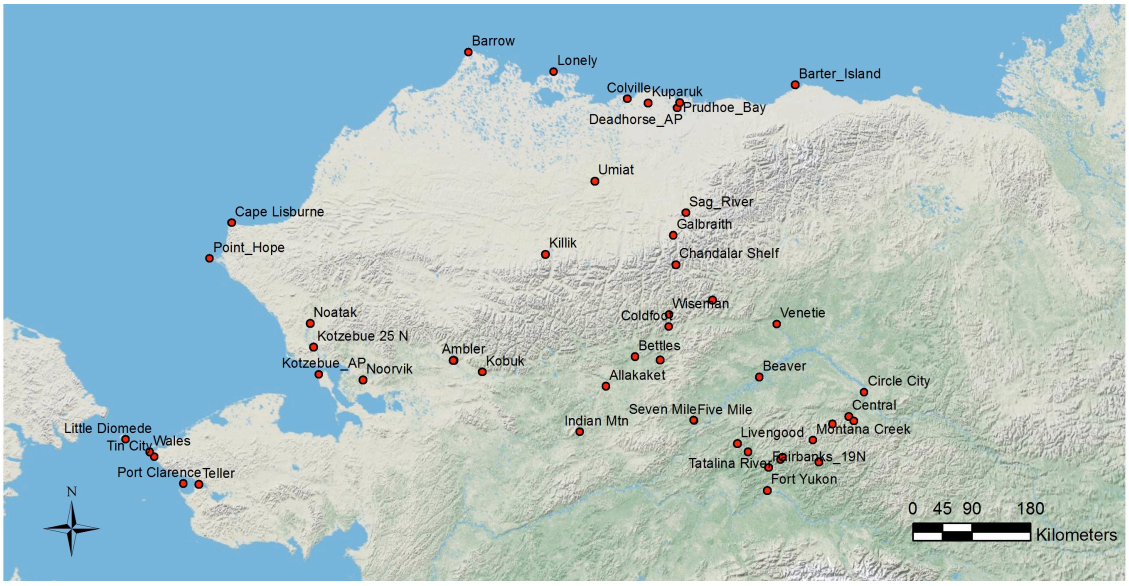

Figure 2.2.2. Locations of the 49 stations with daily snowfall and snow depth information obtained from the NCDC

Hourly data from a total of 32 Remote Automated Weather Stations (RAWS) (Figure 2.2.3) were obtained through the Western Regional Climate Center (http://www.wrcc.dri.edu). This network is designed to assist fire weather monitoring and most stations are thus located in remote areas of Alaska to the south of the Brooks Range (where fire danger is high). The most northerly station in this network is located at Umiat. Elevation for these sites ranges from 45 m above sea level at Kiana to 853 m at Helmut Mountain. For some of these stations, data are more often available in the warm season, or fire season, with infrequent or entirely missing winter observations. The period of record for RAWS sites goes back to 1988 for the longer-term sites, and the early 2000s for the shorter-term sites. The instrument configuration for these sites is standardized, with an anemometer height of 6.5 m and hourly wind speed observations that represent a 10-minute average.

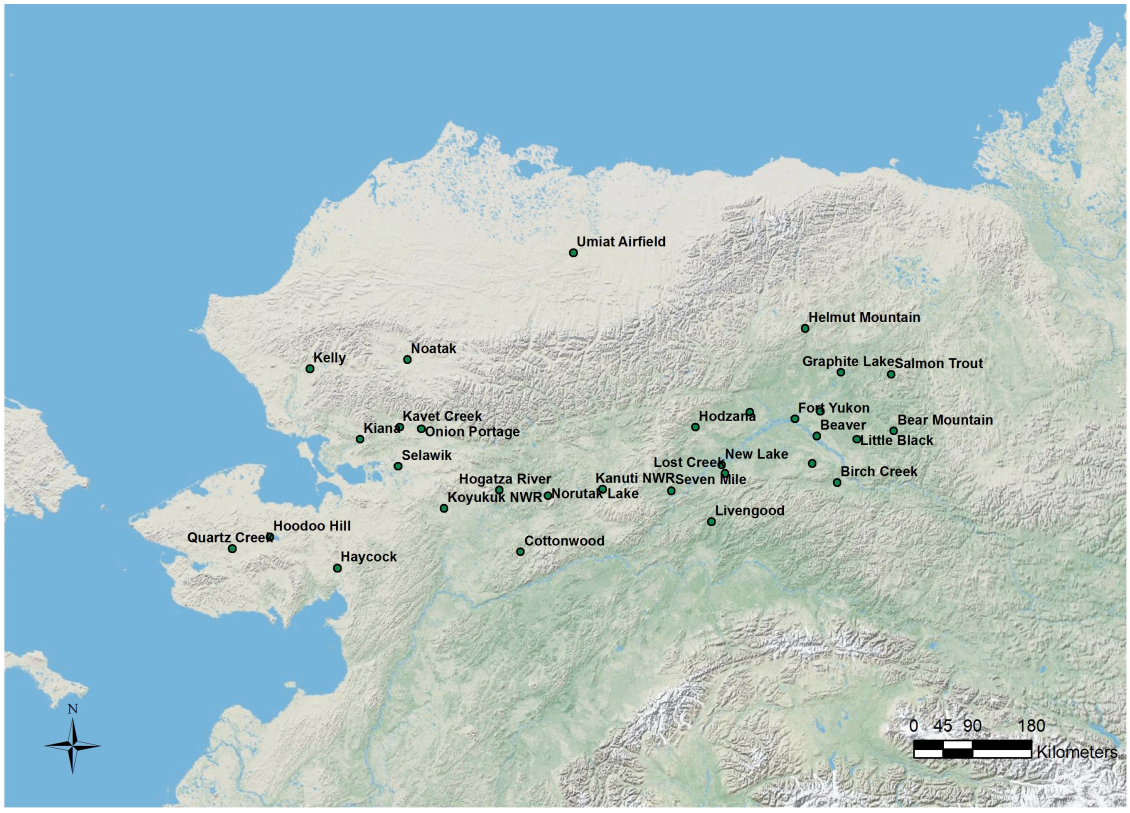

Figure 2.2.3. Locations of the 32 stations in the Remote Automated Weather Station (RAWS) network

Data for six sites in the vicinity of Prudhoe Bay (Figure 2.2.4) were obtained through the Bureau of Ocean Energy Management (BOEM, http://www.boem.gov); five of these had been established in a previous pair of BOEM meteorological studies (OCS Study MMS-2005-069 and OCS Study MMS-2007-011), with the sixth station at Cross Island established as part of a BOEM whaling study (OCS Study MMS-2009-038). Under these three studies, data collection began in January 2001 for stations at Endicott, Northstar, Milne Point, and Badami, with the Cottle Island and Cross Island stations being added to

the network in 2002 (Figure 2.2.4). Cross Island was a temporary station, only reporting data during the whaling seasons (late August to mid-September) of 2002–07. After September 2006, control of the stations at Badami, Cottle Island, and Milne Point was transferred to the University of Alaska Fairbanks (UAF), Water and Environmental Research Center (WERC). The six stations are located at or near the Beaufort Sea coast, with elevations ranging from 5 to 21 m above sea level (the elevation of Cross Island is unspecified, but very near sea level). Hourly-reported winds for the five permanent stations are computed using a 60-minute average and anemometer heights are 10 m (Badami, Cottle Island, Endicott), 14 m (Milne Point), and 23 m (Northstar). Cross Island reported observations every 5 minutes, with an unspecified anemometer height.

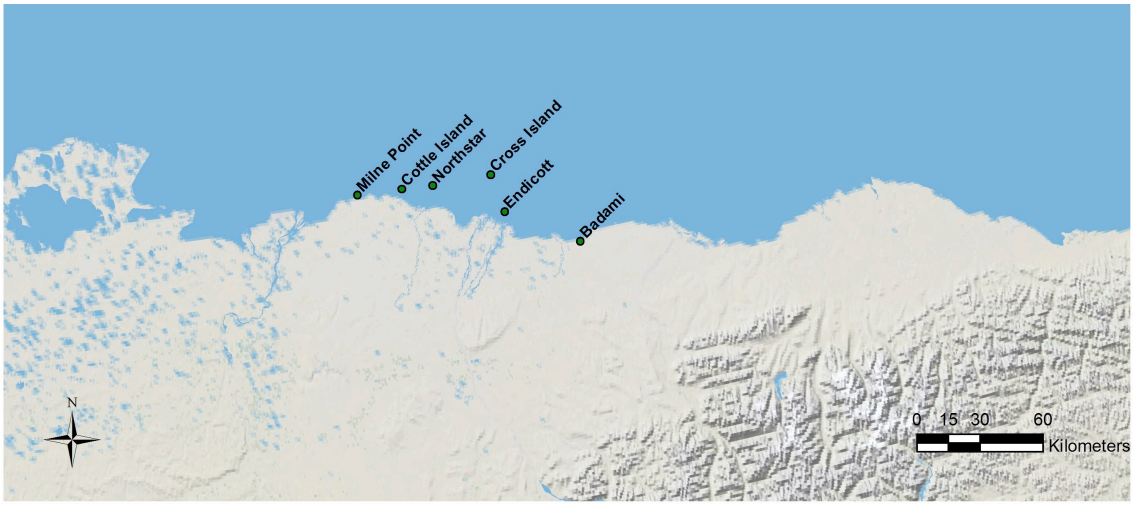

Figure 2.2.4. Locations of the 6 stations in the Bureau of Ocean Energy Management (BOEM) network

The Water and Environmental Research Center (WERC) at UAF maintains an extensive network of surface meteorological stations, primarily in the vicinity of Prudhoe Bay and locations southward along the Dalton Highway and the northern foothills of the Brooks Range (Figure 2.2.5). The few stations not in these areas are located on the Seward Peninsula in western Alaska. These stations have varying lengths of record, with datasets covering a period of 2 to 10 years. Metadata for this network of stations are quite good, with instrument height, make, and model all known. Several of these stations are located at higher altitudes, with elevations of more than 1000 m near the northern foothills of the Brooks Range. There are a total of 30 stations within the WERC network and hourly data were obtained from their website (http://ine.uaf.edu/werc).

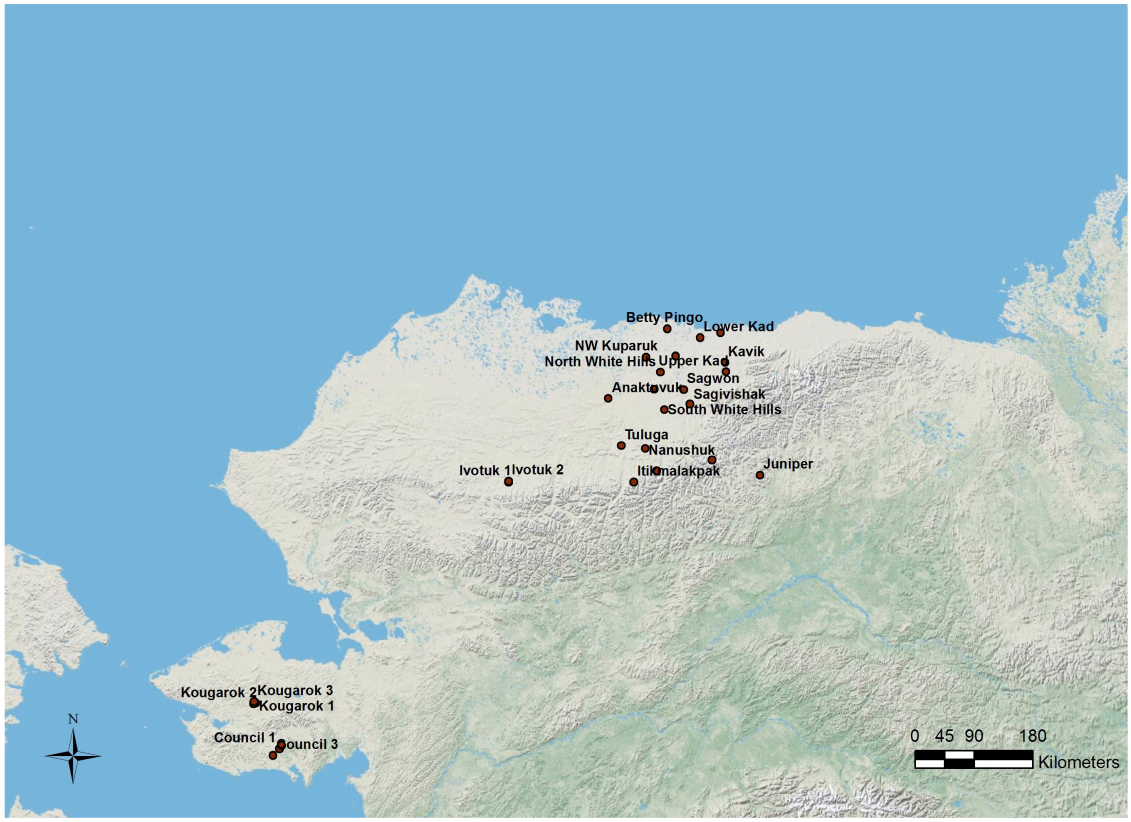

Figure 2.2.5. Locations of the 30 stations in the Water and Environmental Research Center (WERC) network

A station situated in the northern foothills of the Brooks Range is located at Toolik Lake and is part of the Arctic Long Term Ecological Research (LTER) site (http://ecosystems.mbl.edu/arc). Meteorological data are available since 1988. For wind information, the hourly data represent a one-minute average and anemometer instrumentation is mounted at 1- and 5-m heights.

The Arctic coast is also home to two stations (Barrow and Atqasuk) within the Atmospheric Radiation Measurement (ARM) network (Figure 2.2.6). This network, as the name implies, is primarily focused on measuring incoming and outgoing radiation for various spectral wavebands. However, additional meteorological data are also measured, with anemometers mounted at a height of 10 m. These data are observed at the highest frequency of the entire database, with observations made every minute. Data were obtained from the ARM website (http://www.arm.gov).

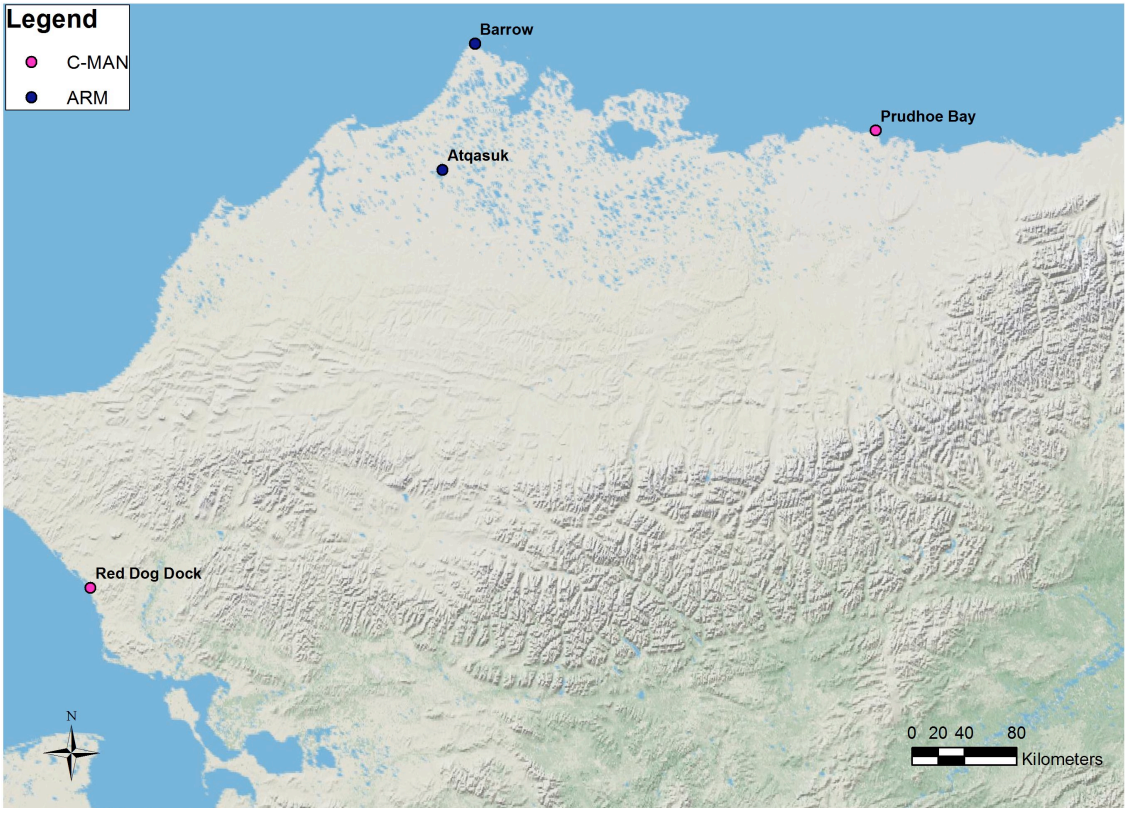

Figure 2.2.6. Locations of the 4 stations in the Atmospheric Radiation Measurement (ARM) network and the Coastal-Marine Automated Network (C-MAN)

Data from two coastal stations (Prudhoe Bay and Red Dog Dock) were obtained from the National Data Buoy Center Coastal-Marine Automated Network (C-MAN) program (Figure 2.2.6). These stations are situated at sea level and the anemometer instrument heights are 38 m for Prudhoe Bay and 17 m for Red Dog Dock. These data are available every six minutes for the period 2005 to 2008 and were downloaded from their website (http://www.ndbc.noaa.gov/cman.php).

Industry provided coastal station data from stations at Point Thomson, Reindeer Island, and Wainwright. These data are short-term, reporting for the latter one-half or one-third of 2009 and include hourly observations.

The United States Geological Survey (USGS) provided data for 10 stations in Alaska, most located along the Arctic coast, with a few additional inland locations (Figure 2.2.7). Hourly data are available for these stations and the starting year varies from 1998 to 2005. Data were obtained courtesy of the USGS (http://www.gtnp.org/index_e.html) and Frank Urban.

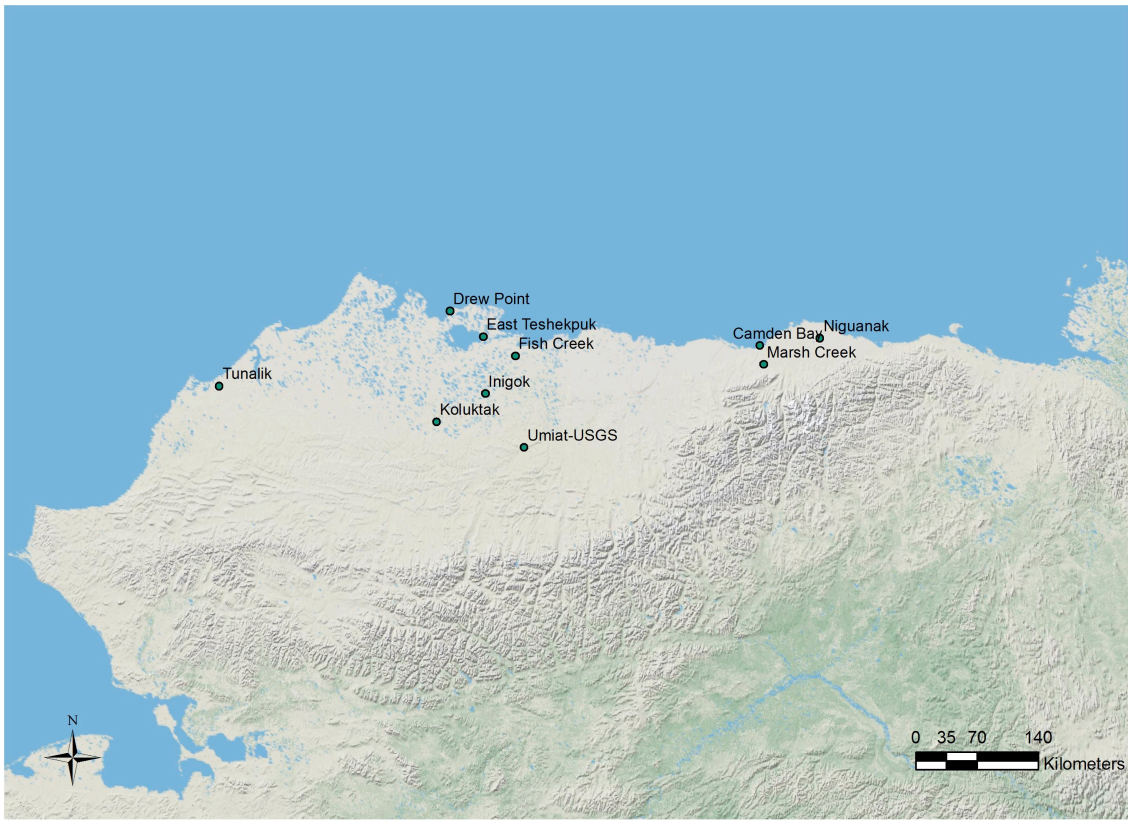

Figure 2.2.7. Locations of the 10 stations in the United States Geological Survey (USGS) network

2.2.2 Offshore Measurements

Shorter-term data are available from a variety of exploratory well sites that operated in the Beaufort and Chukchi Seas from 1986 to 2010 (Figure 2.2.8). These stations were in operation in the Chukchi Sea for one to three months during the open water season, and in the Beaufort Sea both during the open water season (1–3 months) and during the winter months when they occupied landfast ice. The reporting frequency for these data is every hour. The seasons of operation are variable, with the earliest records beginning in 1986 (Phoenix) and later records ending in 2010 (Point McIntyre Pad 2). These data were obtained through BOEM and there exist various data and metadata reports that provide additional information (Fairweather Forecasting, 1991, unpublished reports).

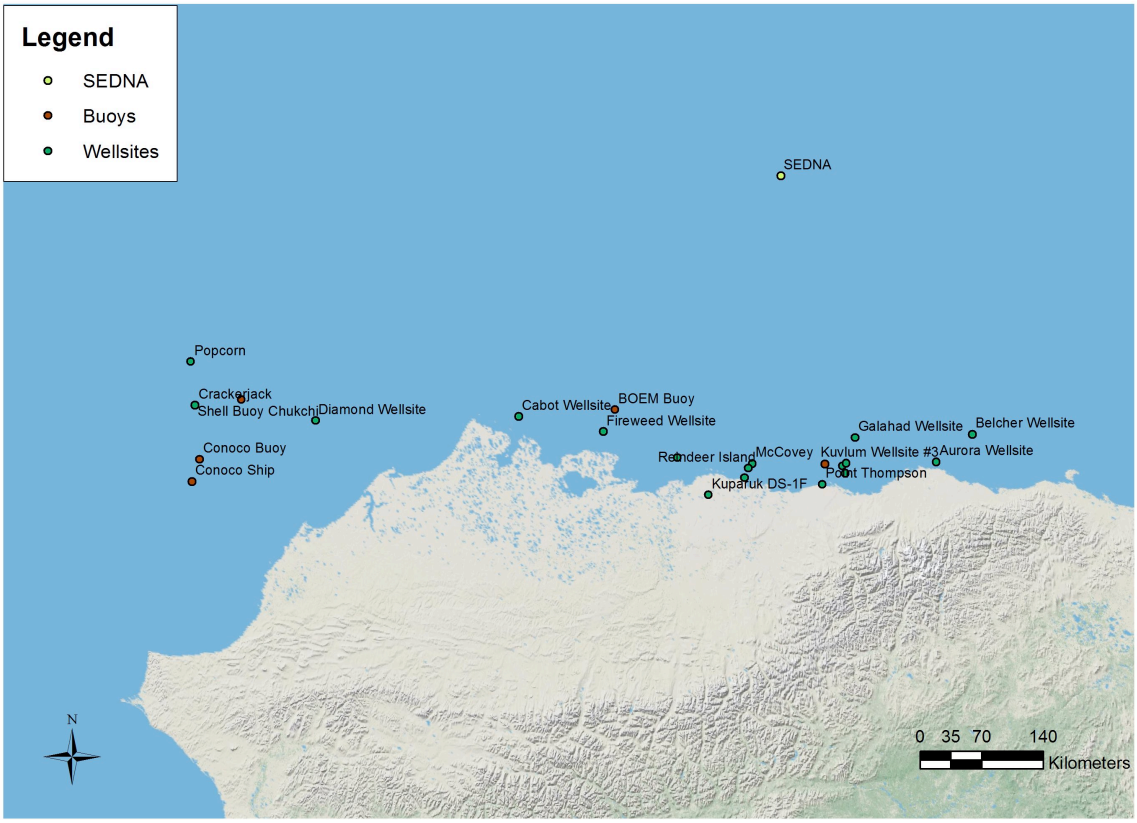

Figure 2.2.8. Locations of the well sites and buoys operating in the Beaufort and Chukchi Seas, along with the ice camp SEDNA

Offshore meteorological data also exist from buoys and ships that were operated in the study domain during the open water season by the ConocoPhillips and Shell oil companies. These represent short-term sites, with data collected for just a few months, and include data from three buoys and one ship (one buoy operated by ConocoPhillips in the Chukchi Sea (2009), and two operated by Shell in the Chukchi Sea (2008–2009) and Beaufort Sea (2009); the ship was operated by ConocoPhillips in the Chukchi (2008)) (Figure 2.2.8). Buoy data are reported every one or two hours and the ConocoPhillips ship data are reported every minute. In addition, the BOEM-funded project summarized in this report, the Beaufort and Chukchi Seas Mesoscale Meteorology Modeling Study, launched a buoy that operated in the western Beaufort Sea from early August to mid-September 2009 (Figure 2.2.8). Meteorological data are available for this time period at a frequency of five minutes.

Observational data from the scientific research vessel *Mirai* were obtained from the Japan Agency for Marine-Earth Science and Technology (JAMSTEC) from their website (http://www.godac.jamstec.go.jp/darwin/e). These data were largely observed within the study domain during the months of September and October and cover the years 1999, 2000, 2002, 2004, 2006, 2008, and 2009. The reporting frequency for these observations is 10 minutes.

Ship data were also obtained through the National Data Buoy Center. Observations from various ships traversing the domain comprise this dataset, which spans the years 2003 to 2009. The observation reporting frequency for these data is variable. When using these data, users must be aware of the shifts and changes in latitude and longitude in the time series since this dataset incorporates and combines data from multiple, distinct vessels. As such, the data cannot be interpreted as a single time series for a single ship track. Instead, observations are organized by timestamp, and consecutive values may not belong to the same ship track. This is the only dataset included here to have this type of time and location discontinuity.

High-quality offshore data were also available from the Sea Ice Experiment: Dynamic Nature of the Arctic (SEDNA), a field campaign that operated an ice camp in the Beaufort Sea (http://research.iarc.uaf.edu/SEDNA). A meteorological tower was installed in the pack ice and observations taken in April 2007, with data reported at 10-minute intervals (Figure 2.2.8). Wind observations were made at heights of 1.9 and 3.1 m, and the data represent 10-minute averages. Data were provided courtesy of Jennifer Hutchings of the International Arctic Research Center, UAF.

2.3 Quality Control of the Meteorological Database

Two major types of error may occur when performing quality control (QC) on meteorological data: a Type I error is the erroneous flagging of good data, and a Type II error is the failure to flag bad data. The frequency of these two types of error is a good indicator for evaluating the performance of QC methods. The purpose of research on QC methods is to produce optimal techniques to identify bad data while minimizing the frequency of Type I and Type II errors.

One of the objectives of the development of automatic quality assurance (QA) procedures for climate data is to reduce the manual workload of human validators. QA procedures have been applied by the NCDC (Guttman and Quayle 1990) in a mix of manual and automatic checks to assess the validity of weather data from cooperative climatological stations. The statistical literature is replete with general guidance about identifying outliers in data (e.g., Barnett and Lewis 1994), but literature concerning the application of techniques specific to quality assessment of climatological data is scant. General testing approaches, such as using threshold and step change criteria, have been designed for the review of single-station data to detect potential outliers (Wade 1987; Reek et al. 1992; Meek and Hatfield 1994; Eischeid et al. 1995; Shafer et al. 2000). Techniques have been expanding recently from procedures based on in-station checks to include procedures for inter-station checks (Wade 1987; Gandin 1988; Eischeid et al. 1995; Hubbard et al. 2005). The latter conduct tests from reference estimates using spatial techniques such as inverse weighting or statistical regressions between stations.

The high temporal-resolution data covering the Beaufort and Chukchi Seas region as collected for this project's observational database will greatly enhance modeling efforts from the regional to the global scale, by way of driving or validating meteorological models. However, techniques to quality control these datasets are not available within an

automatic system. This project thus introduced an enhanced system for application to this database that is based on the traditional QC methods presented in Hubbard et al. (2005).

2.3.1 Introduction to Observational Quality Control

The *upper and lower threshold test* determines whether a given variable (e.g., daily maximum temperature) falls within a specific range for the month in question. This test has been in use for some time and is based on the position of a value with respect to the standard distribution of observations. When relatively young stations are involved, the threshold test is often employed by considering the climatic extremes for the area (Shafer et al. 2000). When the limits are determined based on the statistical distribution, it has been called the *sigma test*, which utilizes the standard deviation (Guttman et al. 1988). The limits for the threshold test for a given meteorological variable x are determined by:

$$\bar{x} - fs < x < \bar{x} + fs \qquad (2.1)$$

where $\bar{x}$ is the daily mean (e.g., mean of daily maximum values for January) and s is the standard deviation of the daily values (e.g., daily maximum values) for the month in question. The variable x may represent any meteorological observation. The variable f is a variable related to the confidence level of a test obtained for the two-sided normal distribution. Being flagged with $f = 3$ represents 99.73% confidence that the data entry is an outlier (three standard deviations away from the mean), while $f = 4$ represents 99.99% confidence that the data entry is an outlier (four standard deviations away from the mean). Multiplying the standard deviation by these values of f gives two different confidence intervals that one can choose for identifying outliers.

An analysis using the methodology of Hubbard et al. (2005) was performed on the entire database (1979–2009) to determine the relationship between the percentage of data passing the test and various values of f. This procedure allows an informed choice regarding how many data points will be flagged in the natural data stream. If the data stream contained no errors, the values not passing the test would therefore all be Type I errors. In operational use, the data flagged as potential Type I errors are considered suspect and subjected to further manual checks; a realistic determination of f is therefore critical to project staff requirements. Graphs were developed to display the potential Type I errors versus f for the threshold test.

An example of a wind speed observation that failed the threshold test is the following observation from Prudhoe Bay (NCDC network). In March 1981, a wind speed value of 50.068 m s^{-1} was recorded. This value was caught by the threshold test as being an outlier and one that is well outside of the normal limits for this station. This represents a good example of how an excessive value was successfully caught by the automated threshold test. Incidentally, this value also failed the step change test, which is discussed below.

Year	month	day	hour	minute	latitude	longitude	**wind speed**
1981	3	6	17	0	70.25	-148.333	**50.068**

Another example of the threshold test catching invalid data was for dew point temperatures observed at Birch Creek (RAWS) during the summer of 2001. Values around −40°C were reported from 26–30 June and were successfully caught by the automated threshold test.

The *step change* (SC) *test* determines whether the difference between consecutive values of a variable fall within the climatologically expected limits of the daily rate of change for the month in question. In this case, the step is defined as the difference between values on days i and $i+1$, for example $x_i - x_{i+1}$. Utilizing this definition of x and calculating the associated mean and variance allow Equation 2.1 to again be used. An analysis of the data determines the relationship between f and the potential Type I errors for the SC test.

A relatively small number of observations and stations failed the step change test. However, data from the Shell buoy in the Chukchi Sea in 2008 failed the SC test when an unrealistic temperature change was reported. The following five consecutive observations from this station illustrate the large jump in temperature at 0200 UTC 15 October 2008 that was caught by this test.

Year	month	day	hour	minute	latitude	longitude	**air temperature**
2008	10	15	0	0	71.508	−164.072	−4.1
2008	10	15	1	0	71.508	−164.072	−3.7
2008	10	15	2	0	71.508	−164.072	**−11.4**
2008	10	15	3	0	71.508	−164.072	−2.8
2008	10	15	4	0	71.508	−164.072	−1.9

Another example of a step change error that was caught by the automated procedure is present in the following hourly data from the Council 1 station (WERC). In this example, duplicate reports were made for 1500 UTC 18 June 2008. Each variable for this observation *except* relative humidity was reported as −999.0. This issue happened multiple times at this location and the test successfully caught these errors in the Council dataset.

Year	month	day	hour	minute	latitude	longitude	**relative humidity**
2005	6	18	13	0	64.843	−163.705	96.2
2005	6	18	14	0	64.843	−163.705	96.1
2005	6	18	15	0	64.843	−163.705	**0.0**
2005	6	18	15	0	64.843	−163.705	95.9

The *persistence test* checks the variability of the measurements. When a sensor fails it will often report a constant value; thus, the standard deviation (s) will become smaller, and if the sensor fails for an entire reporting period, s will be zero. In other cases, the instrument may work intermittently and produce reasonable values interspersed with zeroed values, thereby greatly increasing the variability for the period. Thus, when the variability is either too high or too low the data should be flagged for further checks. The first step in this procedure is to calculate the standard deviation s_{jk} from the daily values for each month (j) and year (k) of the 31-year record. Likewise, the standard deviation of these monthly values (s_{jk}) is calculated over all years to obtain $\overline{s_j}$ and s_j', as shown in Equation 2.2. The persistence test compares the standard deviation for the time period being examined with the expected limits as follows:

$$\overline{s_j} - fs_j' < s < \overline{s_j} + fs_j' \qquad (2.2)$$

The period under consideration passes the persistence test if the above relation holds for the specified value of f.

Persistence tests were shown to catch instances of zero wind speed reported for long periods of time. For the Prudhoe Bay-Auto site (NCDC), the persistence test caught a period of nine days in the winter of 2006 (3–11 January) during which the wind speed was reported as a constant 0.0 m s^{-1}. Below is a sample of the output file, and as the two QC flags denote, this erroneous persistence was caught at both the f = 3 and f = 4 confidence levels (the meaning of the QC flag values will be discussed in Section 2.3.3).

Year	month	day	hour	minute	latitude	longitude	**wind speed**	**flags**
2006	1	3	2	0	70.4	−148.517	**0.0**	**4 4**
2006	1	3	3	0	70.4	−148.517	**0.0**	**4 4**
2006	1	3	4	0	70.4	−148.517	**0.0**	**4 4**

The persistence test also caught a similar instance for the Barrow CRN station in which the anemometer apparently froze. Wind speed values of 0.0 m s^{-1} were reported for a period of 1.5 months during the winter of 2005–06 from late December to mid-February. Similar periods of apparent anemometer freeze-up were again found for various additional portions of the winter at the Barrow CRN site.

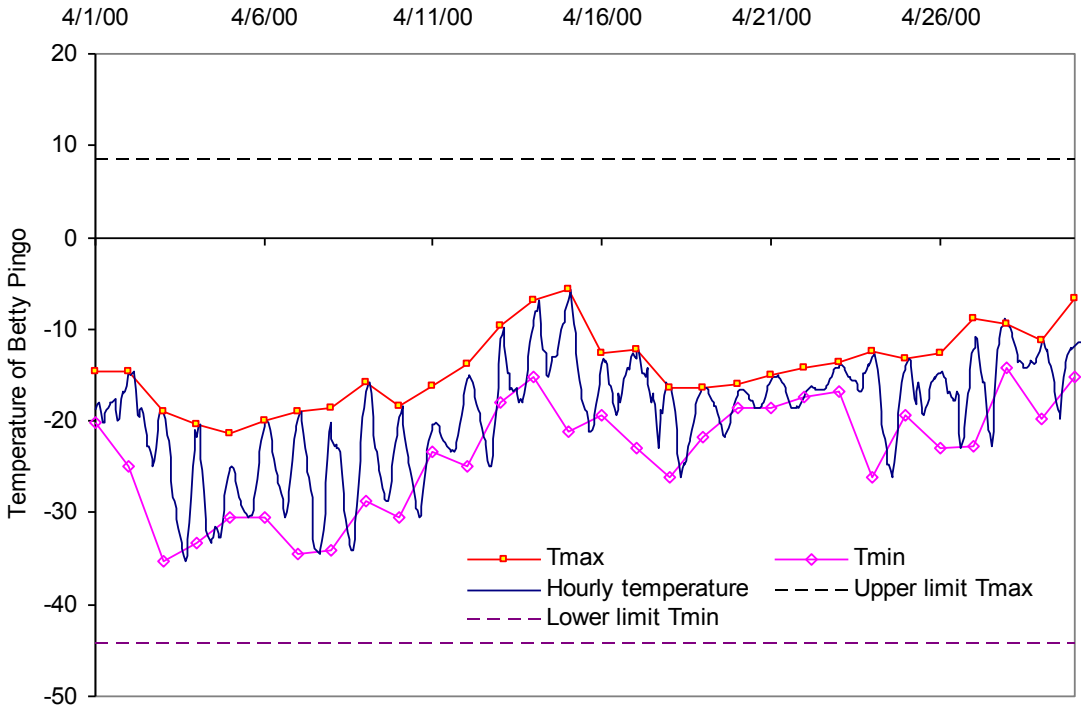

Figure 2.3.1. Example of the maximum and minimum daily temperatures created from high-resolution time series, along with the threshold limits used in the threshold test for Betty Pingo in April 2000

2.3.2 Enhancement to Basic Quality Control Procedures

The traditional basic QC procedures were originally developed for and tested with daily data, and thus need improvement for application to high temporal-resolution data. As part of the modification, the time series of the maximum and minimum daily values were calculated from the high-resolution data; an example of this is shown in Figure 2.3.1 for the Betty Pingo site. The mean (u) and standard deviation (s) of the daily maxima and minima can then be calculated from the time series as u_x, s_x and u_n, s_n, respectively. Thus, limits can be formed by modifying Equation 2.1 as:

$$u_n - fs_n < x < u_x + fs_x \qquad (2.3)$$

This equation forms limits defined by the upper limits of the maximum and lower limits of the minimum. The two dashed lines in Figure 2.3.1 indicate the upper and lower limits of the values for this example. Any value falling outside would be flagged as an outlier for further manual checking.

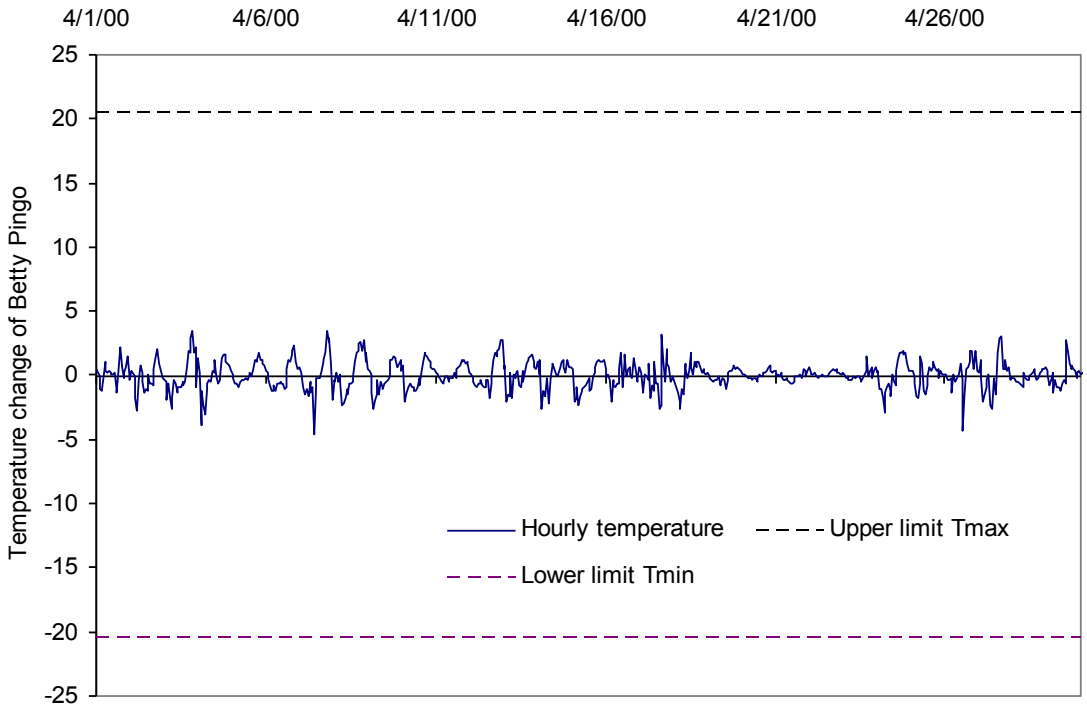

Figure 2.3.2. Example of hourly temperature change (°C) during a one-month period, along with the limits used in the step change method for Betty Pingo in April 2000

The diurnal change of a variable (e.g., temperature) was also calculated from the high-resolution (hourly or sub-hourly) data (e.g., Figure 2.3.2). The mean and standard deviation calculated from the diurnal changes were then used to form the limits. Since positive and negative changes are assumed to have the same probability, Equation 2.3 can be written as:

$$sc_{hr} < u_{sc} + fs_{sc} \qquad (2.4)$$

where sc_{hr} is the value change in a single time step, u_{sc} is the mean daily range, and s_{sc} the standard deviation of the daily range. Any change in value between time steps that falls beyond the limits fails the test and is flagged as an outlier.

The mean and standard deviation of the daily time series of variables were calculated to form the limits expressed in Equations 2.3 and 2.4. Several limits were calculated from the daily time series. In the current application, only air temperature, dew point, and pressure values have normal distributions, and can thus be QC'd for both sides. The other variables do not and thus can only be tested on the high end.

Certain variables required special treatment when performing the QC checks. Hard limits of 0 and 360 degrees were used for wind direction. A 10-inch (254 mm) precipitation value was used as an upper limit, in addition to the parameters calculated from the data itself, which overrides any possible very high precipitation amounts that may exist in the

dataset. The station pressure was also given special treatment, whereby the minimum and maximum pressures were first obtained from all stations. After manual examination, only those with reasonable values were retained in order to calculate the standard deviation of the minimum and maximum pressures as shown in Table 2.3.1.

Table 2.3.1. Computed limits of station pressure. *Max* and *Min* are the maximum and minimum station pressure of all stations, excluding significant outliers. *Stdev(max)* and *Stdev(min)* are the standard deviations of the maximum and minimum station pressures, respectively.

	Jan.	Feb.	Mar.	Apr.	May	Jun.	Jul.	Aug.	Sep.	Oct.	Nov.	Dec.
Max	1088.8	1072.3	1074.4	1072.8	1056.3	1079.2	1054.1	1064.3	1050.4	1082.8	1081.3	1058.0
Stdev(max)	12.2	15.4	11.5	11.4	7.7	11.1	6.8	9.6	6.4	9.1	9.1	12.3
f=3	1125.4	1118.6	1108.9	1107.0	1079.3	1112.4	1074.6	1093.1	1069.7	1110.0	1108.7	1094.9
f=4	1137.6	1134.1	1120.5	1118.5	1087.0	1123.5	1081.4	1102.7	1076.1	1119.1	1117.9	1107.2
Min	911.4	950.0	960.2	940.5	965.2	967.4	967.5	975.4	976.2	960.1	942.9	945.3
Stdev(max)	15.5	14.3	12.8	15.6	11.3	11.8	10.1	8.3	8.3	12.1	12.3	12.2
f=3	864.9	907.2	921.9	893.7	931.2	932.0	937.3	950.5	951.3	923.9	905.9	908.8
f=4	849.5	892.9	909.2	878.1	919.9	920.2	927.3	942.2	943.0	911.9	893.6	896.6

2.3.3 Quality Control Flags

Based on the results of the aforementioned QC tests, each meteorological observation value for all stations was assigned two QC flags. These two flags correspond to tests performed with differing levels of strictness, the first with a value of *f* equal to 4 (less strict) and the second with *f* equal to 3 (more strict). The value of the final QC flag is calculated as a weighted sum of three individual QC flags, as given by:

$$flag = a \times 4 + b \times 2 + c \qquad (2.5)$$

where *flag* is the final QC flag, *a* is the flag for the persistence test, *b* is the flag for the step change test, and *c* is the flag for the threshold test. In all cases, a flag value of 0 denotes that an observed value passed the particular test, while a value of 1 signifies that the test was failed. In the case of the persistence test, a value of 2 further signifies that not enough consecutive data points were available in order to determine success or failure. For hourly data, a minimum number of 15 valid observations within a 72-hour window are required to run the persistence test; otherwise, a value of 2 is assigned to the persistence test flag. Missing observations are assigned a QC flag value of –1.

Thus, given Equation 2.5, the final QC flags for all reported observations have values ranging from 0 to 11, depending on which of the individual QC tests were passed. The range of these is given in Table 2.3.2 as a function of the QC tests passed by the observed value.

Table 2.3.2. Values for QC flags in the observational database as a function of the QC tests passed by the observed value. *P* denotes the test was passed, *F* that it was failed, and *U* that not enough data were available to make a determination.

QC Flag	Persistence	Step Change	Threshold
0	P	P	P
1	P	P	F
2	P	F	P
3	P	F	F
4	F	P	P
5	F	P	F
6	F	F	P
7	F	F	F
8	U	P	P
9	U	P	F
10	U	F	P
11	U	F	F

2.3.4 Results and Summary

The QC methods used in this study detect three types of errors in the observational data. These errors are able to be identified using automated procedures because the identified outliers are statistically significant relative to the surrounding temporal data and the climatologically defined limits. The quality control results for the high-resolution in situ data in the Beaufort and Chukchi Seas region show some interesting patterns. For example, there were cases in which the QC checks identified suspect data entries such as:

1) Missing values denoted by values other than those specified in the metadata of the originating dataset.
2) Incoming shortwave radiation observations that had negative values at some stations, suggesting that additional calibration of the shortwave sensors is needed in order to limit such values to zero.
3) Typos in the entries of one or more variables for stations that do not measure the variable; e.g., the 1-hour precipitation at the stations Buhta Providenja and Cape Parry-Auto in the NCDC network. These data entries were also flagged.

From a manual analysis of the identified errors, most of the flagged data were likely caused by instrumentation failures or by the miscalibration of sensors, such as those that

generated negative shortwave radiation values. A significant number of radiation data entries from the ARM network have values around 0, which may be caused by sensor miscalibration. As a result, a large fraction of data for this variable and network were flagged.

The threshold test does not work for accumulated variables such as 6- and 24-hour precipitation and daily snow depth due to the flagging of too many data at the higher end.

The fraction of flagged data as shown in Table 2.3.3 reflects the overall quality of the different monitoring networks in measuring all observed variables. Across the entire database, the total percentages of flagged data are as follows: 0.99% for the threshold test, 0.02% for the step change test, and 1.34% for the persistence test. As shown in the table, the persistence test (used to detect a sensor reporting a constant value with no change in standard deviation) had the highest failure rate. In addition, a few observation types had much larger-than-average flagged percentages, including daily precipitation (NCDC), daily snow depth (NCDC), shortwave radiation (Toolik Lake), and 1- and 6-hr precipitation (NCDC).

In general, the small fraction of flagged values demonstrates the efficiency of the QC methods adopted in this study, allowing those values that are flagged to be manually checked in order to verify that they are truly invalid. For high-resolution measurements, manually checking the entire database would not be feasible due to the time requirements needed for such a task, and the automated procedures demonstrated here thus greatly reduce the labor involved.

Table 2.3.3. Percentage of flagged data for the three different quality control tests (separated by network and variable)

Network	Variable	Threshold	Step Change	Persistence
ARM	1-Hr Precipitation	0	0	0
	Dew Point	0.01	5.35E−05	0.03
	Longwave	0	0	0.01
	Relative Humidity	0.01	3.31E−05	0.10
	Shortwave	26.37	7.50E−05	2.07
	SLP	0	0	0.20
	Station Pressure	0	0	0.20
	Temperature	0.02	3.53E−04	0.13
	Wind Direction	0	0	4.54
	Wind Speed	0.78	1.26E−03	1.43
BOEM	Dew Point	0.06	3.60E−03	0.64
	Relative Humidity	0	1.06E−03	0.54
	Shortwave	0.03	3.19E−03	3.52
	SLP	2.41	0	0
	Station Pressure	0	6.18E−04	0.03

Network	Variable	Threshold	Step Change	Persistence
	Temperature	0.04	0.05	0.83
	Wind Direction	0	2.68E–03	0.36
	Wind Speed	0.95	0	1.21
Buoys	Dew Point	0	0	0.26
	Relative Humidity	0	0.07	0
	Shortwave	0.03	0	0.09
	SLP	0	0	0
	Station Pressure	0	0	0
	Temperature	0.01	0.03	0.38
	Wind Direction	0.10	0	0.65
	Wind Speed	0.08	0	0.13
C-MAN	SLP	0	0	0.07
	Station Pressure	0	0	0.07
	Temperature	0.05	2.26E–04	0.19
	Wind Direction	0	0	1.46
	Wind Speed	1.31	0	1.70
LTER	1-Hr Precipitation	0.02	0.01	37.81
	1-m Dew Point	0.07	7.11E–04	0.78
	1-m Relative Humidity	7.10E–04	1.42E–03	0.05
	1-m Temperature	0.03	0.03	1.30
	1-m Wind Speed	1.51	0	1.32
	5-m Dew Point	0.07	6.60E–04	0.76
	5-m Relative Humidity	0	6.60E–04	0.08
	5-m Temperature	0.04	0.03	1.28
	5-m Wind Speed	1.30	0	1.23
	Shortwave	27.73	2.54E–03	1.27
	Station Pressure	2.09	0.02	0.16
	Wind Direction	0	0	0
NCDC	1-Hr Precipitation	2.81	0.07	19.63
	6-Hr Precipitation	0.21	3.09E–03	18.79
	24-Hr Precipitation	3.60	0.04	3.54
	Altimeter	0	0.07	0.20
	Dew Point	1.20	0.10	0.44
	Relative Humidity	2.06	0.11	0.32
	SLP	0.00	0.07	0.22
	Snow Depth	6.61	0.01	0.83
	Station Pressure	1.89	0.04	1.98
	Temperature	0.21	0.09	1.30

Network	Variable	Threshold	Step Change	Persistence
	Wind Direction	0	0.02	0.50
	Wind Speed	0.92	0.05	1.76
RAWS	1-Hr Precipitation	0.19	0.07	6.53
	Dew Point	1.69	0.06	1.25
	Relative Humidity	2.60E–04	0.02	2.02
	Shortwave	0.04	0.01	6.64
	Temperature	0.16	0.01	1.64
	Wind Direction	3.22E–03	8.98E–04	1.07
	Wind Speed	0.99	4.02E–03	6.37
Ships	1-Hr Precipitation	0	0	82.75
	Dew Point	0.04	0.01	0.71
	Longwave	0	0	1.17
	Relative Humidity	0.09	0.06	0.18
	Shortwave	0	0	4.99
	SLP	0	0.01	0
	Station Pressure	0	0.02	0
	Temperature	0.10	0.03	1.29
	Wind Direction	0.27	0.43	0.24
	Wind Speed	0.89	0.05	1.16
Well sites	1-Hr Precipitation	0	0	72.57
	Dew Point	0	0	0.77
	Relative Humidity	0	3.85E–03	0.15
	Shortwave	0.02	0	13.20
	Station Pressure	0	0.07	0.29
	Temperature	0.02	1.70E–03	0.91
	Wind Direction	0	0.01	0
	Wind Speed	0.57	3.17E–04	0.53
	Altimeter	0	0.07	0
	SLP	0	0	0
WERC	1-Hr Precipitation	0.48	3.57E–03	40.82
	1-m Dew Point	0.06	3.50E–03	0.99
	1-m Relative Humidity	0.13	3.50E–03	0.60
	1-m Temperature	0.03	9.61E–04	0.99
	3-m Dew Point	0.05	1.71E–03	1.23
	3-m Relative Humidity	4.44E–03	1.28E–03	0.51
	3-m Temperature	0.04	3.48E–03	1.00
	Snow Depth	0.08	3.13E–02	6.25
	Station Pressure	2.94E–03	8.82E–03	18.16

Network	Variable	Threshold	Step Change	Persistence
	Wind Direction	0.01	2.98E−03	0.33
	Wind Speed	1.24	7.89E−03	1.57
	Total	***0.99***	***0.02***	***1.34***

As demonstrated here, the applied in-station QC tests can successfully identify outliers in the observational dataset. However, spatial tests that consider data from neighboring stations can, in some cases, be more robust in identifying errors or outliers when strong correlations between different stations exist. Figure 2.3.3 shows a promising example of the correlation between temperature observations at West Dock and Betty Pingo in May 2000. A strong relationship between measurements at station pairs suggests the potential opportunity for applying the spatial regression test (SRT, Hubbard et al. 2005) to stations that measure the same variables, such as air temperature and wind speed. Further testing of this method is required in order to successfully perform this type of test on the entire observational dataset.

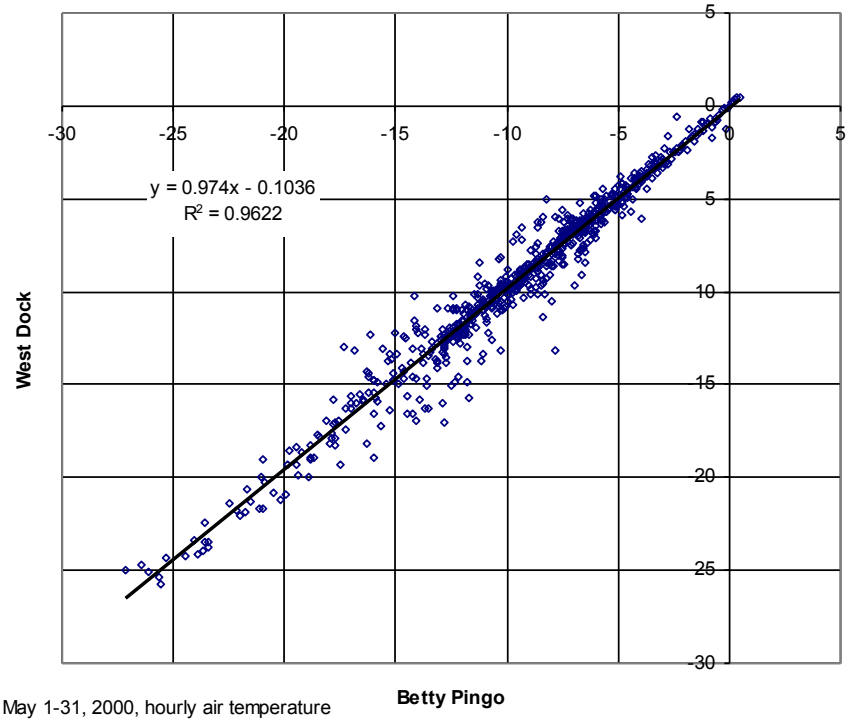

Figure 2.3.3. Example of a strong correlation in the hourly air temperatures (°C) between Betty Pingo and West Dock for May 2000

The three QC methods described in this work perform better when operating on a long-term dataset, and so the short-term periods of record at some stations in the study area may not be efficiently quality controlled if only using the methods detailed here. The lack of a long station history with which to set limits, determine standard deviations, and

establish other parameters used by the three different QC checks limits their utility when applied to short-term datasets.

The automated checks work equally well regardless of network or region. A station-by-station look at the quality control results shows that there are problem stations, rather than problem networks or regions, as there appear to be no major systematic differences in the QC performance with respect to network or region. Some particularly poor-performing stations are the sites with very short and highly discontinuous records, due to the lack of a sufficiently long station history with which to determine the in-station limits, and because the step change and persistence tests require periods of continuous data, without gaps, in order to perform properly. For most of the very short-term sites, this is not the case. As an example, measurements at the Tuktoyaktuk 2 site (NCDC) begin in January 1979 and end in April 1981; however, only 14% of the hours in that timeframe contain observations, with the remaining 86% lacking data. For sites such as these, aside from the use of the threshold test, it is nearly impossible to automate quality control routines. The only alternative would be to check observations hour by hour with those of a neighboring station, if available.

In aggregate, less than 5% of the observational data were flagged (Figure 2.3.4). This relatively low percentage of flagged data is indicative of the overall good quality of the station measurements. For the most part, these data had gone through some form of quality control by their maintaining agencies prior to acquisition by this project. In terms of overall performance, the BOEM, buoys, C-MAN, and exploration well site networks performed better than the ARM, LTER, NCDC, RAWS, ship, and WERC stations. The persistence test was failed more frequently than either the threshold or step change tests for nearly all stations.

A certain portion of the data was not able to undergo the threshold and step change tests (Figure 2.3.4) due to the lack of continuity necessary for these tests to be conducted. As a result, these particular tests could not be applied for some periods of time at various stations. In contrast, the threshold test could be performed on all data, regardless of the presence of missing observations.

When separated by variable, the wind direction and wind speed were flagged the most often, failing QC tests nearly 2% of the time (Figure 2.3.5). In spot-checking the data records, it appears that these tests most often identified cases of zero wind speed and/or wind direction that lasted for periods of several days. It is assumed that sensor failure due to icing was the cause of these events. The spot-checking also found that cases of persistent high wind speeds were flagged by the persistence test. Given the climatology of the coastal region, it is known that such cases do, in fact, periodically occur. It is therefore recommended that users of the database manually check such instances when investigating periods of consistently high wind speed in which the persistence test was failed.

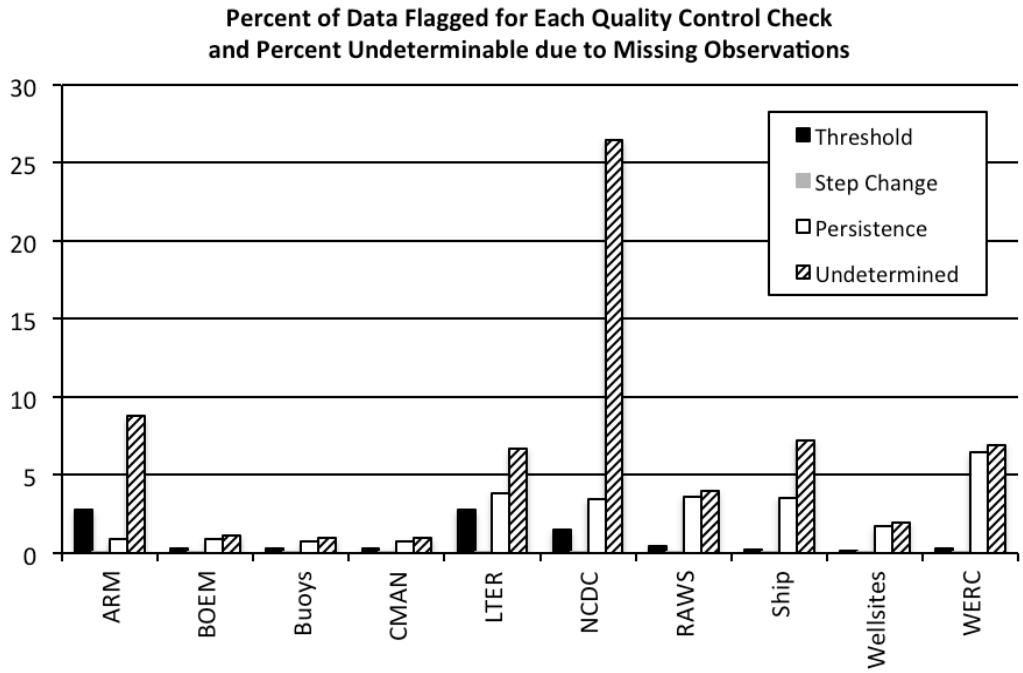

Figure 2.3.4. Total percentage of flagged data for the three automated QC checks as delineated by the major observational networks. Percentage of data that were not able to undergo the step change and persistence tests due to missing observations is also given.

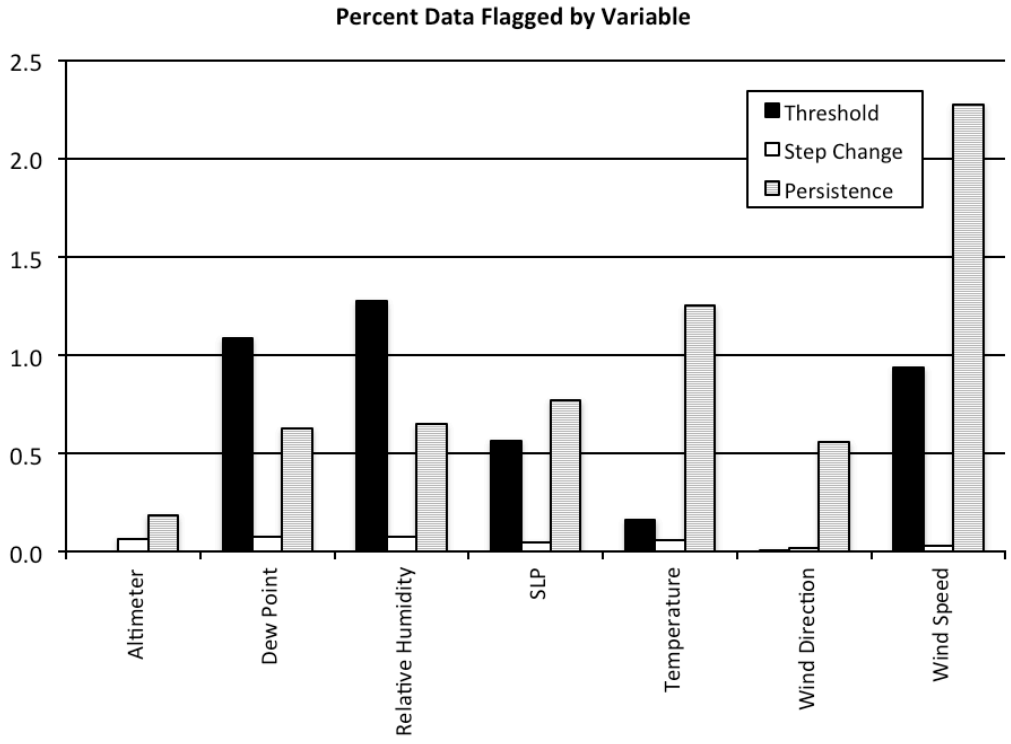

Figure 2.3.5. Total percentage of flagged data as categorized by variable and QC test

2.4 Analysis of the Meteorological Database

2.4.1 Climatology of the Long-Term Observations

Temperature Patterns

For most locations in the study domain, the mean temperature of the warmest month is below 10°C (Figure 2.4.1). The months of June, July, and August have mean temperatures above freezing, while the transitional months of May and September may be above freezing for some years. February is typically the coldest month, with mean temperatures in the –25°C range, with January the coldest for Kotzebue, Umiat, and Inuvik. The region inland from the Beaufort and Chukchi Sea coasts, throughout the Arctic Slope, exhibits a climate that is more continental in nature, with higher temperature variability and warmer summers. See, for example, the temperature variability at the inland stations of Umiat and Inuvik as compared to the coastal sites of Barrow and Deadhorse (Figure 2.4.2). The Brooks Range acts as a geographical dividing line between what is traditionally considered the Arctic Slope and the strong continental climate of the interior. This mountain range acts to block southward-moving systems, sheltering the interior from the influence of the Arctic marine air mass.

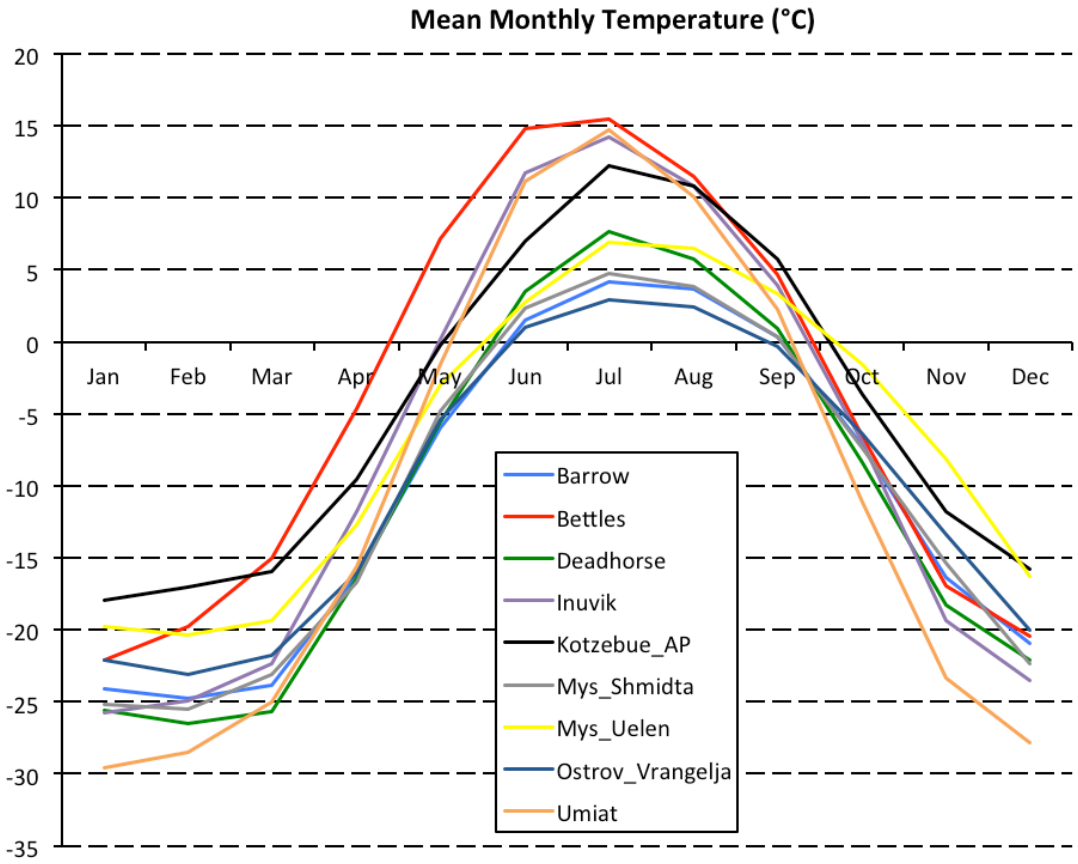

Figure 2.4.1. Mean monthly temperatures (°C) for the long-term stations in the region

Along the Arctic Slope, there is a general longitudinal gradient in temperature from the coast inland that varies with season and local weather conditions, and that exhibits some significant variability. As an example, a comparison of monthly temperature observations between Barrow and Atqasuk shows that Atqasuk is, on average, colder by approximately 3°C from November to March. From May through September, however, Barrow is colder, with the months of June through August displaying the greatest mean temperature difference of 3°C to more than 5°C. The same type of gradient is seen for the Beaufort Sea coastal region. This summertime thermal gradient is what allows the sea breeze phenomenon to take place.

A frequency distribution of the observed temperatures in the region illustrates a predominantly bimodal distribution (Figure 2.4.2). This occurs throughout the domain regardless of proximity to the coast; however, the shape of the distribution varies depending on location. Inland locations experience a wider range of temperatures throughout the year, whereas coastal locations exhibit a more narrow distribution, with fewer extremes. The modes of the distribution are centered in the −20 to −25°C range, indicative of wintertime conditions, and 0°C during the short summer season. The tails of the distribution are widest for the Umiat, Inuvik, and Bettles locations that are 80 km or more from the coast.

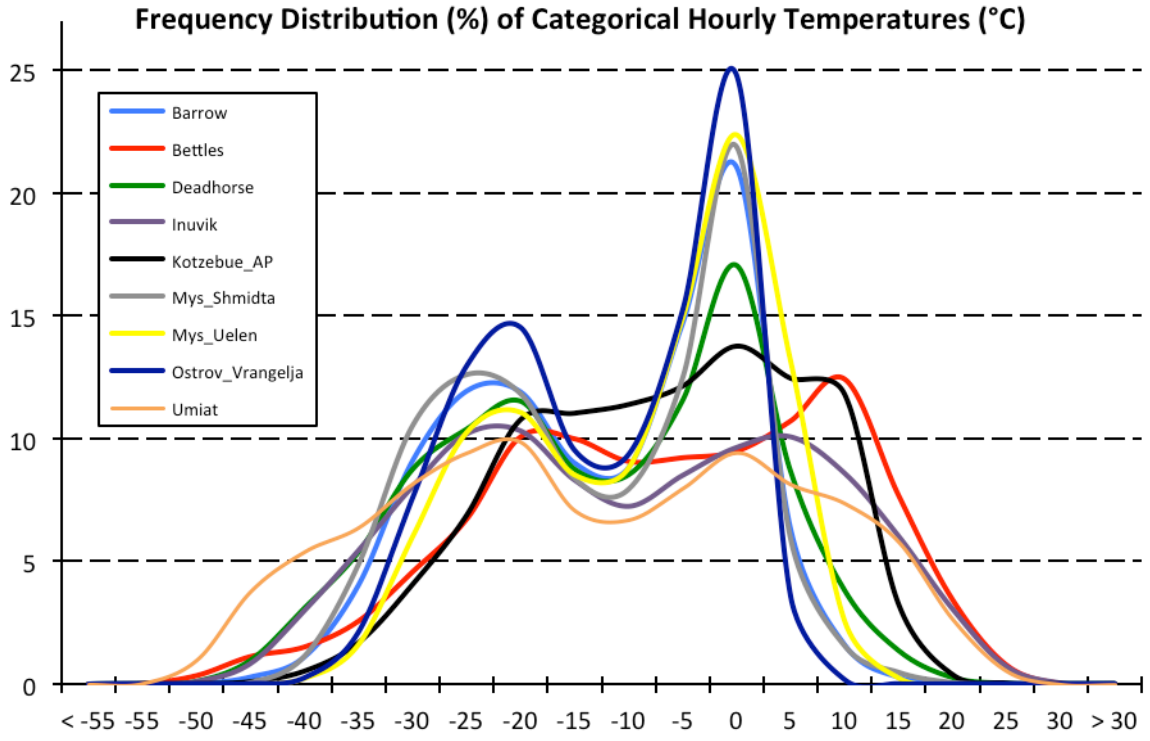

Figure 2.4.2. Frequency distribution of observed temperatures (°C) for the long-term stations

Differences related to location are also evident when looking at temperature extremes. As shown in Figure 2.4.3, the range of observed temperatures for Umiat, Inuvik, and Bettles

is larger than for coastal areas such as those at Ostrov Vrangelja and Barrow, regardless of latitudinal differences.

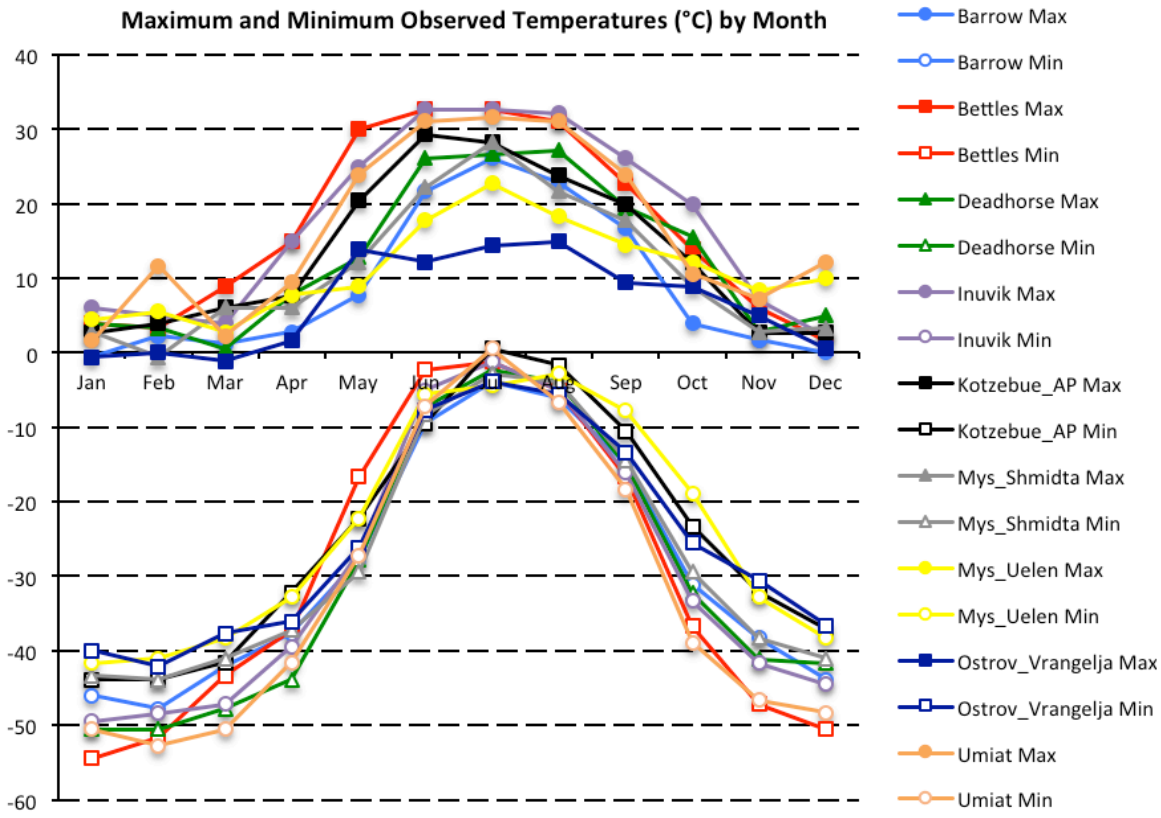

Figure 2.4.3. Monthly maximum and minimum temperatures (°C) for the long-term stations

Winds

Surface wind conditions in the study domain show distinct regional differences that depend on local topography, distance to the coastline, and proximity to semi-permanent pressure patterns. The dominant feature for coastal locations in the domain is the influence of the Beaufort High on the wind direction regime. Along the entire Beaufort and portions of the Chukchi coasts, winds exhibit a strong easterly component, associated with this synoptic-scale pressure feature that is in place during the cold months. Winds transition somewhat during the summer, resulting in a slightly more westerly component. The resulting annual wind rose has a strong east-west bimodal distribution. Detailed wind rose plots for Barrow are shown for the months of February and August (Figures 2.4.4 and 2.4.5, respectively).

For coastal locations in the far western region bordering the Bering Sea (Mys Uelen), or on Wrangell Island (Ostrov Vrangelja) in the far north, the wind regime is more influenced by local topography. As such, the wind direction distribution is less east-and-westerly than at locations such as Barrow or Barter Island. For example, Wrangell Island also displays a strong bimodal distribution, though instead oriented in the north-south

direction. The observing location is situated on the southern edge of Wrangell Island and it is assumed that local topographic features play a part in determining wind directions there.

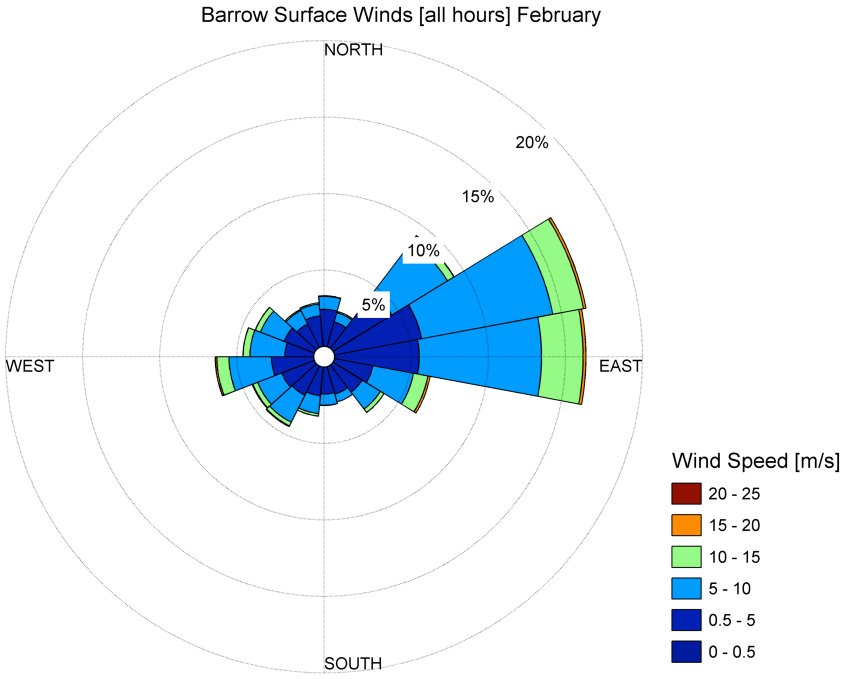

Figure 2.4.4. February wind rose climatology for Barrow (1979–2009)

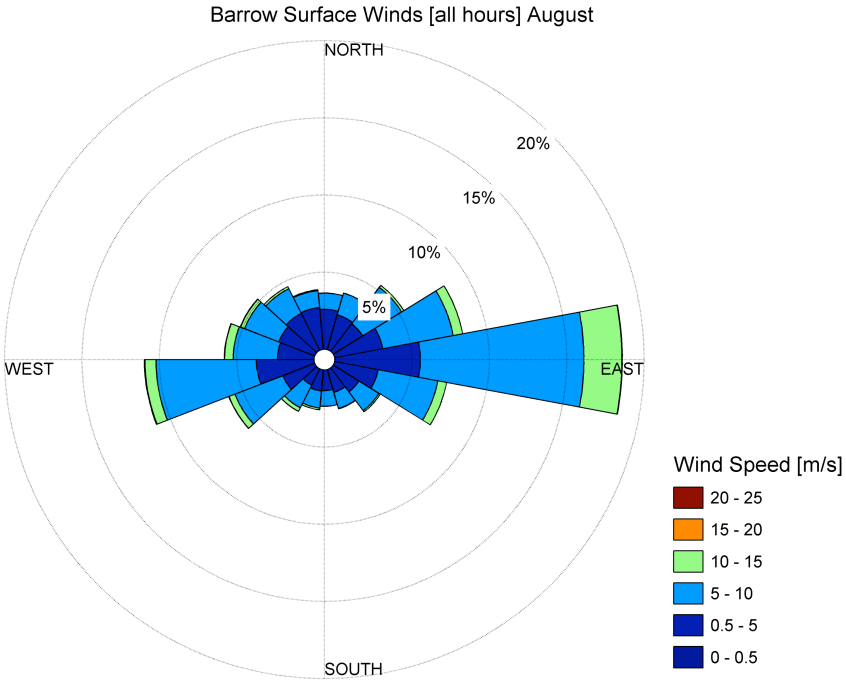

Figure 2.4.5. August wind rose climatology for Barrow (1979–2009)

Wind speed conditions for locations near the coast are consistently high throughout the year with few, if any, periods of calm (Figure 2.4.6). Mean monthly values lie in the 5 to 6 m s^{-1} range for locations such as Barrow, Deadhorse, and Kotzebue. Some coastal locations exhibit seasonal variability in which the lowest wind speeds are found in late spring and summer. The Russian stations Mys Shmidta, Mys Uelen, and Ostrov Vrangelja all have a seasonal maximum in the late autumn and early winter. For all coastal locations, the highest annual wind speeds on the order of 20 to 25 m s^{-1} are found during the winter season, with a minimum during summer (Figure 2.4.7). The winter months are the time of year when storms frequently influence the region, as discussed later in Section 5.3.

The standard deviation of the hourly wind observations shows a similar seasonal variation, with the highest values during winter (3–5 m s^{-1}) and lower values in summer (2–3 m s^{-1}) (Figure 2.4.8). Again, this is indicative of the stormy period that occurs during the cold months, which is characterized by higher variability in wind speeds. Calm conditions occur less than 5% of the time in these coastal environments.

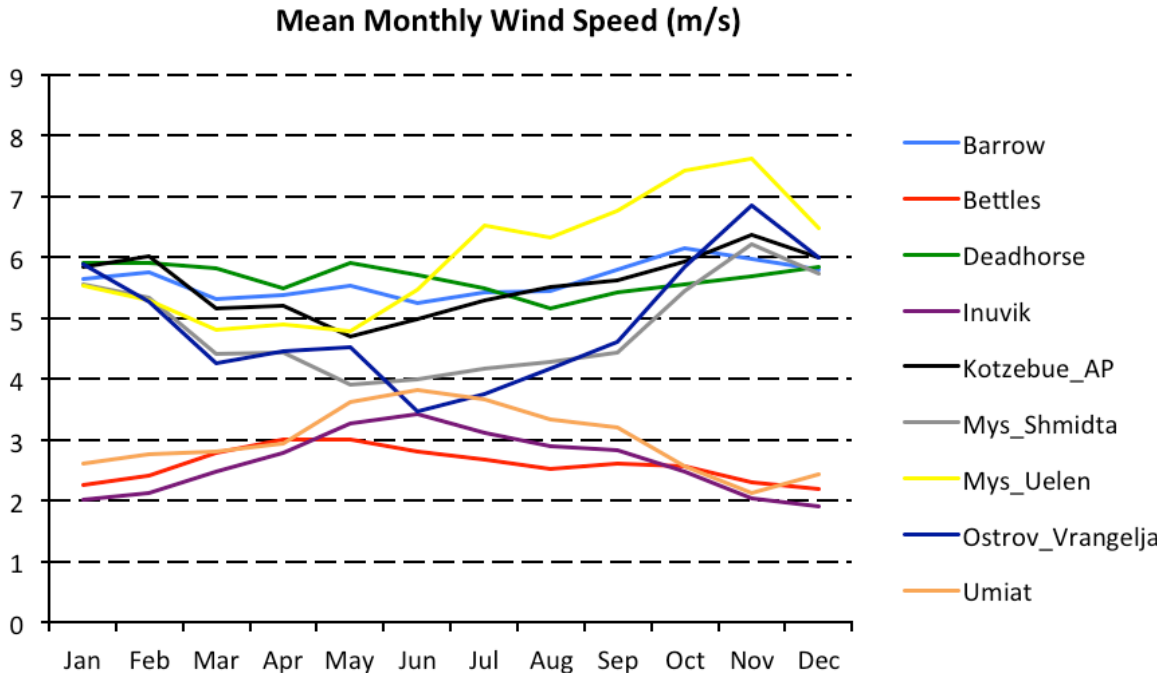

Figure 2.4.6. Mean monthly wind speed (m s^{-1}) by month for the long-term stations

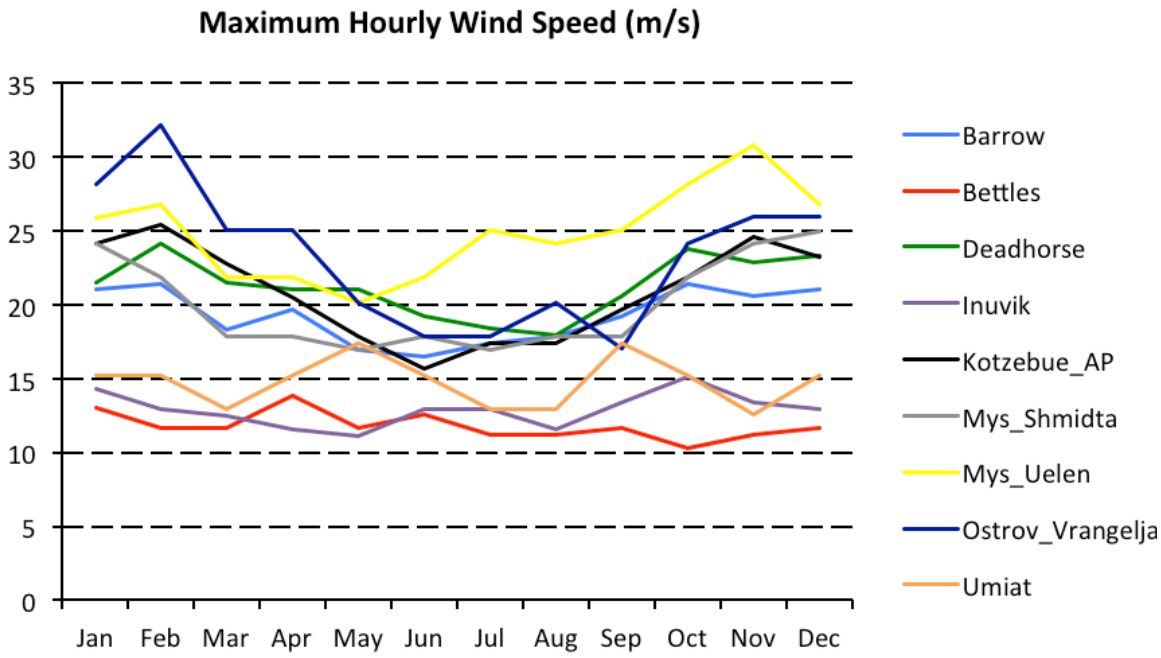

Figure 2.4.7. Maximum observed hourly wind speed (m s^{-1}) by month for the long-term stations

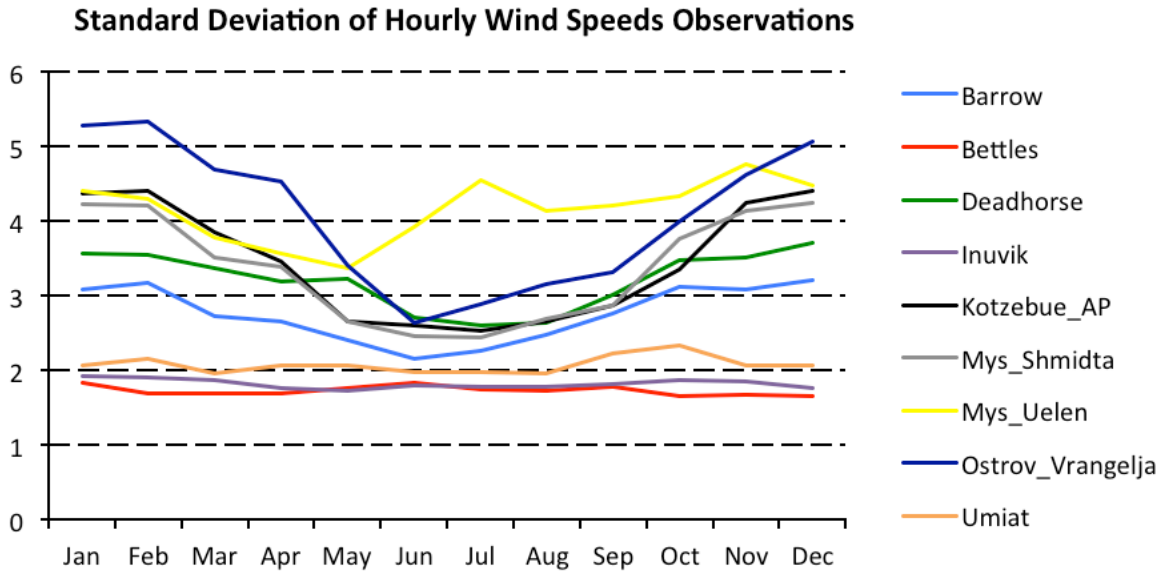

Figure 2.4.8. Standard deviation of hourly wind speed observations (m s^{-1}) by month for the long-term stations

For interior locations such as Bettles, located to the south of the Brooks Range, the wind direction distribution is quite different than for coastal locations. Generally, the mode is not as strong, and in the annual wind rose the directional components are fairly evenly distributed. Wind speed shows a seasonal distribution that is opposite to that seen for coastal locations. The magnitude is much less (2–3 m s^{-1} on average) throughout the year,

and there is a slight increase in speed during the summer months, rather than in the winter. There is little influence from large, organized winter storms in the sheltered region of the central interior south of the Brooks Range, and therefore wind speeds are not high during the cold months. Rather, this area often lies under a dome of high pressure in the cold season, with subsiding air and calm conditions. The summer, when thermal lows develop and produce thunderstorms, is normally the time when localized higher winds occur. Maximum wind speeds observed at interior locations lie in the 10–15 m s^{-1} range; in contrast to the average wind speeds, this shows no discernable seasonal variability. The standard deviation determined from the hourly wind speed observations for each month also shows no seasonal differences, remaining consistently around 2 m s^{-1} throughout the year. The percentage of time with calm conditions is low, though slightly greater than for coastal regions, and ranges from 5% to less than 10%.

Since hourly data are available for each observational network, the diurnal variability in wind speed was also examined. During the core winter months, there was no evident diurnal variation throughout much of the model domain. For example, from October through March there is no discernable diurnal variability in the mean hourly wind speed at Barrow. However, beginning in April and continuing through September, a variation in wind speed arises that corresponds to specific hours of the day. From roughly 2000 Alaska Standard Time (AKST) to approximately 0400 AKST a minimum is observed in the hourly wind speed data. In contrast, the highest speeds occur during the late afternoon and evening hours, with an increase of around 1 m s^{-1} relative to the overnight hours.

Pressure

The pressure field in the study domain shows evidence of several different influences throughout the year. The predominant pressure pattern in the northern part of the domain is the semi-permanent Beaufort High that occurs during winter (Figure 2.4.9). The location and strength of this pattern varies depending on various factors; however, significantly higher pressures are evident at this time of year. The peak in sea level pressure occurs during late winter, with March normally exhibiting the highest values of around 1020 hPa. Afterwards, pressures tend to slowly decrease throughout the spring and summer, reaching a minimum from July to November of approximately 1012 hPa.

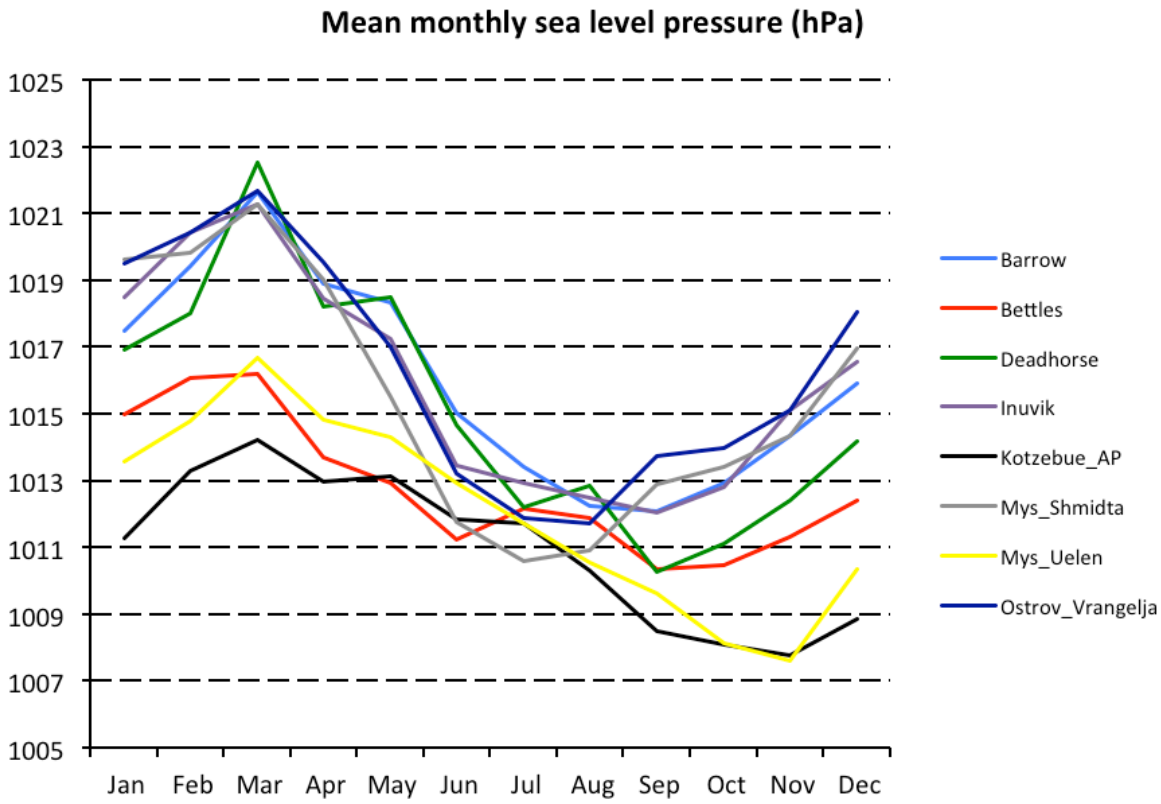

Figure 2.4.9. Mean monthly sea level pressure (hPa) by month for the long-term observing stations

Throughout the domain, there is a clear seasonal pattern to the pressure variability, in which both the highest and lowest pressures are observed during the cold season. Hourly observations are highest from November through March, with values in the 1050 to 1060 hPa range (Figure 2.4.10). During the warm season, in contrast, maxima lie only in the 1030 to 1040 hPa range. The opposite holds true for the minima, however, with the lowest absolute pressure observations occurring during winter. These values tend to be below 980 hPa from October through March, even dropping below 960 hPa in some cases (Figure 2.4.11). During summer, however, the minima are only around 990 hPa. Given this pattern of variability in pressure, it is no surprise that the standard deviation of the hourly observations exhibits a similar seasonal pattern. Mean monthly pressures during the cold months have standard deviations of 15 to 16.5 hPa, while the values are 3 to 4 hPa lower from May through September.

The patterns described here are indicative of the timing of storm systems that traverse the region. These are common during winter, and particularly late autumn, and represent large organized storm events that affect a large area. Summertime storms, though less frequent, are not uncommon and have been shown to produce damaging winds and wave action leading to coastal erosion. For the most part, however, these are more localized, and in the interior portion of the domain summer storms are mostly convective in nature.

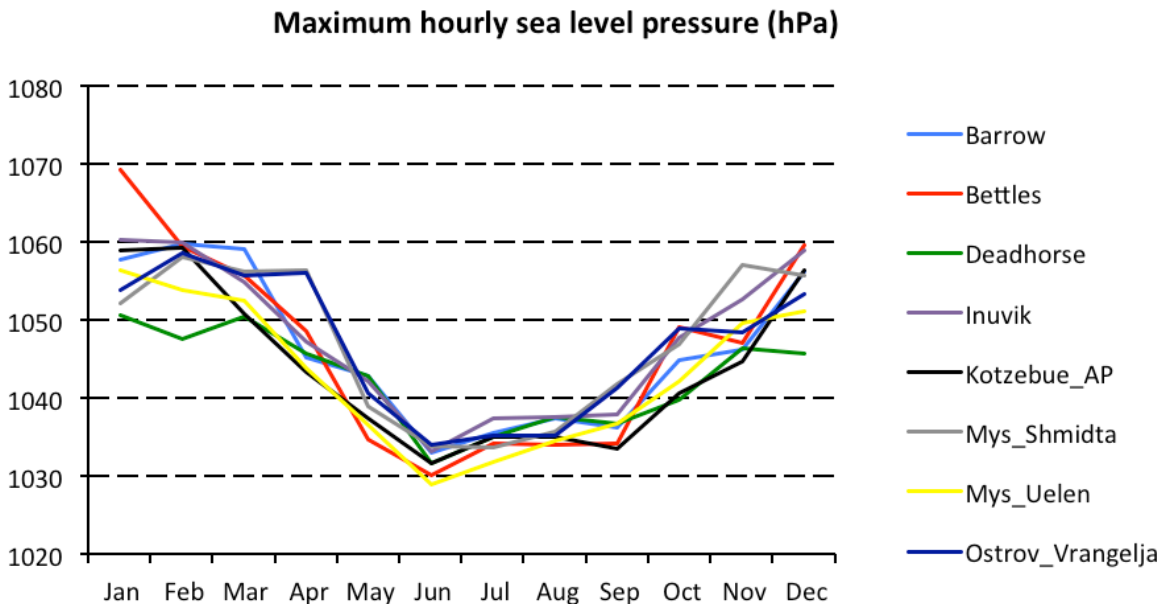

Figure 2.4.10. Observed maximum sea level pressure (hPa) by month for the long-term stations

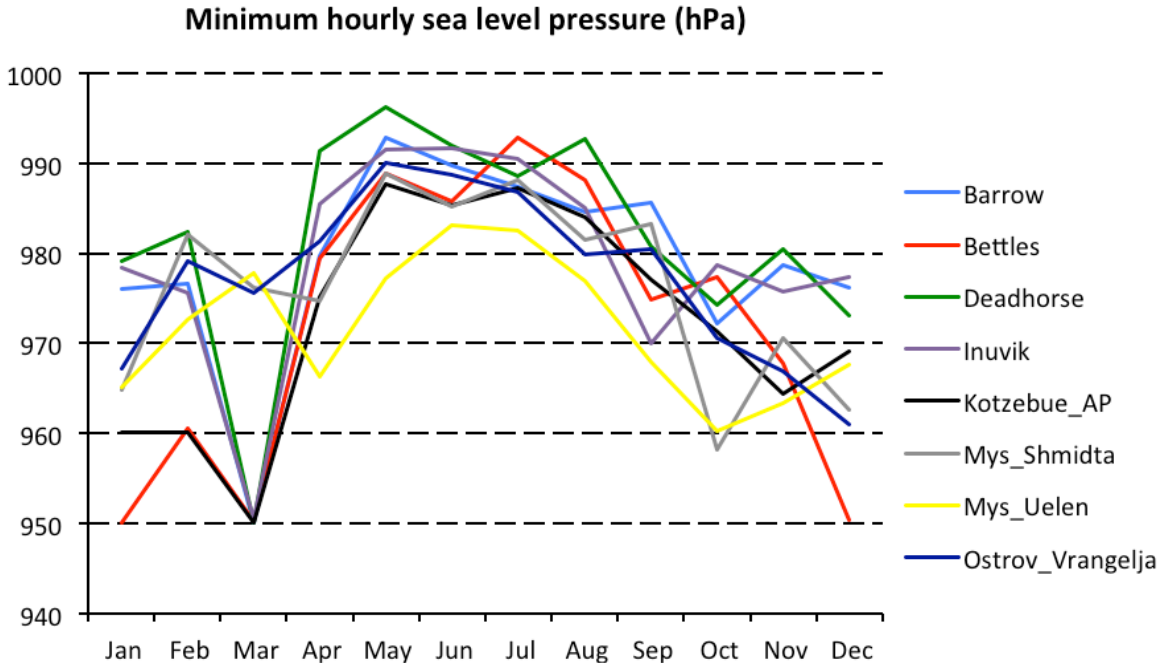

Figure 2.4.11. Minimum observed sea level pressure (hPa) by month for the long-term stations

2.4.2 Short-Term Observations

Offshore Locations

There are no long-term offshore observations in the database because the source of these data are purely temporary or transient platforms such as buoys, exploration well sites, ships, and ice camps. Due to their short periods of record, these observations are not necessarily indicative of the climatology of their location; rather, they more likely represent the local meteorology and synoptic conditions during particular months or over a single year. However, analysis of these data (see Figure 2.2.8 for their locations) allows for an investigation into conditions in offshore areas, a critical region that is of particular importance for this study. For most of these stations, observations are only available during the late summer and early autumn months.

Wind speed observations from these short-term sites show similar values as compared with the long-term coastal locations, with averages of around 6 m s^{-1}. However, the monthly averages range from 3 m s^{-1} (Kuvlum 2, July and August) up to 10 m s^{-1} (Popcorn, September and October). The standard deviation for the hourly winds is in the 3–4 m s^{-1} range. Wind rose information for these offshore short-term sites reveals that the northeast and southwest quadrants normally exhibit the highest average wind speeds.

With the exception of the Phoenix well site, no offshore sites reported temperature data throughout the year. Phoenix (operating from 1990 to 1991) has mean monthly temperatures at or above freezing from June through September. The warmest month is August and the coldest is February, with absolute observed maxima and minima of 13.9°C (July) and −42.6°C (February). Monthly summer temperatures for other offshore sites in the region exhibit mean values above freezing primarily from June through September. In nearly all cases, August is the warmest month, with absolute maximum temperatures that approach 14°C. In the case of Northstar, Cottle Island, and Endicott, summer temperatures peak from 15 to 20°C. A temperature frequency distribution histogram shows that observations most frequently occur in the −10 to 0°C range. At the Phoenix well site, the distribution peaks in the −5 to 0°C category.

Observations from the BOEM buoy, in operation during late summer 2009, represent a high-quality, though short-term, offshore dataset. Data are also available for Shell- and ConocoPhillips-maintained buoys in the Chukchi and Beaufort Seas for 2008 and 2009, in addition to the SEDNA field campaign in the far north of the domain, which operated for two weeks in April 2007. It is difficult to directly compare statistics from these sites with those of the long-term stations, as many represent only one or two seasons of data, rather than 31 years. However, these short-term sites represent the only offshore in situ observations available (other than ship data), though by their nature they are indicative of meteorological, rather than climatological, conditions in the region. Winds at the buoy sites occur most frequently in the 4 to 6 m s^{-1} range, and calm conditions prevail less than 1% of the time (except at the SEDNA ice camp, for which it is 5%). The standard deviation of the hourly observations is approximately 3 m s^{-1}. Wind directions are somewhat variable, but are primarily northerly for the offshore buoys.

Well sites in the Beaufort and Chukchi Seas represent an additional offshore dataset and, again, are indicative of meteorological, rather than climatological, conditions of the region. Calm wind conditions occur less than 5% of the time and the most frequent wind speed is 4 to 6 m s^{-1}. The Popcorn well site, in operation during September and October 1989, exhibits the highest average wind speed and a high frequency of winds over 12 m s^{-1}, most of which come from an east-northeasterly direction. The standard deviation of wind speed observations for all the collected well sites is a little more than 3 m s^{-1}. Wind rose plots show a general predominance of northeasterly winds, with a second mode in the southwest quadrant. Kuvlum 2 and 3 and Wild Weasel, on the other hand, exhibit more of an east-west bimodal wind direction distribution, influenced by the orientation of the Brooks Range.

Near-Shore Observations

Quite a number of shorter-term observing sites are located on land in the near-shore region of the Beaufort and Chukchi Seas. There are several BOEM and WERC network sites that have five or fewer years of data, particularly in the vicinity of Prudhoe Bay. The BOEM and surrounding supplemental locations have been summarized in a previous study (Hoefler Consulting Group 2007), which describes the temperature and wind patterns for these locations on or near the Beaufort coast. Since the metadata are known and the quality of these data is high, the conditions observed here should be taken as accurate. Many of the same statistics generated in the Hoefler report are also presented here. Wind rose plots illustrate the frequency of onshore winds during the summer months; wind speeds are in the 5 m s^{-1} range along the coast, and decrease farther inland. Temperature statistics are comparable to the longer-term stations for both warm and cold months, and the frequency distribution of hourly temperature observations also shows the same bimodal tendency, with peaks in the –25°C and 0°C ranges.

Data from the WERC network varies in record length, but the spatial representation for the Prudhoe Bay region of the Arctic Slope is quite good, in contrast to the rest of the domain. For analysis, these stations have been divided into four categories, grouped with increasing distance from the coast: coastal, near coast, inland, and Brooks Range, as indicated in Figures 2.4.12–2.4.15, respectively. Mean monthly temperatures for these stations illustrate differences corresponding to their proximity to the coast. Warmer summers are evident for locations farther inland, with monthly temperatures exceeding 10°C.

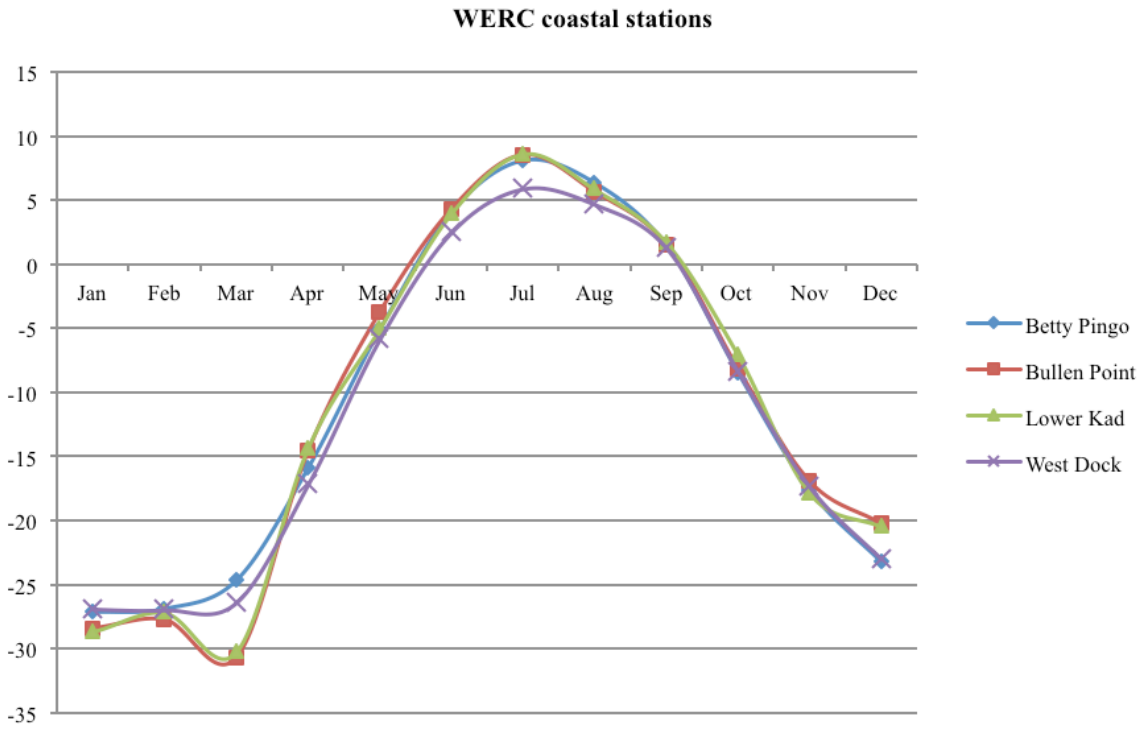

Figure 2.4.12. Mean monthly temperature (°C) for coastal stations in the WERC network

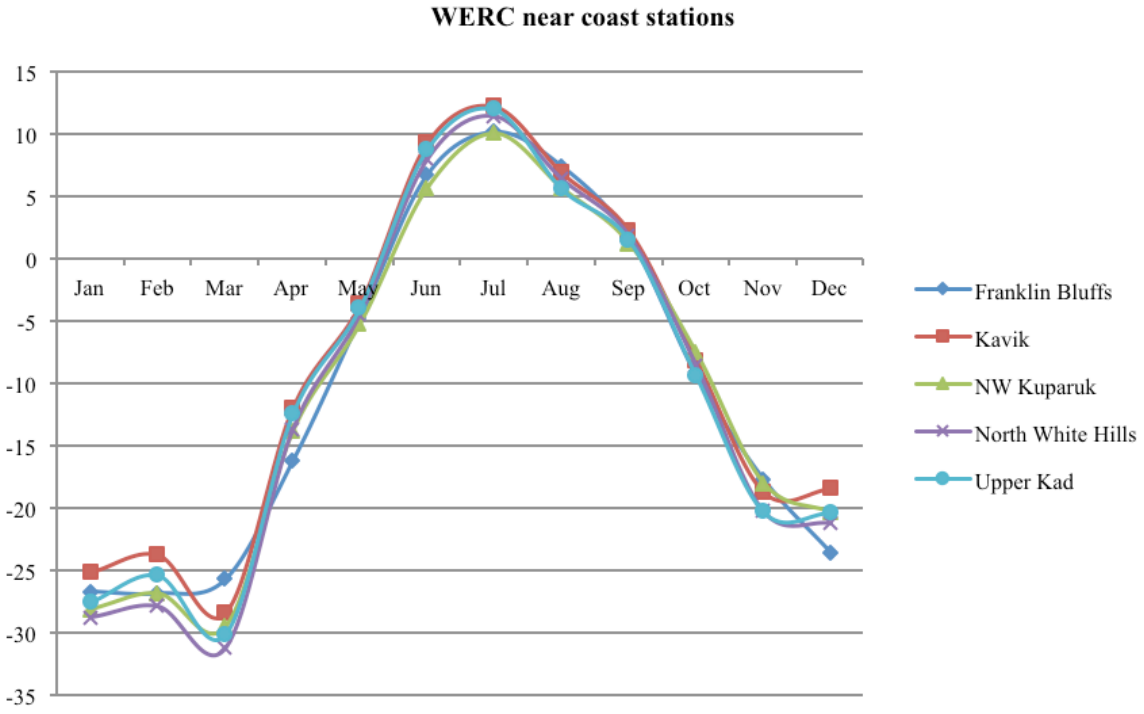

Figure 2.4.13. Mean monthly temperature (°C) for near-coastal stations in the WERC network.

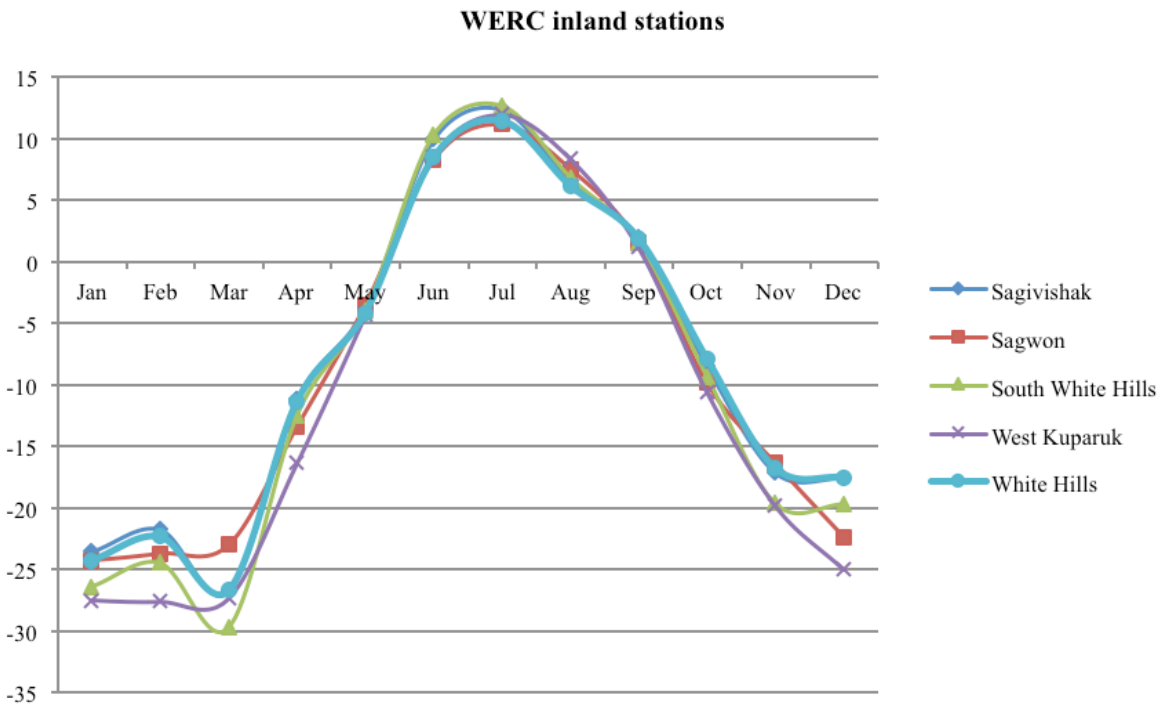

Figure 2.4.14. Mean monthly temperature (°C) for inland stations in the WERC network

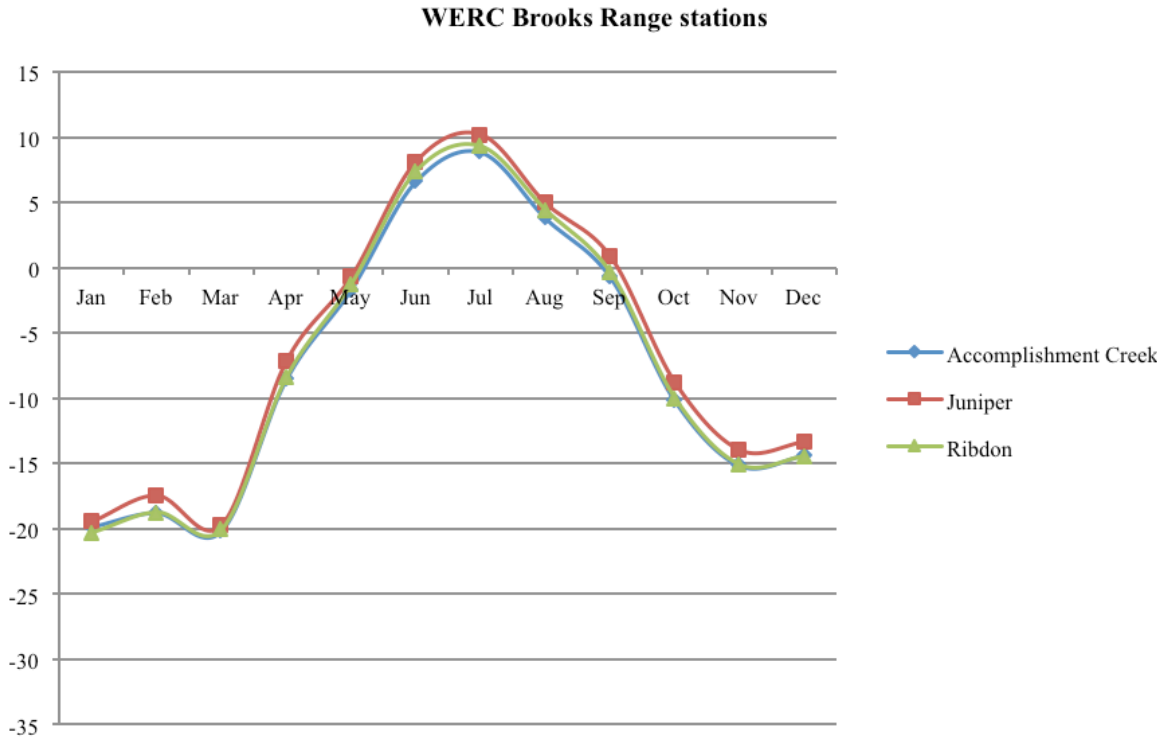

Figure 2.4.15. Mean monthly temperature (°C) for Brooks Range stations in the WERC network

2.4.3 Inter-Network Comparison at Barrow

There are several surface observing stations in the vicinity of Barrow, representing three different networks (NCDC, ARM, and the Climate Reference Network (CRN)). The metadata for these networks, such as instrument height, are all known. Therefore, it is assumed that differences in the observations accurately represent the microclimatology of the Barrow area. Detailed comparisons were performed among these three datasets at hourly and monthly time scales. Since comparisons were only made for corresponding time frames, the period of record presented here is relatively short, as the CRN and ARM sites have only been in place for the last several years, as compared to 31 years for the Barrow airport (NCDC) site.

Among the Barrow airport (NCDC), ARM, and CRN sites, the airport has consistently higher temperatures. The difference is greatest during the winter months, with the airport averaging from 0.5 to 1.4°C warmer. During August, September, and October, the air temperatures at the three locations around Barrow are quite similar, with a difference of just 0.2°C or less. The location of the airport station is on the southern edge of town, while the other two sites are situated a slight distance away from town. The warmer conditions in town represent a documented urban heat island effect (Hinkel et al. 2003). Up to a 2.2°C temperature difference has been found between temperatures in town and those of rural areas outside Barrow.

Wind speed was also compared between the Barrow ARM and airport sites (wind speed at 10 m is not available from the CRN location). The airport location reports a consistently higher average wind speed, with differences on the order of 1 m s^{-1}. This observed difference could be the result of differences in instrumentation, since the two sites do not use the same make and model of anemometer. Instrument exposure and localized influences could also play a role in the observed difference.

2.4.4 Upper-Air Observations

Radiosonde data are available for a subset of stations in the database. These data were obtained from the Integrated Global Radiosonde Archive through the NCDC (http://www.ncdc.noaa.gov/oa/climate/igra). Twice-daily data at 0000 UTC and 1200 UTC are available for the period 1979 to 2009, though the Russian stations only have records through 1999 and Barter Island only through 1988. The stations with upper-air data include Barrow, Barter Island, Inuvik, Kotzebue, Mys Shmidta, Mys Uelen, and Ostrov Vrangelja, all of which are also long-term surface observing stations. The 850-hPa level was chosen for detailed analysis as this height lies above the boundary layer and thus outside of the direct influence of the surface.

As illustrated in Figure 2.4.16, the modal wind direction at the 850-hPa level varies seasonally for most locations. During the cold months, the prevailing direction is northeast-to-easterly, presumably in association with the Beaufort High. One exception is at Inuvik, which, unlike the others, is not located on the coast, but rather a bit inland on

the Canadian Mackenzie River Delta. For the majority of the stations, the modal direction during the warmer months of June to October is predominantly from the west.

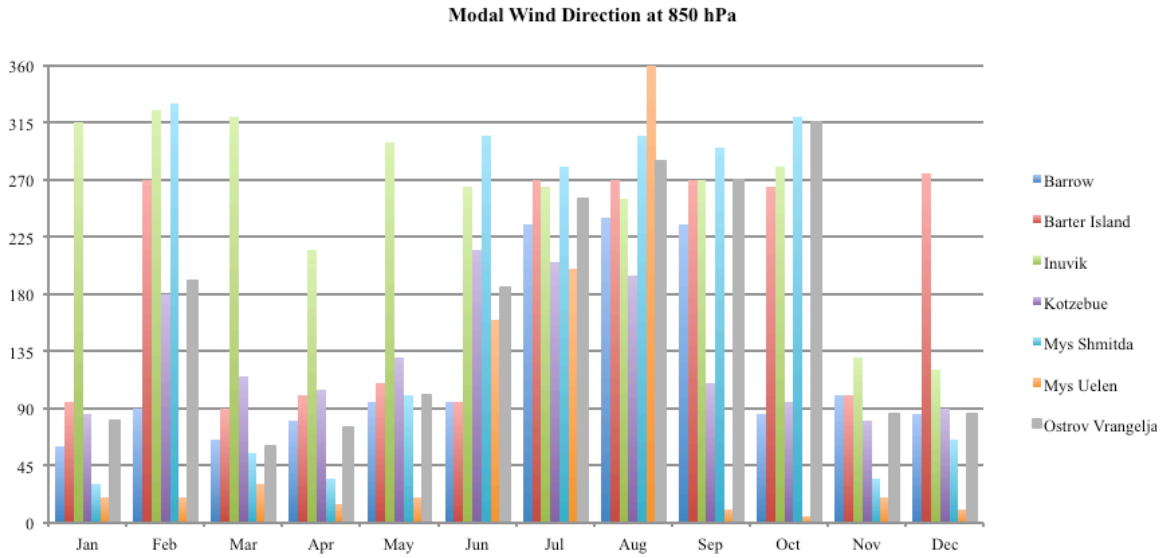

Figure 2.4.16. Monthly mode of the wind direction (degrees) for the 850-hPa level at locations where radiosonde data are available

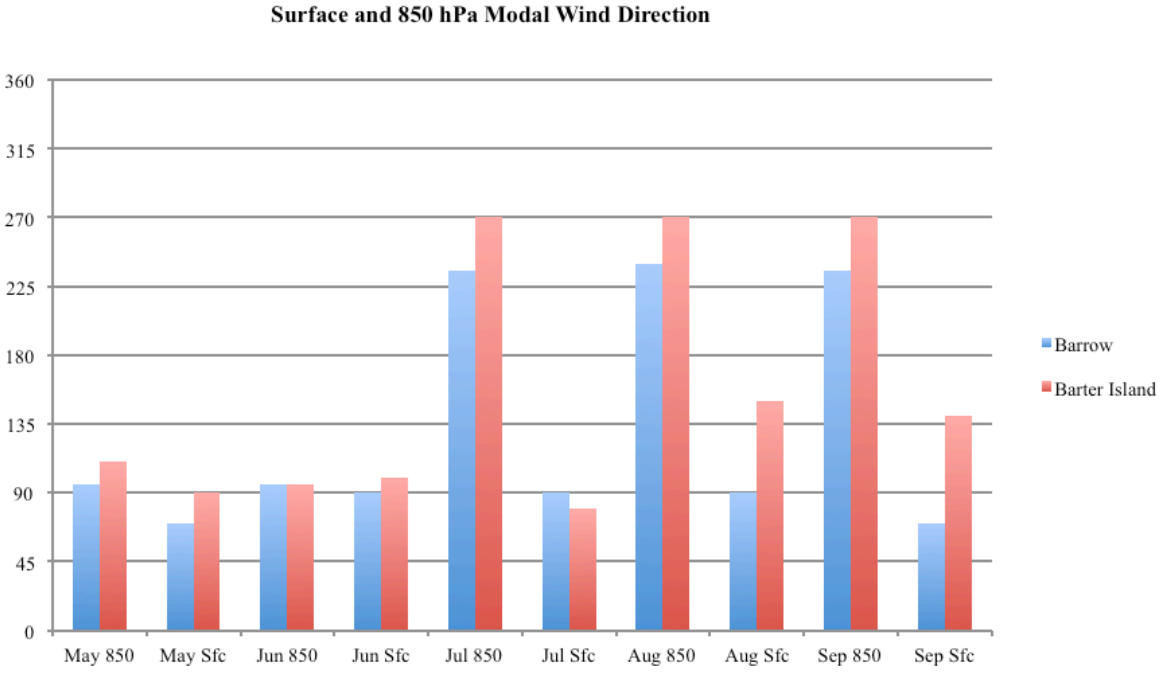

Figure 2.4.17. May to September wind direction (degrees) mode at the surface and 850-hPa level for Barrow and Barter Island

Of particular interest in upper-air investigations is the sea breeze, revealed through a comparison of 850-hPa and surface observations. For Barrow and Barter Island in

particular, the surface and upper-air levels display distinct differences in modal wind direction for the warm season of July to September (Figure 2.4.17), approaching a complete reversal of 180 degrees in some cases. This indicates a turning of the wind from the surface to 850 hPa, which is only evident during the warm season and is indicative of the influence of the sea breeze in the boundary layer.

2.4.5 Climate Trends

In recent years, the Arctic has seen dramatic changes in nearly all aspects of its environment. One of the most striking changes has been observed in one of its most defining characteristics: sea ice (Stroeve et al. 2012). It has been suggested that due to declining concentrations in sea ice, specifically multiyear ice, that strong warming trends will be observed in months typically defined by ice cover for Arctic locations with a direct coastal influence (Comiso 2012; Maslowski et al. 2012).

Linear trends in temperature and wind speed were calculated for the long-term observing stations in the study area for the years 1979–2009. Trends in temperature were calculated from the monthly mean values, both for each month and for the warm season as a whole (May–September). In calculating the monthly mean values, months were considered missing if less than 70% of the hourly observations were available. Missing individual monthly values were replaced by the mean value for that month over the observational period.

Mann–Kendall trend tests (Mann 1945; Kendall 1975) were performed on the time series, both for each month and for the warm season as a whole to determine if the calculated trends were significant at the 95% confidence level (α=0.05) for each variable. The Mann–Kendall trend test has been widely used in climate studies to determine the significance of trends observed in time series of climate data. Non-parametric tests, such as Mann–Kendall, are thought to be more suitable for analysis of climate data since the tests are not dependent on the normality of the data distribution. In addition, Mann–Kendall is based on a function of the ranks of the data rather than their actual values (Yue et al. 2002; Hamed 2008). As a result, the trend analysis is less sensitive to outliers and provides a clearer picture of the overall trend (Hamed 2008).

Temperature trends for the long-term stations in the study region display wide variability in both significance and magnitude. Four stations (Bettles, Deadhorse, Inuvik, and Kotzebue) show little or no significant evidence of warming over the study period (Table 2.4.1). Of this group, only Inuvik and Deadhorse display months with significant positive trends (95% confidence level) in temperature: November in Deadhorse (+0.17°C yr^{-1}) and December in Inuvik (+0.17°C yr^{-1}). For all other months, these four stations show both positive and negative trends of varying magnitude, though with none achieving a 95% confidence level. Among these stations, no clear seasonal pattern is evident. Stations under the influence of the Chukchi Sea (Barrow, Mys Shmidta, Mys Uelen, and Ostrov Vrangelja), however, display significant warming trends in several months throughout the year, most notably for September through December. In the previous group, the only significant trends were also seen in these months, and were also positive. On an

interesting side note, the only months in the Chukchi region displaying negative (though not significant) trends in temperature were January and February. This winter cooling is consistent with findings in a satellite-based analysis of temperature trends by Comiso (2003) for the Chukchi region. Comiso (2003) attributed this trend to a 1–8% increase in sea ice during these months from 1979–2003, further suggesting a strong link to sea ice cover and temperature trends.

Table 2.4.1. Temperature trend (°C yr^{-1}) in surface temperature for the period 1979–2009. Boldface red type indicates statistical significance at the 95% confidence level (boldface black, 90% level).

	Jan	Feb	Mar	Apr	May	Jun	Jul	Aug	Sep	Oct	Nov	Dec	*Ann*
Barrow	–0.03	0.04	0.01	**0.13**	0.05	0.02	0.03	0.05	**0.12**	**0.22**	**0.19**	**0.15**	***0.08***
Bettles	–0.09	0.15	–0.14	0.07	–0.01	0.02	0.00	0.00	0.06	0.02	–0.02	0.10	*0.01*
Deadhorse	–0.03	0.07	–0.03	0.10	0.03	0.03	–0.02	–0.02	0.05	**0.11**	**0.17**	0.10	*0.04*
Inuvik	0.07	0.14	–0.02	0.14	0.03	0.01	–0.01	–0.03	0.04	0.04	**0.15**	**0.17**	***0.06***
Kotzebue	–0.18	0.05	–0.09	0.08	–0.01	0.02	0.02	0.01	0.06	0.04	–0.02	0.06	*0.01*
Mys Shmidta	–0.09	–0.06	0.08	0.09	**0.13**	**0.05**	**0.06**	**0.11**	**0.13**	**0.18**	**0.16**	**0.15**	***0.08***
Mys Uelen	–0.09	0.00	0.07	0.09	**0.07**	**0.05**	0.03	0.05	**0.08**	**0.10**	**0.14**	0.10	***0.06***
Ostrov Vrangelja	–0.03	0.00	0.08	**0.09**	**0.09**	**0.03**	**0.06**	**0.06**	**0.15**	**0.20**	**0.16**	**0.15**	***0.09***

2.5 Summary

This section outlines the climatological conditions at the eight long-term stations across the model domain. These locations represent both coastal and inland Arctic environments. Clear differences are evident between these two environments, with maritime regions displaying lower temperature variability, higher overall temperatures, and higher wind speeds compared to inland stations. Of the long-term sites, the lowest temperature variability is found at Ostrov Vrangelja (in a strong maritime climate regime), whereas the highest variability is found at Umiat (in a strong continental climate regime). During the warm season, Umiat and Inuvik display quite similar mean temperatures—both are inland, though Umiat is much farther from the coast than is Inuvik. During the winter months, Umiat exhibits the lowest temperatures overall. A frequency distribution for all the observations shows a clear bimodal tendency, with peaks in the –25°C and 0°C ranges, indicative of the cold and warm seasons, respectively.

Winds average approximately 4–7 m s^{-1} for locations in the domain along the coast and are in the 2–3 m s^{-1} range for inland locations. Maximum wind speeds are highest in the winter and lowest in the summer for most locations, and peak in the 20–30 m s^{-1} range. For inland sites, maximum wind speeds are 15 m s^{-1} or less. Wind directions vary by location, depending on such factors as proximity to the Beaufort High semi-permanent pressure pattern, characterized by strong anticyclonic winds, as well as proximity to the coast and local topography.

Many shorter-term observing stations (both offshore and onshore) are present in the database, with some only operating for a one-month time frame. Although data from these locations are indicative of meteorological, rather than climatological, conditions, it is still of interest to compare some of them to the long-term sites. This comparison is especially beneficial in understanding the nature of offshore climate conditions when looking at buoy and well site data. Wind and temperature data for offshore sites show similarities to the long-term coastal locations. In particular, wind speeds are comparable, the frequency of calm conditions is similarly low, and wind directions are likewise northerly. Near-shore observations in the BOEM and WERC networks provide another means of comparison with the long-term sites. These have the added benefit of providing high spatial detail in the Prudhoe Bay area.

Through the incorporation of radiosonde observations (measured at Barrow, Barter Island, Inuvik, Kotzebue, Mys Shmidta, Mys Uelen, and Ostrov Vrangelja), surface and upper-air conditions can be compared. In doing so, wind direction differences are evident between the surface and 850-hPa levels in the summer months, indicating a turning of the wind and the predominance of a sea breeze circulation.

Finally, monthly temperature trends show the nature of the warming for this region since 1979. The late autumn months show trends that are statistically significant, with warming on the order of 0.15°C yr^{-1}. October is the month with the strongest warming trend overall, with Barrow exhibiting a warming of 0.22°C yr^{-1}. For nearly all stations, January trends show a slight cooling, which is likely linked to regional trends in sea ice.

3 Development of a Physically Optimized Modeling System for the Chukchi–Beaufort High-Resolution Atmospheric Reanalysis (CBHAR)

3.1 Introduction

While the analysis of observational data is critical in determining the climatology of the Chukchi–Beaufort Seas region, both the sparse distribution and relatively short data periods of many of the available stations in the study domain make such an analysis incomplete. In order to better understand the finely detailed, regional-scale surface wind field over the Chukchi–Beaufort Seas and Arctic Slope, the WRF model and its data assimilation system WRFDA have thus been utilized to generate a long-term, high-resolution reanalysis over the study area that can be used to supplement the existing observational record. The result of this reanalysis effort is the 31-year Chukchi–Beaufort

High-Resolution Atmospheric Reanalysis (CBHAR), in which numerical model output was combined with the observational database detailed in Section 2, along with additional satellite retrievals, over the 31-year period 1979–2009 through data assimilation techniques. Examples of similar reanalysis datasets include the European Centre for Medium-Range Weather Forecasts (ECMWF) 40-Year Re-analysis (ERA-40) (Uppala et al. 2005) and Interim Reanalysis (ERA-I) (Dee et al. 2011), the Japanese 25-Year Reanalysis (JRA-25) (Onogi et al. 2007), and the National Centers for Environmental Prediction (NCEP)/National Center for Atmospheric Research (NCAR) Reanalysis (Kalnay et al. 1996) and North American Regional Reanalysis (NARR) (Mesinger et al. 2006). The ERA-40, ERA-I, JRA-25, and NCEP reanalyses are comprised of global data at relatively coarse resolutions, making them difficult to apply in mesoscale studies. NARR, on the other hand, is a regional reanalysis with 32-km grid spacing. However, the domain for the current study lies in the far northwest corner of the NARR domain, which causes concern regarding potential boundary effects in the data. To counter these problems and develop a high-quality product suitable for high-resolution analysis of the climate in the study domain, this effort was devised to generate a regional reanalysis with 10-km grid spacing for more accurately capturing the finer-scale processes of the region's surface wind field than was possible in previously existing products.

To establish the WRF/WRFDA modeling system for use over the Chukchi–Beaufort Seas and Arctic Slope, the foremost challenge was the determination of the most appropriate model configuration. The WRF model is a widely used community mesoscale model developed by NCAR and its partners. As described by Skamarock et al. (2008), the WRF dynamical core solves fully compressible nonhydrostatic governing equations on the Arakawa C-grid staggered horizontal grid and terrain-following hydrostatic-pressure vertical coordinate using 3rd-order Runge–Kutta time-split integration. Processes that occur at the sub-grid scale are described by various physical parameterization schemes that are selectable by the user depending on their particular needs. Two distinct dynamical cores are available: the Advanced Research WRF (ARW), which was developed and is maintained by NCAR, and the Nonhydrostatic Mesoscale Model (NMM), which was developed by NCEP with support from the Developmental Testbed Center. In this study, the ARW dynamical core was used due to the extensive testing and improvements that were previously made for its use in simulating the Arctic atmosphere (Hines and Bromwich 2008; Bromwich et al. 2009; Hines et al. 2011). WRF also contains a bevy of physical parameterization options that simulate microphysical, convective, radiative, planetary boundary layer (PBL), surface layer, and land-surface processes. Choosing the most suitable schemes is critical for generating high-quality model output. However, different regions experience variable conditions and present unique problems, and the optimal setup for one area may not necessarily be applicable to another. This is especially true in the Arctic, which presents many unique modeling challenges that parameterization schemes developed for and primarily tested in the tropics and mid-latitudes may be unable to adequately address. To confront this challenge, extensive model sensitivity simulations were conducted as a part of this study

to optimize the configuration of physical parameterizations for application over the Chukchi–Beaufort Seas and Arctic Slope.

The data assimilation package used to generate the CBHAR reanalysis was WRFDA, which has been designed to be a flexible, state-of-the-art atmospheric data assimilation system including options for both three-dimensional (3DVAR) and four-dimensional (4DVAR) variational data assimilation. In this study, the 3DVAR assimilation technique was adopted to generate the final high-resolution reanalysis. 4DVAR was not considered due to its relatively high computational cost (Barker et al. 2004, 2012), making it unfeasible for the ultimate goal of producing a long-term (31-year) reanalysis. The variational data assimilation system WRFDA determines its optimal analysis through the use of information that includes model background error (BE) and observational measurement error. Thus, determining the model BE and selecting the observational data to be assimilated were the critical steps necessary for optimizing the WRFDA assimilation configuration for the production of CBHAR. As with the determination of the best-performing parameterization configuration, this optimization was determined through a set of sensitivity experimental simulations.

Another essential effort conducted in the modeling aspect of this project was the implementation into the WRF model of more advanced model physical parameterizations that have been specifically designed for the unique Arctic environment. One of these efforts was the coupling of a thermodynamic sea ice model (Zhang and Zhang 2001); the other was the adoption of various improvements to WRF, known as Polar WRF, made by the Polar Meteorology Group at the Ohio State University (OSU), such as the use of variable sea ice thickness (Hines and Bromwich 2008; Bromwich et al. 2009; Hines et al. 2011). In addition to these efforts, tests were conducted to optimize the selection of model forcing and boundary data. The details of each of these efforts are documented in Sections 3.2–3.5.

3.2 Optimization of Model Physical Parameterization Configuration

As introduced in Section 3.1, the WRF model contains a bevy of options that control which physical parameterization schemes are used to simulate microphysical, convective, radiative, PBL, surface layer, and land-surface processes. The selection of the most suitable and best-performing parameterization schemes can be critical for achieving the best possible performance from a model. To address this challenge, a series of sensitivity test simulations were conducted in order to attempt to optimize the WRF physical parameterization configuration for application over the Chukchi–Beaufort Seas and Arctic Slope, especially as it relates to the simulation of the area's surface wind field. Each of the classes of model physical parameterizations, including shortwave and longwave radiation, microphysics, PBL, and land-surface processes, were independently tested. The simulation results were verified against the quality-controlled observational database described in Section 2 of this report using the statistical metrics described in Appendix B. A total of three sets of sensitivity tests, covering different seasons, were performed:

- First was a series of one-month tests for September 2004, a time of year which represents the transitional season from summer to winter conditions. During this period, the study domain includes sea ice, open water, snow cover, and bare ground conditions, and can thus serve as a representative period for the varied conditions found throughout the year.
- Second, additional simulations were conducted on a domain centered on the location of the Surface Heat Budget of the Arctic (SHEBA) field experiment. SHEBA produced a unique one-year offshore observational dataset in the Arctic, allowing the performance of the various parameterizations to be further tested for offshore Arctic conditions.
- Third was a series of one-month tests for August 2009, which represents the warmest month in the study area and is thus suitable for comparing the performance of different convective parameterizations.

Clearly, the optimized configuration as determined from these sensitivity tests should not necessarily be considered as absolutely optimal, since it is effectively impossible to test all possible combinations of the available parameterizations for all conditions that could potentially exist in the study region. Instead, judicious choices were made in order to select a small, representative subset of the possible sensitivity tests to determine what might be considered a local maximum in model configuration space. In addition to the tests described here, previous published work was also researched (e.g., Hines and Bromwich 2008; Bromwich et al. 2009; Cassano et al. 2011; Porter et al. 2011; Hines et al. 2011; Wilson et al. 2011) and their results were taken into consideration as well.

3.2.1 Sensitivity Tests: September 2004

Sensitivity Test Design

The modeling domain for the initial sensitivity tests was established as shown in Figure 1.1.2, covering the Chukchi–Beaufort Seas and adjacent land areas of Russia, Alaska, and Canada. The domain has dimensions of 235 by 136 points, with a grid spacing of 10 km and 49 vertical levels. The oceanic portion of the domain experiences high variability throughout the year in its sea ice coverage, and the land portion similarly varies in its snow coverage. Both sea ice and snow cover are important to the thermal contrast that exists between land and ocean and that plays a significant role in driving near-surface circulation patterns. As such, to properly test the model's performance, it is essential to select a representative simulation time period that contains both ice-free and ice-covered ocean, as well as bare and snow-covered land, and also includes the transitional period between the two states. The month of September 2004 was therefore chosen as the test period, as the study region experiences each of these varied conditions during this time. When conducting the simulations, the month was subdivided into eight 4.5-day periods, which were run independently and initialized every fourth day at 1200 UTC, with the first 12 hours of each simulation treated as model spin-up and not used in the validation. Thus, in stitching together the final four days of each simulation, hourly time series could

be created, extending from 0000 UTC 2 September to 0000 UTC 4 October, series which were then used for model verification.

In order to perform as complete a test as possible of the available physical parameterizations, a control experiment (CTRL) that utilized WRF v3.2 and the following model physical parameterizations (Table 3.2.1) was first run:

Table 3.2.1. Model physical parameterizations in the CTRL simulation

Parameterization	Configuration
Cumulus	Kain–Fritsch scheme (**KF**) (Kain 2004)
Microphysics	WRF Single-Moment 6-class (**WSM6**) (Hong and Lim 2006)
Longwave radiation	Community Atmosphere Model (CAM) longwave (**CLW**) (Collins et al. 2004)
Shortwave radiation	CAM shortwave (**CSW**) (Collins et al. 2004)
Planetary boundary layer	Yonsei University (**YSU**) PBL (Hong et al. 2006)
Land-surface model	**NOAH** land-surface model (LSM) (Chen and Dudhia 2001)

Based around the configuration of the CTRL experiment, one or two of the physical parameterizations were changed at a time and various combinations were tested, ultimately evaluating a total of eight microphysics, three longwave (LW), four shortwave (SW), six PBL, and one land-surface options, as summarized in Table 3.2.2. The available cumulus parameterization schemes were also compared, though in a separate set of sensitivity simulations for August 2009 (Section 3.2.3), as August represents the warmest month in the region and thus a period when more convective events are expected to occur. As the Noah LSM is the only land-surface scheme in WRF that includes sophisticated land-surface processes and considers some additional Arctic surface processes, such as sea ice and frozen soil, it was determined to be the only LSM suitable for this study and was thus used for all sensitivity tests. The external forcing data used in these tests, utilized both for initialization and boundary conditions, was the North American Regional Reanalysis (NARR).

The hourly in situ observations used for verification of the model output in September 2004 (Figure 3.2.1), collected and quality controlled as described in Section 2 of this report, included 96 stations that observed temperature, wind, and pressure; 23 stations that measured shortwave irradiance from the ARM (2) and RAWS (21) networks; and two ARM stations that measured longwave irradiance. In addition to the in situ data, sensitivity test results were also verified against observations from the SeaWinds instrument on board the National Aeronautics and Space Administration (NASA) Quick Scatterometer (QuikSCAT) satellite. This dataset consists of measurements of surface (10-m) wind speed and direction at a spacing of 12.5 km over open, ice-free ocean areas. In all cases, model output at the closest land point (for stations) or water point (for QuikSCAT data) to the location of the observations was compared with the measurements, and the mean bias and correlation coefficients (Appendix B) then

calculated across the entire domain over the entire simulation period in order to evaluate the overall performance of the model physical schemes.

Table 3.2.2. Identifiers of model physical parameterizations in the sensitivity tests

CTRL	**KF** cumulus, **WSM6** microphysics, **CLW** Longwave, **CSW** Shortwave, **YSU** PBL, **NOAH** LSM
Microphysics	
Lin	Purdue Lin (Lin et al. 1983; Tao et al. 1989)
Ferr	Ferrier (Eta) (Ryan 1996)
WSM6	WSM6 as used in CTRL
Godd	Goddard (Tao and Simpson 1993)
Thom	Thompson (Thompson et al. 2004)
Morr	Morrison 2-moment (Morrison et al. 2009)
nThom	New Thompson (Thompson et al. 2008)
MY2m	Milbrandt–Yau 2-moment (Milbrandt and Yau 2005)
Longwave Radiation	
RLW	Rapid Radiative Transfer Model (RRTM) longwave (Mlawer et al. 1997)
CLW	CLW as used in CTRL
RgLW	RRTMG (RRTM for General Circulation Models (GCMs)) longwave (Iacono et al. 2008)
Shortwave Radiation	
SSW	Dudhia simple shortwave (Dudhia 1989)
GSW	Goddard shortwave (Chou and Suarez 1994)
CSW	CSW as used in CTRL
RgSW	RRTMG (RRTM for GCMs) shortwave (Iacono et al. 2008)
Land-Surface Model	
NOAH	NOAH as used in CTRL
Planetary Boundary Layer	
YSU	YSU as used in CTRL
MYJ	Mellor–Yamada–Janjic (Mellor and Yamada 1982; Janjic 2002)
ACM2	Asymmetrical Convective Model 2 (Pleim 2007)
QNSE	Quasi-Normal Scale Elimination (Sukoriansky et al. 2006)
MYN2	MYNN 2.5-level TKE scheme (Zhang et al. 2011)
Bola	Bougeault and Lacarrere (Bougeault and Lacarrere 1989)

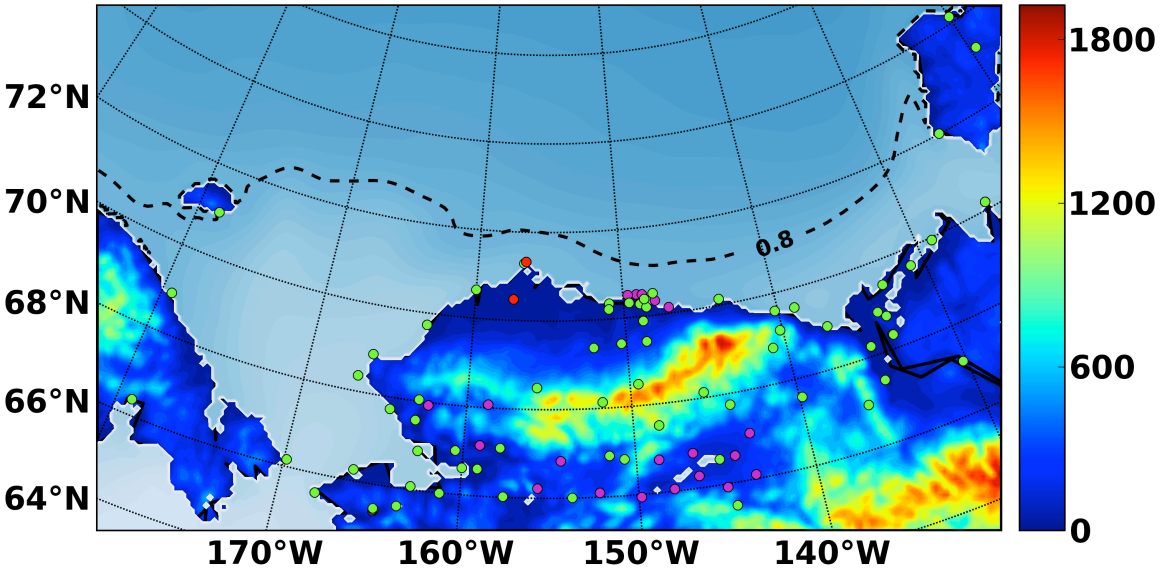

Figure 3.2.1. Distribution of the 96 observational stations over the CBHAR modeling domain used for model verification of the physical parameterization sensitivity simulations. Two ARM stations are indicated by red dots, 21 RAWS stations by magenta dots, and other networks by green dots.

Sensitivity Test Results

Radiation

The parameterization of radiative processes is an important element in the modeling of the surface heat budget, and consequently also has an impact on the simulation of surface winds. Shortwave and longwave irradiances are modeled separately, and so WRF includes a distinct set of options for each. In WRF v3.2, four longwave and six shortwave parameterizations are available, of which three of the former and four of the latter are currently supported and applicable to the modeling configuration for this study. Thus, a total of nine radiation sensitivity tests (Table 3.2.3), with experiment identifiers as given in Table 3.2.2, were conducted. These tests included RRTM longwave (RLW) and its combination with simple shortwave (SSW), Goddard shortwave (GSW), and CAM shortwave (CSW); CAM longwave and its combination with SSW, GSW, CAM, and RRTMG shortwave (RgSW); and RRTMG longwave (RgLW) and its combination with CSW and RgSW. Some combinations resulted in model instability, causing the simulations to crash, so not every possible combination produced verifiable results. The ARM sites at Barrow and Atqasuk measure both longwave and shortwave irradiance, and their observations were used to verify the sensitivity results.

Table 3.2.3. Identifiers of radiation sensitivity tests

Sensitivity test	Physical parameterizations
RLWSSW	RLW (RRTM longwave) + SSW (Dudhia simple shortwave)
RLWGSW	RLW (RRTM longwave) + GSW (Goddard shortwave)
RLWCSW	RLW (RRTM longwave) + CSW (CAM shortwave)
CLWSSW	CLW (CAM longwave) + SSW (Dudhia simple shortwave)
CLWGSW	CLW (CAM longwave) + GSW (Goddard shortwave)
CLWCSW	CLW (CAM longwave) + CSW (CAM shortwave)
CLWRgSW	CLW (CAM longwave) + RgSW (RRTMG shortwave)
RgLWCSW	RgLW (RRTMG longwave) + CSW (CAM shortwave)
RgLWRgSW	RgLW (RRTMG longwave) + RgSW (RRTMG shortwave)

The comparison of downward longwave irradiance bias and correlation among the nine radiation sensitivity tests, as verified against the ARM observations (Figure 3.2.2), shows that all of the radiation schemes produce a negative bias and that the results are aligned into three basic groups, each corresponding to a different longwave radiation scheme (RLW, CLW, and RgLW). The CLW group tends to have a relatively large bias and small correlation. In contrast, the bias produced by RLW is relatively small, with a correlation larger than 0.5. Differences within each group result from the choice of shortwave scheme; obviously, the shortwave schemes have little interaction with the longwave schemes in the simulation of longwave irradiance as shown here. Time series comparisons of observed and modeled longwave irradiance (Figure 3.2.3), averaged over the ARM sites, show that the three different longwave radiation schemes (RLW, CLW, and RgLW) all tend to exhibit larger fluctuations than the observations, while generally underestimating the values.

For shortwave irradiance, observations are available from both the ARM and RAWS networks, resulting in a total of 23 stations for verification. The comparison of downward shortwave irradiance biases (Figure 3.2.4) shows that the SSW scheme tends to produce a negative bias with a relatively small correlation when not paired with the RLW scheme, while the rest generate positive biases with similar correlations of around 0.85. The comparison of daily averaged downward shortwave irradiance (Figure 3.2.5), averaged over the entire simulation period and over the ARM and RAWS stations, confirms that the SSW scheme underestimates shortwave irradiance, and that the other schemes all overestimate it by about 80 W m^{-2} during midday. Similar results at both the ARM and RAWS sites further confirm that the quality-controlled RAWS measurements are a useful addition to this model verification effort. Thus, so far it has been shown that:

- All the longwave schemes underestimate downward longwave irradiance when verified against ARM measurements, and biases in the RLW and RgLW schemes are relatively small.
- The SSW shortwave scheme underestimates downward shortwave irradiance.

- The CSW, GSW, and RgSW shortwave schemes perform similarly in overestimating downward shortwave irradiance, though a relatively small bias is seen in RgSW.

The impacts of the radiation schemes on the simulation of 2-m air temperature are depicted in Figure 3.2.6, in which averaged diurnal cycles of modeled and observed surface temperatures are compared. The CLWSSW combination generates the coldest temperatures throughout the entire day. Compared to the cold surface temperatures from CLWSSW, temperatures produced by the RLWSSW, CLWGSW, CLWCSW, and CLWRgSW tests are warmer by about 1°C, and warmer by about 2°C in the RLWGSW, RLWCSW, RgLWCSW, and RgLWRgSW tests during both the day and night. Modeled temperatures simulated by the different radiation schemes are consistent with the irradiance bias seen for each scheme. For instance, the coldest temperatures, produced by CLWSSW, likely result from the relatively large negative bias in longwave irradiance generated by the CLW scheme, combined with the negative bias in shortwave irradiance from SSW. When the CLW scheme is replaced by the RLW scheme, which has a relatively small negative bias in longwave irradiance, the surface temperature generated by RLWSSW is warmer by about 1°C. Further, when the SSW scheme is replaced by either the GSW or CSW schemes, which have positive biases in shortwave irradiance instead of the negative bias from SSW, the surface temperature in RLWGSW and RLWCSW is further increased by an additional 1°C.

During the day, shortwave and longwave radiation schemes interact to impact the simulation of surface temperature. Comparison between the modeled and observed temperatures (Figure 3.2.6) suggests that the negatively biased longwave irradiance in the RLW and RgLW schemes (Figure 3.2.2) serves to offset the positively biased shortwave radiance from the GSW, CSW, and RgSW schemes (Figure 3.2.4), resulting in a better agreement between simulations and observations during the hours of maximum irradiance as shown in the RLWGSW, RLWCSW, RgLWCSW, and RgLWRgSW tests.

In terms of radiation dependence, the performance in simulating nighttime temperatures is primarily related to the choice of longwave radiation scheme. Thus, one should expect better temperature modeling by the RLW or RgLW schemes, which produce relatively small biases in longwave irradiance. However, a better agreement with the observed evening temperatures is seen with the CLW scheme, which tends to produce large negative biases in longwave irradiance. The reason for this seeming discrepancy between bias in the longwave irradiance and accuracy of the temperature simulation is most likely due to other processes, such as the presence of near-surface temperature inversions, involved in the simulation of surface temperature. Over areas with complex topography, inversions frequently occur at night and are a persistent challenge for regional- and larger-scale models to accurately capture due to the lack of sufficiently fine resolution in the lower boundary layer. The effect of inadequately modeling the strength of an inversion, making it too weak, is a warm bias in the surface temperature. Thus, the offsetting effects of a warm bias due to insufficiently modeling inversion strength and the cold bias due to negatively biased longwave irradiance combine to produce better nighttime temperature in most tests with the CLW scheme (Figure 3.2.6).

The final determination for which radiation schemes were selected was based on an overall error analysis. The negative bias in longwave irradiance by the RLW and RgLW schemes is relatively small, while at the same time the positive bias in shortwave irradiance by the RgSW scheme tends to be the smallest, leading the RgLW and RgSW schemes to *temporarily* be chosen for use in the production of CBHAR, pending the results of additional sensitivity tests.

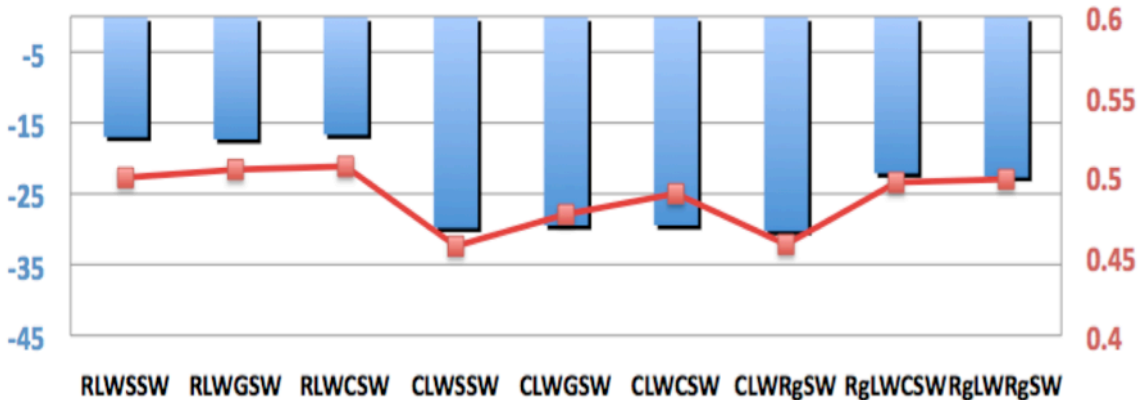

Figure 3.2.2. Downward longwave irradiance bias (W m^{-2}, blue) and correlation (red) in the radiation sensitivity tests, as verified against observations from 2 ARM stations during September 2004

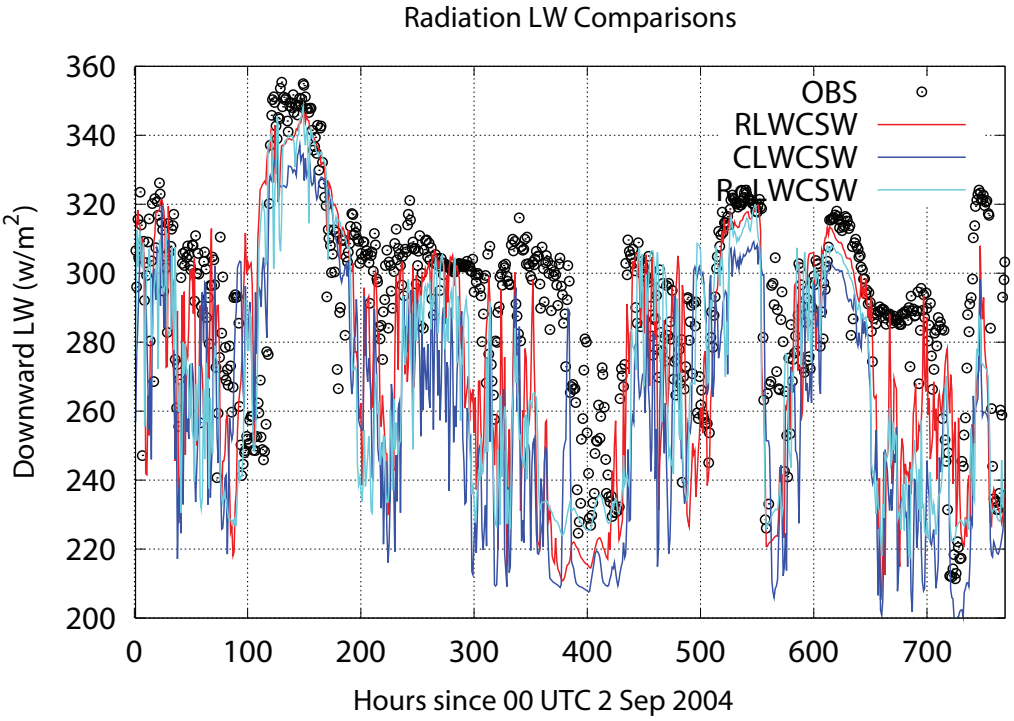

Figure 3.2.3. Modeled (lines) and observed (dots) downward longwave irradiance (W m^{-2}) in the radiation sensitivity tests, averaged over 2 ARM stations during September 2004

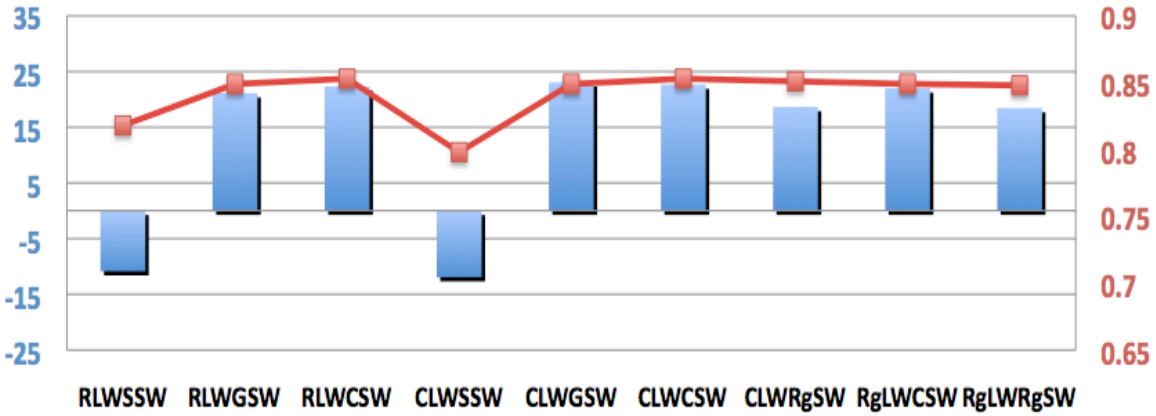

Figure 3.2.4. Downward shortwave irradiance bias (W m^{-2}, blue) and correlation (red) in the radiation sensitivity tests, as verified against observations from 23 ARM and RAWS stations during September 2004

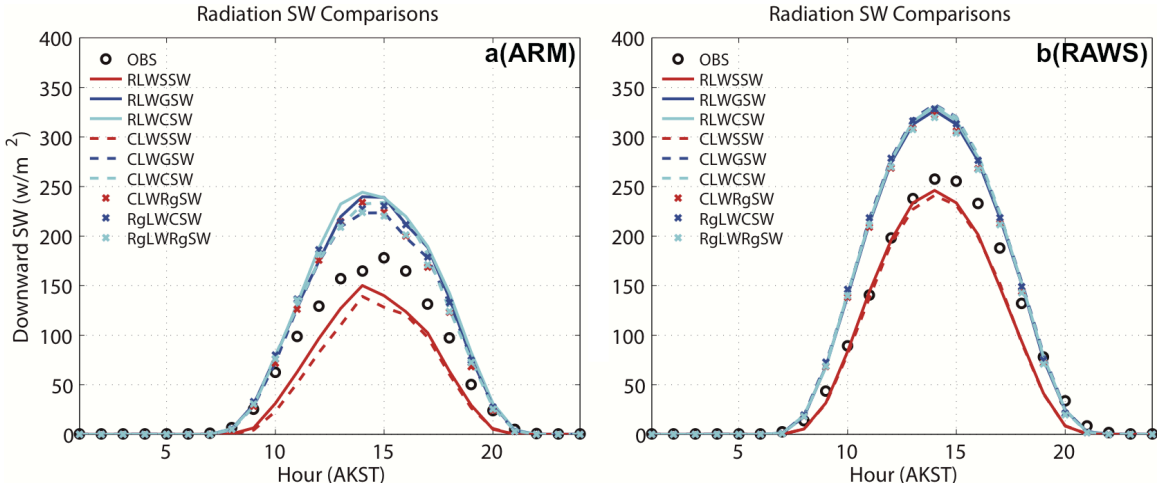

Figure 3.2.5. Daily mean downward shortwave irradiance (W m^{-2}) in the radiation sensitivity tests, averaged over (a) 2 ARM and (b) 21 RAWS stations during September 2004

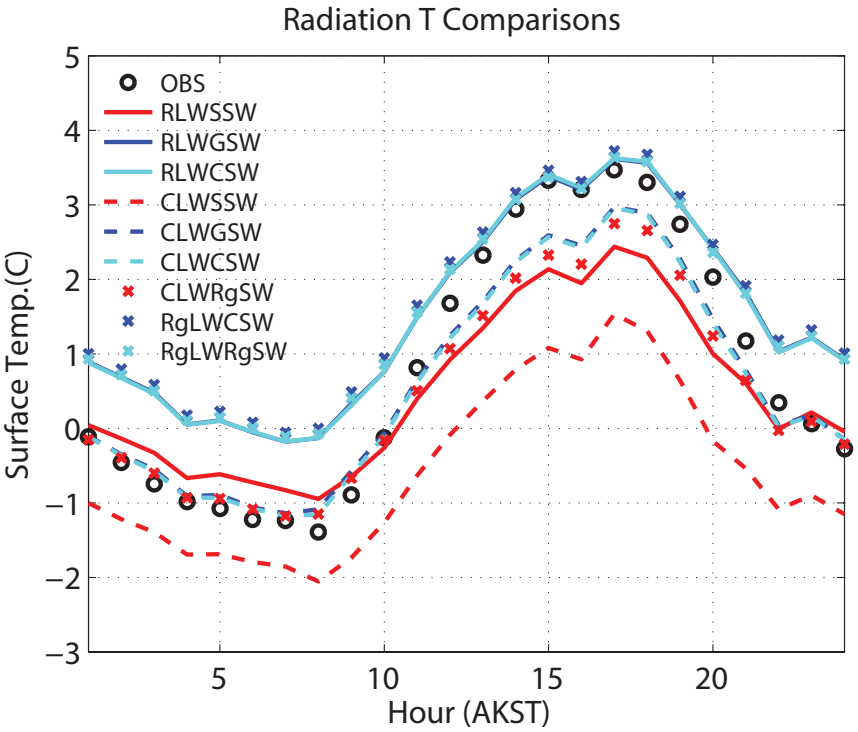

Figure 3.2.6. Daily mean 2-m temperature (°C) in the radiation sensitivity tests, averaged over 96 stations during September 2004

Microphysics

One of the major challenges in atmospheric modeling, and of prime importance for controlling the surface heat budget, is the accurate simulation of clouds. This is especially true in the Arctic, where the slightest forcing can generate clouds in the bitterly cold atmosphere, which at the same time can have dramatic effects on near-surface temperatures. WRF v3.2 contains 12 microphysical options, including one that is only suitable for use in idealized studies and three that are simplified versions of other options, leaving eight choices that could conceivably be selected as the preferred scheme for this study. Thus, a total of eight microphysics sensitivity tests, with experiment identifiers as given in Table 3.2.2, were conducted. They include Lin (Purdue Lin), Ferr (Ferrier (Eta)), WSM6 (WRF Single-Moment 6-Class), Godd (Goddard), Thom (Thompson), Morr (Morrison 2-moment), nThom (New Thompson), and MY2m (Milbrandt–Yau 2-moment).

As was the case for the radiation sensitivity tests, a comparison of downward longwave irradiance bias and correlation for the eight microphysics sensitivity tests (Figure 3.2.7) shows that negative biases exist for all schemes. Among them, the bias for the Thom scheme is relatively small. One phenomenon present in these results is that better correlation is always accompanied by larger (negative) biases, though all the correlation coefficients are relatively small.

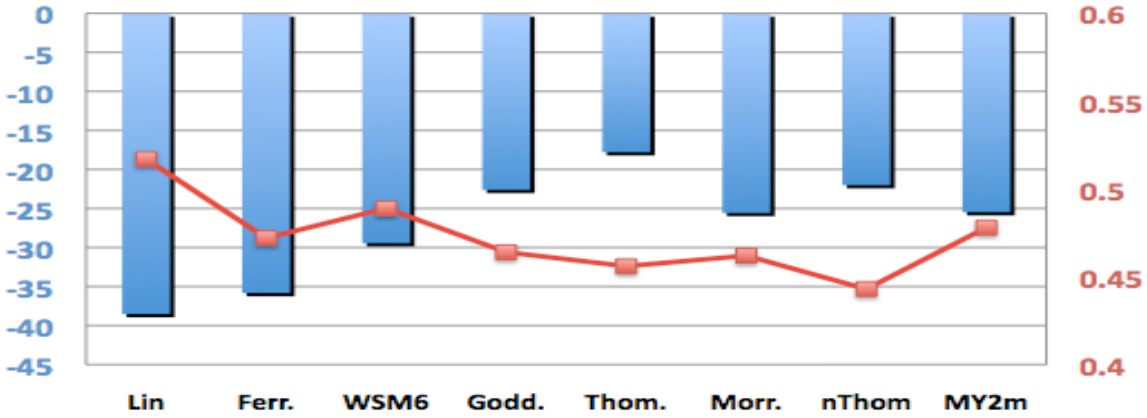

Figure 3.2.7. Downward longwave irradiance bias (W m^{-2}, blue) and correlation (red) in the microphysics sensitivity tests, as verified against observations from 2 ARM stations during September 2004

The comparison of daily mean downward shortwave irradiance (Figure 3.2.8), averaged over the entire simulation period and all 23 stations, shows that the degree of overestimation produced by the CSW scheme can be modulated by the choice of microphysics scheme. The Ferr and WSM6 schemes produce relatively large biases compared to the other schemes.

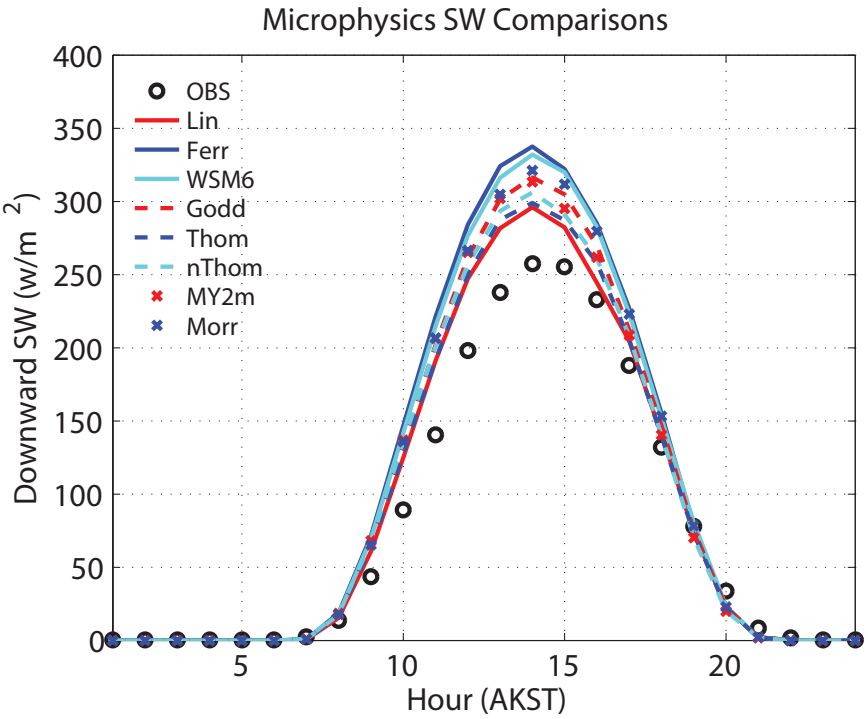

Figure 3.2.8. Daily mean shortwave irradiance (W m^{-2}) in the microphysics sensitivity tests, averaged over 23 ARM and RAWS stations during September 2004

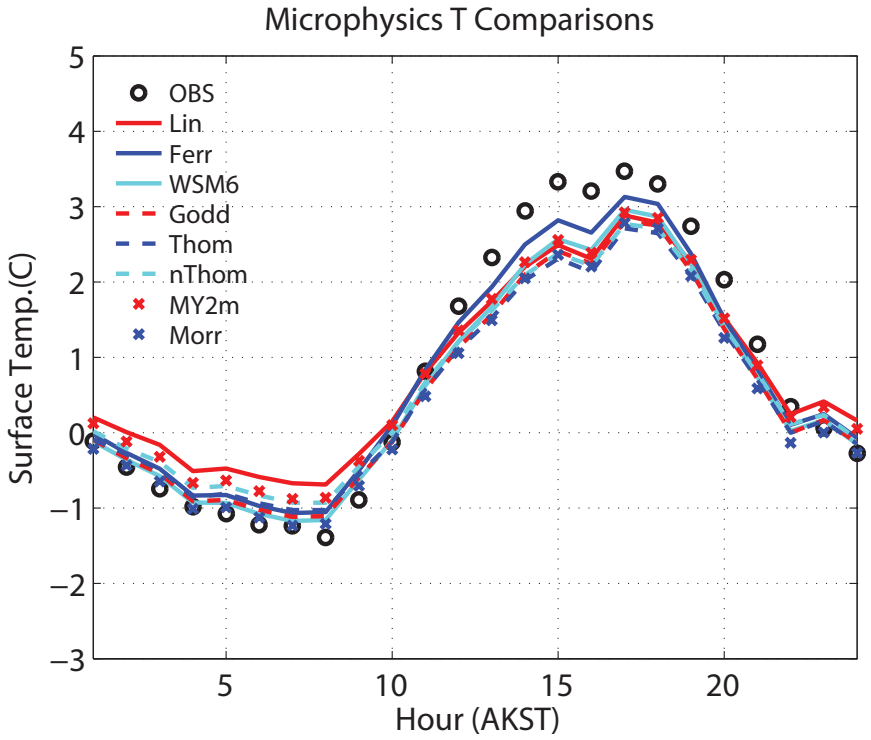

Figure 3.2.9. Daily mean 2-m temperature (°C) in the microphysics sensitivity tests, averaged over 96 stations during September 2004

As shown in Figure 3.2.6, the combination of CLW and CSW (CLWCSW) generates a cold bias in the simulation of daytime 2-m surface temperatures. This cold bias exists in all the microphysics tests as well (Figure 3.2.9), and the impacts from different microphysics schemes are relatively small.

Interactions between Radiation and Microphysics

As seen from the results of the radiation sensitivity tests (Figure 3.2.5), the CSW, GSW, and RgSW schemes all perform similarly in overestimating downward shortwave irradiance when used with WSM6 microphysics (sensitivity test names ending with CSW, GSW, and RgSW). However, when combined with other microphysics schemes, the overestimation of shortwave irradiance can be reduced to some degree, as seen when comparing the CSW scheme to the GSW scheme (Figures 3.2.10 and 3.2.11). The underestimated downward longwave irradiance by the CLW scheme is always stronger than that of the RLW scheme no matter which microphysics scheme is used (Figure 3.2.12).

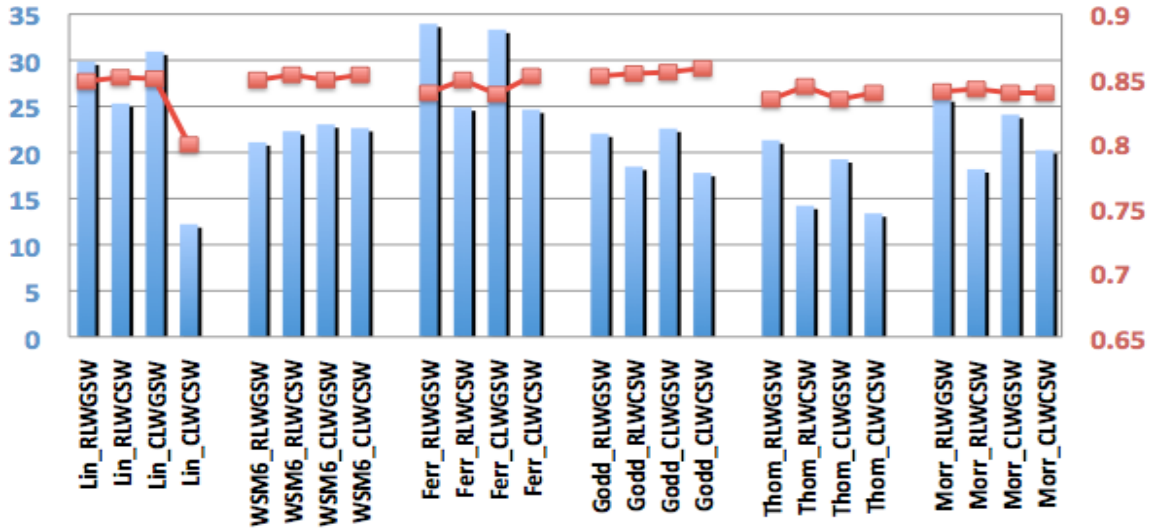

Figure 3.2.10. Downward shortwave irradiance bias (W m^{-2}, blue) and correlation (red) in the radiation-microphysics sensitivity tests, as verified against observations from 23 ARM and RAWS stations during September 2004

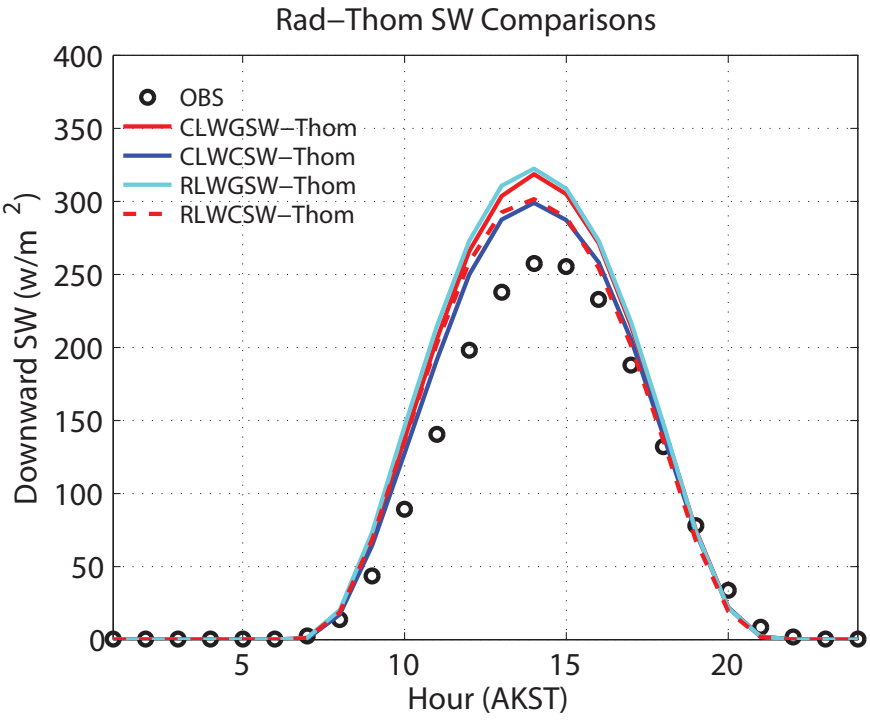

Figure 3.2.11. Daily mean downward shortwave irradiance (W m^{-2}) in the radiation-microphysics sensitivity tests, averaged over 23 ARM and RAWS stations during September 2004

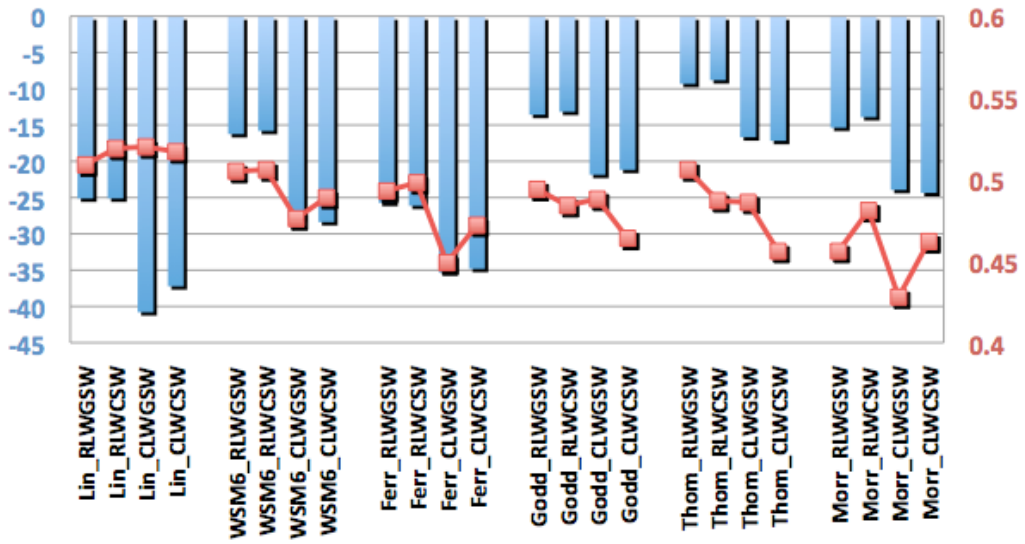

Figure 3.2.12. Downward longwave irradiance bias (W m^{-2}, blue) and correlation (red) in the radiation-microphysics sensitivity tests, as verified against observations from 2 ARM stations during September 2004

The performance of the various radiation and microphysics schemes, and their associated interactions, can be summarized as:

- The RLW scheme tends to produce relatively small biases in downward longwave irradiance when combined with different shortwave and microphysics schemes.
- The CSW scheme tends to produce relatively small biases in downward shortwave irradiance when combined with different longwave schemes and most microphysics schemes (except WSM6).

Thus, it becomes a challenge to select the optimal radiation schemes for use with a microphysics scheme other than WSM6. Most microphysics schemes serve to reduce biases in the CSW downward shortwave and RLW downward longwave irradiances. A similar reduction in bias is also found in the RgLW downward longwave irradiance (not shown). Considering that RRTMG is an updated, enhanced, and streamlined version of the older RRTM parameterization, the choice becomes one between the CAM and RRTMG schemes. The Thom microphysics scheme seems to reduce the irradiance biases more effectively than other schemes, leading it to be temporarily favored for the final production of CBHAR. However, according to Hines et al. (2011) and Bromwich et al. (2013), the RRTMG radiation and Morr microphysics schemes work reasonably well for accurately simulating the polar atmosphere. A further comparison between the CAM and RRTMG radiation schemes, and between the Thom and Morr microphysics schemes, will be discussed in Section 3.2.2 through the use of offshore SHEBA observations.

Planetary Boundary Layer (PBL)

The most important model physical parameterization option for influencing the simulation of near-surface winds is the planetary boundary layer (PBL) scheme. In

regional-scale model configurations such as the one used here, the number of vertical levels in the PBL is insufficient to fully resolve the complex and spatially inhomogeneous boundary layer processes. At the same time, accounting for these processes is of the utmost importance for calculating surface fluxes and simulating near-surface weather conditions. The model thus includes schemes to parameterize PBL processes and calculate the necessary fluxes. One of the functions of the PBL scheme is to calculate the 2-m temperature and moisture and 10-m winds that are ultimately used to validate the model output against station observations. These data also contribute to the final surface reanalysis that is the ultimate aim of this project. As such, the proper selection of the PBL scheme is critical, not only to maximize the performance of the model as a whole, but to ensure the accurate calculation of near-surface variables. WRF v3.2 includes a total of eight PBL options, six of which are currently supported and potentially suitable for the simulations conducted in this project. Thus, a total of six PBL schemes (YSU, MYJ, ACM2, QNSE, MYN2, and Bola) were tested in combination with the Noah LSM.

The downward longwave irradiance produced by the sensitivity tests YSU, MYJ, and ACM2 has a relatively smaller bias and better correlation compared to that from the other three schemes (Figure 3.2.13). On the other hand, most of the PBL schemes performed similarly in simulating downward shortwave irradiance (Figure 3.2.14). A close look at the performance of ACM2 shows it to have the smallest biases in the modeling of both shortwave and longwave irradiance. However, a strong noisy signal was discovered in the surface temperature field of subsequent ACM2 simulations, a highly unrealistic artifact that was not present with the use of other PBL schemes such as YSU and MYJ. This signal was found to regularly occur over sea-ice-covered areas, and given that a large portion of the study domain is normally covered by sea ice, ACM2 was ruled out from consideration in the determination of the final model configuration and from further use in this study.

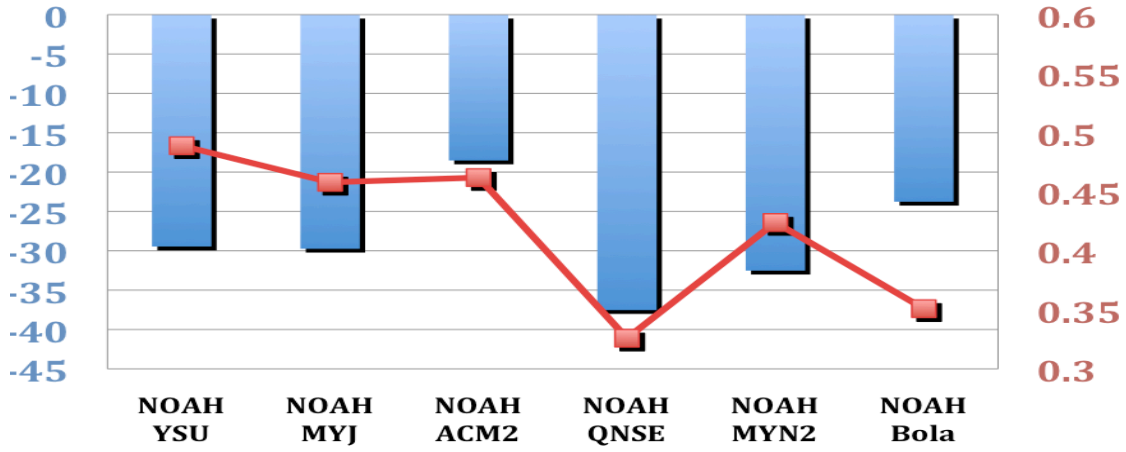

Figure 3.2.13. Downward longwave irradiance bias (W m^{-2}, blue) and correlation (red) in the PBL sensitivity tests, as verified against observations from 2 ARM stations during September 2004

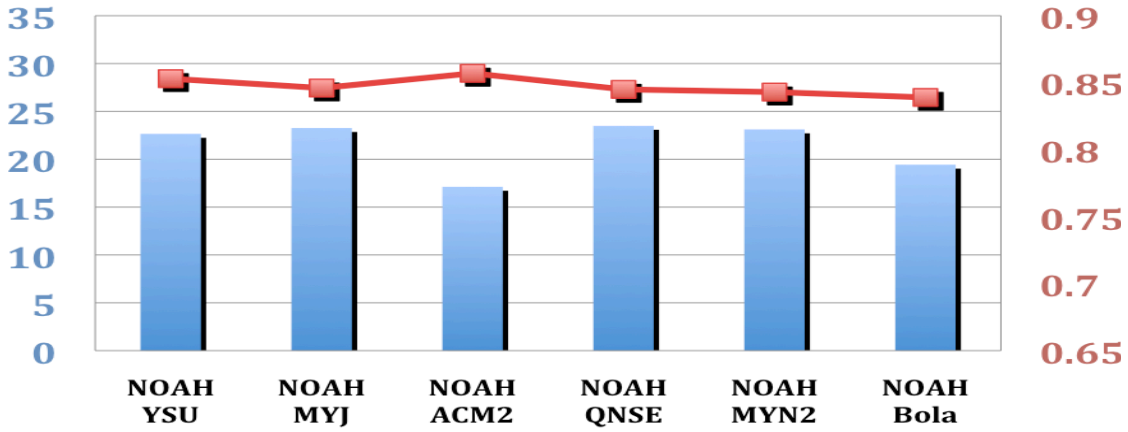

Figure 3.2.14. Downward shortwave irradiance bias (W m^{-2}, blue) and correlation (red) in the PBL sensitivity tests, as verified against observations from 23 ARM and RAWS stations during September 2004

Comparison of the PBL impact on the simulation of 2-m temperature (Figures 3.2.15 and 3.2.16) shows that most schemes perform similarly during the day but generate different temperatures at night. The YSU scheme produces the warmest surface temperatures, while MYN2 creates the coldest; the remainder of the schemes perform similarly to one another. An overall error analysis (Figure 3.2.16), examining the root-mean-square error (RMSE, Appendix B) of the modeled surface temperatures, indicates that the YSU and MYJ PBL schemes produce comparable results and generate smaller errors than the others.

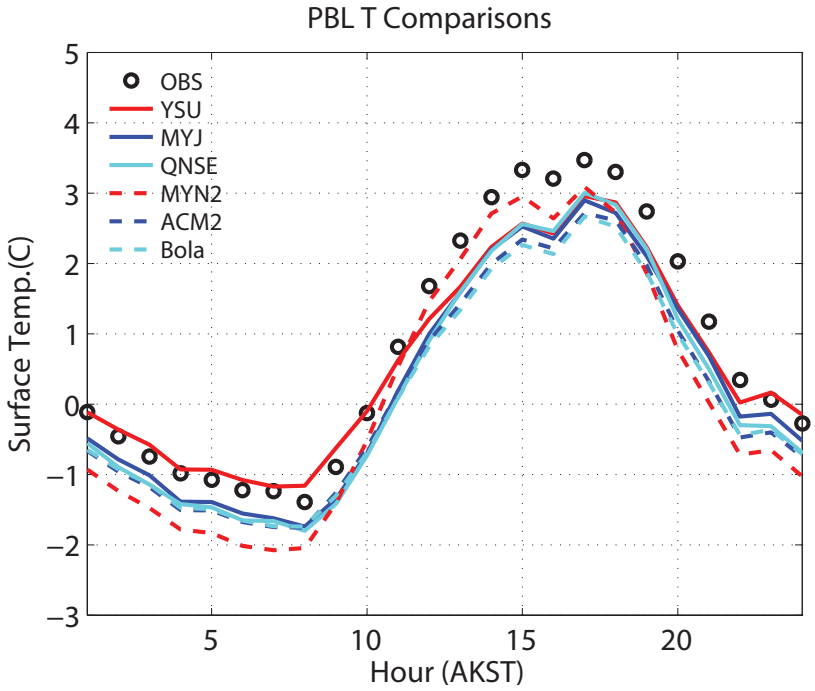

Figure 3.2.15. Daily mean 2-m temperature (°C) in the PBL sensitivity tests, averaged over 96 stations during September 2004

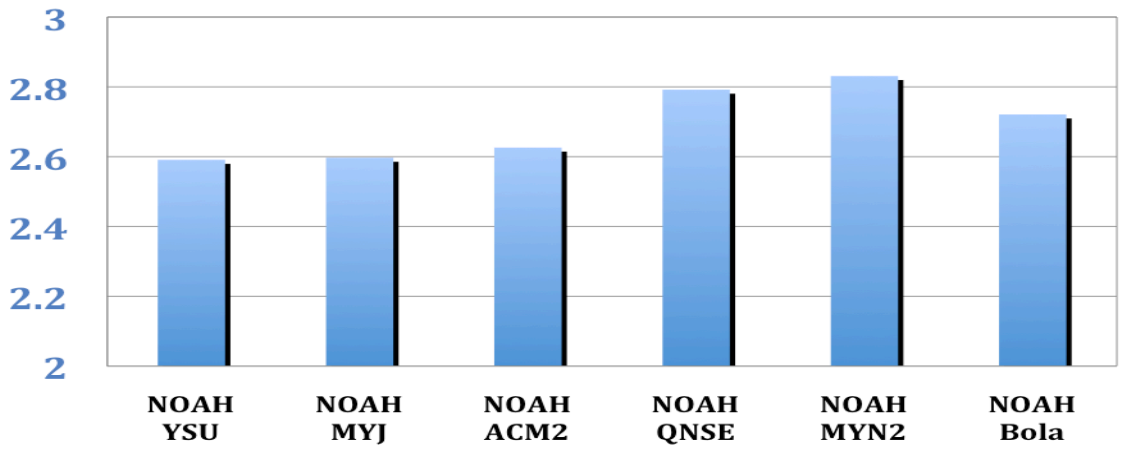

Figure 3.2.16. RMSE of 2-m temperature (°C) in the PBL sensitivity tests, as verified against observations from 96 stations during September 2004

Among all the types of model physical parameterizations, the PBL scheme has a comparatively larger impact on the modeling of the surface wind field. Comparison of the 10-m wind speed time series, averaged over the 96 stations during the entire simulation period of September 2004 (Figure 3.2.17), indicates that the PBL schemes MYJ and QNSE tend to generate stronger winds relative to the other schemes. This can be further confirmed by the comparison of wind speed biases shown in Figure 3.2.18, in which QNSE and MYJ generate slightly larger positive biases than the others. On the other hand, the biases in wind direction (Figure 3.2.19) show the opposite result: the MYJ and QNSE schemes have overall smaller biases. This presents a challenge in determining which PBL scheme should be included in the final model configuration for the production of CBHAR. To help address this, the RMSE and correlation of the wind vectors were calculated against observations from the 96 stations. The vector correlation was calculated following the method introduced by Crosby et al. (1993), in which it is calculated using the orthogonal components of the vectors. As shown in Figure 3.2.20, ACM2 generates the smallest error. However, as mentioned above, ACM2 was not a candidate for use in the final model configuration due to its numerical instability. In addition, QNSE and MYN2 proved to be too unstable for use in a production simulation, often causing the model to crash and exhibiting other unpredictable behavior. Thus, synthesizing the results of the simulation of both the surface temperature and wind fields, the PBL schemes YSU and MYJ were selected as *finalists* to be considered for use in the final production simulation.

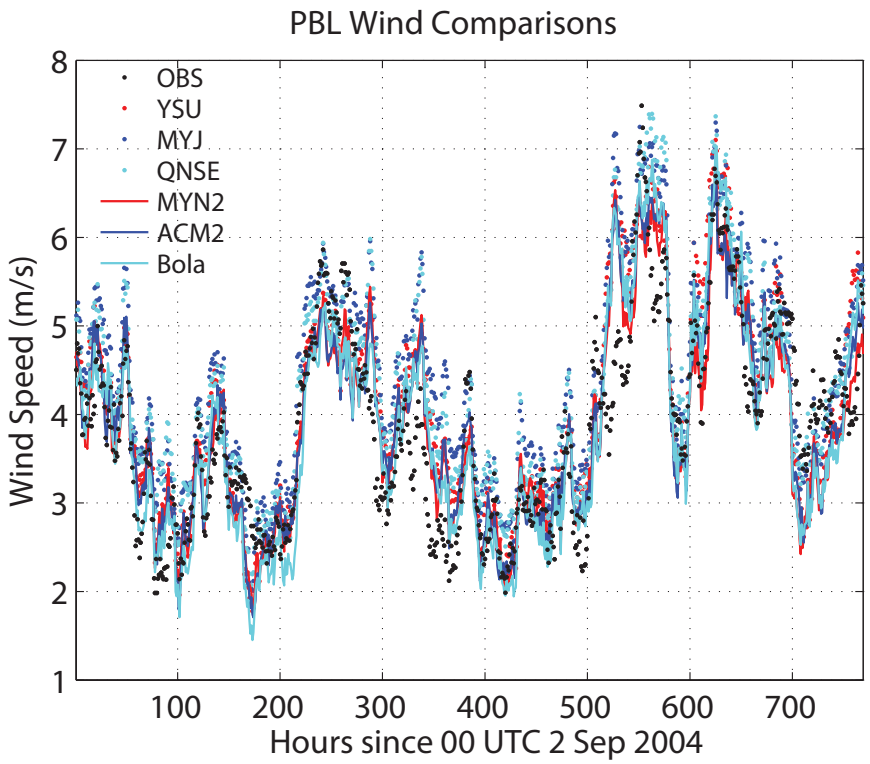

Figure 3.2.17. Time series comparison of 10-m wind speeds (m s^{-1}) in the PBL sensitivity tests, averaged over 96 stations during September 2004

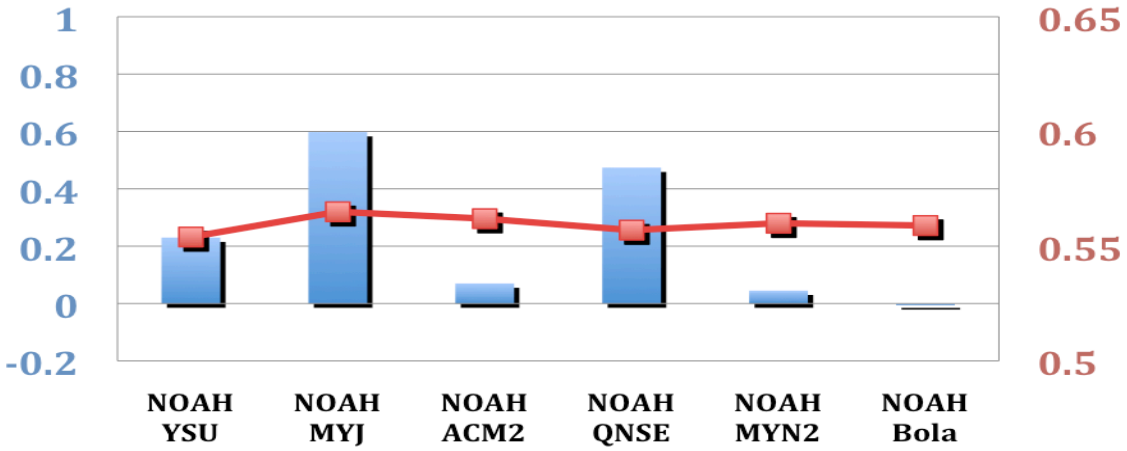

Figure 3.2.18. 10-m wind speed bias (m s^{-1}, blue) and correlation (red) in the PBL sensitivity tests, as verified against observations from 96 stations during September 2004

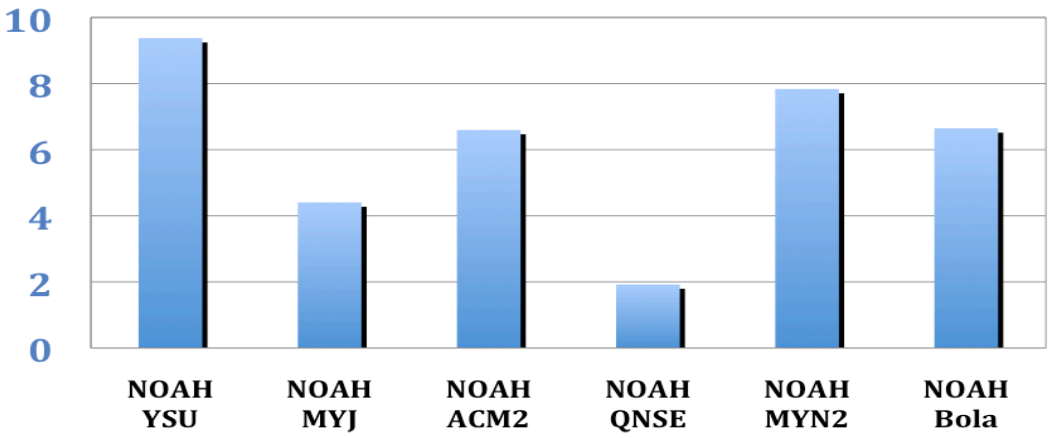

Figure 3.2.19. 10-m wind direction bias (degrees) in the PBL sensitivity tests, as verified against observations from 96 stations during September 2004

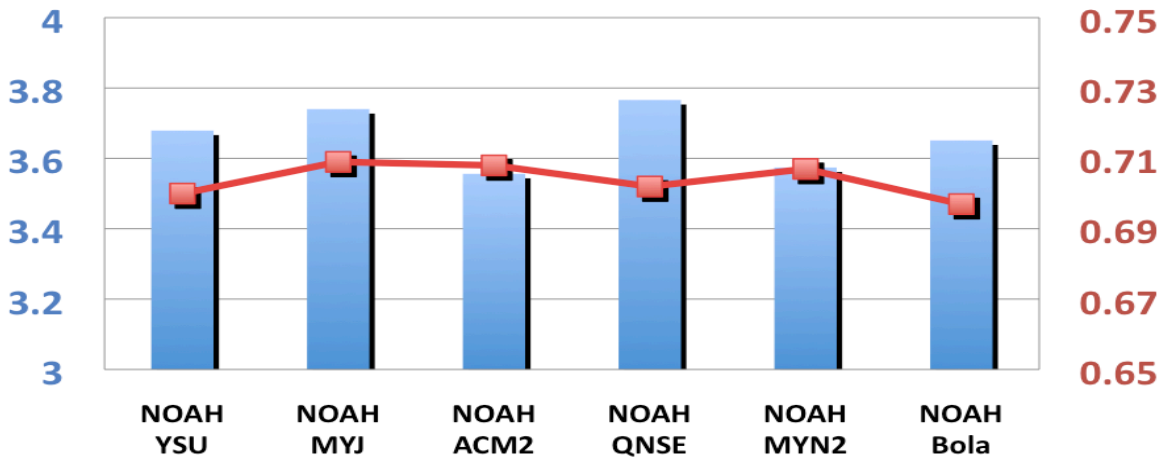

Figure 3.2.20. 10-m wind vector RMSE (m s^{-1}, blue) and correlation (red) in the PBL sensitivity tests, as verified against observations from 96 stations during September 2004

3.2.2 Sensitivity Tests Covering the SHEBA Period

Based on the results presented in Section 3.2.1, a total of five additional sensitivity simulations (Table 3.2.4), using a domain centered on the site of the SHEBA field experiment (Figure 3.2.21), were conducted to further evaluate WRF physical parameterizations in offshore Arctic conditions. SHEBA produced valuable, long-term (one year) observations in an Arctic region where no fixed stations exist, allowing the results of the model physical parameterization tests given in the previous section to be amended. As discussed in Section 3.2.1, when a microphysics option other than WSM6 is used, the scheme helps to reduce biases both in the downward shortwave irradiance produced by CSW and the downward longwave irradiance generated by RgLW; Thom microphysics tends to reduce them most effectively. On the other hand, according to Hines et al. (2011) and Bromwich et al. (2013), the RRTMG radiation and Morr

microphysics schemes work reasonably well in simulating the polar atmosphere. To clarify matters, additional sensitivity tests were run, comparing results from the CAM and RRTMG radiation schemes, as well as the Thom and Morr microphysics schemes, with SHEBA measurements. In addition, as discussed in Section 3.2.1, the two PBL schemes YSU and MYJ had been previously selected as finalists for use in the production of CBHAR. To more effectively distinguish between them, the YSU and MYJ schemes were thus also further evaluated through the use of SHEBA measurements.

Table 3.2.4. Sensitivity tests run for the SHEBA period (parameterizations used other than those identified here were NOAH LSM and KF cumulus)

Sensitivity test		Physical parameterizations	Simulation period
Microphysics	YSU-Thom-CLW-CSW	MYJ PBL/Thompson microphysics /CAM longwave/CAM shortwave	Dec 1997
Microphysics	YSU-Morr-CLW-CSW	YSU PBL/Morrison microphysics /CAM longwave/CAM shortwave	Dec 1997
Radiation	YSU-Morr-RgLW-RgSW	YSU PBL/Morrison microphysics /RRTMG longwave/RRTMG shortwave	July 1998
Radiation	YSU-Morr-CLW-CSW	YSU PBL/Morrison microphysics /CAM longwave/CAM shortwave	July 1998
PBL	MYJ-Morr-CLW-CSW	MYJ PBL/Morrison microphysics /CAM longwave/CAM shortwave	July 1998

The modeling domain used for these tests has dimensions of 235 by 235 points with a grid spacing of 10 km and 49 vertical levels. It is essentially a modified form of the study domain shown in Figure 1.1.2, expanded in the north-south direction and shifted slightly northward; the configuration of the vertical levels is identical. As the expanded domain extends beyond the limits of NARR, the global ERA-Interim reanalysis was instead used to provide initial and boundary conditions to the model. In order to evaluate the performance of the model for both summer and winter conditions in the Arctic offshore region, two different simulation periods were selected. The first period, representing the Arctic winter, began at 0000 UTC 1 December 1997 and ended at 0000 UTC 1 January 1998. The second, representing the Arctic summer, began at 0000 UTC 1 July 1998 and ended at 0000 UTC 1 August 1998, which is a particularly ideal period for the evaluation of shortwave radiation schemes. In the same manner as the sensitivity tests described in Section 3.2.1, the simulation periods were subdivided into a series of 4.5-day periods, which were run independently and initialized every fourth day at 1200 UTC, with the first 12 hours of each simulation treated as spin-up and not used in the validation.

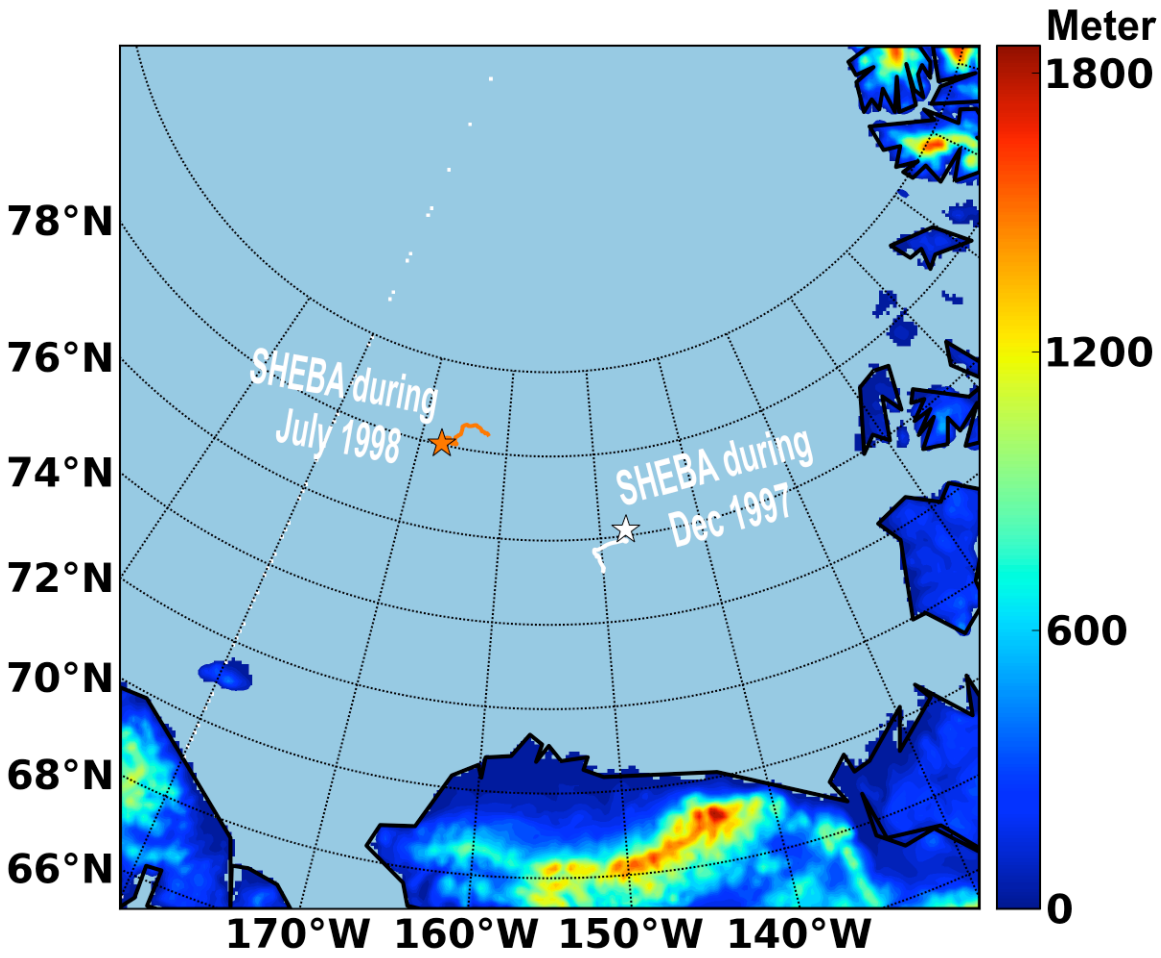

Figure 3.2.21. Sensitivity simulation domain encompassing the SHEBA locations for tests during December 1997 (white track; the star indicates the SHEBA location at the beginning of the month) and July 1998 (orange track)

Both the Thom and Morr schemes include two-moment microphysics, which can improve the simulated aggregation process of mixed-phase clouds by allowing for better representation of particle number concentration and is essential for reasonably modeling clouds in the Arctic (Girard and Curry 2001; Morrison et al. 2003; Shupe and Intrieri 2004). The accurate simulation of clouds is particularly important in the winter months due to their emitted longwave radiation, which plays a crucial role in determining the surface energy balance in the absence of direct solar forcing. As such, the December 1997 SHEBA case was selected in order to further evaluate the microphysics schemes. Overall, the Morr and Thom schemes performed very similarly at the SHEBA site for the simulation of downward longwave irradiance, 2-m temperature, and 10-m wind vectors (Table 3.2.5). Considering that the Morr scheme has been widely used in modeling studies of the polar atmosphere (Hines et al. 2011; Barton and Veron 2012; Claremar et al. 2012; Tastula et al. 2012), combined with its strong performance in both these and the prior sensitivity tests, a decision was made to use the *Morr* scheme in the final model configuration for generating the 31-year CBHAR reanalysis.

Table 3.2.5. RMSE of downward longwave irradiance (W m^{-2}), 2-m temperature (°C), and 10-m wind vector (m s^{-1}) for the microphysics sensitivity tests during December 1997 as verified against SHEBA measurements

Sensitivity test	Longwave (W m^{-2})	Temperature (°C)	Wind vector (m s^{-1})
YSU-Morr-CLW-CSW	21.43	8.27	2.05
YSU-Thom-CLW-CSW	21.25	8.22	2.00

Since shortwave radiation is relatively non-existent during the winter months in the study region, the July 1998 case was instead selected for the radiation sensitivity tests, so that both downward short- and longwave irradiances could be calibrated concurrently. The CAM and RRTMG radiation schemes were tested while paired with the Morr microphysics scheme and verified against SHEBA measurements (Table 3.2.6). The verification results indicate that the CAM and RRTMG schemes perform similarly in the simulation of downward longwave irradiance, but RRTMG outperforms CAM in modeling downward shortwave irradiance. As a result, an improved surface temperature is achieved by the RRTMG scheme. A slight improvement in surface wind vector is also found in the simulation using RRTMG. Therefore, a clear decision was made to use *RRTMG* as both the short- and longwave radiation parameterizations in the final model configuration for the production of the 31-year CBHAR reanalysis.

Table 3.2.6. Same as Table 3.2.5 but for the radiation sensitivity tests during July 1998

Sensitivity test	Longwave (W m^{-2})	Shortwave (W m^{-2})	Temperature (°C)	Wind vector (m s^{-1})
YSU-Morr-CLW-CSW	23.41	90.96	2.12	2.76
YSU-Morr-RgLW-RgSW	23.66	86.04	1.17	2.58

The summer SHEBA case was also used to compare the performance of the YSU and MYJ PBL schemes (Table 3.2.7). Overall, these two schemes perform similarly in terms of modeling the downward longwave irradiance, surface temperature, and wind vector, though MYJ outperforms YSU for downward shortwave irradiance. Therefore, *MYJ* was chosen to be the PBL parameterization in the final model configuration.

Table 3.2.7. Same as Table 3.2.5 but for the PBL sensitivity tests during July 1998

Sensitivity test	Longwave ($W\ m^{-2}$)	Shortwave ($W\ m^{-2}$)	Temperature (°C)	Wind vector ($m\ s^{-1}$)
YSU-Morr-CLW-CSW	23.41	90.96	2.12	2.76
MYJ-Morr-CLW-CSW	23.43	87.51	2.23	2.90

Aside from the above model physical parameterization options, WRF also includes the ability to select parameterizations that govern the atmospheric surface layer, land-surface treatment, and sub-grid-scale convection processes. As the surface layer represents the bottom part of the boundary layer, the surface layer schemes are inextricably linked to the choice of PBL, and each PBL option is only designed to work with a select number (often only one) of the surface layer schemes. The MYJ PBL scheme, selected for the final model configuration, is only compatible with the *Eta similarity surface layer*, and so this was necessarily selected as part of the final model configuration as well. Similarly, of the available land-surface models, the only one that is designed to work with the current version of the Polar WRF modifications employed in the final configuration (see Section 3.3.2), as well as the most physically advanced model, is the *Noah LSM*.

3.2.3 Sensitivity Tests Covering August 2009

As with the sensitivity tests conducted for the period of September 2004, the same domain (Figure 1.1.2) and integration design as described in Section 3.2.1 were again used to conduct another series of sensitivity tests for the period of August 2009 in order to evaluate the performance of the available cumulus parameterization schemes. A total of four cumulus schemes are available in WRF v3.2 and were tested as shown in Table 3.2.8. The RMSE of the cumulus sensitivity tests as verified against surface observations during August 2009 was compared for the variables of longwave and shortwave irradiance, 2-m temperature, and 10-m wind vector (Table 3.2.9). The comparison shows that the cumulus scheme directly impacts the modeling of irradiance, and both the Grell–Devenyi and Grell-3D ensemble schemes produce smaller errors for both long- and shortwave irradiance, contributing to a relatively small error for surface temperature as well. Thus, the more advanced of the two, the *Grell-3D ensemble cumulus* parameterization, was selected for use in producing the final CBHAR reanalysis.

Table 3.2.8 Sensitivity tests covering August 2009 (parameterizations used other than those identified below were Morr microphysics, RRTMG radiation, MYJ PBL, and NOAH LSM)

Sensitivity test	Physical parameterization
KF	Kain–Fritsch cumulus
BMJ	Betts–Miller–Janjic cumulus (Janjic 1994, 2000)
GD	Grell–Devenyi ensemble cumulus (Grell and Devenyi 2002)
Grell-3D	Grell-3D ensemble cumulus (Grell and Devenyi 2002)

Table 3.2.9. RMSE of cumulus sensitivity tests as verified against surface observations of long- and shortwave irradiance (W m^{-2}), 2-m temperature (°C), and 10-m wind vector (m s^{-1})

Sensitivity test	Longwave (W m^{-2})	Shortwave (W m^{-2})	Temperature (°C)	Wind vector (m s^{-1})
KF	34.68	151.09	3.23	3.47
BMJ	33.75	147.59	3.22	3.47
GD	31.02	139.13	3.15	3.41
Grell-3D	31.92	138.88	3.15	3.41

3.3 Improvements to Model Physical Parameterizations

Efforts conducted to implement more advanced model physical parameterizations in the WRF model included the coupling of a thermodynamic sea ice model (Zhang and Zhang 2001) and adoption of some improvements to WRF, termed Polar WRF, made by the Polar Meteorology Group at OSU. These two efforts are summarized in Sections 3.3.1 and 3.3.2, respectively.

3.3.1 Coupling of Thermodynamic Sea Ice

CBHAR uses a model domain that is half-covered by ocean, which in turn is seasonally covered by sea ice for much of the year. It is therefore naturally important for the WRF model to be able to accurately characterize sea ice thermodynamic processes in order to properly simulate surface temperatures, and by extension other linked variables such as near-surface wind. By default, sea ice processes are treated by the Noah land-surface model in a way not altogether different from other types of land cover, which can result in significant errors in the simulation of surface temperature. For example, the albedo of sea ice, which plays a significant role in the calculation of the surface energy balance, particularly in the spring through autumn months, is hard coded as a constant value in the Noah LSM, and sea ice is assumed to have snow cover all year long. In reality, sea ice albedo varies dramatically throughout the year, sometimes even in the same day, as snow accumulates and melts on the sea ice surface. The snow-free bare ice often present in the

summer months has a completely different radiative character than mid-winter sea ice topped with a snowpack, leading to very different thermodynamic calculations. If these types of differences are not accounted for, surface energy fluxes over much of the domain will have significant errors, leading to major biases in the reanalyzed fields. In order to address this native deficiency in the Noah LSM, a thermodynamic sea ice model (Zhang and Zhang 2001) was coupled to WRF for the production of the final CBHAR reanalysis, leading to improved simulation of surface temperatures and fluxes, as described below.

In the coupled model, the treatment of sea ice thermodynamics follows Hibler (1979) and Parkinson and Washington (1979). The net energy flux over the sea ice surface H_{Ti} is given by:

$$H_{Ti} = R - F + H + E \qquad (3.1)$$

where

$$R = R_s(1-\alpha) + R_l$$

$$F = \varepsilon\sigma T_i^4$$

$$H = \rho C_p C_h V(T_a - T_i)$$

$$E = L\rho C_p V(q_a - q_i)$$

Here, R is the incoming total radiative flux at the ocean surface, F is the outgoing longwave radiative flux from the ocean surface, and H and E are the sensible and latent heat fluxes between the atmosphere and ocean, respectively. In addition, R_s and R_l are the downward shortwave and longwave radiative fluxes (calculated by the atmospheric model), respectively, and α is the surface albedo, which is calculated following Gardner and Sharp (2010). ε is the ice-surface emissivity (0.95), σ is the Stefan–Boltzmann constant (5.67×10^{-8}), and the air density ρ, air heat capacity C_p, surface exchange coefficient for heat and moisture C_h, and surface wind speed V are all defined from the atmospheric model. L is the latent heat and T and q represent surface temperature and specific humidity, respectively, with subscript a representing atmosphere and subscript i representing sea ice. T_a and q_a are defined from the atmospheric model.

A Newton/Raphson iteration scheme is used to resolve the sea ice temperature from the above surface energy balances. When snow cover exists on the sea ice, a similar method is used to resolve the snow surface temperature. The interface between snow and sea ice contains the following balance between the conductive fluxes of snow and sea ice:

$$\frac{C_s}{h_s}(T_i - T_s) = \frac{C_i}{h_i}(T_b - T_i) \qquad (3.2)$$

Here, C is the thermal conductivity, h is the thickness, and T is the skin surface temperature of the snow or ice layer, with the subscripts s and i denoting snow and ice, respectively. T_b represents the bottom temperature of the sea ice layer, i.e. the freezing point of the seawater below the ice.

As mentioned above, a physically based broadband albedo parameterization (Gardner and Sharp 2010) was incorporated into the sea ice model. This parameterization calculates albedo as a function of ice-grain specific surface area, concentration of light-absorbing carbon, solar zenith angle, cloud optical thickness, and depth of the overlying snow layer. Combining these terms, given an input snow cover analysis, yields a more flexible, dynamic characterization of the sea ice albedo and generates realistic values for all conditions throughout the year, without the need for artificial techniques for directly specifying the albedo. The new albedo parameterization has the added advantage of accounting for the observed spectral shift in broadband albedo that occurs under varying cloud conditions and solar angles. To determine the appropriate value for the ice-grain surface area in the study region, values of snow cover, solar angle, and cloud thickness data taken from model simulations conducted over the entire SHEBA experimental period (1997–98) were used, in combination with high-frequency observed albedos. This calculated specific surface area was then used in the CBHAR production simulation. For the carbon concentration, a typical value for Arctic carbon loading of 7 ppm was taken from the observations of Doherty et al. (2010), who measured carbon values throughout the Arctic region, including at sites in the Beaufort Sea.

Though the presence of sea ice plays a major role in the meteorology of the Chukchi–Beaufort Seas region through modification of the surface condition, due to the remote location and difficulty in maintaining observational platforms on the constantly changing ice there exist very little observational data gathered from the surface of the ice itself. Owing to the lack of such verification data in the CBHAR domain, the performance of the model was instead tested on the SHEBA-centered domain used for some of the model physical parameterization sensitivity tests (Figure 3.2.21). As before, two cases were chosen: one in winter, for the month of December 1997, and the other in summer, for the month of July 1998. Both a control simulation without the sea ice model and a sea ice coupled simulation were performed for each case and the results were verified against SHEBA field measurements.

For the summer simulation (July 1998), WRF was initialized with the ERA-I reanalysis and the Canadian Meteorological Centre (CMC) 25-km daily snow depth dataset and run for one month. During summer, sea ice surface albedo experiences high variability compared to the rest of the year, and so this simulation provided a good opportunity to examine the model's performance in simulating sea ice albedo. The SHEBA campaign observed surface albedo via two methods: (1) a high-frequency measurement made at a fixed observation tower, and (2) a line measurement, a daily-reported average albedo measured at various points along a 500-m survey line, incorporating the effects of horizontal variability, including the important impacts on albedo of melt ponds. As seen in Figure 3.3.1, the control simulation used the constant surface albedo of 0.8 as set by default in the Noah LSM, which is obviously not representative of real-world conditions. In contrast, the coupled sea ice model captured the observed variation in albedo relatively well, particularly when compared with the point measurements taken at the tower. Since the sea ice albedo parameterization does not account for any effects from melt ponds, which tend to reduce the ice albedo, the model did not capture the small line-averaged albedo values observed at the end of July. The short-term maxima in the tower-observed

albedo represent fresh snowfall events, which dramatically increase the reflectance of the normally bare ice prior to rapidly melting. Such localized events could also not be captured by WRF, which took its snow cover conditions from the daily 25-km CMC dataset.

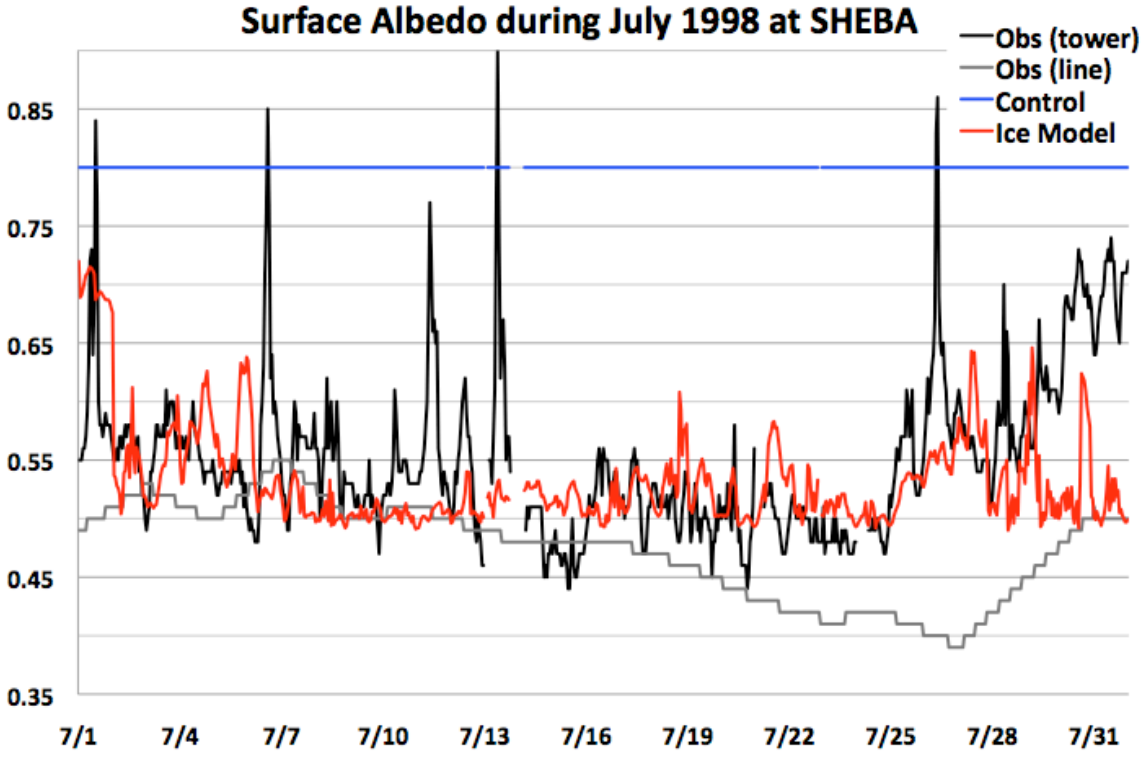

Figure 3.3.1. Comparison of surface albedo between SHEBA observations (black and grey) and control (blue) and sea ice coupled (red) simulations during July 1998

Ultimately, the primary goal of coupling the sea ice model with WRF is to more accurately simulate sea ice surface temperature, and by extension surface fluxes to the atmosphere, which can in turn impact the modeling of near-surface meteorology. As ice-surface temperatures are relatively constant during the summer months, for the most part remaining close to the melting point, a winter case was instead used to evaluate the performance of the coupled model in simulating sea ice temperatures. A one-month simulation was performed for December 1997 using the same model configuration as the summer case. Figure 3.3.2 shows that the coupled model succeeded in improving the simulation of sea ice temperatures relative to the control simulation. In particular, the relatively strong cold bias produced by the control simulation (up to 10°C in the latter half of December 1997) is significantly reduced or eliminated altogether, although the coupled model reduced extreme cold minima throughout the entire period.

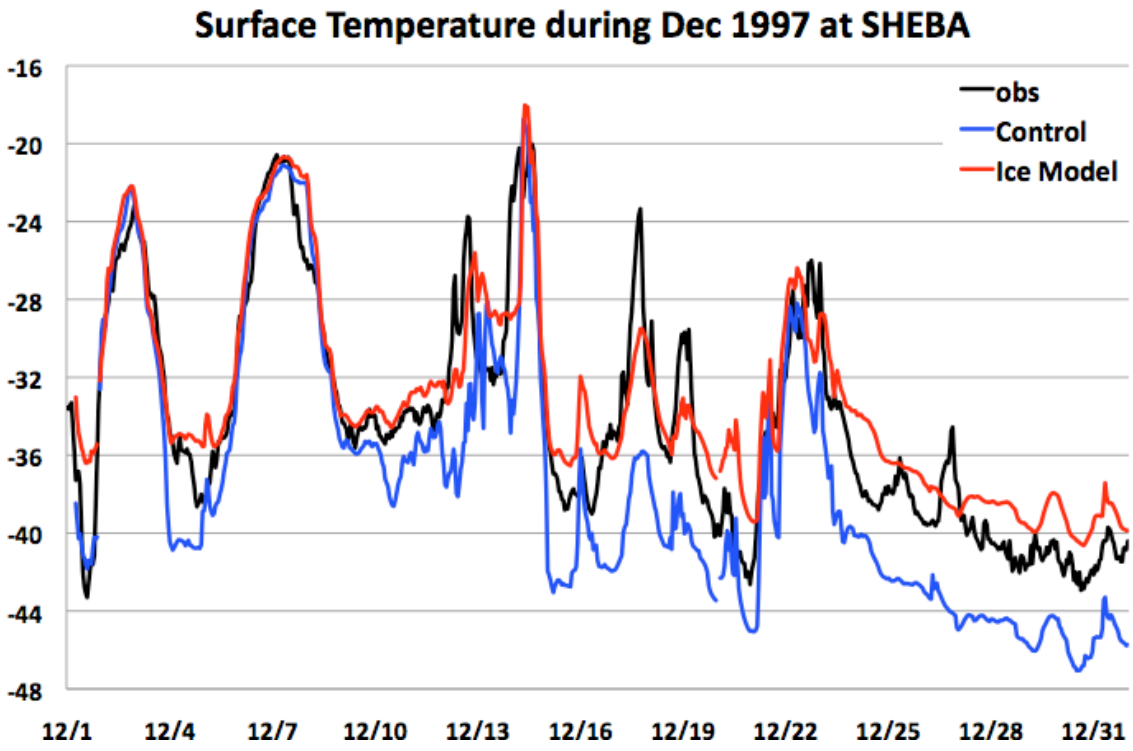

Figure 3.3.2. Sea ice skin temperature (°C) time series for SHEBA observations (black) and control (blue) and coupled sea ice (red) simulations during December 1997

The results presented here, demonstrating an accurate, dynamic calculation of the sea ice albedo, combined with an improved simulation of sea ice surface temperature, confirm that the sea ice model that has been coupled with WRF serves to significantly improve the thermodynamic treatment of sea ice in the model. This coupling was therefore applied in the final model configuration used for the production of the CBHAR reanalysis.

3.3.2 Adoption of Polar WRF Improvements

The Polar Meteorology Group at OSU has made a package of code changes to the WRF model, called Polar WRF, available to the public since late 2009. Polar WRF contains several modifications to the standard WRF model, intended to improve the overall performance of the model for the polar regions. Chief among these are modifications to the Noah LSM that allow WRF to incorporate variable sea ice thickness data, in place of the constant 3-m thickness value set by default in the model. The thickness of the ice layer impacts heat transfer between the atmosphere and the liquid ocean beneath the ice, thus affecting the surface temperature calculation performed by the coupled sea ice model introduced in Section 3.3.1. In addition, Polar WRF includes a change that sets the bottom temperature of sea ice to –1.8°C, instead of the default –2.0°C. These sea ice thickness and ice parameter modifications were tested and included in the final WRF configuration. It should be noted that the Polar WRF distribution also includes additional options, including variable sea ice albedo, an alternate calculation of the snow/ice surface

energy balance, and a change to the thermal conductivity of the top soil layer for tundra land-use categories, representing a peat (organic) layer that is found atop the soil of the Arctic Slope. These latter options were not utilized in the final configuration, either due to a more advanced option already existing in the coupled sea ice model (in the case of variable ice albedo), or as a result of sensitivity testing, which demonstrated degraded performance when the options were used in the study area.

In order to check the efficacy of using the selected Polar WRF modifications in conjunction with the coupled sea ice model, sensitivity tests were conducted for a two-month period (Nov–Dec 1997) over the SHEBA domain (Figure 3.2.21). For these tests, in addition to the simulation with the standard WRF model (CTRL), simulations were conducted with the standard Polar WRF codes (PWRF), as well as with WRF coupled with the thermodynamic sea ice model and selected modifications from Polar WRF (WRF-ice). A summary of these tests is given in Table 3.3.1. Verification was performed against the SHEBA observations, with the RMSE calculated for various thermodynamic variables, as given in Table 3.3.2.

Table 3.3.1. Sensitivity simulations comparing WRF, Polar WRF, and WRF-ice

Sensitivity test	Configuration
CTRL	Standard WRF model configured with Morr microphysics, KF cumulus, CLW longwave, CSW shortwave, YSU PBL, and NOAH LSM
PWRF	Polar WRF with the same configuration as CTRL
WRF-ice	Same configuration as CTRL, except using the coupled thermodynamic sea ice model and selected Polar WRF options, namely variable sea ice thickness and a bottom sea ice temperature of −1.8°C

Table 3.3.2. RMSE of surface air temperature (°C), surface skin temperature (°C), and sensible and latent heat fluxes (W m^{-2}) for sensitivity simulations during November–December 1997 as verified against SHEBA observations

Sensitivity test	Surface air temperature (°C)	Ice skin temperature (°C)	Sensible heat flux (W m^{-2})	Latent heat flux (W m^{-2})
CTRL	2.50	4.11	18.35	1.96
PWRF	2.74	3.74	10.88	1.84
WRF-ice	2.50	3.38	11.40	1.85

The results demonstrate that WRF-ice, in which WRF is coupled with the thermodynamic sea ice model and selected Polar WRF improvements are adopted, generates better results in the simulation of both surface air temperature and sea ice skin temperature relative to both the standard WRF and Polar WRF models. Though the sensible heat flux is slightly worse, it may, in fact, may be artificially low in the case of Polar WRF, as both the air

and skin temperatures, which are its primary governing factors, saw decreased accuracy relative to the use of the sea ice model. Given these results, demonstrating the success of both selectively incorporating Polar WRF options, particularly variable sea ice thickness, and coupling the thermodynamic sea ice model with WRF, the use of selected Polar WRF improvements and the coupled sea ice model were thus included in the final model configuration for the production of CBHAR.

3.4 Optimization of Data Assimilation Configuration

Forecast simulations of as little as a few days can generate errors due to inaccuracy in the forcing data and limitations of the model itself. The longer the model runs, the more the errors accumulate. This is particularly true for simulations with constrained boundaries as conducted for this project. The drift induced by the influence of lateral boundary conditions grows with time and can be attributed to the chaotic nature of the flow. Thus, it is necessary to constrain the model solution in some form, to ensure that it is not allowed to deviate too far from reality. There are generally two ways that this can be accomplished:

1) Nudging the model solution to a known, "correct" reanalysis, such as that provided to the model at initialization.
2) Assimilating additional observations into the model, thereby generating a new reanalysis as was done for the initialization of the model simulation, and repeating this action whenever additional observations are available until the end of the desired simulation period is reached.

Which of the two methods (nudging or assimilation) best improves the model results, and could a combination of the two (whereby new analyses are generated via data assimilation, with the model simultaneously nudged to the forcing data) perform even better? This question was explored in this effort through the use of WRF v3.2 and its data assimilation system WRFDA, a flexible, state-of-the-art atmospheric data assimilation package. The research efforts investigating the relative performance of both data assimilation and reanalysis nudging are summarized in Sections 3.4.1–3.4.4.

3.4.1 Data Assimilation Sensitivity Test Design

Data assimilation has proven to be a useful technique for constraining the model solution and reducing model errors, as seen in the production of many reanalyses such as ERA-I and NARR. However, assimilating extra data into an analysis does not necessarily improve the quality of the subsequent simulation for all parameters. It is therefore necessary to test the effect of assimilating each observation type in order to determine whether or not to include it in the final production simulation. In addition, the WRFDA assimilation system determines its optimal analysis through the use of information that includes model background error (BE) and observational error. The dynamic model results are combined with observations using weights inversely related to their respective errors. Each observation data type is characterized by its own error distribution, dependent on the accuracy of the individual observation system, but model errors are not fixed and can be affected by the choice of model domain and configuration. Thus, model

background errors must be determined prior to the performing of any data assimilation. In order to best optimize the WRFDA assimilation system for the production of CBHAR, two sets of sensitivity experiments were conducted as described in the following two sections:

- Section 3.4.2 describes tests for the evaluation of model BE sensitivity.
- Section 3.4.3 details tests for evaluating the potential observation data types to be assimilated.

The model domain used for these tests was the same as in Figure 1.1.2. The physical parameterization schemes used in the assimilation tests are listed below (Table 3.4.1):

Table 3.4.1. Configuration of WRF physical parameterizations in the assimilation sensitivity tests

Physical parameterization	Configuration
Cumulus	KF cumulus
Microphysics	Morr microphysics
Longwave radiation	RgLW longwave
Shortwave radiation	RgSW shortwave
Planetary boundary layer	YSU PBL
Land-surface model	NOAH LSM

The selected simulation periods included two separate months in 2009: January was chosen to represent winter conditions and July was used for summer conditions. The oceanic portion of the domain experiences high variability throughout the year in its sea ice coverage and surface temperature, and the land similarly varies in its snow cover and thermal profile. This high level of variability thus provides a good opportunity for investigating the performance of WRFDA by examining the two extreme months of January and July.

The in situ observational data tested for assimilation by WRFDA included surface observations from 122 stations distributed throughout the model domain, along with three radiosonde stations, as indicated in Figure 3.4.1. These in situ observations were collected from different data sources and were quality controlled as described in Section 2. The satellite retrievals tested with WRFDA included Quick Scatterometer (QuikSCAT) ocean-surface winds; temperature and moisture profiles from both the Moderate Resolution Imaging Spectroradiometer (MODIS) and Constellation Observing System for Meteorology, Ionosphere, and Climate (COSMIC) platforms; and upper-level polar winds from both the MODIS and Advanced High Resolution Radiometer (AVHRR) platforms. The QuikSCAT surface winds are available over open water at a resolution of 12.5 km and cover the period from July 1999 to November 2009. The MODIS-retrieved moisture and temperature profiles include 20 vertical levels (from 1000 to 5 hPa) at a horizontal spacing of 5 km and are available since March 2000. The

COSMIC retrievals provide temperature and moisture profiles, thinned here to 26 vertical levels (from 1000 to 10 hPa), and are available beginning in July 2006. The AVHRR-derived polar wind product has a grid spacing of 5 km, and is available from the beginning of 1982, while MODIS-derived polar winds have a grid spacing of 2 km and are available beginning in July 2002. Both polar wind products consist of a single wind observation at each available grid point, reported at varying levels depending on the altitude of the clouds used to determine the wind vectors.

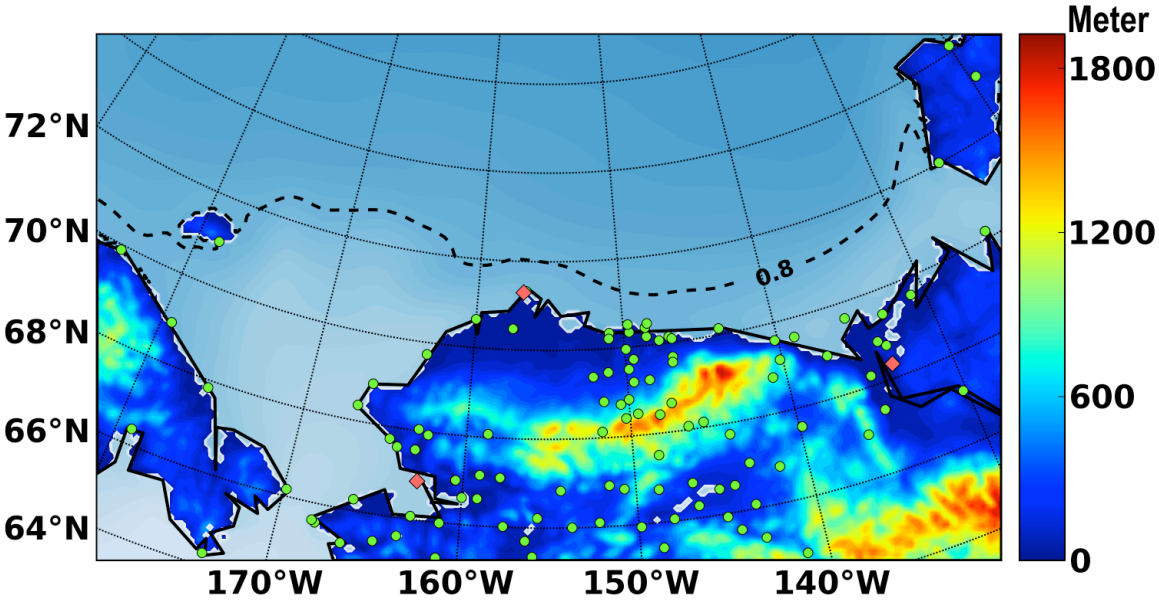

Figure 3.4.1. Distribution of the 122 observational stations used in WRFDA assimilation sensitivity tests and verification. In situ surface stations are indicated by green dots, and radiosonde stations by red diamonds.

In all of the sensitivity simulations, the model was re-initialized from ERA-I forcing data every 2 days and run for 2 days and 6 hours, during which time the available observational data were assimilated every 6 hours (including at the initial hour). Only data within ±1.5 hours of the assimilation hour were used. The results from the first 6 hours of each run were used as model spin-up and removed from consideration, with the remaining 2-day periods pieced together to form a continuous time series. In addition to the assimilation runs, a control simulation (CTRL), in which no data were assimilated but which was otherwise identical to the assimilation runs, including the stop-restart cycle every 6 hours, was also conducted for the purposes of comparing and evaluating the sensitivity results.

3.4.2 Sensitivity of WRFDA to Model Background Error

WRFDA offers the option of using either built-in global model BE (BE-GFS) or user-customized model BE in its data assimilation process. The built-in BE is generated from Global Forecast System (GFS) forecasts, produced by NCAR with a horizontal grid spacing of about 80 km, and can be used for any domain due to its global coverage

(Barker et al. 2004). Customized BE can be calculated following the National Meteorological Center (NMC) method (Parrish and Derber 1992), in which the differences between 12- and 24-hour model forecasts that are valid at the same time are first calculated, with the model BE estimated after averaging all forecast differences over a given period of time and the error covariances calculated. In this study, the 12- and 24-hour forecasts for the entire year of 2009 were first generated with the model configuration listed in Table 3.4.1. The differences between the 12- and 24-hour forecasts were then averaged, both over the entire year and for each month individually, in order to produce both yearly-averaged BE (BE-1yr) and monthly-averaged BE (BE-Jan, BE-Jul), respectively.

A total of five simulations, including one control and four sensitivity runs (Table 3.4.2), were conducted in order to evaluate the sensitivity of WRFDA to model BE in the assimilation of in situ surface observations. In addition to the built-in model BE-GFS, customized model BEs, including the yearly-averaged BE-1yr and monthly-averaged BE for January (BE-Jan) and July (BE-Jul), were independently tested in the sensitivity experiments BE-GFS, BE-1yr, BE-Jan, and BE-Jul. The simulation periods included January and July 2009 for most of the sensitivity experiments, with the exceptions that BE-Jan was only used for January 2009 and BE-Jul only for July 2009.

Table 3.4.2. Sensitivity tests for evaluating model background error

Sensitivity test	Data assimilated	Background Error (BE)	Simulation period
BE-GFS	In situ surface observations	Built-in global BE	January & July 2009
BE-1yr	In situ surface observations	Customized BE from 1-year (2009) simulation	January & July 2009
BE-Jul	In situ surface observations	Customized BE from 1-month (July 2009) simulation	July 2009
BE-Jan	In situ surface observations	Customized BE from 1-month (January 2009) simulation	January 2009
CTRL	**No data assimilated**		January & July 2009

The impacts of the model BEs on assimilation performance were determined through verification against the collected radiosondes and surface observations at hours when assimilation was not performed, as well as against QuikSCAT winds. Verified quantities included sea level pressure (SLP), 2-m air temperature (T), 10-m wind vector (VEC), and upper-level temperature and wind vector (Table 3.4.3). When verifying against surface observations, the stations were divided into two groups, coastal and inland stations, in order to distinguish the performance of the assimilation between complex terrain and flat, coastal areas. Surface stations located within 30 km of the shoreline were designated as coastal stations, with those farther from shore designated as inland stations. Using this

criterion, there were a total of 56 coastal stations and 66 inland stations available within the model domain for this period.

Comparisons of RMSEs among the control and sensitivity simulations as verified against all three types of observations for both the January and July cases (Table 3.4.3) demonstrate that the built-in model BE (BE-GFS) significantly degrades the model performance in the study area, generating much greater errors than the control simulation in which no data were assimilated. This comparison suggests that in order to achieve positive impacts from data assimilation via WRFDA, usage of the built-in model BE should be avoided. On the other hand, the customized model BEs, both yearly- and monthly-averaged, generally serve to enhance the model performance, reducing the errors for most of the examined variables. A close look at the comparison further demonstrates that the improvements in SLP and the surface wind field by the customized BEs are seen continually throughout both the cold and warm months. For temperature, however, a slight negative effect is present in the January case, even with the use of customized BEs. This indicates that accurately modeling the strong surface temperature inversion characteristic of Arctic winter remains a challenge for the WRF model. Accordingly, the estimated model BEs might not fully represent the actual model performance in such conditions, resulting in a degradation of the data assimilation performance. Across the experiments, the performance of the monthly- and yearly-averaged BEs is similar, indicating that including seasonal variability in the customized BEs is relatively insignificant in this study.

Table 3.4.3. Verification of BE tests against different observations for 2-m temperature (T) (°C), sea level pressure (SLP) (hPa), and 10-m wind vector (VEC) (m s^{-1}) (RMSEs (improved in bold) are averaged over all stations; when verified against surface in situ stations, coastal and inland stations are verified separately.)

Sensitivity tests		Surface observation						Radiosonde		QuikSCAT
		T (°C)		SLP (hPa)		VEC (m s^{-1})		T (°C)	VEC (m s^{-1})	VEC (m s^{-1})
		Coast	Inland	Coast	Inland	Coast	Inland			
Jul	CTRL	2.69	**3.77**	1.15	1.69	3.18	3.28	**1.08**	2.92	3.42
	BE-GFS	2.75	4.34	1.27	1.96	3.34	3.56	1.97	4.26	3.74
	BE-1yr	**2.44**	3.79	**1.05**	**1.68**	**3.01**	**3.13**	1.08	**2.89**	**3.32**
	BE-Jul	**2.44**	3.77	**1.02**	**1.65**	**3.00**	**3.10**	1.09	2.94	**3.32**
Jan	CTRL	**5.64**	6.15	1.54	**4.54**	3.80	3.93	**2.03**	4.32	No QuikSCAT during ice-covered season
	BE-GFS	6.92	7.54	1.69	5.00	4.22	4.10	4.18	6.34	
	BE-1yr	5.94	**6.03**	**1.33**	4.54	**3.66**	**3.79**	2.09	**4.30**	
	BE-Jan	6.10	**6.04**	**1.35**	4.60	**3.67**	**3.78**	2.13	4.33	

Assimilating in situ surface observations generates different impacts on coastal and inland areas. In the BE-GFS experiment, surface temperature was degraded by 2% (23%)

in the coastal areas, and by 15% (23%) inland when compared to the CTRL simulation in July (January), while the RMSEs for surface wind vector were 5% (11%) and 9% (4%) larger in July (January) for the coastal and inland stations, respectively (Table 3.4.3). This indicates that the built-in model BE generated by the coarse-resolution simulation (~80 km grid spacing) is more problematic during winter and over complex terrain. Greater overall improvements can be achieved in the coastal region relative to inland areas through the use of customized model BEs. During summer, surface temperature and SLP in the coastal areas were improved by 9% and 9–11%, respectively, while the impacts were very small inland. For the surface wind field, improvements were similar for the coastal and inland areas, with 5% (4%) improvement at the coastal stations and 5% (4%) inland during July (January). Similar to the difficulty that the model has in simulating inversions, the fact that the inland area is characterized by complex topography presents a challenge for WRF in accurately capturing many terrain-induced finer-scale details. Because model BE does not represent the actual model error relative to observations, but rather the average difference between one forecast time and another, BE can be underestimated in situations where the model performs inherently poorly. Thus, the performance of the assimilation can be hampered due to a less accurate estimation of model BE.

Since the coastal area receives a greater benefit from assimilation, the averaged 48-hour simulation cycle of the temperature and wind vector RMSEs, as averaged over the 56 coastal stations, is compared for the month of July 2009 across all the sensitivity tests (Figure 3.4.2). Over the averaged simulation cycle, both monthly- and yearly-averaged customized model BEs performed very similarly in improving the model results throughout the entire diurnal cycle. On the other hand, the built-in model BE (BE-GFS) degraded the model results, particularly for near-surface temperature during the day.

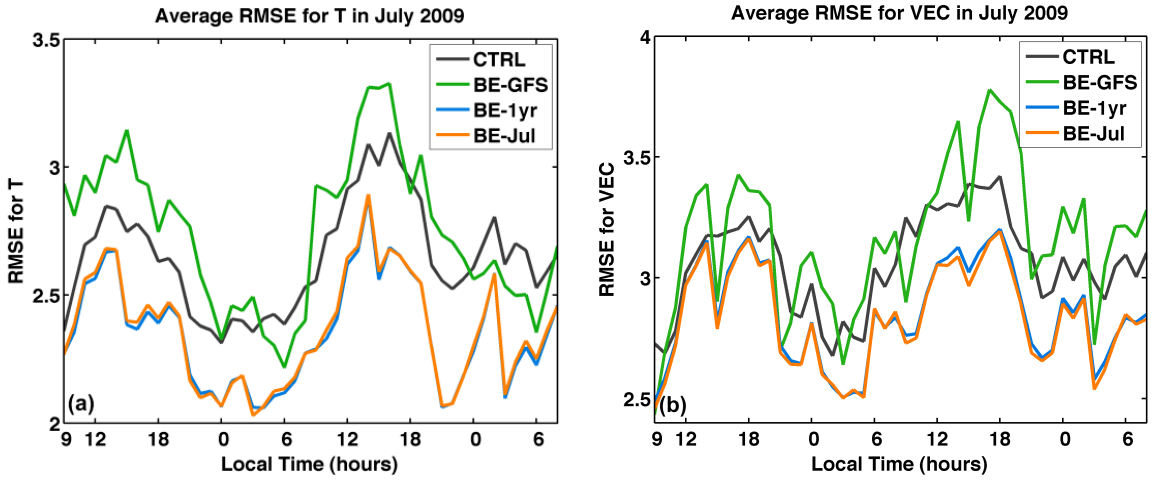

Figure 3.4.2. RMSE of (a) 2-m temperature (°C) and (b) 10-m wind vector (m s^{-1}) as verified against 56 coastal stations over the 48-hour cold-start model cycle for BE experiments in July 2009

From the comparison of RMSEs calculated against radiosondes (Table 3.4.3), even though only in situ surface observations were assimilated by the WRFDA system, it's seen that the upper atmosphere can also be impacted nontrivially when the built-in model BE is used; the impacts from customized model BEs were very small, however. The built-in BE increased the RMSEs by more than 40–100% relative to the control simulation. Comparisons of the RMSE profiles among all the simulations for July 2009 show that the errors introduced by use of the built-in model BE gradually decrease with height, and are equivalent to values of the other simulations at or above 300 hPa (Figure 3.4.3), indicating that the negative effect is three-dimensional even though only two-dimensional data were assimilated.

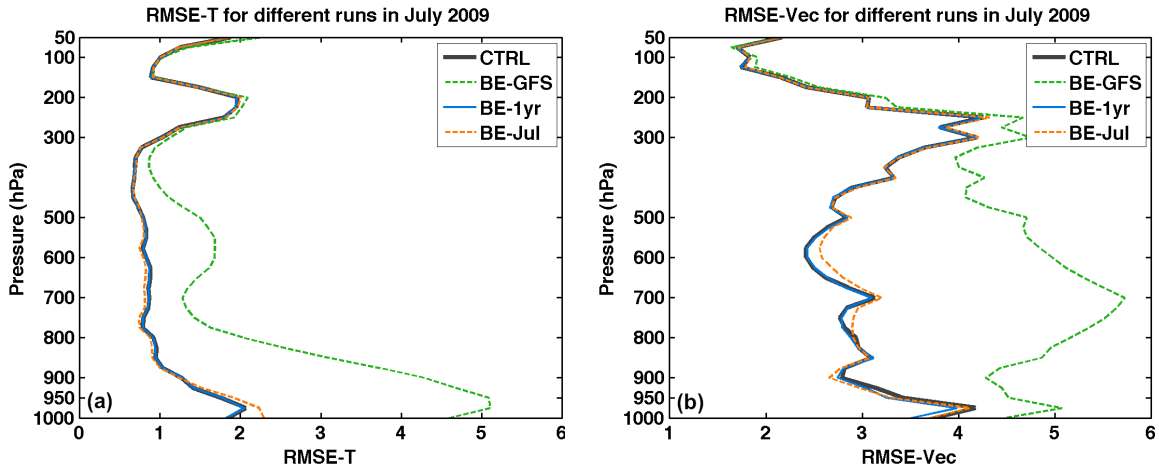

Figure 3.4.3. Monthly-averaged profiles of RMSE, averaged over all radiosonde stations for (a) temperature (°C) and (b) wind vector (m s^{-1}) for BE experiments in July 2009

As again shown in Table 3.4.3, improvements in wind speed and direction, as verified against QuikSCAT winds, can also be achieved by the use of customized model BEs even though no QuikSCAT data were assimilated. The built-in model BE, however, degraded the performance of WRFDA, increasing errors in both wind speed and direction. The improvements seen with the customized BEs are most likely due to improved surface winds along the coastal areas where coastal station observations were assimilated.

3.4.3 Performance Analysis of WRFDA Assimilation of Multiple Datasets

A total of six data assimilation tests were conducted, as summarized in Table 3.4.4, to evaluate whether assimilation of various observational data types via WRFDA would enhance the model performance. The collected surface observations include hourly 2-m temperature and humidity, 10-m wind, and pressure. Radiosonde profiles include 12-hourly pressure, geopotential height, temperature, humidity, and wind on vertical levels extending from the surface to the stratosphere. QuikSCAT sea-surface winds are measured over ice-free ocean areas at a horizontal grid spacing of 12.5 km, and are

available several times daily in the study domain. MODIS retrievals provide twice-daily temperature and moisture profiles on 20 vertical levels (1000, 950, 920, 850, 780, 700, 620, 500, 400, 300, 250, 200, 150, 100, 70, 50, 30, 20, 10, 5 hPa) with 5-km grid spacing. COSMIC profiles used here include temperature and moisture on 26 vertical levels (1000, 975, 950, 925, 900, 850, 800, 750, 700, 650, 600, 550, 500, 450, 400, 350, 300, 250, 200, 150, 100, 70, 50, 30, 20, 10 hPa) and report 2–5 profiles in the study domain each day. Polar winds are reported at either a grid spacing of 2 km (MODIS) or 5 km (AVHRR), with each available grid point containing a single wind vector observation at varying levels, and are available within the study domain nearly every hour of the day. All sensitivity experiments herein used the customized model BE from sensitivity experiment BE-1yr (Table 3.4.2). When verifying the sensitivity test results against observations, only unassimilated data were used in order to maintain independence between the simulations and the verification dataset. Since radiosonde profiles are typically only available at 0000 UTC and 1200 UTC, which coincide with data assimilation times in these tests, model output from the previous hour (i.e., 2300 UTC and 1100 UTC) was instead used when verifying against radiosonde observations. The relative success achieved through assimilating each type of data is analyzed by comparing the RMSEs among the control and sensitivity simulations (Tables 3.4.5, 3.4.8, and 3.4.9) and are detailed below.

Table 3.4.4. Sensitivity tests used to evaluate assimilation of different observational sources

Sensitivity test	Data assimilated
CTRL	**No data assimilated**
SFC	In situ surface observations
SONDE	Radiosonde profiles
QSCAT	QuikSCAT ocean-surface winds
COSMIC	COSMIC profiles
PWIND	MODIS and AVHRR polar winds

Assimilation of In Situ Surface Observations

Sensitivity experiment SFC (Table 3.4.4), in which the model BE from BE-1yr was used for the assimilation of surface station observations, is equivalent to the sensitivity experiment BE-1yr in Table 3.4.2 for the July case. As discussed in Section 3.4.2, assimilation of in situ surface observations generates improvements in most verified variables, particularly surface wind. Greater improvements are seen in the coastal region, where surface temperature was improved by 9% and wind by 5%, while the impact inland is relatively small. When the model results are verified against QuikSCAT winds, improvements are also seen. Therefore, the assimilation of in situ surface observations does help to improve the model performance in simulating most surface variables, particularly surface winds.

Assimilation of Radiosonde Profiles

In the study area, a total of three sounding stations (Barrow, Inuvik, and Kotzebue) made observations during the experiment period of July 2009; two soundings per day from each station were assimilated in the assimilation experiment SONDE (Table 3.4.4). The comparison of RMSEs between the CTRL and SONDE simulations (Table 3.4.5) indicates that the assimilation of radiosonde measurements not only improves the model's simulation of upper-air variables (where model output one hour prior to the assimilation times was used for verification in order to maintain independence from the observations), but also affects the simulation of surface variables as verified against surface in situ observations and QuikSCAT winds. Due to the very limited number of soundings available in the study region, the RMSEs of upper-air temperatures and winds were only slightly reduced in this experiment, by about 1–2%. At the surface, temperature and SLP were improved by about 2% and 3%, respectively, in the coastal region. The surface wind over the ocean was also slightly improved, as verified against QuikSCAT data. Overall, this experiment indicates that a consistently positive impact can be achieved through the assimilation of radiosonde measurements.

Table 3.4.5. Same as Table 3.4.3, but for sensitivity tests assimilating different observational sources

Sensitivity test	Surface observation						Radiosonde		QuikSCAT
	T (°C)		SLP (hPa)		VEC (m s^{-1})		T (°C)	VEC (m s^{-1})	VEC (m s^{-1})
	Coast	Inland	Coast	Inland	Coast	Inland			
CTRL	2.69	**3.77**	1.15	1.69	3.18	3.28	1.08	2.93	3.42
SFC	**2.44**	3.79	**1.05**	**1.68**	**3.01**	**3.13**	1.08	2.93	**3.32**
SONDE	**2.64**	3.77	**1.11**	**1.68**	**3.16**	**3.27**	**1.06**	**2.91**	**3.39**
QSCAT	**2.68**	3.78	1.15	**1.66**	3.18	**3.25**	**1.07**	2.93	**3.06**

Assimilation of QuikSCAT Surface Winds

Assimilation of QuikSCAT ocean-surface winds was evaluated with the assimilation experiment QSCAT (Table 3.4.4). QuikSCAT winds provide measurements of surface wind vectors over open water in the absence of sea ice (Figure 3.4.4a). During the experiment period of July 2009, a meteorological buoy was deployed by this project off the Beaufort Sea coast near Barrow, where it collected a month-long offshore meteorological dataset of near-surface winds, among other variables (http://knik.iarc.uaf.edu/buoy09). In order to better understand the accuracy of QuikSCAT winds in the study region, the wind speeds measured by the buoy are compared with QuikSCAT retrievals (Figure 3.4.4b). The correlation between the buoy measurements and QuikSCAT surface winds for the period of 5 August–15 September 2009 is 0.83, with an RMSE of just 0.82 m s^{-1}, indicating that the quality of QuikSCAT winds in the study area is satisfactory.

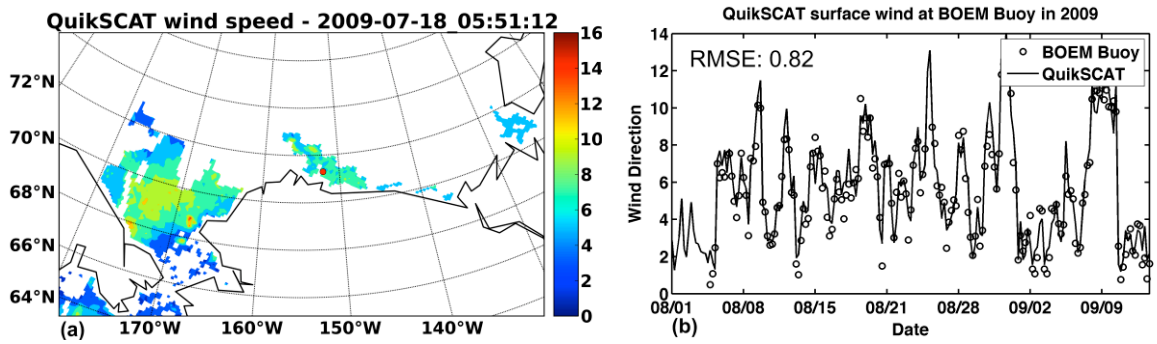

Figure 3.4.4. (a) Snapshot of QuikSCAT surface wind speed (m s^{-1}) (color) in the model domain at 0551 UTC 18 July 2009; (b) QuikSCAT surface wind speed (m s^{-1}) versus BOEM buoy (71.29°N, 152.14°W) observed wind speed (m s^{-1}) in August–September 2009. The red dot in (a) represents the BOEM buoy location.

During the open water season, e.g. July 2009, when there are QuikSCAT winds available in the study area, assimilation of QuikSCAT surface winds demonstrates a positive influence on the simulation of the offshore surface wind field. As before, model output from experiment QSCAT was verified against both in situ measurements and QuikSCAT winds at non-assimilation hours and the RMSE calculated (Table 3.4.5). This comparison demonstrates that assimilating QuikSCAT winds can significantly reduce the RMSE of surface wind vectors over open water as verified against unassimilated QuikSCAT winds. Wind vectors were improved by 11% relative to the control run.

Assimilation of Satellite-Retrieved Profiles

MODIS profiles are available from 2–3 satellite passes per day over the study area, with a horizontal grid spacing of about 5 km and 20 vertical levels extending from 1000 to 5 hPa. After the data is thinned to a spacing of approximately 120 km in order to prevent oversaturation, which can cause diminished results (e.g., Liu and Rabier 2002), there remain approximately 1900 MODIS profiles per day across the model domain available to be assimilated by WRFDA.

MODIS profile data are accompanied by quality control flags that indicate the conditions under which they were collected. For example, the cloud mask flag (CM) indicates the presence of clouds, and the snow/ice background flag (SI) indicates whether the surface was covered by snow or sea ice (Table 3.4.6). To characterize the quality of data marked by these flags in the study area, the MODIS profiles for 2009 were divided into groups according to their CM and SI flags and verified against sounding observations at the three available radiosonde stations. A comparison of temperature RMSE profiles (Figure 3.4.5) shows that the profiles retrieved under a snow or ice background condition (SI=0) contain errors that are 30–50% larger than those that were not (SI=1). A similar contrast is present between profiles retrieved under cloudy conditions (CM=0,1) and clear sky (CM=2,3). In addition, the data errors are highly variable with height. The RMSE at 1000 hPa is up to two times larger than at the upper levels (850 to 300 hPa).

Table 3.4.6. List of MODIS retrieval flags

Flag	Interpretation Key
Cloud Mask (CM)	0 = Confidently Cloudy 1 = Probably Cloudy 2 = Probably Clear 3 = Confidently Clear
Snow/Ice Background (SI)	0 = Yes 1 = No

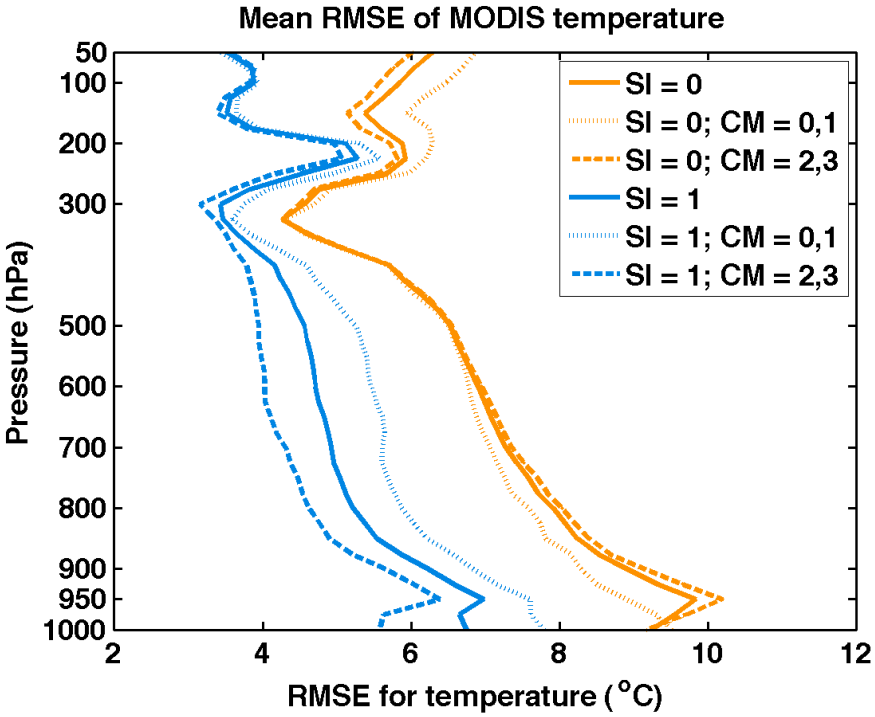

Figure 3.4.5. Mean RMSE profiles of MODIS-retrieved temperature (°C) with different QC flags in 2009, as verified against all radiosonde stations in the study area

Considering the variations in MODIS profile quality, a series of sensitivity experiments was conducted in which MODIS profiles were screened by the CM and SI flags examined in Figure 3.4.5 (Table 3.4.7). The purpose of this was to determine the optimal configuration for assimilating MODIS profiles via WRFDA in order to generate the best-quality final CBHAR reanalysis. In these experiments, MODIS data were either assimilated at all levels (MODIS) or only between 850 and 300 hPa (MODIS-MID). The sensitivity simulations were evaluated in the same way as before, with the model results (SLP, T, and VEC) verified against unassimilated radiosondes, surface observations, and QuikSCAT winds. Comparisons of the results from the sensitivity experiments MODIS, MODIS-MID, and CTRL (Table 3.4.8) demonstrate that assimilation of unfiltered

MODIS retrievals (experiment 'MODIS') made the results worse relative to the CTRL simulation for almost all examined variables. The experiment 'MODIS' produced surface wind (VEC) RMSE more than 2% larger than CTRL over land, and more than 7% larger over the ocean. Perhaps surprisingly, the experiment that selectively assimilated vertical levels of the retrievals (MODIS-MID) did little to improve the poor performance of the 'MODIS' experiment. The results from MODIS-MID were also worse than CTRL, with RMSE about 3% larger for the surface wind and 1% for surface temperature in coastal areas.

Table 3.4.7. MODIS assimilation sensitivity tests

Test	Snow/Ice background (SI)	Cloud mask (CM)	Vertical levels
MODIS	All background (0, 1)	All sky (0, 1, 2, 3)	All levels
MODIS-MID	All background (0, 1)	All sky (0, 1, 2, 3)	850–300 hPa
MODIS-QA	Snow/ice-free background (1)	Clear sky (2, 3)	All levels

Table 3.4.8. Same as Table 3.4.3, but for sensitivity tests assimilating MODIS profiles

Sensitivity tests	Surface observation						Radiosonde		QuikSCAT
	T (°C)		SLP (hPa)		VEC (m s^{-1})		T (°C)	VEC (m s^{-1})	VEC (m s^{-1})
	Coast	Inland	Coast	Inland	Coast	Inland			
CTRL	**2.69**	**3.77**	1.15	1.69	**3.18**	**3.28**	**1.08**	**2.93**	**3.42**
MODIS	2.75	3.77	**1.11**	**1.66**	3.30	3.36	1.16	3.19	3.69
MODIS-MID	2.73	3.79	**1.12**	**1.66**	3.27	3.38	1.14	3.09	3.60

In addition to the level-selective experiment MODIS-MID, the MODIS profiles may also be screened through the use of the CM and SI flags. Experiment MODIS-QA was conducted to examine the model performance when assimilating only MODIS profiles that have a snow/ice-free background (SI=1) and were measured under either probably clear (CM=2) or confidently clear (CM=3) sky conditions. In order to understand the vertical effects of assimilating MODIS retrievals, model-simulated temperature profiles from the experiments CTRL, 'MODIS', and MODIS-QA were compared at all levels and averaged over the entire simulation period of July 2009 at Barrow (Figure 3.4.6). Comparisons of the monthly-averaged bias profiles among all the sensitivity tests show that the unfiltered experiment 'MODIS' overcorrected the warm bias generated by the CTRL experiment for the middle and lower atmosphere (below ~500 hPa), and produced a cold bias of up to 0.5°C. When the MODIS profiles were selectively assimilated on the basis of quality assurance flags (experiment MODIS-QA), an improvement is seen in temperature for almost all levels, reducing both the cold bias in the middle and lower atmosphere (below ~300 hPa) and the warm bias in the upper atmosphere (above ~300 hPa). Selectively assimilating MODIS profiles via the WRFDA system through the use of quality assurance flags, such as those indicating snow/ice-free background and/or clear

sky conditions, is therefore essential for avoiding degradation of assimilation performance.

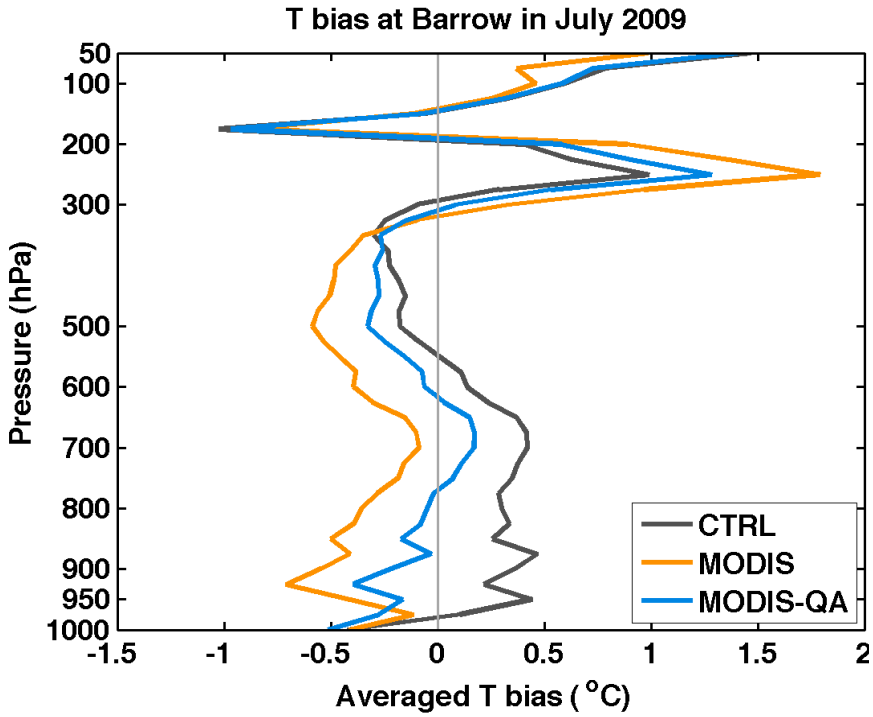

Figure 3.4.6. Monthly-averaged profiles of temperature bias (°C) at Barrow in July 2009 for experiments CTRL, MODIS, and MODIS-QA, as verified against radiosonde data at various vertical levels

COSMIC-retrieved profiles represent an opportunity for further augmenting the upper-air data assimilation in this study, with about 20 profiles per day available in the study domain. The profiles have a total of 6 more vertical levels and 7 more levels below 300 hPa than those from MODIS. When evaluating the effect of assimilating COSMIC profiles, the impacts of filtering with quality control flags were not considered due to the fact that COSMIC products are not accompanied by QC-flag information, suggesting that third-party sources are required in order to conduct a filtering procedure, which could result in inconsistencies. The experimental results (COSMIC) were verified separately against surface station (coastal and inland stations separately), radiosonde, and QuikSCAT observations for temperature, SLP, and wind speed and direction (Table 3.4.9). Generally, the assimilation of COSMIC profiles was able to produce a very slight positive effect for both surface and upper-air variables, which initially encouraged their use as one of the observation types to be assimilated into CBHAR. However, given the very short-term availability of COSMIC data (2006–09), it was ultimately decided to remove them from consideration for this application. In light of the positive, though slight, impacts of COSMIC assimilation, should the period of the reanalysis be extended further, the possibility of their inclusion should be re-examined.

Table 3.4.9. Same as Table 3.4.3, but for sensitivity tests assimilating COSMIC profiles

Sensitivity test	Surface observation						Radiosonde		QuikSCAT
	T (°C)		SLP (hPa)		VEC (m s^{-1})		T (°C)	VEC (m s^{-1})	VEC (m s^{-1})
	Coast	Inland	Coast	Inland	Coast	Inland			
CTRL	**2.69**	3.77	1.15	1.69	3.18	3.27	1.08	2.93	3.42
COSMIC	2.71	**3.76**	**1.10**	**1.67**	3.18	**3.26**	**1.07**	**2.92**	3.42

Assimilation of Polar Winds

Polar winds are derived from satellite measurements of infrared and water vapor channels, whereby the movements of clouds are tracked from one satellite pass to the next and the difference in location used to determine the wind vector at the altitude of the tracked clouds. As such, polar winds are only available at cloudy locations, and on a single vertical level for each reported grid point. This limited vertical extent, and location generally far from the surface, suggests that the assimilation of polar winds may have a relatively small impact on the near-surface variables that are the focus of this reanalysis effort. Nevertheless, given their long-term and frequent availability (since 1982 for AVHRR and 2002 for MODIS, and nearly every hour somewhere in the study domain), a sensitivity experiment (PWIND) was conducted in order to determine whether polar winds should be included in the final reanalysis configuration. The experimental results (PWIND) were verified against surface station observations. Perhaps unsurprisingly, the assimilation of these single-level, upper-air winds had only an extremely slight, though positive, impact on near-surface variables (not shown). Nevertheless, despite this insignificant impact on the surface, it was decided to include them in the final modeling configuration both due to the length of their observational record, and the fact that winds are a primary focus of this reanalysis effort.

Based on the above sensitivity analysis, it was determined that the assimilation of surface observations, radiosondes, QuikSCAT ocean-surface winds, MODIS and AVHRR polar winds, and selected MODIS profiles each adds value to the modeling results. The observational set assimilated into the final 31-year CBHAR reanalysis thus included *in situ surface observations, radiosondes, QuikSCAT ocean-surface winds, polar winds, and selected MODIS-retrieved profiles*.

3.4.4 Optimization of Analysis Nudging Configuration

When performing long-term regional simulations, the use of a nudging technique is essential for guiding model solutions toward an existing reanalysis and to prevent lateral-boundary-induced drift from growing too large. WRF contains two three-dimensional analysis nudging options:

1) Grid point nudging: each grid point is directly nudged toward the larger-scale reanalysis dataset; and

2) Spectral nudging: model fields are decomposed in Fourier series into fields with different wavenumbers, and only coarser scales below a given wavenumber are then nudged; this technique better allows smaller-scale model information to be retained.

Within each nudging option, there exist three different degrees of nudging in the vertical dimension: one can nudge all levels, including the boundary layer; one can limit nudging to those levels above a specified model level; or one can limit nudging to the region above the model-defined boundary layer. In addition, one can selectively nudge certain variables (among temperature, water vapor, geopotential height (spectral nudging only), and winds), leaving the others to be freely determined by the model. Thus, tests are needed to determine both which level of nudging performs best and whether to include winds, the focus of this reanalysis effort, in the nudge. For spectral nudging, another consideration is to determine the optimal wavenumber (which controls the spatial scale of waves to be nudged) for the size of the domain being used. To answer these questions, a series of nudging sensitivity tests was conducted for two simulation periods, one in the winter of 2009 (February) and the other in the summer of the same year (August), with the modeling results verified against surface observations. For comparison, a control simulation (ctrl) without any analysis nudging was also conducted. The RMSE of modeled wind vectors from the various nudging simulation tests (Figure 3.4.7) demonstrates that:

1) Analysis nudging generally improves the simulations.
2) Spectral nudging with wavenumber 3 (experiment nudg-spec-all-3) outperforms the other nudging algorithms.
3) Nudging at all vertical levels and all variables (experiments with “all” in their name) is superior to selective nudging.

Thus, spectral nudging with a wavenumber of 3, on all vertical levels and for all variables, was selected for use in the final model configuration for the production of the 31-year CBHAR simulation.

Both data assimilation and analysis nudging have so far been shown to improve the performance of the model simulations. Does the combination of these two techniques lead to further improvements? To answer this, simulations using a combination of both data assimilation of surface observations and three-wavenumber spectral nudging for the same time periods as above were conducted and compared with the modeling results in which data assimilation or reanalysis nudging were individually utilized. The comparisons (Figure 3.4.8) clearly demonstrate that combining data assimilation and spectral nudging produces further improvements over those seen with each technique used separately.

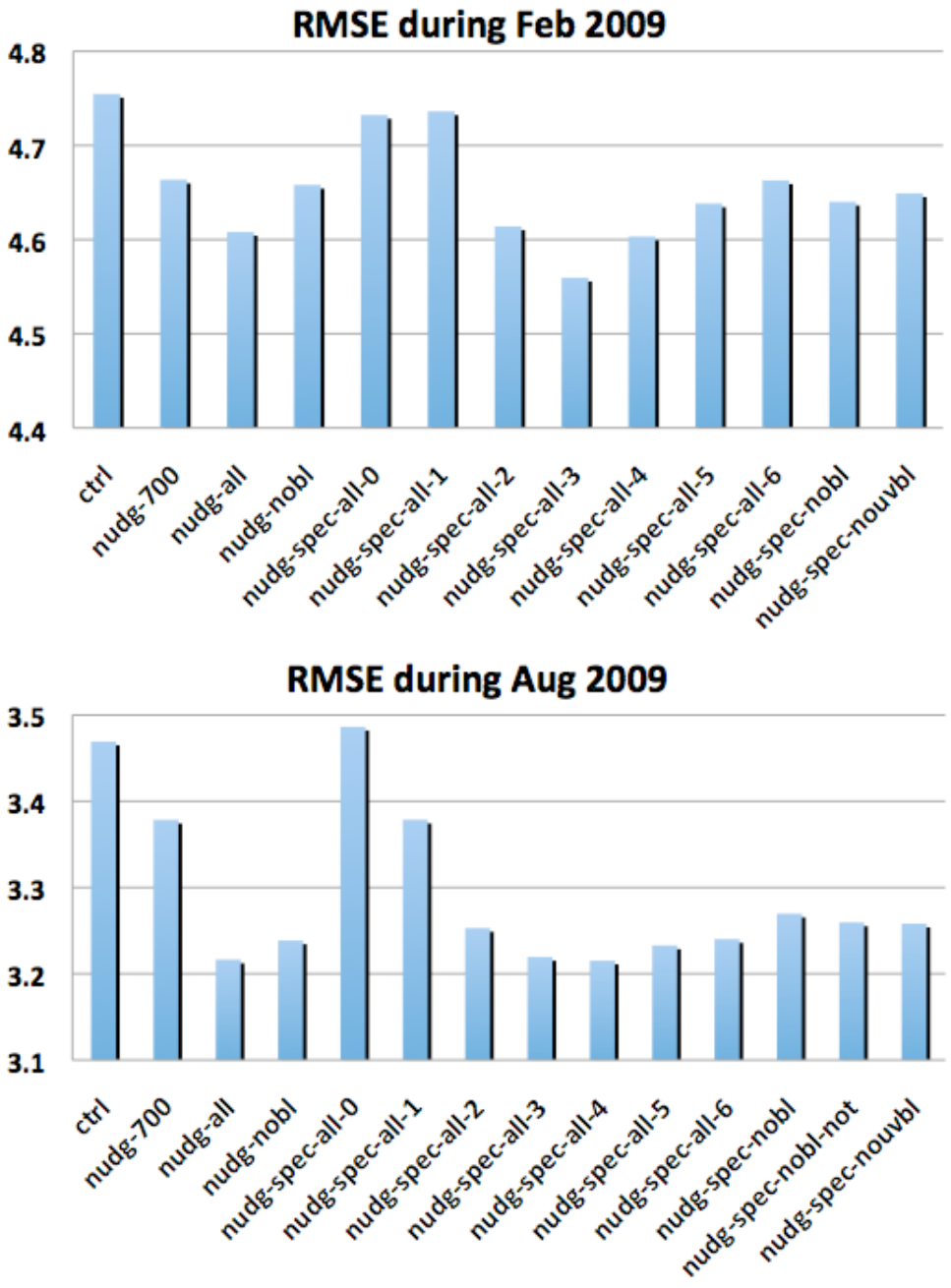

Figure 3.4.7. RMSE of modeled wind vectors (m s^{-1}) from control (ctrl) and various nudging simulations, as verified against surface observations during February (top) and August (bottom) 2009

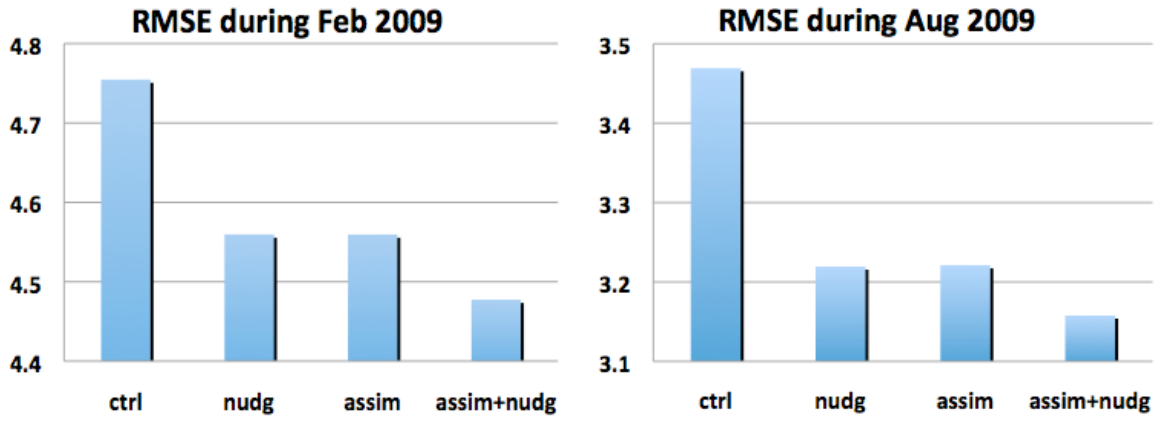

Figure 3.4.8. RMSE of modeled wind vectors (m s^{-1}) from control (ctrl), nudging (nudg), assimilation (assim), and combined assimilation and nudging (assim+nudg) simulations, as verified against surface observations during February (left) and August (right) 2009

3.5 Model Data Selections

Regional atmospheric models that cover a limited area, such as WRF, require specification of the lateral boundary conditions that surround the modeled domain. In real-data applications, these are provided by gridded data from larger-scale models. Selection of the larger-scale forcing data for use with WRF to generate the CBHAR reanalysis is summarized in Section 3.5.1. In addition, WRF also requires lower boundary conditions, such as land-use information. Selection of the lower boundary data to be used by WRF in the production of CBHAR is discussed in Section 3.5.2.

3.5.1 Large-Scale Forcing Data

The initial and boundary conditions needed by WRF simulations are generally derived from larger-scale model simulations or reanalyses. While many such global or larger-scale regional models exist, for a long-term historical retrospective such as this project entails, a large-scale gridded historical dataset, such as a reanalysis, that encompasses the same time period is required, of which only a few exist. Some, such as the NCEP/NCAR Reanalysis can be eliminated from consideration due to their coarse horizontal resolution that limits their accuracy at local and regional scales, making them unsuitable for scaling down to the 10-km grid spacing employed for CBHAR without using additional outer grids, which would be computationally unfeasible. Others, such as ERA-40 and JRA-25, do not cover CBHAR's entire 31-year time period, which would introduce potentially problematic discontinuities should they be utilized. Still others, such as the NASA Modern-Era Retrospective Analysis for Research and Applications (MERRA) (Rienecker et al. 2011) and the NCEP Climate Forecast System Reanalysis (CFSR) (Saha et al. 2010) became available to researchers only recently, and too late to be considered for use in this project. After removal of the unworkable options, only two remained for consideration: the NARR and ERA-I reanalyses.

NARR, as the name implies, is a regional reanalysis product that covers the entire North American continent. It is produced with NCEP's Eta model, downscaled from the NCEP/Department of Energy (DOE) Reanalysis 2, and is available from 1979 through the present at a horizontal grid spacing of 32 km and a 3-hourly frequency. ERA-I, on the other hand, is a global reanalysis generated with the ECMWF Integrated Forecast System (IFS) and is also available from 1979 through the present, albeit at a lower horizontal (0.7°, ~77 km by 20 km in the study area) and temporal (6-hourly) resolution. Both modeling systems assimilate observational data into model simulations in order to produce their respective reanalyses. Given the higher resolution, both spatial and temporal, of NARR, one might expect higher accuracy in its representation of mesoscale meteorological features. However, this cannot be assumed and so a series of sensitivity tests were conducted in order to determine the most accurate source of large-scale forcing data that would ultimately be used for the production of CBHAR.

As noted in Section 3.2.1, the initial suite of physical parameterization sensitivity tests was carried out using NARR as the forcing data, both due to its relatively high resolution and the fact that ERA-I became available just recently, after this study had already begun. With the introduction of ERA-I, several sensitivity tests were conducted using the same configuration as the sensitivity tests with NARR for September 2004 in order to investigate the effectiveness of using the new reanalysis (see Tables 3.2.1 and 3.2.2 in Section 3.2.1 for additional details about the configuration of the model physical parameterization tests). The wind vector RMSE for both the NARR and ERA-I sensitivity tests is compared in Figure 3.5.1, as verified against surface station observations.

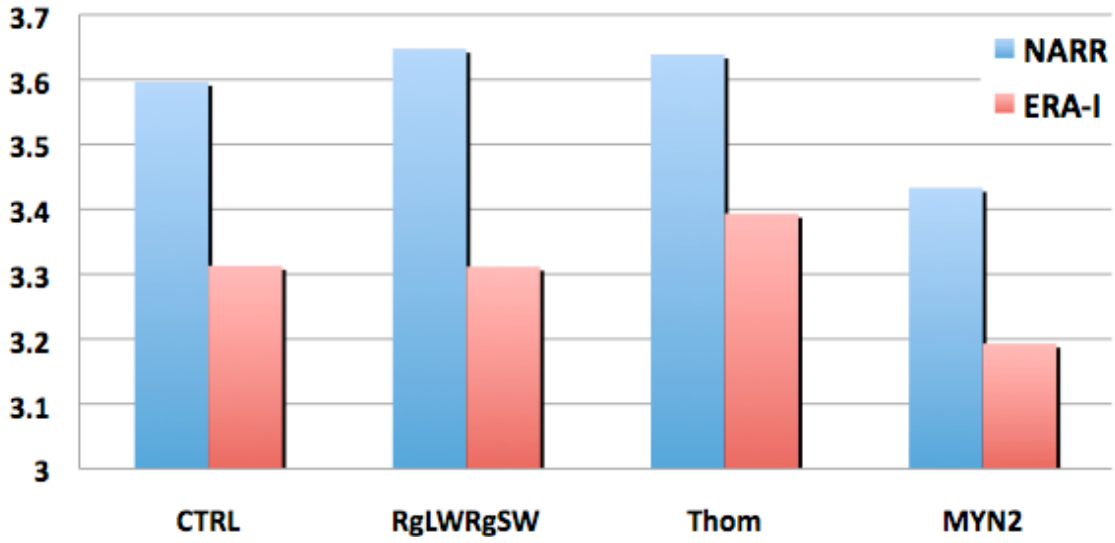

Figure 3.5.1. Wind vector RMSE (m s^{-1}) for various WRF physical parameterization sensitivity tests in September 2004 when using NARR vs. ERA-I as large-scale forcing data

It is clear that no matter the physical parameterization options used, ERA-I produces consistently better results, not only for surface winds but also for every other model variable investigated (not shown). From these results, it is obvious that ERA-I is the superior choice for the selection of forcing data in order to generate the most accurate possible results in the CBHAR reanalysis.

3.5.2 WRF Land-Use Dataset

The WRF package includes two different datasets for providing land-use information to the model: the 24-category USGS dataset and the 20-category MODIS land-cover classification of the International Geosphere-Biosphere Programme, as modified for use with the Noah land-surface model. Not only can the two differ in how they categorize a particular plot of land, but also the land-use parameters themselves (e.g., albedo, roughness, moisture availability) can vary between the two for the same category. Particularly for a region like Alaska, which is complex geographically and topographically, and for a study that is focused primarily on surface parameters, it is important to make a proper selection and ensure that the most accurate simulation is produced. To this end, sensitivity tests were conducted to investigate which land-use dataset available in WRF would be used for the final CBHAR configuration.

For these tests, the simulation period of August 2009 was chosen in order to avoid the presence of snow cover, which would have potentially masked the effects of the differences in the underlying land-use classifications. One-month-long tests for August 2009 were conducted in concert with tests of WRF's cumulus parameterizations, as detailed in Section 3.2.3. The model configuration with the Grell-3D cumulus scheme (Table 3.2.6) was used in the tests USGS and MODIS, in which the USGS and MODIS land-use data were used, respectively. RMSE values for the model results as verified against surface station observations are shown below in Table 3.5.1.

Table 3.5.1. RMSE of land-use data sensitivity tests as verified against surface observations for long- and shortwave irradiance (W m^{-2}), 2-m temperature (°C), and 10-m wind vector (m s^{-1})

Sensitivity test	Longwave (W m^{-2})	Shortwave (W m^{-2})	Temperature (°C)	Wind vector (m s^{-1})
USGS	31.9	138.9	3.15	3.41
MODIS	30.8	139.3	3.12	3.37

While the differences in RMSE between simulations using USGS and MODIS datasets were, for the most part, relatively small, MODIS land use did outperform USGS for most of the variables examined, in particular surface temperature and winds, which are of prime importance for this study. Due to this slight, but consistent, advantage recorded with the use of the MODIS land-use dataset, it was selected to be part of the final CBHAR configuration.

3.6 Final Model Configuration and Production of CBHAR

Based on the results of all the sensitivity tests and further model improvements (Sections 3.2–3.5), including the coupling of a thermodynamic sea ice model with WRF (Section 3.3.1), a finalized model configuration was developed for use in the production of the 31-year CBHAR reanalysis that represents one of the focal points of this study. Each component of the configuration, from the datasets used to the model physical options selected to the procedure used to generate the final reanalysis, is summarized in this section. While extensive efforts have been made to optimize the model configuration and data usage for generating CBHAR, the use of a necessarily imperfect model, changes in the data assimilated over time, and the replacement of instruments which produce the observations assimilated may all inject errors into the reanalysis (Trenberth et al. 2001). Like every other reanalysis product, the CBHAR reanalysis cannot be free from these errors.

3.6.1 Initial and Boundary Conditions

Three-dimensional atmospheric initial and boundary conditions, along with most of the surface conditions and the gridded analysis to which WRF was spectrally nudged in generating CBHAR, were provided by the ERA-I reanalysis, the selection of which was discussed in Section 3.5.1. The fact that the study area is characterized by seasonal sea ice over the ocean and snow on land further necessitates that a careful preparation must be made for the specification of sea surface temperature (SST), sea ice concentration (SIC) and thickness (SIT), snow depth, and snow water equivalent (SWE). To maintain consistency with the atmospheric fields, SST was taken from ERA-I for use with the CBHAR reanalysis. To provide sea ice conditions, the NASA Bootstrap sea ice concentration derived from the Scanning Multichannel Microwave Radiometer (SMMR) on board the Nimbus-7 satellite and the Special Sensor Microwave/Imager (SSM/I) instrument on Defense Meteorological Satellite Program (DMSP) satellites was acquired from the National Snow and Ice Data Center (NSIDC). These data are available at a grid spacing of 25 km, and at a daily frequency since July 1987 and semi-daily prior to that. SIT was taken from the 6-hourly CFSR, a recently developed reanalysis product produced by NCEP at a 0.5° grid spacing. Due to the unavoidable discrepancies between the selected SIT and SIC datasets, the SIC distribution was treated as the true areal coverage, and for points where SIC was available and SIT was not, the SIT value was set to the closest available value in the CFSR dataset.

Snow depth and snow water equivalent are critical variables in the study area but are not included over sea ice in ERA-I, and at a relatively low resolution over land. Thus, the snow depth on land was acquired from the 32-km NARR reanalysis, which in turn was taken from the 47-km daily U.S. Air Force Weather Agency (AFWA) snow depth analysis. The AFWA analysis is not produced over sea ice, and so snow data (SWE) on ice were taken from the CFSR reanalysis. Since the AFWA analysis only provides snow depth, and CFSR only provides SWE, another data source of snow density was required in order to calculate SWE over land and snow depth over sea ice. The daily global CMC snow depth analysis provided by NSIDC, which includes SWE as calculated from snow

density climatological lookup tables, was used for this purpose. CMC data only exist since 1998, and so to fill in data for prior years the daily-average snow density values calculated for each day of the year over the 1998–2009 period were instead applied.

3.6.2 Final Model Configuration

As determined through the sensitivity tests detailed in Section 3.2, WRF was configured to use 10-km grid spacing and 49 vertical levels with the following physical parameterization options for the production of the final CBHAR reanalysis: Morrison microphysics, RRTMG longwave and shortwave radiation, Grell-3D cumulus, MYJ PBL and surface layer, and the Noah LSM. As summarized in Section 3.3, a new thermodynamic sea ice model was also coupled with WRF and selected Polar WRF options were adopted as well, namely the use of variable sea ice thickness data and a more realistic bottom sea ice temperature.

Section 3.4 summarized the results of testing the assimilation of various observational data and satellite retrievals with the WRFDA assimilation system in order to produce reanalysis output. As a result, WRFDA was configured to assimilate in situ surface station and radiosonde observations of temperature, dew point, wind vectors, and pressure (geopotential height for radiosondes), satellite-derived QuikSCAT ocean-surface winds, polar winds derived from MODIS and AVHRR measurements, and selected temperature and moisture profiles retrieved from MODIS data. A customized model background error file created specifically for the CBHAR domain was included in the CBHAR reanalysis configuration. Spectral nudging to the input ERA-I reanalysis was also utilized with a horizontal wavenumber of 3.

The selection of forcing data was discussed in Sections 3.5 and 3.6.1, with the result that ERA-I was used to provide initial and boundary conditions for the three-dimensional atmospheric fields, as well as most of the surface fields, in the final WRF simulations. For the sea ice and snow data needed by WRF, NASA Bootstrap SIC, CFSR SIT, NARR snow depth over land, and CFSR SWE over sea ice were used. A summary of the final optimized model configuration is given in Figure 3.6.1.

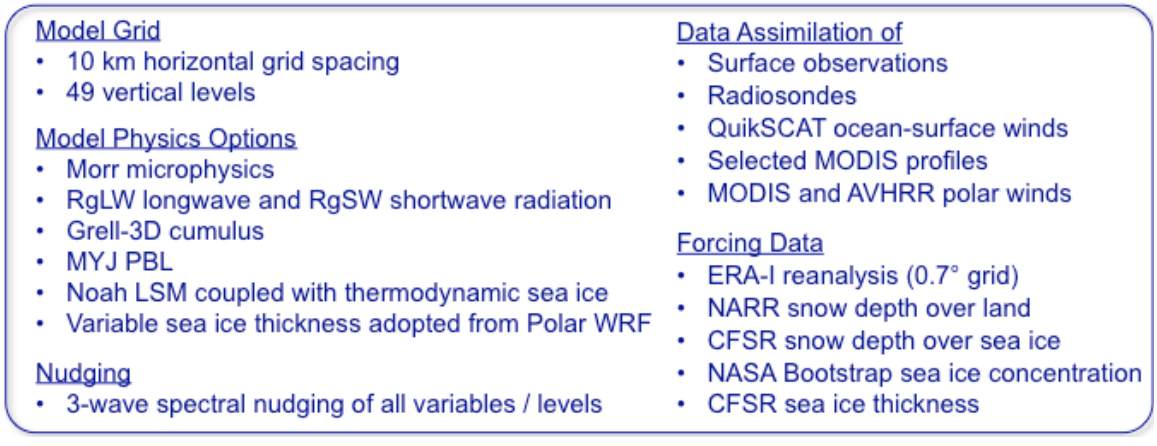

Figure 3.6.1. Optimized model configuration for CBHAR

3.6.3 Production of CBHAR

Once the forcing data was processed for input into the WRF simulation and the model configuration finalized, the final step was to produce the CBHAR reanalysis. This was accomplished at the Arctic Region Supercomputing Center, UAF through a parallelized, iterative process whereby a series of 54-hour simulations, initialized every two days throughout the 31-year study period, were produced, as summarized in Figure 3.6.2. Within each of these simulations, WRF was first initialized at 1200 UTC and observations within 30 minutes of the initialization time were assimilated. The model was integrated for an hour, stopped, and more observations assimilated at 1300 UTC. This process was repeated for the entire 54-hour cycle, with the first 6 output times (hours 1200–1700 UTC of the initial day) discarded, having only been used to spin up the model. The remaining 48 output hours (the output of each assimilation cycle) were kept in order to become part of the final product. In this way, a total of 5663 simulations were performed and the final two days of each simulation kept, resulting in the final 31-year CBHAR reanalysis.

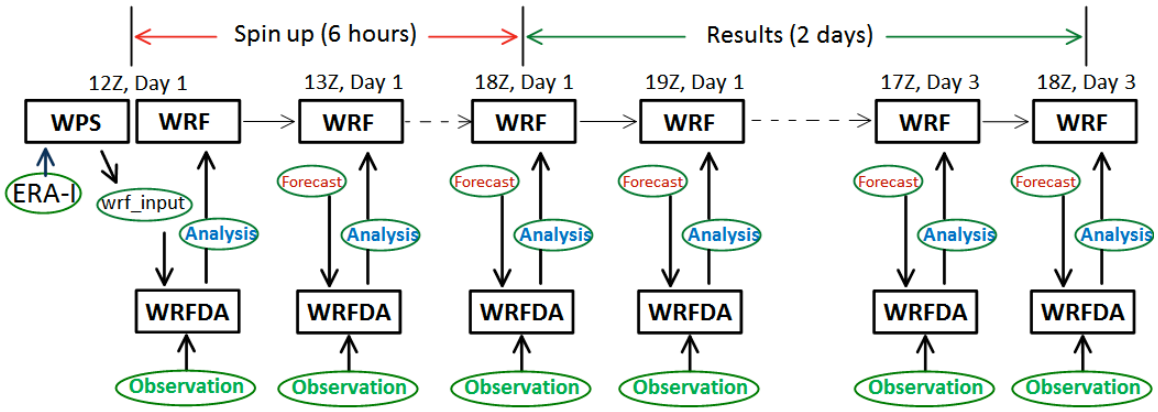

Figure 3.6.2. Process used to generate each of the 54-hour modeling cycles used to produce CBHAR. WPS is the WRF preprocessing system, which creates WRF input files. The first 6 hours of each cycle were used as model spin-up and discarded, with the remaining 48 hours contributing to the reanalysis. Due to overlap between adjacent cycles, the final 1800 UTC analysis was also discarded.

4 Performance Evaluation of the Chukchi-Beaufort High-Resolution Atmospheric Reanalysis (CBHAR)

4.1 Introduction

As discussed in the previous sections, great care has been taken to produce the highest-quality long-term regional reanalysis possible for the Chukchi–Beaufort Seas region. Significant efforts have been carried out in order to assemble a rigorously quality-controlled observational database and to assimilate these data into an optimized modeling configuration that has been thoroughly tested for varying conditions in the study area.

The resultant modeling system has been used to produce a high-resolution reanalysis that is designed to represent a highly accurate description of the atmospheric fields in the region over the 31-year period 1979–2009. Although this reanalysis is the product of an effort ultimately devoted to its accuracy, it is necessary to thoroughly evaluate the final output and determine whether the effort has been successful in its objectives. Throughout the course of this study, the simulation of the near-surface wind field has been of primary importance, and indeed is the most significant parameter to be evaluated. As such, it is naturally the primary parameter selected for validation of the CBHAR reanalysis. However, since the model is an interactive system, one that simulates numerous physically dependent fields, errors in surface wind may also result from model discrepancies related to other parameters in the model. It is imperative to evaluate and understand the overall performance of the model simulations and to monitor their dynamic and thermodynamic consistency. Accordingly, in addition to the surface wind field, near-surface temperature has also been utilized for the validation of the reanalysis in order to quantify its thermodynamic performance, which has implications for applications that rely on the determination of near-surface atmospheric stability, such as studies of air pollution transport. To better gauge the relative quality of the CBHAR reanalysis fields, the ERA-Interim reanalysis has been used as a baseline for comparison and has been verified in a similar manner.

An unfortunate consequence of the necessity to produce as accurate a reanalysis as possible, requiring the assimilation of all available observational data, is that no independent observational dataset exists for the purposes of model verification. Thus, the same observations that were assimilated into CBHAR were necessarily used to verify the reanalysis as presented in this section. To mitigate the inherent advantage that this may confer on CBHAR relative to ERA-Interim, which was validated in the same manner but which undoubtedly assimilated fewer data from local networks and field programs, such as RAWS, WERC, and offshore well sites, only observations from the widely available NCDC ISH database (see Figure 2.2.1) were utilized in the following surface station verification analysis given in Section 4.2. Though ECMWF does not publish a listing of station data assimilated into ERA-I, the NCDC database primarily consists of the standard METAR-reporting airports and permanent weather stations that would most likely be assimilated into any global reanalysis product. Usage of this database alone thus reduces as much as possible any advantage inherent to CBHAR as a result of the greater number of observations assimilated, and aims to ensure that both CBHAR and ERA-I are verified with a common station dataset containing observations that were assimilated into each.

In order to evaluate the reanalysis output in offshore areas, which are a prime consideration of this study, reanalysis data were also evaluated using QuikSCAT ocean-surface winds. Like the NCDC data, QuikSCAT observations were assimilated into both CBHAR and ERA-Interim, leading to a fair comparison between the two. In addition, though not a focus of this project, upper-air variables were also verified in order to evaluate the performance of the reanalysis output above the surface. As with the other verification datasets, radiosonde data that had been assimilated into both products were used for the evaluation.

In the following statistical analysis, the metrics focused on will be RMSE and correlation, as defined in Appendix B. Combining the use of RMSE, which gives an overall measure of the error in a modeled field, with correlation, which evaluates how successfully the field matches the observed pattern, can give a reliable picture of the accuracy of modeled output. Certainly, if the RMSE is lower and correlation higher for one product relative to another, it can safely be said that it contains a more accurate representation of the field in question. On the other hand, if both the RMSE and correlation are higher, it suggests the presence of a persistent bias in the product with the higher correlation; the modeled pattern is more accurate, hence the higher correlation, but the bias increases the overall error, leading simultaneously to a larger overall RMSE.

4.2 Verification against Surface Station Observations

The CBHAR reanalysis was verified against the database of quality-controlled NCDC station observations assembled as part of this project as described in Section 2, comprising over 100 stations across all land areas (along with a few offshore locations) throughout the entire model domain. As mentioned in Section 4.1, only NCDC stations were used in the verification to avoid conferring an unfair advantage to CBHAR relative to the global reanalysis ERA-I, which is less likely to have assimilated data from local networks and field programs. The available observed variables of 2-m temperature and 10-m wind speed, wind direction, wind vector, and the zonal (U) and meridional (V) wind components were used to validate the model fields. Other observed variables, such as dew point, SLP, and precipitation were not calibrated as a part of this study and therefore were not used to verify the performance of the reanalysis at the surface. Since near-surface temperatures and winds were the primary focus of this reanalysis effort, they were selected as the basis on which to determine the quality of the resultant model data. Model output fields were interpolated to the station locations using a standard bilinear interpolation, and the statistical measures of root-mean-square error (RMSE) and correlation (CORR) calculated for a variety of different time groupings. To provide a baseline against which CBHAR data could be compared, the ERA-I reanalysis data that were used as initial and boundary conditions for the current reanalysis—and to this point one of, if not the most accurate reanalysis available for the study region—were verified in the same manner. The following comparison of the error present in both reanalyses thus quantifies the improvements generated by the current model configuration and reanalysis techniques detailed in Section 3.

In many of the following figures, rather than show a side-by-side comparison of the actual values of the verification statistics for ERA-I and CBHAR, the relative differences between the statistics of the two reanalyses are instead shown. For RMSE and CORR, the difference between the two is normalized according to the ERA-I statistic, in order to demonstrate the percentage improvement (or degradation) in CBHAR relative to ERA-I. The formulas for these normalized statistical differences are given below:

$$\Delta RMSE = \frac{RMSE_{ERA} - RMSE_{CBHAR}}{RMSE_{ERA}} \qquad (4.1)$$

$$\Delta CORR = \frac{CORR_{CBHAR} - CORR_{ERA}}{CORR_{ERA}} \qquad (4.2)$$

Here, the *ERA* and *CBHAR* subscripts refer to the values calculated for the ERA-I and CBHAR reanalyses, respectively. In both cases, the numerators are defined such that an improvement in CBHAR (i.e., either a reduction in RMSE or an increase in CORR) results in a positive value for the statistic.

To begin with, Figure 4.2.1 shows ΔRMSE and ΔCORR for near-surface temperature and wind variables as verified over all stations and all 6-hourly output times (0000, 0600, 1200, and 1800 UTC) for the entire 31-year study period. Only the 6-hr times were used in this comparison, rather than the hourly data present in CBHAR, in order to provide a proper comparison to ERA-I, which only includes 6-hr data. This comparison shows that the error has been greatly reduced for all of the surface wind variables, with improvements in RMSE ranging from 13–16%. CORR for the wind variables has likewise been significantly improved, showing gains of 8–12%. In addition, the error in the surface air temperature has also been improved, though to a lesser degree and without a corresponding increase in correlation. These overall results are very encouraging, as producing a high-quality surface wind reanalysis is the primary objective of this project. The improvement in temperature is also beneficial and is indicative of an improved characterization of the near-surface atmospheric stability.

Though it is encouraging that the simulation of surface variables has been significantly improved domain-wide, a closer examination is in order. After all, it is to be expected that a higher-resolution model, with its corresponding higher-resolution topography, will naturally produce more accurate winds, solely by virtue of having more accurately specified orographic features. However, as the aim of this project centers on winds over ocean areas, such improvements to inland areas are not of the highest concern. To investigate how much of this overall improvement in the winds was due to such effects, the station set was divided into those stations within 30 km of the coast and those farther inland, with separate verifications conducted for each. This division resulted in a total of 65 stations in the coastal zone and 38 in the inland region. The verification results for the coastal and inland subsets are shown in Figures 4.2.2 and 4.2.3, respectively. As with the overall results in Figure 4.2.1, both zones exhibit improvements to the RMSE and correlation for all wind variables, demonstrating the success of CBHAR in simulating winds with increased accuracy for both coastal and inland locations. Interestingly, this comparison also shows that the improvement to the RMSE for all of the wind-related variables is actually significantly larger in the coastal areas, with reductions in error of 15–18%, with a much smaller improvement inland. The correlations are improved to a greater degree away from the coast, however, suggesting an expected benefit from higher-resolution topography. This greater reduction in error near the coast is a very positive result, and indicates that major improvements to the winds have been made in the areas where they are most needed for the purposes of this project. Compared with the winds, 2-m temperature is improved to a lesser extent in both regions, with improvements of 5.1% and 1.4% in the inland and coastal areas, respectively.

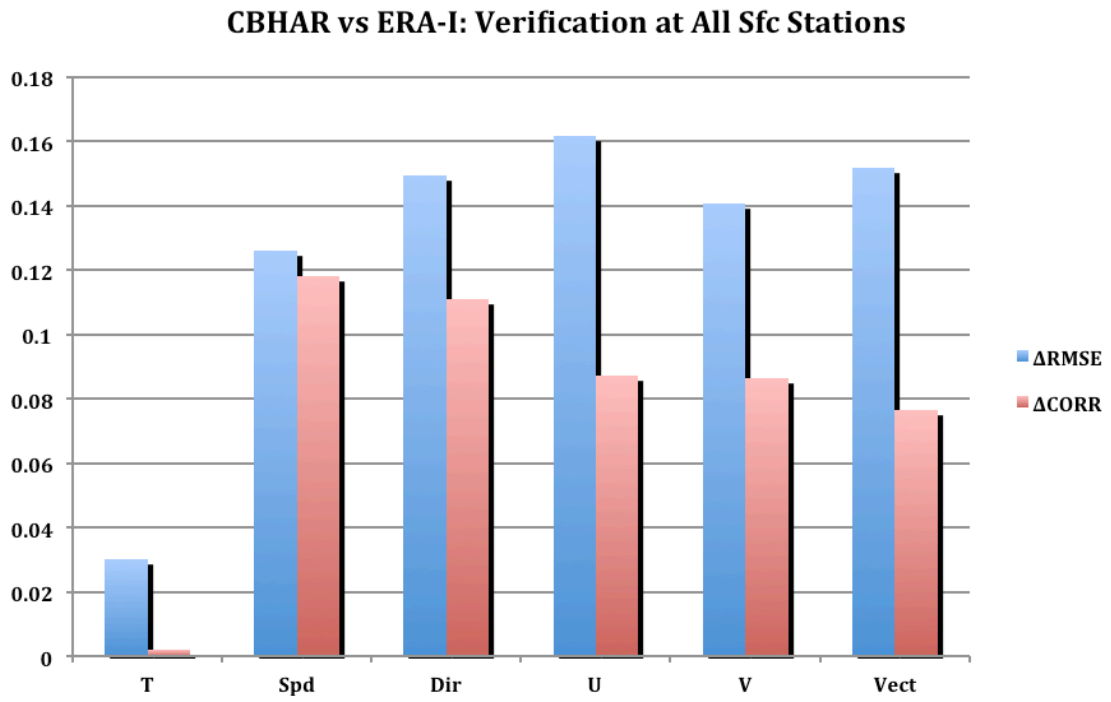

Figure 4.2.1. ΔRMSE and ΔCORR for 2-m air temperature (T) and 10-m wind speed (Spd), direction (Dir), U&V components, and wind vector (Vect), as verified for 6-hourly output against all collected NCDC surface station observations for the entire 31-year period. For each statistic, values represent the percentage improvement in CBHAR relative to ERA-I.

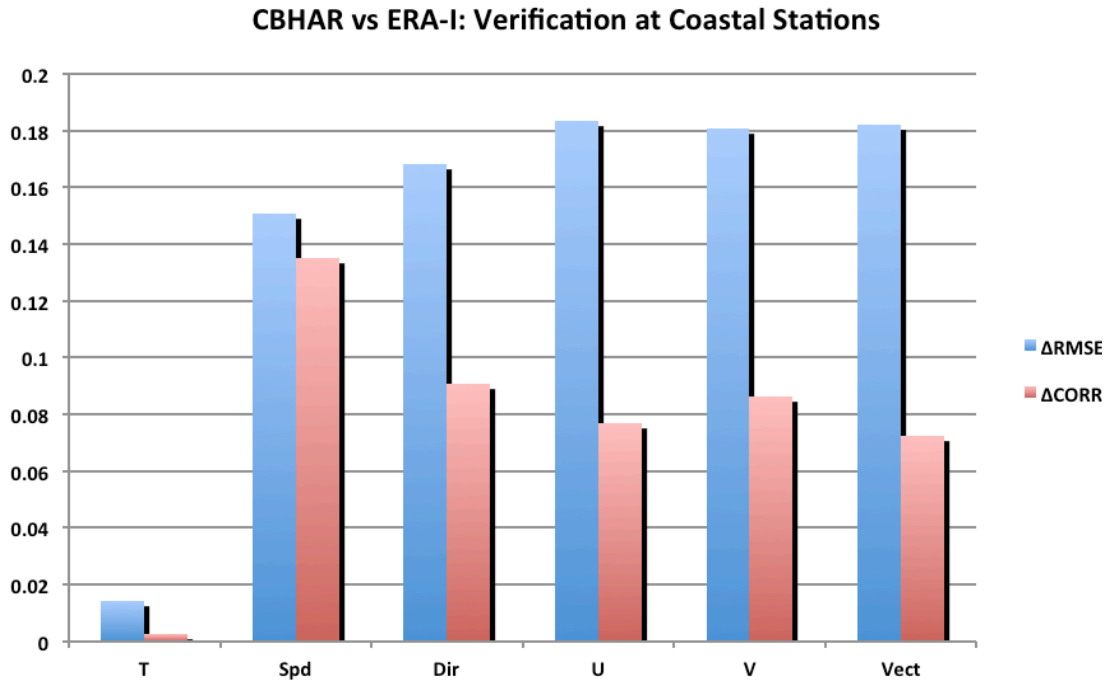

Figure 4.2.2. Same as Figure 4.2.1, but for verification against coastal stations

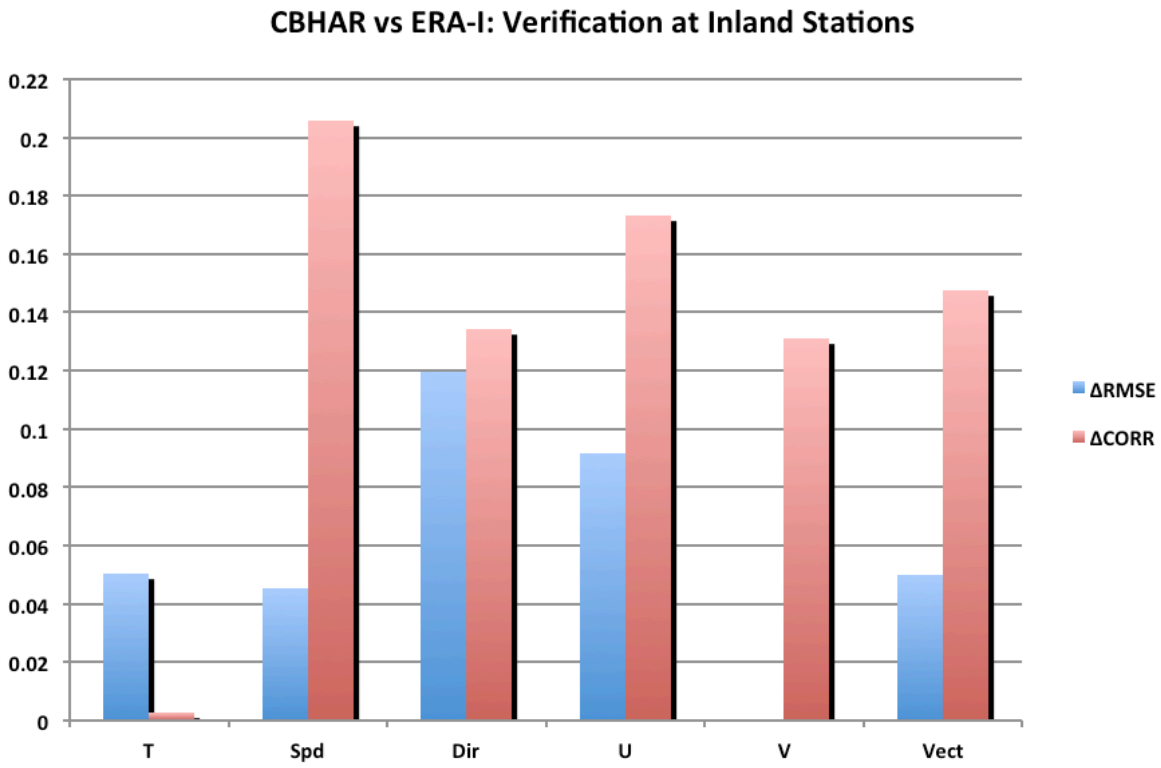

Figure 4.2.3. Same as Figure 4.2.1, but for verification against inland stations

4.3 Verification against QuikSCAT Ocean-Surface Winds

Naturally, the vast majority of the collected station data for this project come from points situated on land. Although it is reassuring that stations near the coast see an enhancement in the characterization of surface winds, a question naturally arises about the kinds of improvements seen in actual offshore areas. Though a large dataset of offshore in situ observations is unavailable, due to the annual encroachment of sea ice in the Chukchi–Beaufort Seas making the deployment of permanent buoys impossible, the QuikSCAT satellite-derived ocean surface wind product, measured by the SeaWinds scatterometer and assimilated as part of the production of both CBHAR and ERA-I, offers an opportunity to validate surface winds over ocean areas. As shown previously in Figure 3.4.4b, despite being a satellite product, QuikSCAT data provide a highly accurate measure of offshore wind conditions as compared to buoy observations, and are thus suitable for use in model validation. Unfortunately, due to the nature of the measurement method, QuikSCAT winds are only available for open water areas far from the coastline, and are thus limited in their seasonal availability. Despite this limitation, they still provide the best option for evaluating model results over wide swaths of the ocean basin in the study area. As was the case with station observations, the fact that QuikSCAT data were assimilated in the production of CBHAR means that they do not represent an independent verification dataset. However, as they were also assimilated into ERA-I, a direct comparison of the relative performance of the two reanalyses remains valid. It should be noted that since QuikSCAT observations are only available since 1999, the

verification presented in this section is thus applicable to the last decade of the study period.

CBHAR and ERA-I data were validated against the available QuikSCAT winds, bilinearly interpolating the reanalysis data to observational locations in the same manner as was done for surface station data. Results from this comparison, compiled for the entire 31-year period, are given in Figure 4.3.1. Impressive gains are seen for all surface wind variables in this comparison, with RMSE reduced by about 16–19% and correlation increased 9–17%, values that are remarkably similar to those observed for the coastal land stations. This result is achieved despite the fact that there is a presumed reduced benefit for higher-resolution models over the open ocean, where resolving neither orographic features nor the coastline or sea ice edge is a relevant issue. In addition, the relatively small-scale circulations, such as the sea breeze, which develop along and across coastal boundaries, are presumably factors of lesser importance far away from the coast than they are on land and in immediate offshore areas. In sum, the overall quality and consistency of these results, combined with those achieved for the coastal land stations, provides great confidence in the accuracy of the offshore winds in CBHAR, and suggests that this new reanalysis will greatly benefit applications that require the accurate specification of historical surface wind data.

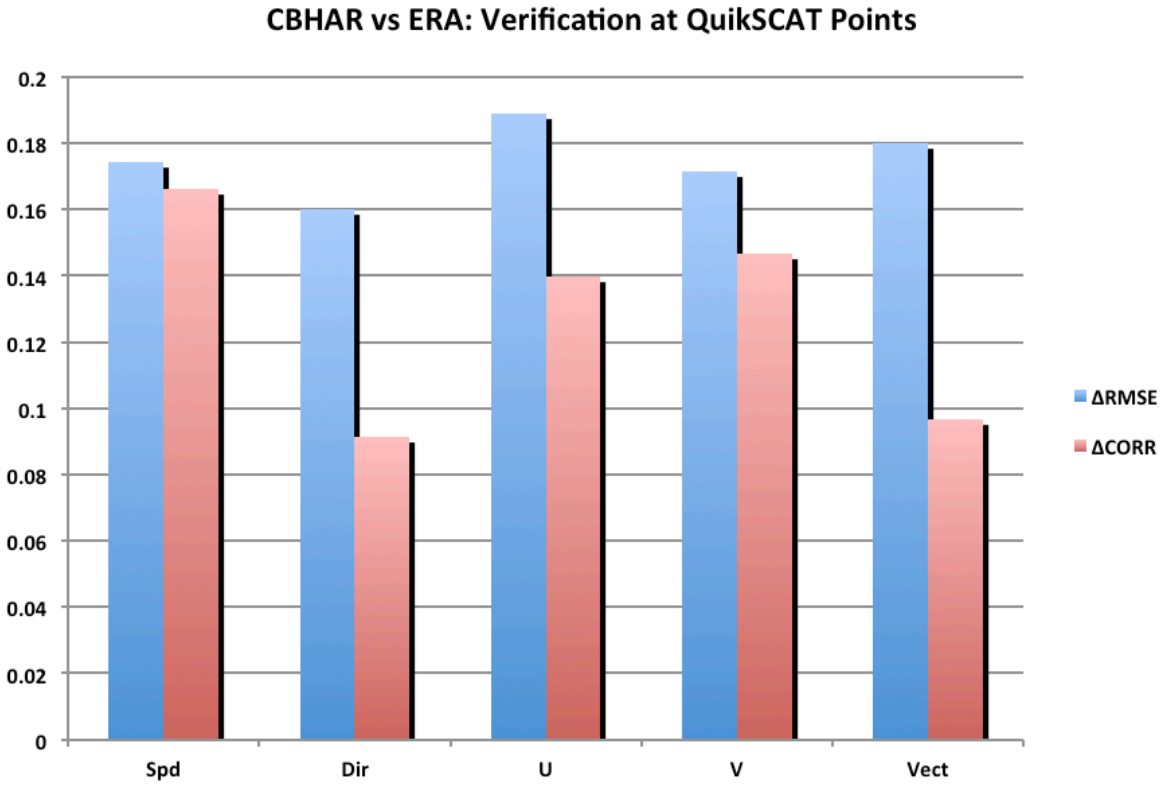

Figure 4.3.1. ΔRMSE and ΔCORR for 10-m wind speed (Spd), direction (Dir), U&V components, and wind vector (Vect), as verified for 6-hourly output against QuikSCAT data for the entire 31-year period.

4.4 Seasonal and Diurnal Error Analyses

It has been established in Sections 4.2 and 4.3 that the new CBHAR reanalysis provides a significant improvement to surface winds across the entire model domain, and particularly in areas near the coast and offshore, as compared to ERA-I. The statistics thus far have been calculated over the entire 31-year reanalysis period (or in the case of QuikSCAT, the entire 10-year observational period). How do they vary with season and time of day? To answer these questions, verifications of CBHAR and ERA-I were produced for each of the months of the year and hours of the day, in order to depict the seasonal and diurnal evolution of the performance of each of the validated model variables. As before, only 6-hourly data were included in the verification in order to make a consistent comparison between the two reanalyses.

Figure 4.4.1 shows the average monthly 2-m temperature RMSE for CBHAR and ERA-I, while Figure 4.4.2 shows monthly ΔRMSE and ΔCORR. As one would expect, errors are generally lower in the reanalyses in the warmer months, when variability in atmospheric conditions is at a minimum, and greatly increase during the winter. As suggested by the results of the overall error analysis in Section 4.2, the impacts of CBHAR on temperatures are relatively small through most of the year. However, the greatest improvements, both proportionally and in absolute terms, are seen over the late winter months, with errors reduced by nearly 6% in January and April, and 10–11% in February and March. These gains are somewhat offset in the summer months of July and August, however, when the RMSE is increased by 4–5%. The relative size of the improvements tends to mirror the relative magnitudes of the actual RMSE values; when total errors are larger, the improvements tend to be larger as well. The marked difference between error reductions in winter versus summer perhaps indicates a greater capability of CBHAR to represent the surface-based temperature inversions that are so important to near-surface weather and atmospheric stability throughout the region in the winter months.

The statistics for the surface wind variables (wind speed, direction, and vector), as shown in Figures 4.4.3–4.4.8, on the other hand, display no such mixed results. As with temperature, the RMSE for wind speed and wind vector is largest in the winter months, when the variability of weather conditions is high, and declines during the summer, when the variability is at its minimum. Interestingly, the error in wind direction does not follow this same pattern, remaining relatively constant throughout the annual cycle, though with a slight decline in the autumn. A key difference between the wind statistics and those of temperature, however, is that the percentage gains seen in RMSE and CORR are remarkably consistent and consistently positive throughout the entire year, with significant error reductions in wind vector of 14–16% and increased correlations of 6–9%. Similar consistent results are seen individually in the wind speed and direction. These results further serve to demonstrate the consistently high quality of the reanalyzed surface wind fields of CBHAR and give additional confidence in their overall accuracy.

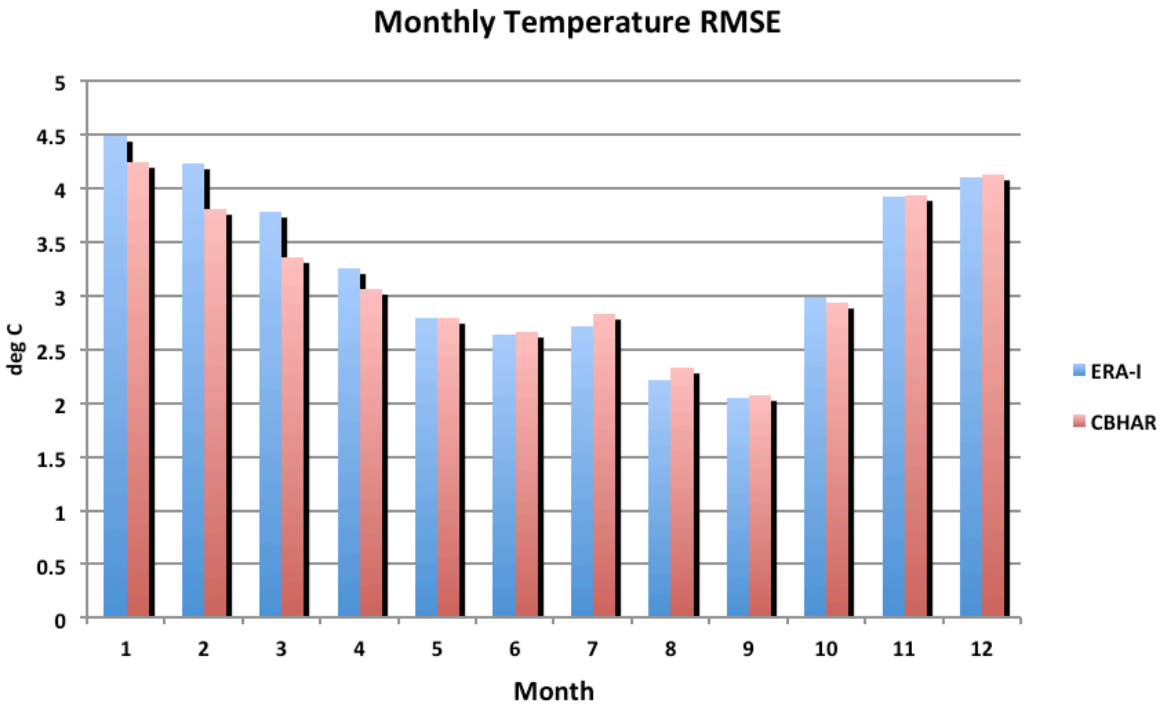

Figure 4.4.1. Monthly-averaged RMSE for 2-m air temperature (°C) in CBHAR (red) and ERA-Interim (blue), as verified against NCDC stations

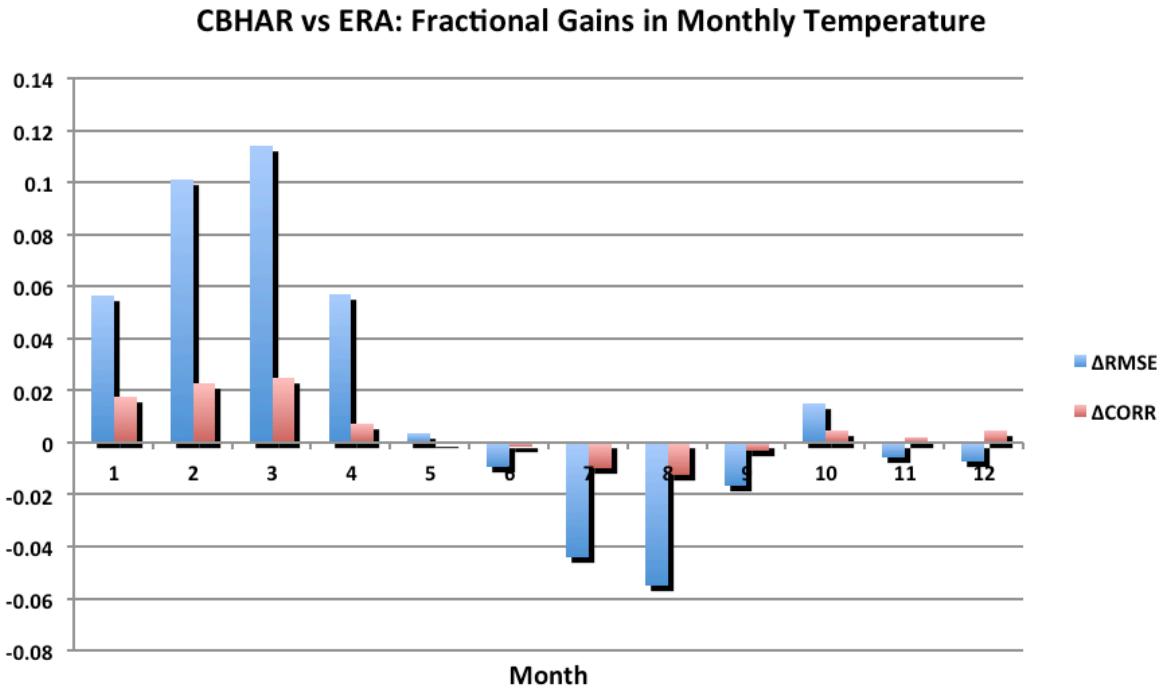

Figure 4.4.2. Monthly-averaged fractional improvement in 2-m air temperature RMSE (ΔRMSE) and correlation (ΔCORR) for CBHAR relative to ERA-Interim, as verified against NCDC stations

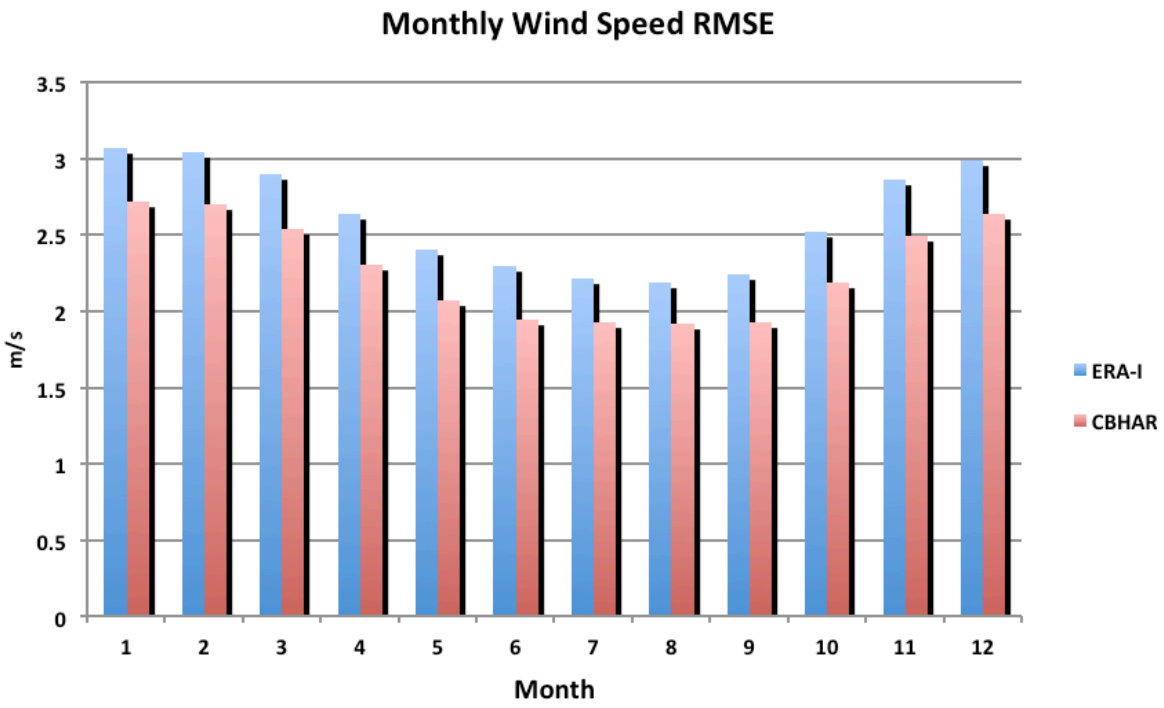

Figure 4.4.3. Same as Figure 4.4.1, but for 10-m wind speed (m s^{-1})

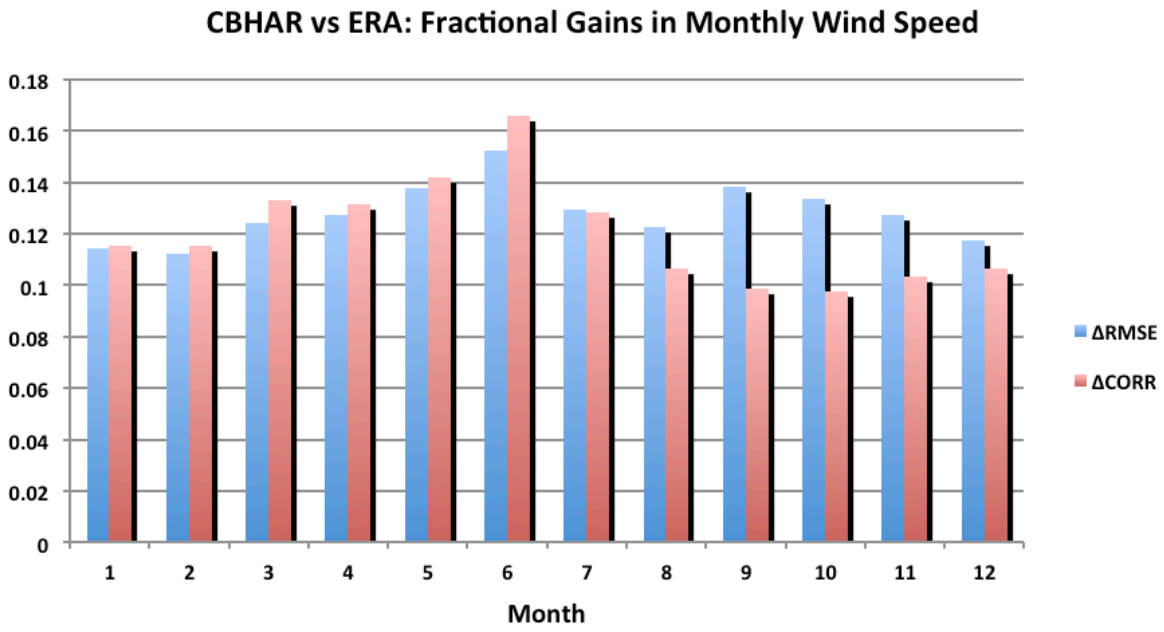

Figure 4.4.4. Same as Figure 4.4.2, but for 10-m wind speed

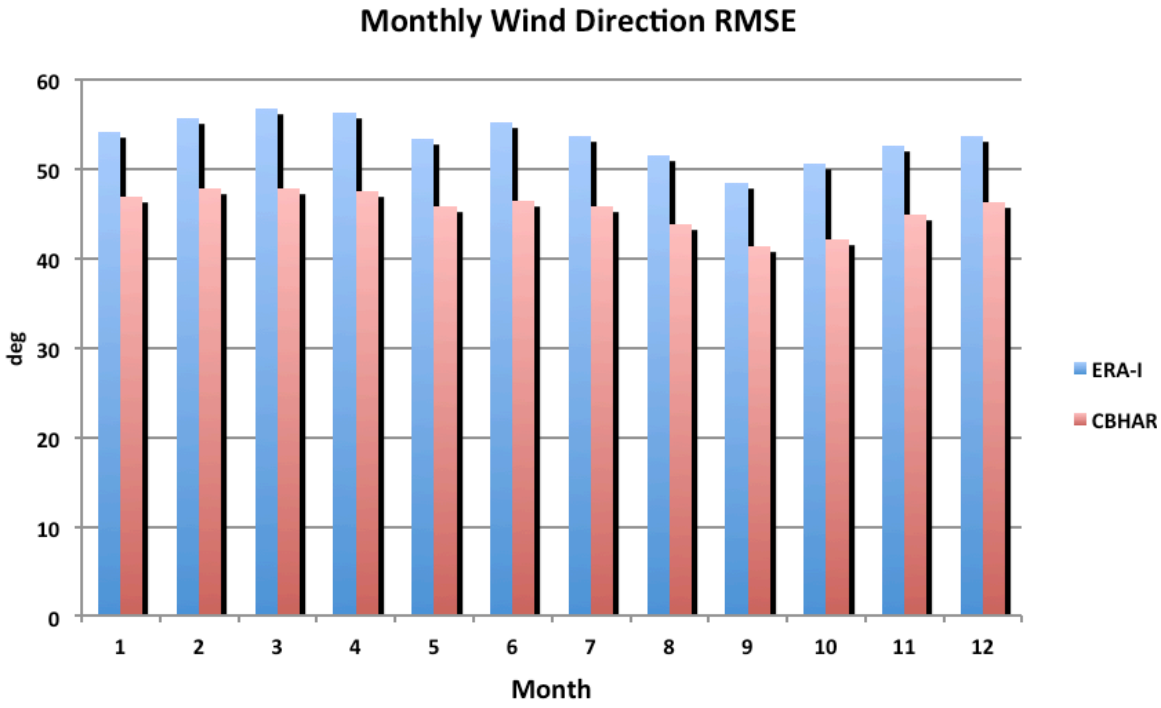

Figure 4.4.5. Same as Figure 4.4.1, but for 10-m wind direction (degrees)

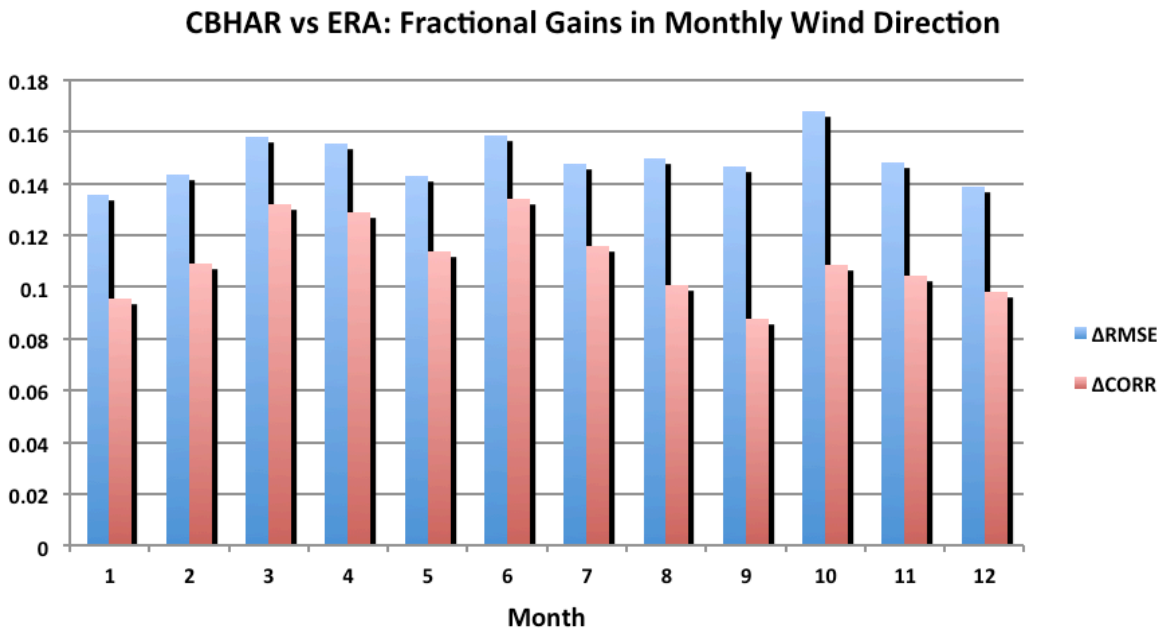

Figure 4.4.6. Same as Figure 4.4.2, but for 10-m wind direction

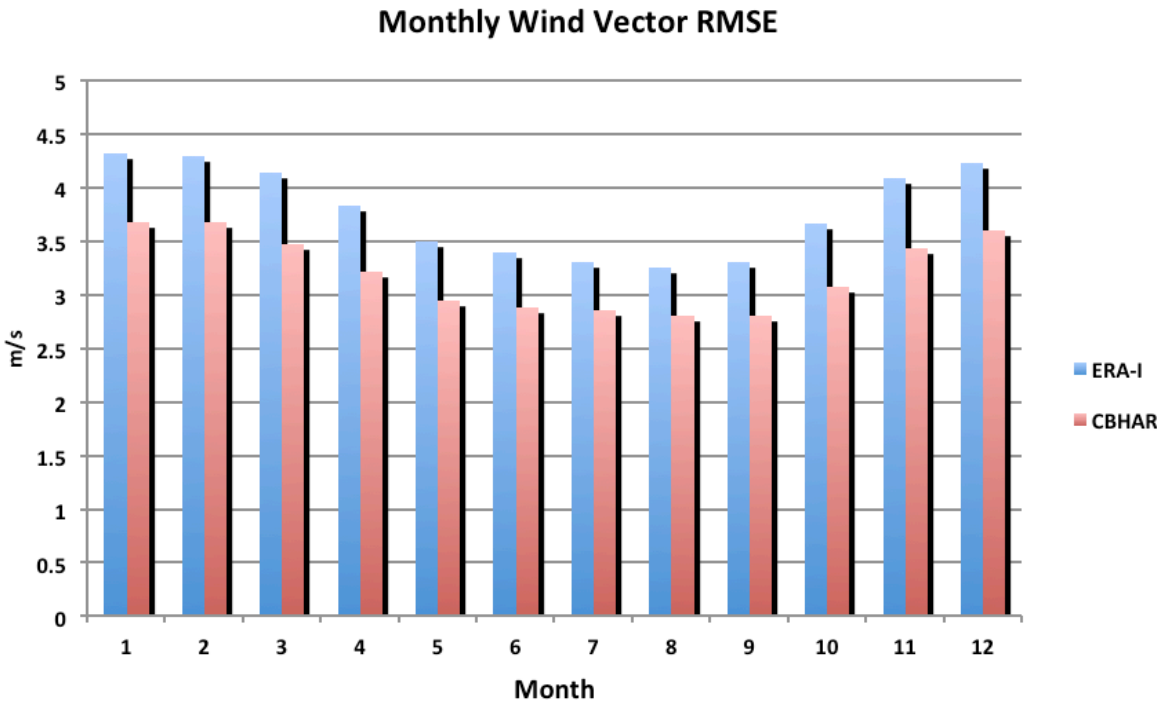

Figure 4.4.7. Same as Figure 4.4.1, but for 10-m wind vector (m s^{-1})

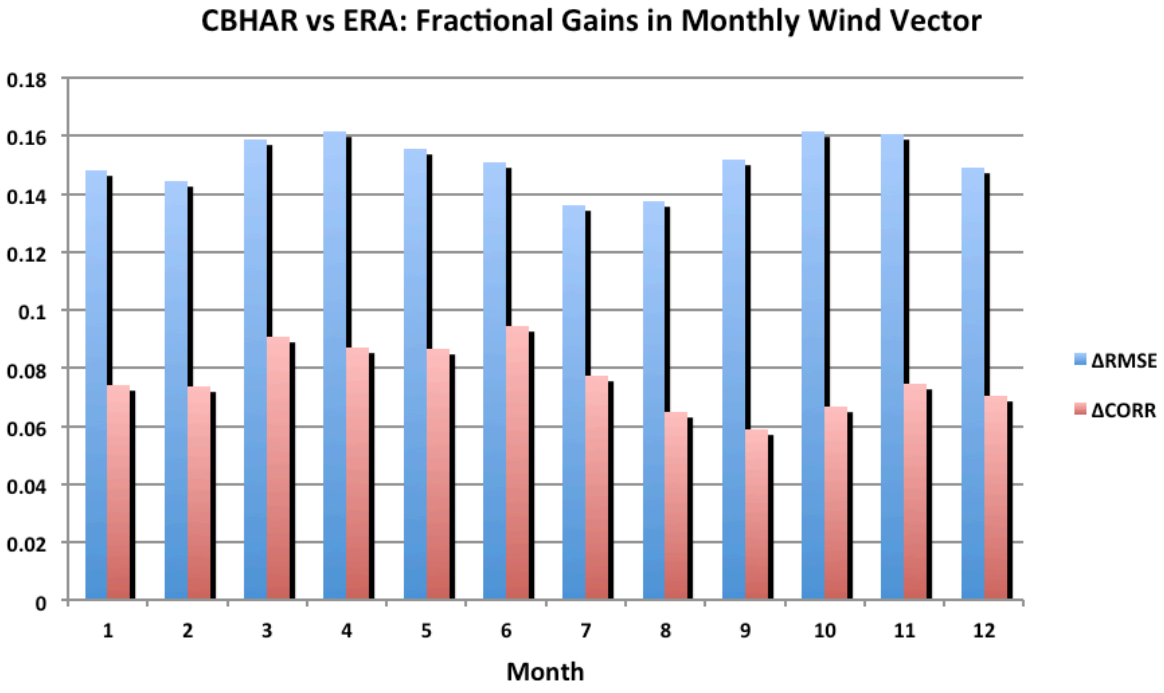

Figure 4.4.8. Same as Figure 4.4.2, but for 10-m wind vector

Moving on to the diurnal cycle, it was noticed during the course of the verification produced for this analysis that, as is to be expected, the reanalysis errors in both ERA-I and CBHAR were not consistent among the NCDC stations used for verification. Due to different geographical and environmental factors associated with their locations, some stations are, naturally, not as accurately represented in the reanalyses as are others. However, it was discovered that there was a noticeable bias in the observational reporting frequency of certain of these stations, such that the 3- and 6-hourly errors, averaged over all available stations, were markedly different from those of the intermediate hours, leading to noticeable discontinuities in the average hourly verification statistics. This was not a problem for the statistical analyses presented to this point, as only 6-hourly data were used for verification, due to ERA-I having a 6-hr frequency. It becomes an issue for the hourly verification of CBHAR, however, and so to correct for this observational bias, only those stations that regularly report at an hourly interval throughout the entire day, and over their entire station history, were selected for use in the following analysis. Doing so ensures that the set of observations used for verification at each hour is consistent over the entire diurnal cycle, mitigating any possible biases resulting from the use of different sets of stations for different hours. This filtering resulted in a set of 42 hourly-reporting NCDC stations that were used for this analysis.

Figures 4.4.9 and 4.4.10 show the hourly-averaged RMSE of near-surface temperature and wind vector, respectively, for CBHAR compared to ERA-I. Temperature error exhibits a distinct diurnal variation, peaking for the two reanalyses at 0800–0900 AKST, the time of day when the boundary layer begins to activate (aside from the Arctic winter, which lacks a diurnal cycle), and reaching its minimum at 2100 AKST, when the PBL has greater stability. This error pattern mirrors that of the average monthly errors, which peaked during months with greater meteorological variability and fell when variability declined. The wind vector RMSE follows a similar pattern, though a peak in the error at 1500 AKST and with far less diurnal variation. There is relatively consistent behavior throughout the course of the period, with temperature and winds always performing better in CBHAR than in ERA-I, and with a similar degree of improvement throughout the day. It is encouraging to see that the CBHAR RMSE for temperatures, and particularly winds, is significantly less than the errors present in ERA-I for all hours. As with the other verifications performed, the degree and consistency of the improvements seen in CBHAR surface wind demonstrate the fundamental quality of the reanalysis.

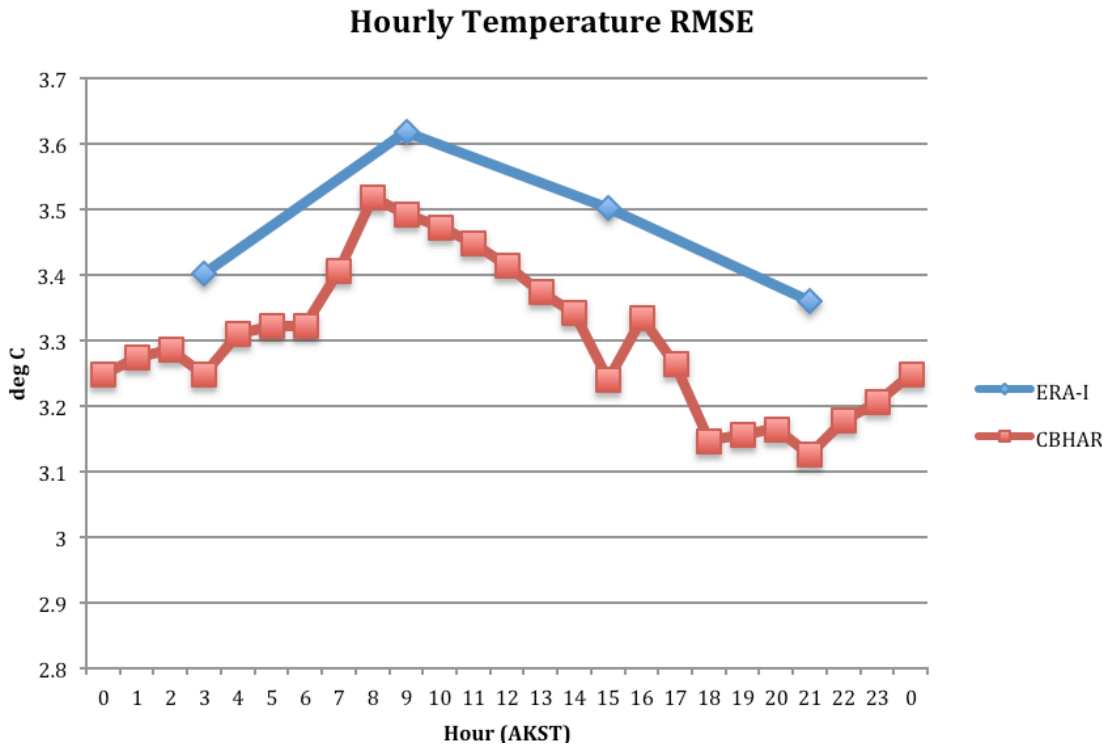

Figure 4.4.9. Hourly-averaged RMSE for 2-m air temperature (°C) in CBHAR (red) and ERA-Interim (blue), as verified against hourly-reporting NCDC stations

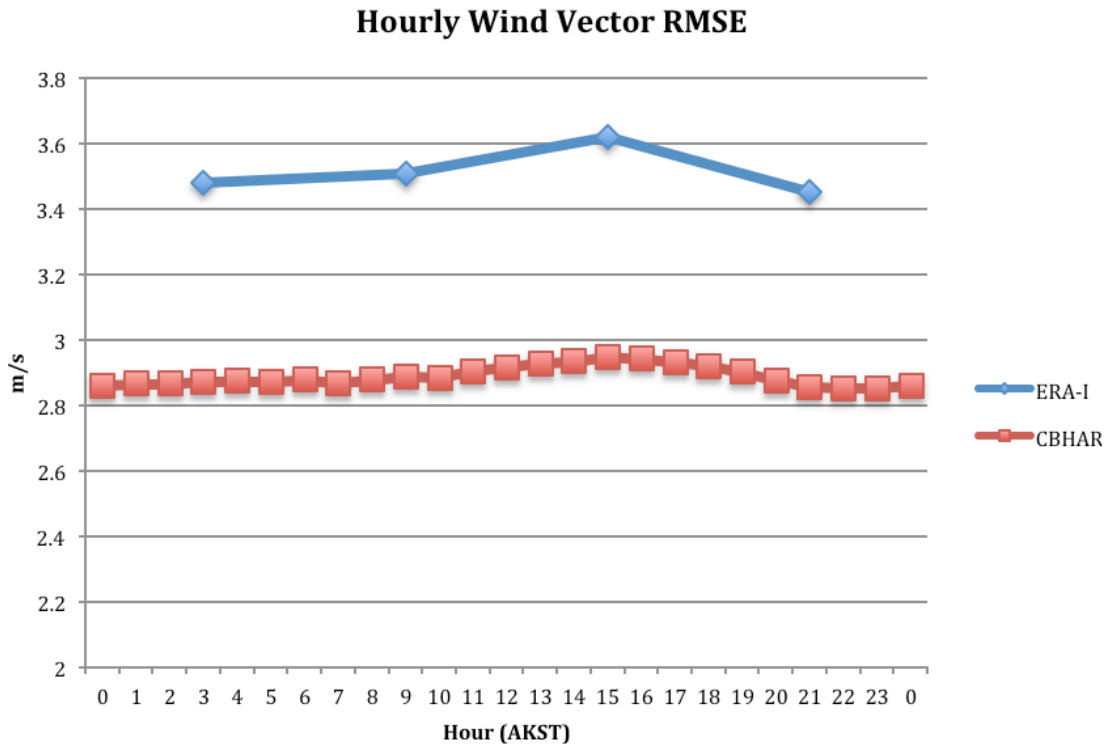

Figure 4.4.10. Same as Figure 4.4.9, but for 10-m wind vector (m s^{-1})

4.5 Verification against Radiosondes

Although not a primary focus of this reanalysis effort, it is still instructive to examine the performance of the model in representing the upper atmosphere. Unfortunately, only eight radiosonde sites exist in the model domain to serve as a basis for model error calculations, and only three of these are available throughout the entire period: Barrow, Kotzebue, and Inuvik. While this is not nearly enough to give a proper representation of the three-dimensional atmosphere across the entire region, it is still worthwhile to look at how the new CBHAR reanalysis compares to ERA-I. It should be noted that, as was the case with the QuikSCAT and station data, the radiosonde data used here for verification were also assimilated into both CBHAR and ERA-I and hence do not represent an independent dataset. However, since this is a relative comparison of the performance of the two reanalyses, and both assimilated the same radiosonde data used for verification, the comparison remains valid. Given the pivotal role that moisture content plays in determining atmospheric stability, the verification presented below was also performed on dew point temperatures, in addition to the standard temperature and wind variables. At each of the radiosonde locations, both the modeled and observed temperature, dew point, and wind fields were vertically interpolated to constant pressure levels every 25 hPa and the reanalysis output verified using the model grid point closest to the station location.

Figures 4.5.1–4.5.3 show the vertical RMSE profile for temperature, dew point, and wind vector for CBHAR versus ERA-I, respectively, as averaged across the available radiosonde locations for the entire 31-year study period. To better illustrate the differences in RMSE, Figure 4.5.4 shows ΔRMSE for the three variables. For temperature and winds, the expected pattern is seen, with larger errors near the surface and around the tropopause, levels where the atmospheric variability is highest. Dew point error increases vertically to a maximum in the stratosphere, no doubt largely due to the difficulty in making accurate measurements in the low pressure, very low moisture conditions at those levels. CBHAR generally tracks ERA-I closely for the thermodynamic variables, with a notable improvement in temperature near the surface of more than 20%, and with reduced error throughout the boundary layer, through the 850-hPa pressure level. In addition, mid- and upper-level dew points above 750 hPa show significantly increased accuracy in CBHAR. Unfortunately, winds show no such improvements at upper levels, though the increase in RMSE is relatively small, around 5% through most of the profile. In contrast, levels near the surface exhibit better performance, with a ΔRMSE of around 10%. This latter result is consistent with the great improvements in surface winds demonstrated by verification with surface station and QuikSCAT measurements. The improvement in boundary-layer temperatures constitutes an enhancement to the representation of near-surface atmospheric stability, which should be of benefit to air pollution applications.

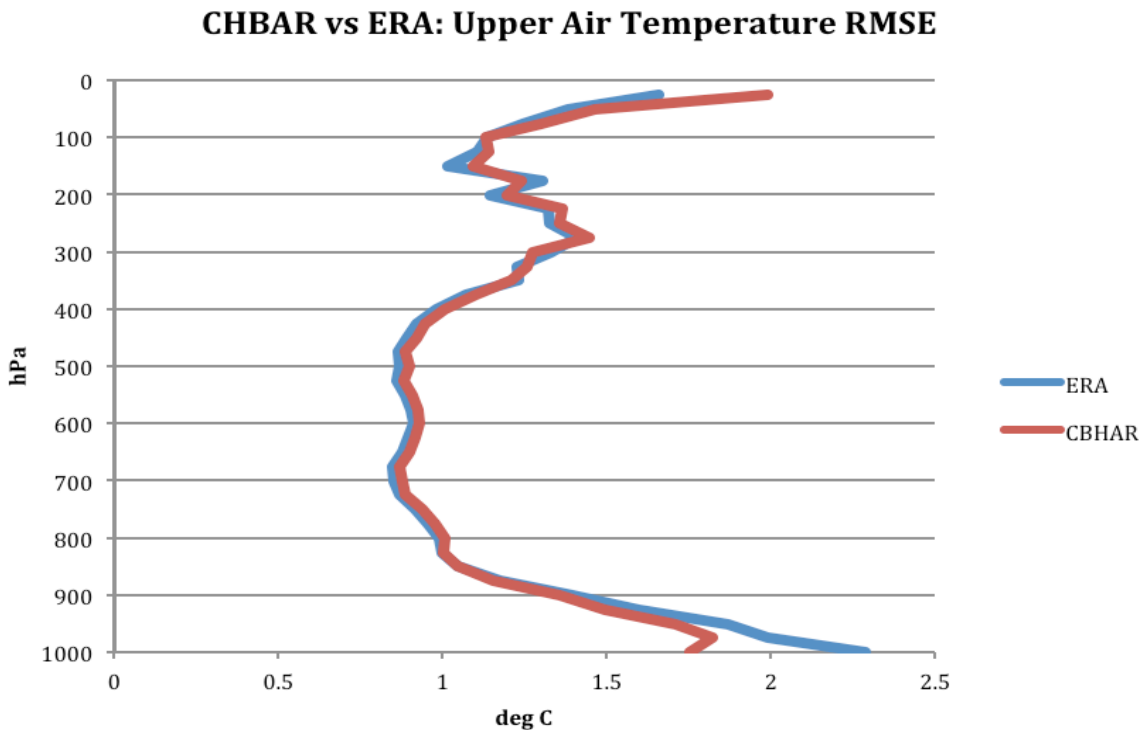

Figure 4.5.1. RMSE profile for temperature (°C) in CBHAR (red) and ERA-Interim (blue) as verified against all available radiosonde measurements for the entire 31-year period

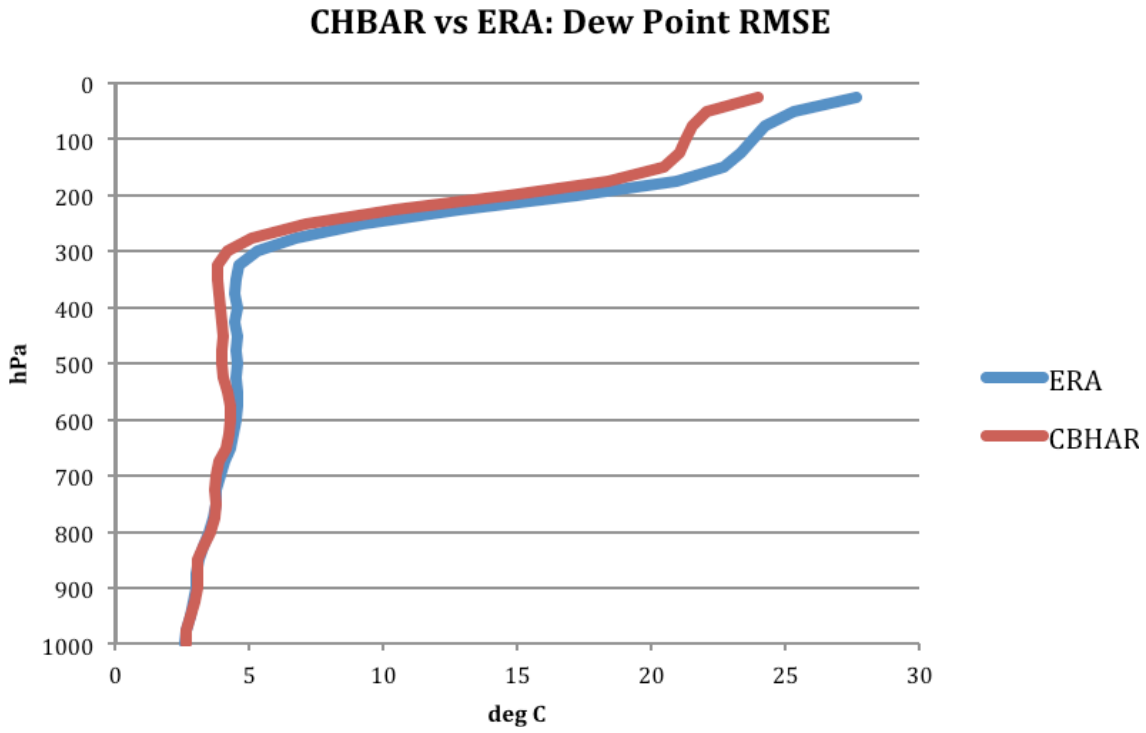

Figure 4.5.2. Same as Figure 4.5.1, but for dew point (°C)

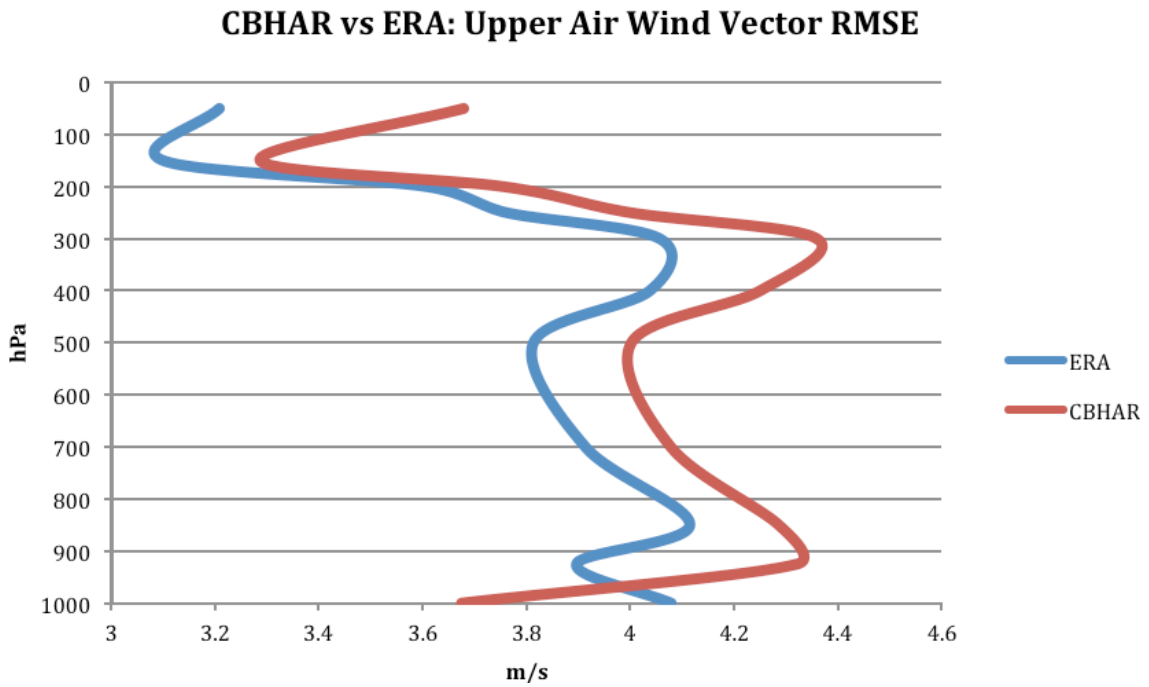

Figure 4.5.3. Same as Figure 4.5.1, but for wind vector (m s^{-1})

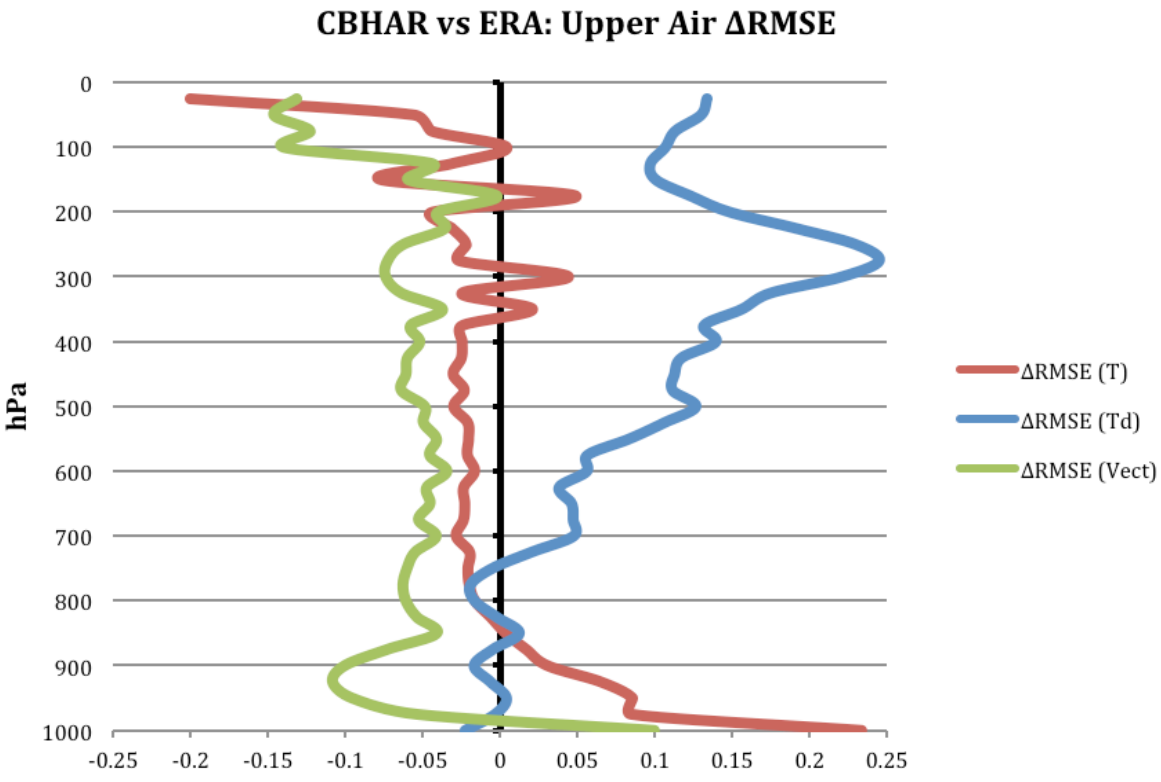

Figure 4.5.4. ΔRMSE for upper-air temperature (red), dew point (blue), and wind vector (green) as verified against all available radiosonde measurements for the entire 31-year period

5 Surface Climate in the Chukchi–Beaufort High-Resolution Atmospheric Reanalysis (CBHAR)

In this section, the climatology of the study area, including the interannual variability, long-term changes, and extremes of the region's weather patterns, focusing in particular on near-surface winds, will be analyzed using the new CBHAR reanalysis. There is an imperative to conduct this analysis for use in various applications, due to rapid ongoing environmental changes and a lack of credible surface climate information in the study region. CBHAR is particularly well suited to this sort of analysis due to its high resolution and well-described regional physics, which allow it to resolve finer-scale processes caused by complex topography (i.e., the Brooks Range), variable sea ice and ocean properties, and their interactions. This regional analysis will add significant information to the understanding of the Arctic climate as a whole. Variables analyzed include 2-m temperature, the 10-m wind field, SST, and sea ice concentration/extent. As in the previous section, the results are compared to those of ERA-Interim, in order to further evaluate the overall performance of CBHAR.

5.1 Large-Scale Surface Wind Field Analysis

5.1.1 Analysis Approach for the Basin-Scale Surface Wind Field

This section will present a detailed climatology of the surface winds in CBHAR, including analysis of the long-term climatology as well as the linear trends in the surface wind speeds. A wind direction climatology will also be discussed. In the following analysis, the monthly-average wind speeds were calculated by averaging the data over all output times for each month of the 31-year reanalysis period, while the monthly maximum wind speeds were determined by identifying the maximum wind speed for each month over the same period. To calculate the percentile wind speeds, the speeds were first sorted from smallest to largest at each grid point. The rank R_k was then calculated as follows:

$$R_k = N\frac{P}{100} + 0.5 \qquad (5.1)$$

where N is the total number of values and P is the percentile (90 or 95 here). Let P_{95} represent the 95th percentile value. Thus,

$$P_{95} = R_{dec}(A(R_{whole}+1) - A(R_{whole})) + A(R_{whole}) \qquad (5.2)$$

where R_{whole} and R_{dec} are the whole and decimal parts of the rank as calculated with Equation 5.1, respectively, and A is the sorted array at each grid point.

The trends of monthly-average and 95th-percentile wind speeds were also analyzed for the entire 31-year period through the use of a linear regression approach, in which a positive value indicates an increase in wind speed and a negative value represents a decrease over the 31-year period. To investigate the variation of extreme wind events,

defined as occurrences of wind speed greater than the monthly 95th-percentile wind as calculated over the entire 31-year period, their frequency, expressed as a percentage, was calculated over a specified time period. For the wind direction climatology, the directions were first grouped into quadrants, and the monthly frequency of wind directions in each quadrant then calculated for each month over the 31-year period.

5.1.2 SLP and Surface Wind Speed Climatology

To begin with, the monthly mean SLP from 1979–2009 is analyzed as shown in Figure 5.1.1. The Beaufort High reaches its peak in March with a pressure of ~1024 hPa and is centered to the north of Barrow. By June, it weakens to ~1015 hPa and moves to the east, becoming centered in the middle of the Beaufort Sea. From July to September, the Beaufort High weakens further, reaching a minimum central SLP of ~1010 to 1012 hPa. The High strengthens again from October to December and begins to move back to the north of Barrow with pressures between 1017 and ~1021 hPa. The largest pressure gradient occurs in the Chukchi Sea when both the Beaufort High and Aleutian Low strengthen, particularly between October and March, with the gradient reaching its maximum in November. Overall, CBHAR successfully captures the climatological seasonal evolution of the synoptic-scale Beaufort High and its associated SLP. This climatological evolution matches that previously documented using NARR reanalysis data, in which the same evolutionary trajectory was found (Stegall and Zhang 2012).

The long-term climatology of the surface wind from 1979–2009 is detailed below. This analysis includes climatologies of the average wind speed, 95th-percentile wind speed, and wind direction. Figure 5.1.2 shows the 31-year average wind speed for each month of the year. Generally, the high climatological wind speeds are distributed from the Bering Strait to the shelf area of the Chukchi and Beaufort Seas, with the maximum monthly average wind speed occurring over the Bering Strait. The wind speed exhibits an obvious seasonality, with higher speeds in winter and lower values in summer. The highest wind speeds occur in October and November, reaching up to ~6 m s^{-1} over the Beaufort Sea and ~9 m s^{-1} over the Chukchi, while the lowest wind speeds appear in June. Both CBHAR and a parallel analysis using NARR (Stegall and Zhang 2012) show the consistent seasonality of surface wind speeds, though NARR data show the months with maximum speeds to be September and October. When compared with other large-scale reanalysis products and the in situ observations collected within the study domain, however, CBHAR gives a better estimate of the time of the maximum wind speed occurrence.

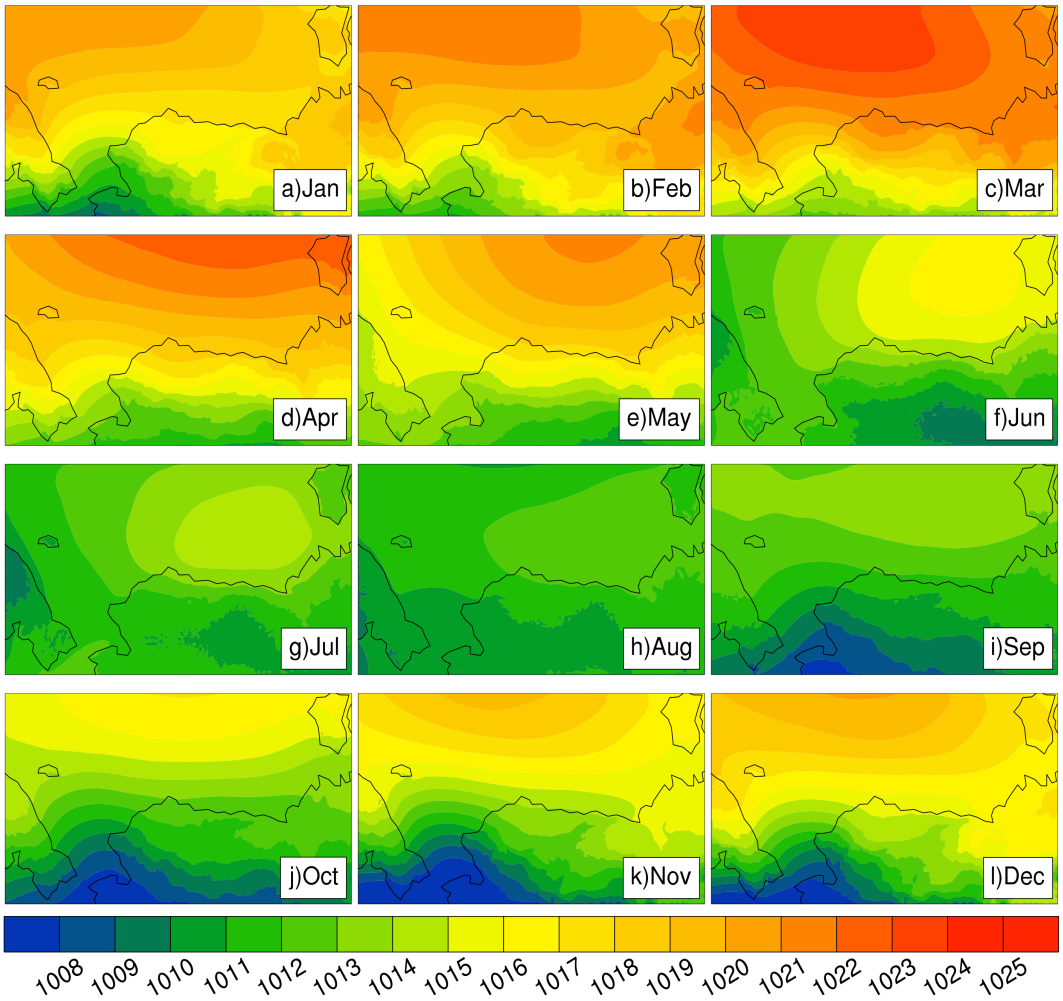

Figure 5.1.1. Climatological monthly mean sea level pressure (SLP, hPa) for 1979–2009 in CBHAR

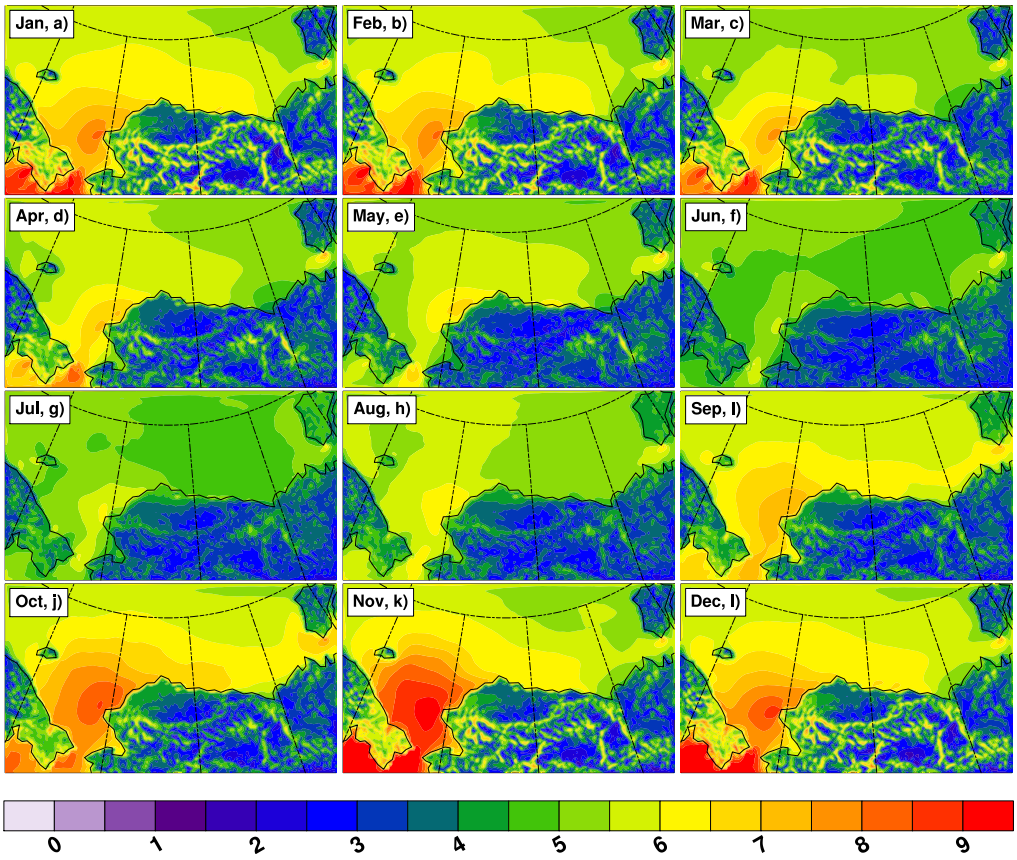

Figure 5.1.2. Climatological monthly mean wind speed (m s^{-1}) for 1979–2009 in CBHAR

The average wind speeds in CBHAR, when compared to NARR (Figure 3 in Stegall and Zhang 2012), demonstrate that CBHAR wind speeds are consistently higher. From December through April, CBHAR winds over the Beaufort Sea range from ~4 to 6 m s^{-1}, whereas NARR wind speeds are below 4 m s^{-1}. During these same months, the Chukchi Sea wind speeds in CBHAR range from ~6 m s^{-1} to above 8 m s^{-1}, while NARR wind speeds lie between 4 and ~6 m s^{-1}. Similarly, from May through August, CBHAR wind speeds have values of about 4 to 6 m s^{-1}, with NARR largely exhibiting speeds below 4 m s^{-1}, except for July and August when the NARR speeds increase up to 6 m s^{-1} over the Chukchi Sea. From September through November, NARR wind speeds increase up to a maximum of ~9 m s^{-1} over the Chukchi Sea in October, while CBHAR wind speeds increase up to a high of ~9 m s^{-1} in November over the same area. In NARR, winds over the Beaufort Sea during these months are primarily at or below ~5 m s^{-1}, while in CBHAR they are at or below ~6 to 6.5 m s^{-1}. The presence of higher wind speeds in CBHAR relative to NARR suggests that CBHAR better captures reality, as compared to other large-scale reanalysis datasets and in situ observations. A major reason for this increased accuracy is the use of ERA-Interim as the forcing reanalysis dataset for the production of the new regional reanalysis. ERA-I is generally considered the best product among the new generation of global reanalysis products, and its quality translates into

greater accuracy in CBHAR. Figure 5.1.3 shows the ERA-I average wind speeds over the same 31-year period, with the speeds also consistently higher than in NARR. A detailed comparison between CBHAR and ERA-I is given below. The other major reason for the discrepancy between CBHAR and NARR is the use of optimized model physical parameterizations in the CBHAR reanalysis system, which were selected specifically for their performance in the study region as detailed in Section 3.

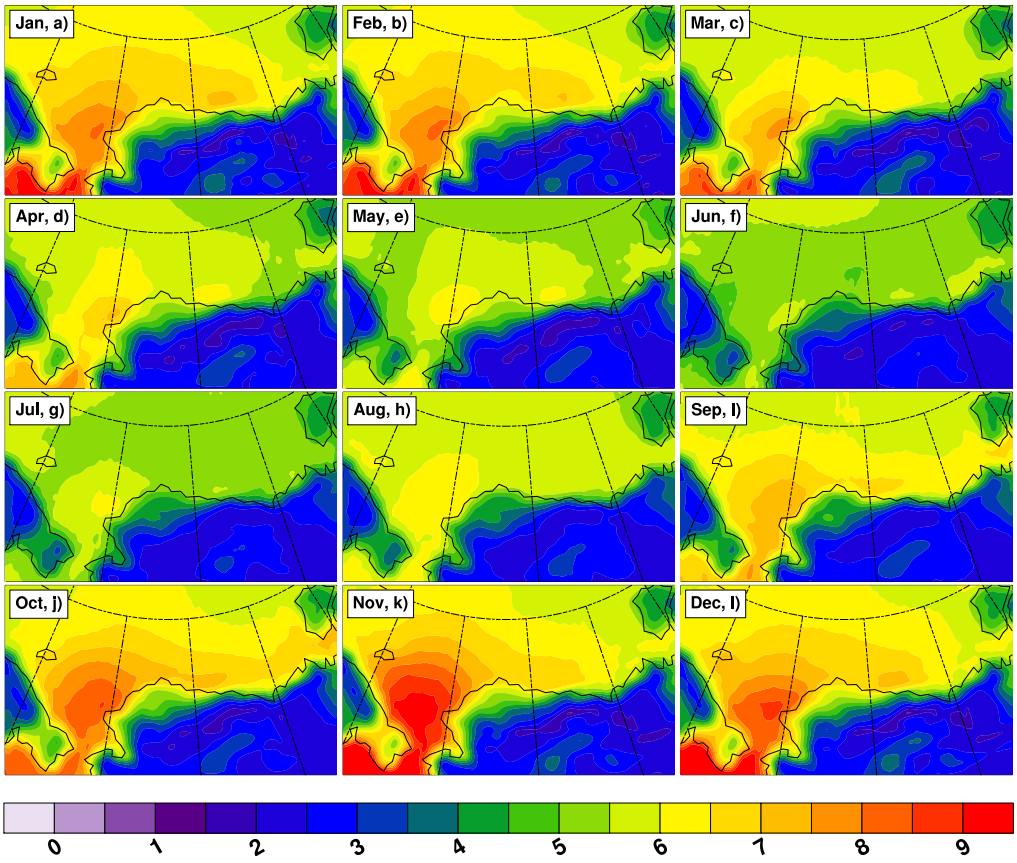

Figure 5.1.3. Climatological monthly mean wind speed (m s^{-1}) for 1979–2009 in ERA-Interim

In comparison to ERA-I, CBHAR exhibits similar basin-scale seasonality in the surface wind field, with the added benefit that CBHAR is able to capture many high-resolution features and processes not present in the former's wind field (Figure 5.1.2 vs. Figure 5.1.3). Figure 5.1.3 displays the average surface wind speeds for each month in ERA-I and confirms the similar seasonality as in CBHAR. This is not unexpected, as ERA-I was used to drive the production of CBHAR. Wind speeds over the ocean compare favorably between ERA-I and CBHAR, though it is quite clear that CBHAR better captures topographically influenced wind features than does ERA-Interim. For example, during the autumn and winter seasons, higher wind speeds (~6 m s^{-1}) exist over the Brooks Range and the interior of Alaska in CBHAR. This could be a signature of drainage and/or mountain/valley breezes, features that are not present in the ERA-I data shown in Figure

5.1.3. Another difference between the two reanalyses is that ERA-I has consistently higher wind speeds over the coasts, with differences of about 2 m s^{-1}. This difference is most likely primarily due to the much coarser grid spacing present in ERA-Interim than in CBHAR.

An analysis of the 95th-percentile wind speeds in CBHAR, given in Figure 5.1.4, shows that the strongest wind speeds occur in the autumn and winter seasons (October–March). A similar geographic pattern and seasonal cycle are seen in the 95th-percentile winds as in the climatological means (Figure 5.1.2). The strongest winds occur primarily over the Chukchi Sea with speeds of ~14–15 m s^{-1}. Wind speeds of ~12–13 m s^{-1} can be seen in October and November over the Beaufort Sea, and primarily along the Alaska coast. A close examination suggests that the area of large 95th-percentile wind speed extends farther eastward along the Alaskan Beaufort coast than in the mean wind field, although the primary area of highest wind speed is similarly situated over the Bering Strait.

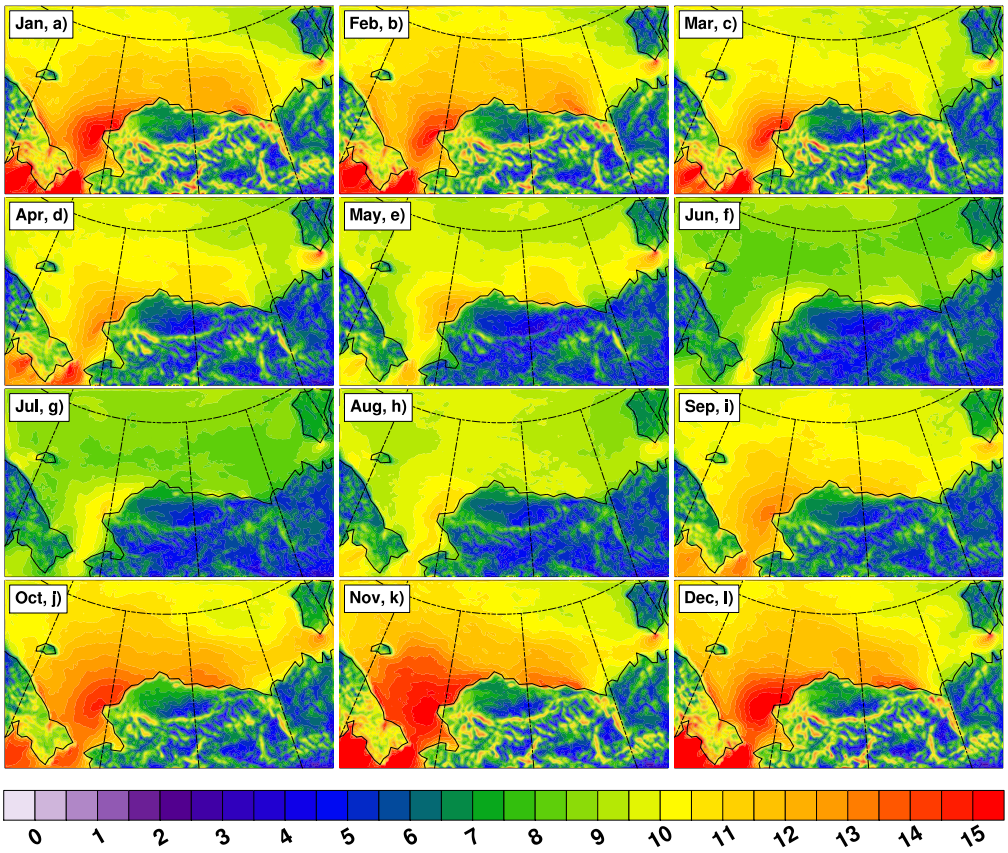

Figure 5.1.4. Monthly 95th-percentile wind speed (m s^{-1}) for 1979–2009 in CBHAR

For comparison, Figure 5.1.5 shows the 95th-percentile wind speeds in the ERA-I data. A very similar seasonality is present as that seen in CBHAR. A very evident difference between the two, however, is that the 95th-percentile winds in ERA-I are noticeably higher than those of CBHAR, particularly over the Beaufort Sea, with a difference of around 2 m s^{-1}. The biggest difference is in November, where most of the offshore areas

have wind speeds of ~13 m s^{-1} to above 15 m s^{-1} in ERA-I. In CBHAR, however, similar magnitudes of the wind speed are primarily limited to the Chukchi Sea. These differences are possibly due to the treatment of sea ice in the global model used to produce ERA-I. Further investigation would be needed to better understand the large differences seen in the month of November, as well as the consistently higher 95th-percentile wind speeds in ERA-I. As with the average wind speeds, CBHAR captures possible drainage and/or mountain/valley breezes during the autumn and winter months that are lacking in the larger-scale reanalysis.

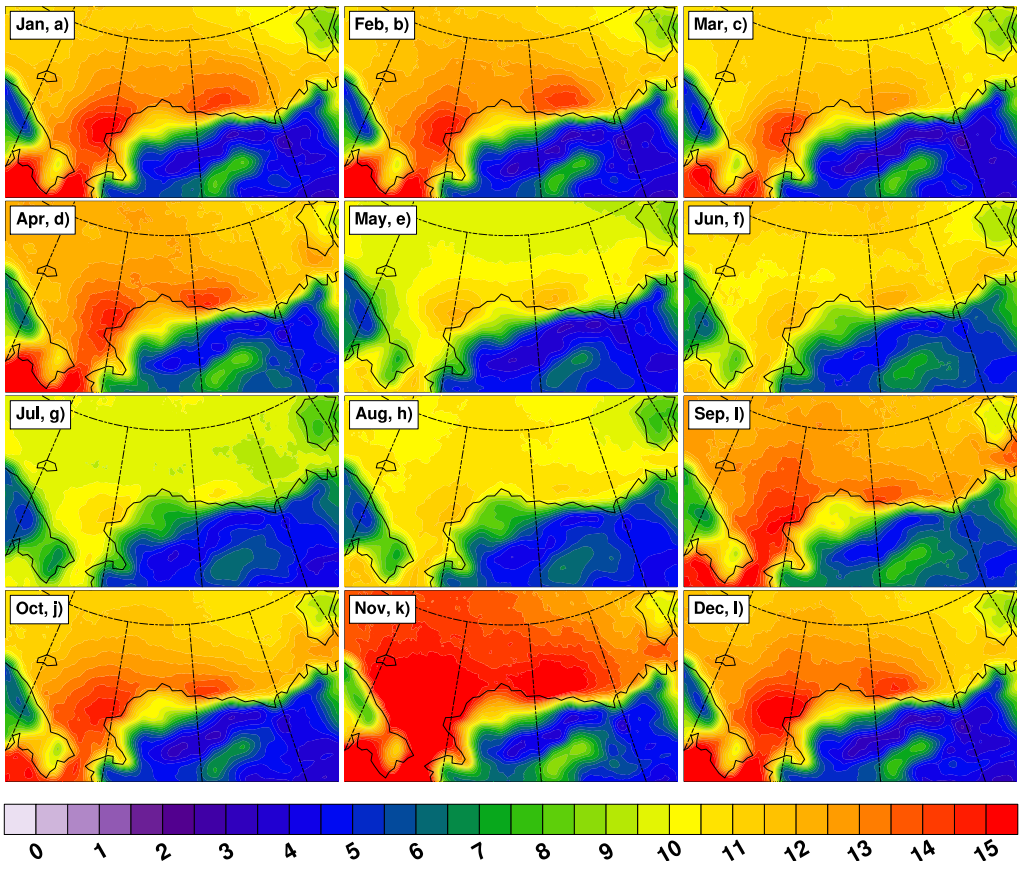

Figure 5.1.5. Monthly 95th-percentile wind speed (m s^{-1}) for 1979–2009 in ERA-Interim

To further understand the frequency of different wind speeds over the study domain, a probability density function (PDF) analysis was conducted for each month of the year (Figure 5.1.6). It was found that the peak frequency of any individual speed occurs in June and July for a wind speed of around 4 m s^{-1}. For most of the months, the highest frequency occurs for wind speeds ranging between 4–6 m s^{-1}. The frequency of wind speeds greater than 9 m s^{-1} increases in October and November. Figure 5.1.7 shows PDFs of the surface wind speeds over the entire year and throughout the full 31-year time period for both CBHAR and ERA-I. CBHAR exhibits a peak frequency at ~3.5 m s^{-1}, while the most frequent speed in ERA-I is ~2 m s^{-1}. However, the higher wind speeds of

~7–13 m s^{-1} exhibit greater frequency in ERA-I, which is consistent with the findings discussed above.

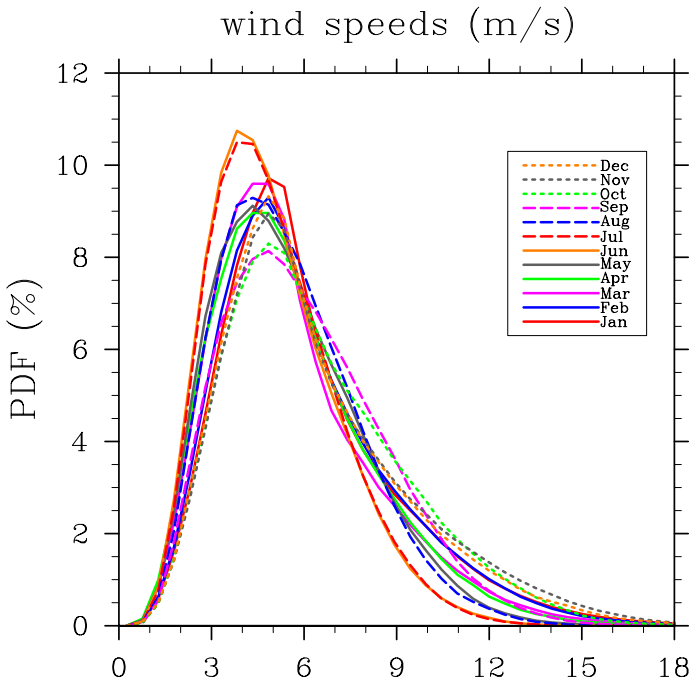

Figure 5.1.6. Probability Density Functions (PDFs) of the climatological monthly surface wind speed in CBHAR

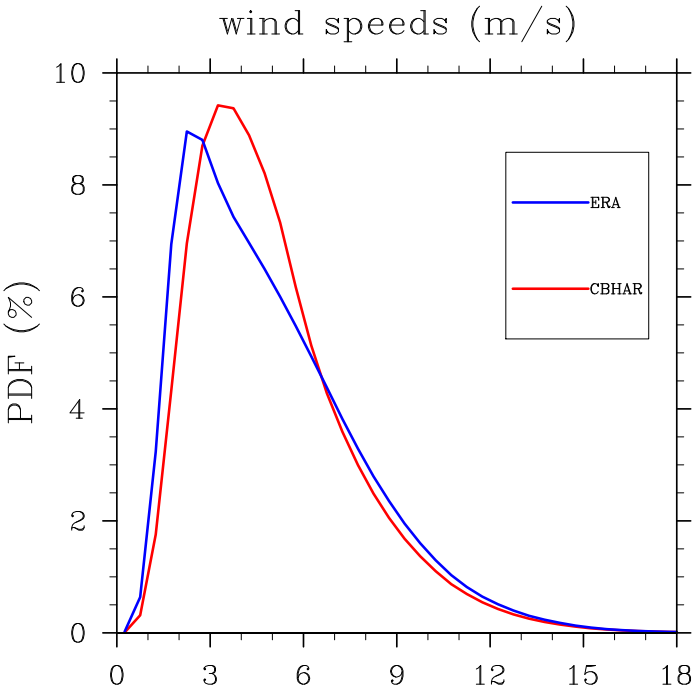

Figure 5.1.7. PDFs of surface wind speed for ERA-Interim (blue) and CBHAR (red)

It is also relevant to investigate possible diurnal signatures in the wind speed for each season. In this section, the wind speeds are divided into those over land and ocean points. This allows an analysis to be done to identify at which times of year diurnal signatures occur over the ocean as well as land. Figure 5.1.8 shows the hourly CBHAR wind speeds averaged over the study region for the 31-year period, separated into those over ocean (blue) and land (red). From late March through May, a clear diurnal signature exists over the ocean. This feature is significantly less pronounced, though still present, through mid-September, before disappearing for the remainder of the year. Over land, the diurnal signature begins in April and is clear until about mid-October. This diurnal signature agrees well with that seen by Stegall and Zhang (2012). However, the ocean wind speeds are much higher than the NARR wind speeds they observed. This agrees with the discussion of the differential wind speeds between CBHAR and NARR given above. Another reason for this discrepancy in the domain-averaged speeds is that the study region used by Stegall and Zhang (2012) extended from the Bering Strait north to about 76°N. The CBHAR domain, on the other hand, extends farther north, but more importantly it also includes most of the Bering Sea and a small piece of the North Pacific Ocean, which include some of the highest average wind speeds in the study area (Figures 5.1.2 and 5.1.4). In addition, the CBHAR ocean wind speeds are much higher than those over land, whereas Stegall and Zhang (2012) found that in NARR, the ocean and land wind speeds were much more similar. This difference between CBHAR and NARR might be due to the treatment of sea ice in the NARR model vs. that in CBHAR. Also, as the wind speeds in the Bering Sea/Pacific Ocean are some of the highest in the region, when they are included in the averages shown in Figure 5.1.8, the ocean wind speeds are increased relative to those over land. Figure 5.1.9 similarly shows the 31-year 6-hourly average wind speeds in ERA-I. As with CBHAR, the ocean wind speeds are significantly higher than those over land. However, during the months of March through May the diurnal variability is weaker than in CBHAR, most likely due in part to the effect of only having data four times per day vs. the hourly data available in CBHAR, causing ERA-I to miss the diurnal maxima and minima.

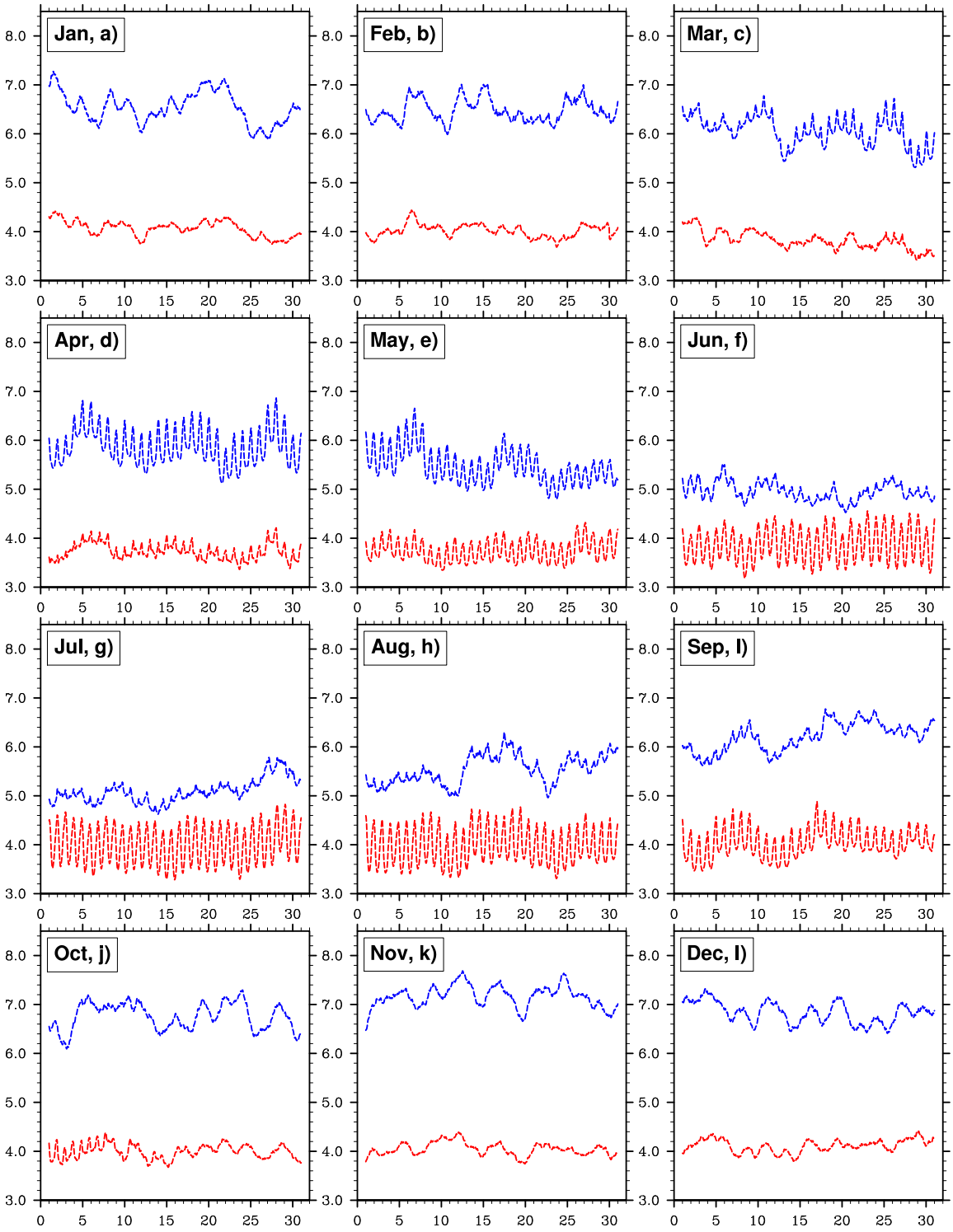

Figure 5.1.8. Hourly mean wind speed (m s^{-1}) over the ocean (blue) and land (red) in CBHAR, averaged over the study region for 1979–2009

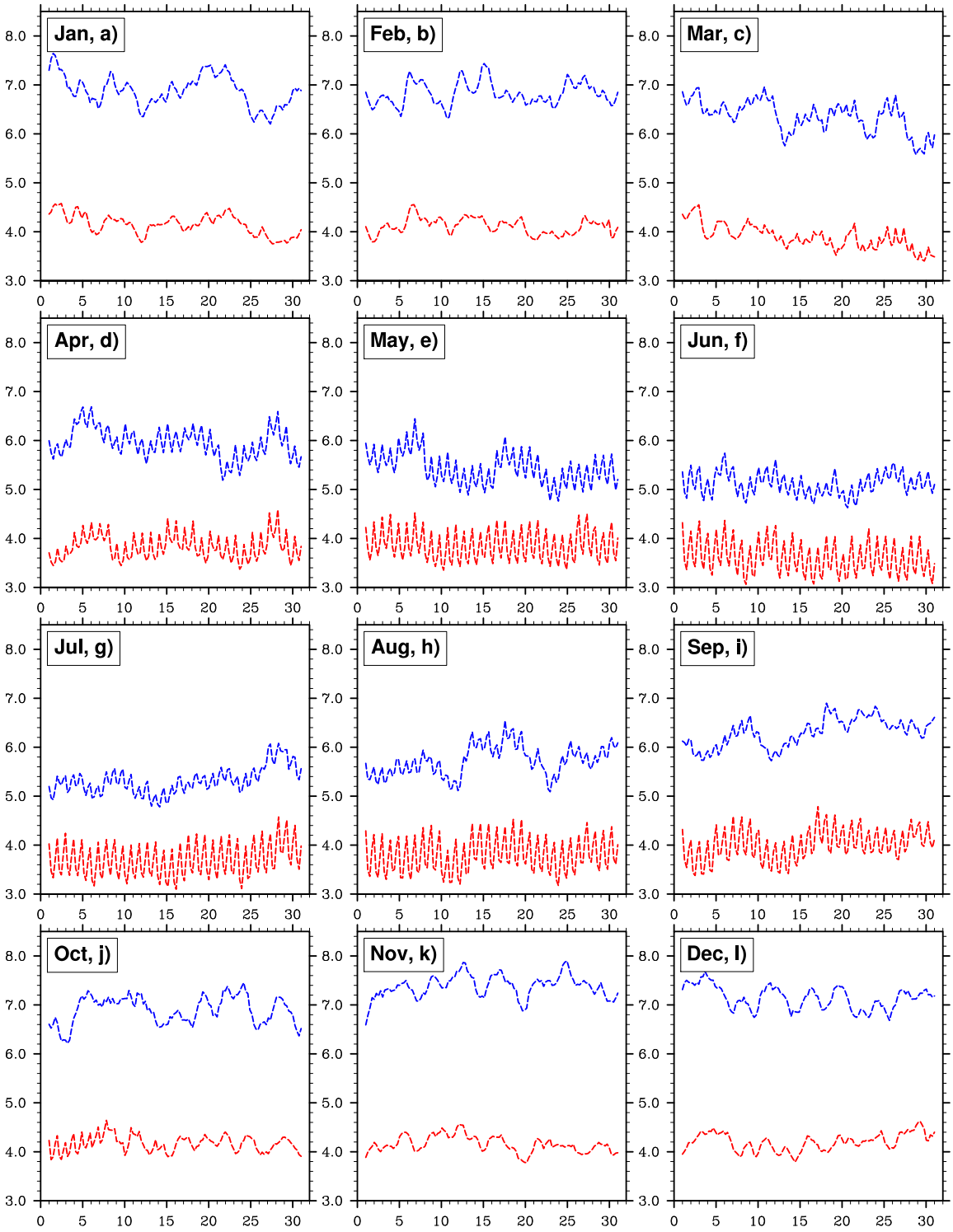

Figure 5.1.9. 6-hourly mean wind speed (m s^{-1}) over the ocean (blue) and land (red) in ERA-Interim, averaged over the study region for 1979–2009

5.1.3 Surface Wind Direction Climatology

To investigate the wind direction climatology, directions were first divided into quadrants, with 0–90° representing winds from the northeast (NE), 90–180° from the southeast (SE), 180–270° from the southwest (SW), and 270–360° from the northwest (NW). The monthly frequency of wind directions in each quadrant was then calculated for each month over the entire 31-year period. Figure 5.1.10 highlights the climatology of the northeast wind direction (0–90°) in CBHAR. Northeast winds clearly prevail for most of the year within the study area, a result of the dominant influence of the Beaufort High. In the months of June and July, the frequency of the northeast wind direction decreases, primarily due to a weakening of the Beaufort High during summer and the formation of a summer low in the Arctic. The frequency of NE wind in ERA-I (Figure 5.1.11) is similar to that in CBHAR, including its seasonality. However, similar to what was seen in the wind speed climatology, ERA-I does not capture the topographic features nearly as well as CBHAR. The differences in the NE wind frequency over the Brooks Range and eastern Siberia are most likely the result of mesoscale circulations, such as mountain/valley breezes and the mountain barrier effect.

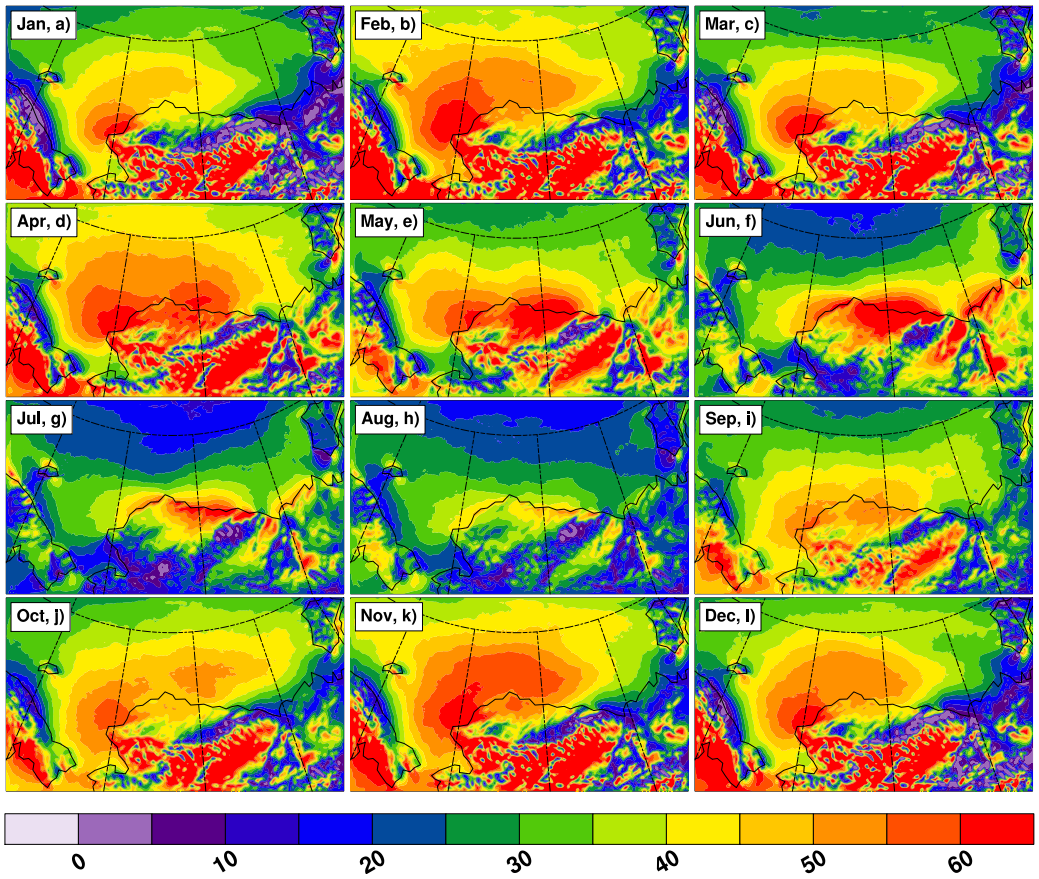

Figure 5.1.10. Monthly northeast wind direction (0–90°) frequency in CBHAR, expressed as a percentage (%)

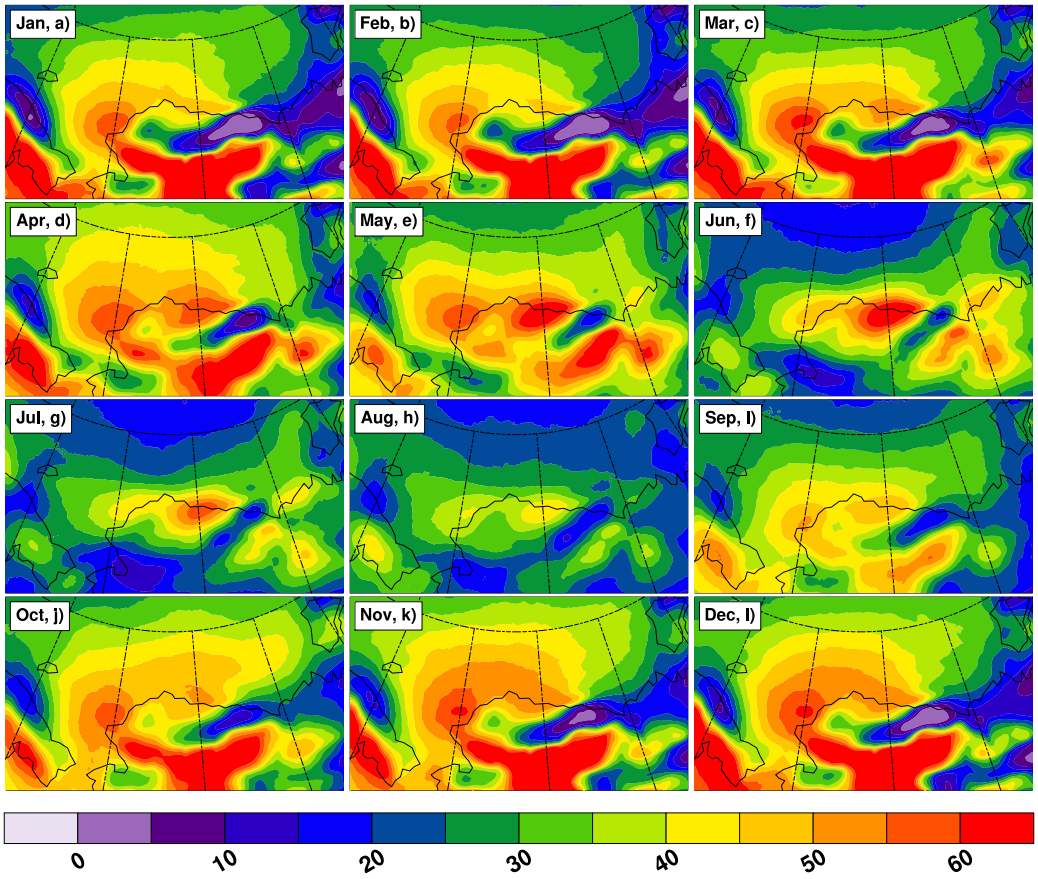

Figure 5.1.11. Monthly northeast wind direction (0–90°) frequency in ERA-Interim, expressed as a percentage (%)

Although the northeast wind dominates the study area, wind from other directions can also be influential. Thus, southwest and northwest winds in CBHAR, averaged over the cold season including the months of January–May and October–December, were also analyzed (Figure 5.1.12a,b). This analysis reveals the presence of a high percentage of southwest and northwest winds, particularly along the Brooks Range in Alaska and along the Chukotka Mountains in eastern Siberia. Some of the anomalous SW winds along the Brooks Range, particularly those around its eastern end near Canada, could be the result of cold-air damming against the mountain barrier. However, the SW winds near the ridgeline of the Brooks Range and along its western section could represent mountain downslope breezes that flow from the top of the range toward the Arctic Slope. In a similar way, the SW winds present on the northern slope of the Chukotka Mountains are also most likely due to the mountain breeze effect. The anomalous NW winds along the Chukotka Mountains are the result of the mountain barrier effect.

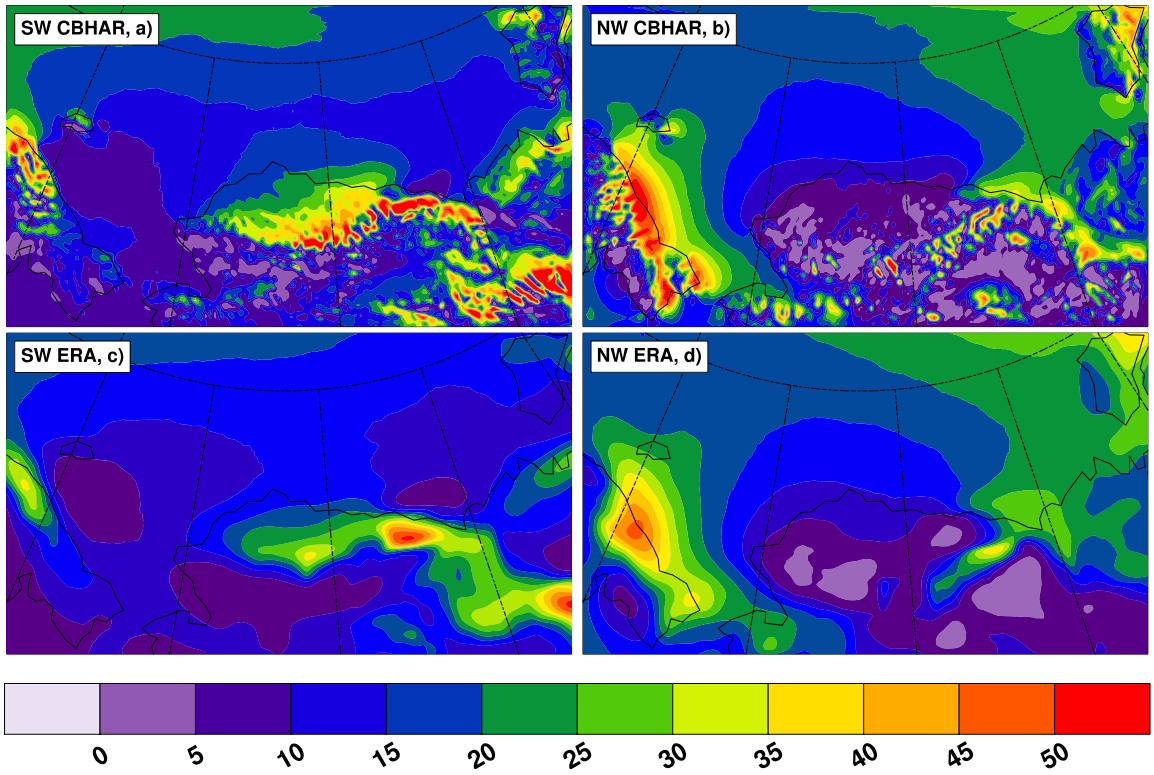

Figure 5.1.12. Frequency of southwest and northwest winds in CBHAR (a and b) and ERA-Interim (c and d), averaged over the cold months of January–May and October–December and expressed as a percentage (%)

A high frequency of northwest winds also occurs in the region around the Mackenzie River, including the Mackenzie Delta, in the northern Yukon. Small et al. (2011) also observed anomalous NW winds in this region. They conclude that these could be the result of NW surface winds overlain with NW 925 hPa geostrophic winds, and observed a strong correlation of surface winds with those from 1000 to 850 hPa, as well as a tendency towards lower stability, suggesting the mixing of momentum throughout the lower atmospheric column (1000 to 850 hPa). They also link this feature to synoptic SLP patterns, such as an anomalously strong high-pressure ridge over eastern Siberia and the Bering Sea, contributing to a pressure rise over the Brooks Range and cold-air damming that results in an alteration of the pressure gradient along the coast. The ERA-I data shown in Figure 5.1.12c,d also captures the anomalous features seen in CBHAR. However, the frequency (percentage) of these features is lower by about 10%. In addition, the detailed mesoscale features seen over the mountains in CBHAR are not present in ERA-I. Over the Mackenzie River valley and delta, the anomalous winds are present, but lower in frequency (25–30% vs. 35–45%) and much less prominent.

5.1.4 Variability and Changes in Surface Wind Speed and Direction

Based on the results of the above climatological analysis, the interannual variability and long-term changes in the CBHAR monthly surface wind speeds were further examined, with a simultaneous comparison made to ERA-Interim. Direct comparisons of monthly mean and 95th-percentile wind speeds between CBHAR and ERA-I are shown in Figures 5.1.13 and 5.1.14, respectively. Both figures show that the trends in CBHAR and ERA-I are nearly the same. Again, ERA-I wind speeds, particularly the 95th-percentile winds, are slightly higher than those in CBHAR, which is consistent with the findings in Section 5.1.2. The trends in CBHAR and ERA-I are nearly the same, and only the trend in October is significant at the 95% level using the t-test. Notable increasing trends of 0.27 m s^{-1} decade^{-1} and 0.26 m s^{-1} decade^{-1} exist for the October 95th-percentile winds in CBHAR and ERA-I, respectively.

Given their completely distinct geographic features, this interannual variability analysis was also performed over ocean and land areas separately, as shown for CBHAR in Figure 5.1.15. Generally, ocean surface wind speeds are larger than those on land due to the lower surface friction typically present over water surfaces. According to the time series shown in Figure 5.1.15, both ocean and land surface wind speeds exhibit interannual variability throughout the year, with the amplitude varying from month to month. Superimposed on this interannual variability lie varying rates of upward and downward trends. However, only the trends in August and October over the ocean, and September and November over land are significant at the 95% level using the t-test. A pronounced increasing trend of 0.26 m s^{-1} decade^{-1} exists over the ocean in October.

The interannual variability of extreme surface wind speeds was also examined separately over ocean and land areas for CBHAR as shown in Figure 5.1.16, exhibiting very similar features to those of the monthly mean winds, except for an obviously larger wind speed. A stronger increasing trend of 0.48 m s^{-1} decade^{-1} occurs in the extreme surface wind speed over the ocean in October. For comparison, Figures 5.1.17 and 5.1.18 show the wind speed trends over land and ocean for the ERA-I data. The trends are very similar to those in CBHAR, although the 95th-percentile wind speeds are higher, especially in November. Figure 5.1.19 displays the frequency of extreme winds, defined as the percentage of winds occurring above the 95th-percentile wind speeds for both CBHAR and ERA-I. Both datasets show very similar results. Clearly, the trends in Figure 5.1.19 are similar to the trends seen in the previous figures, with October showing the largest overall increasing trend. This agrees with the findings of Stegall and Zhang (2012), except that they also found relatively strong positive trends in other months, such as September, November, and December, in the NARR reanalysis.

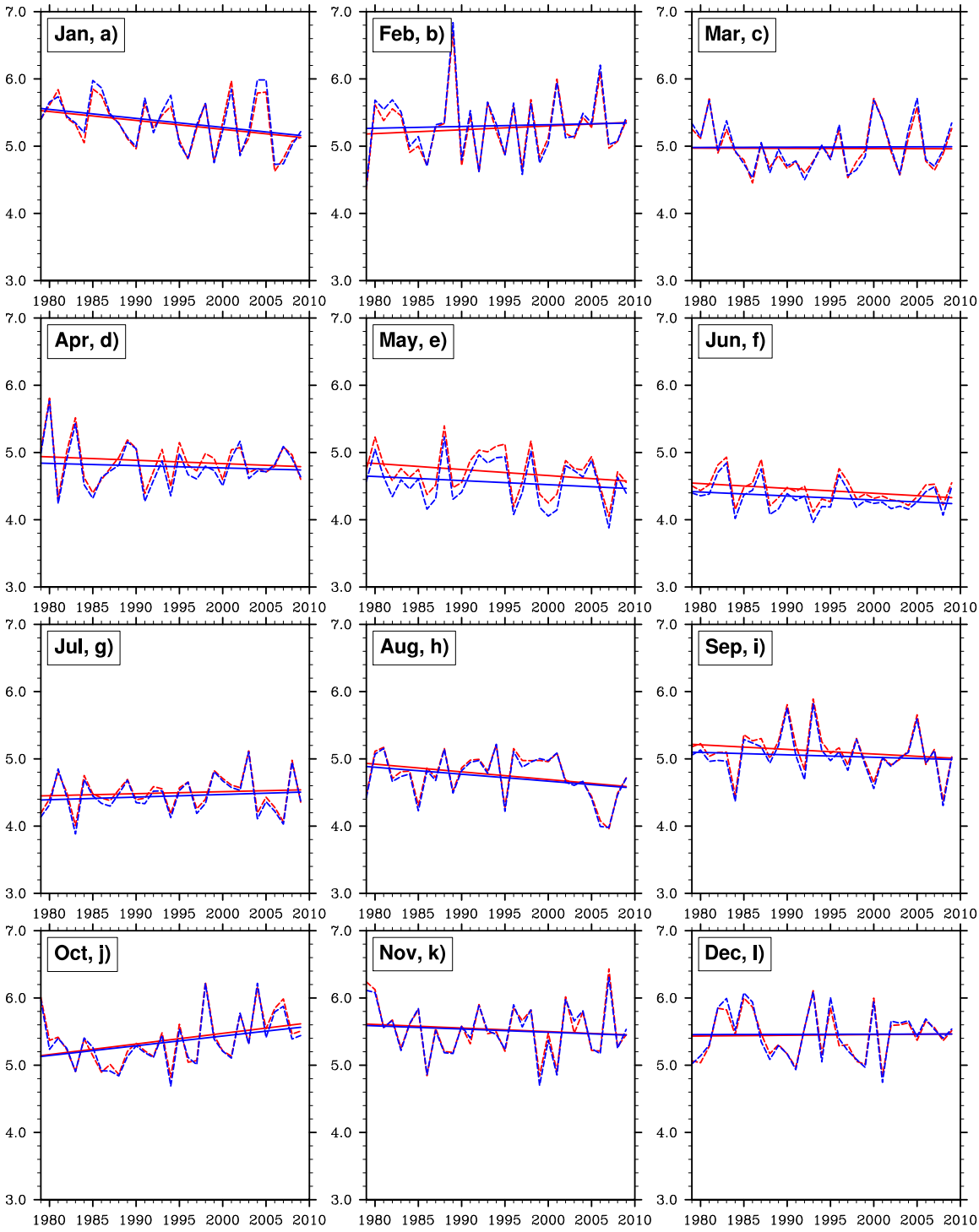

Figure 5.1.13. Monthly mean surface wind speed (m s^{-1}) and its linear trends for 1979–2009 in CBHAR (red) and ERA-Interim (blue)

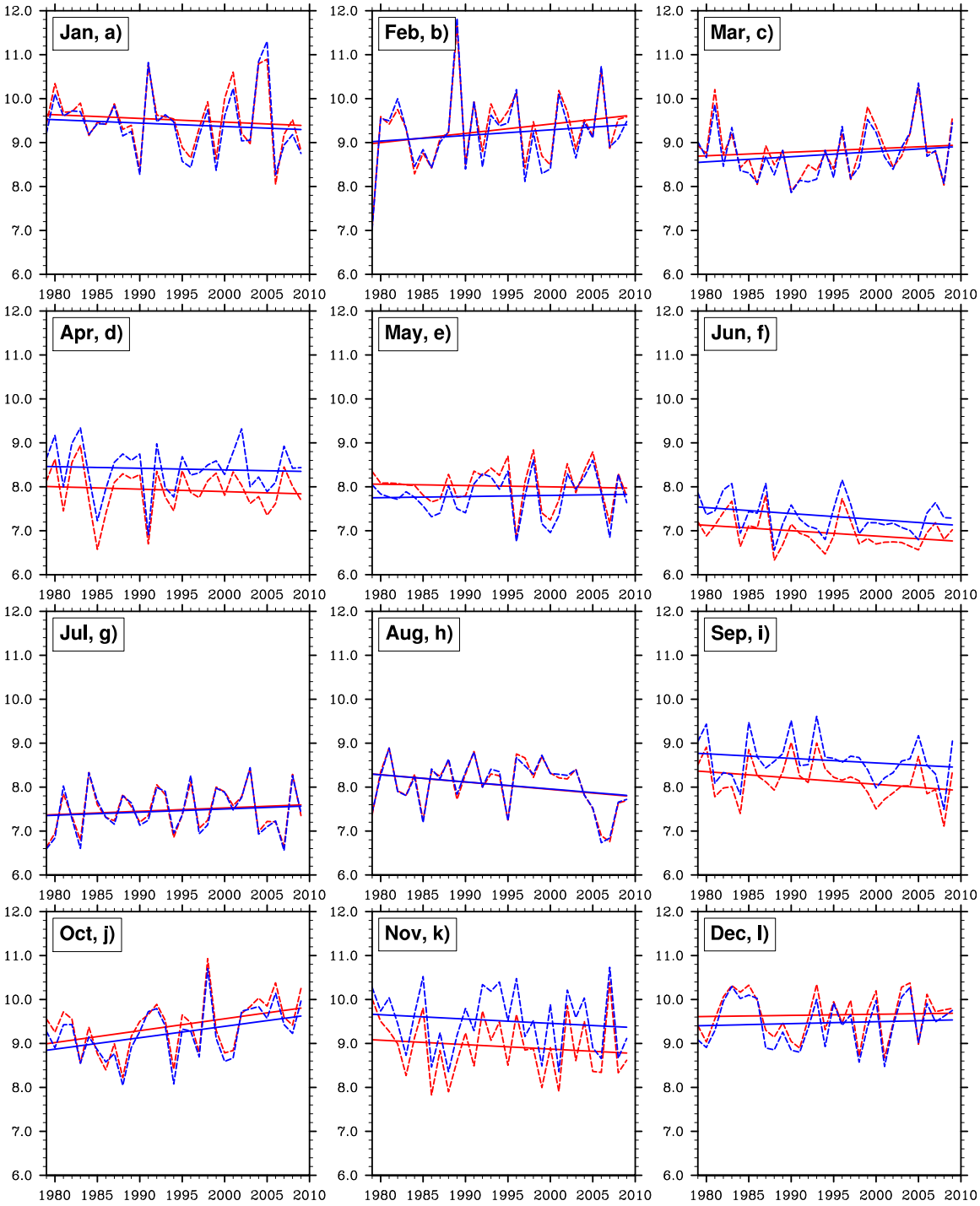

Figure 5.1.14. Monthly mean 95th-percentile wind speed (m s^{-1}) and its linear trends for 1979–2009 in CBHAR (red) and ERA-Interim (blue)

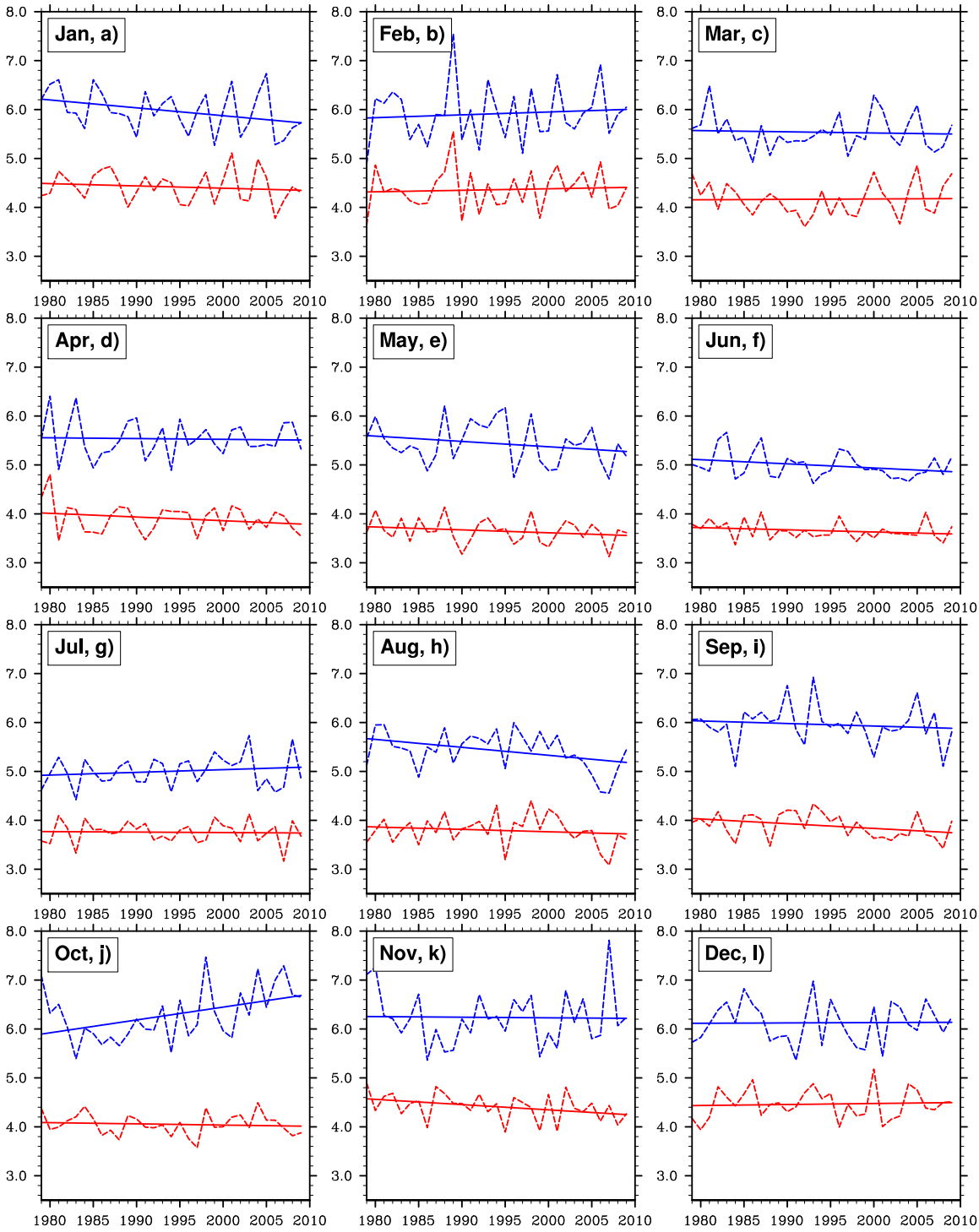

Figure 5.1.15. Monthly mean surface wind speed (m s^{-1}) and its linear trends for 1979–2009 over ocean (blue) and land (red) in CBHAR

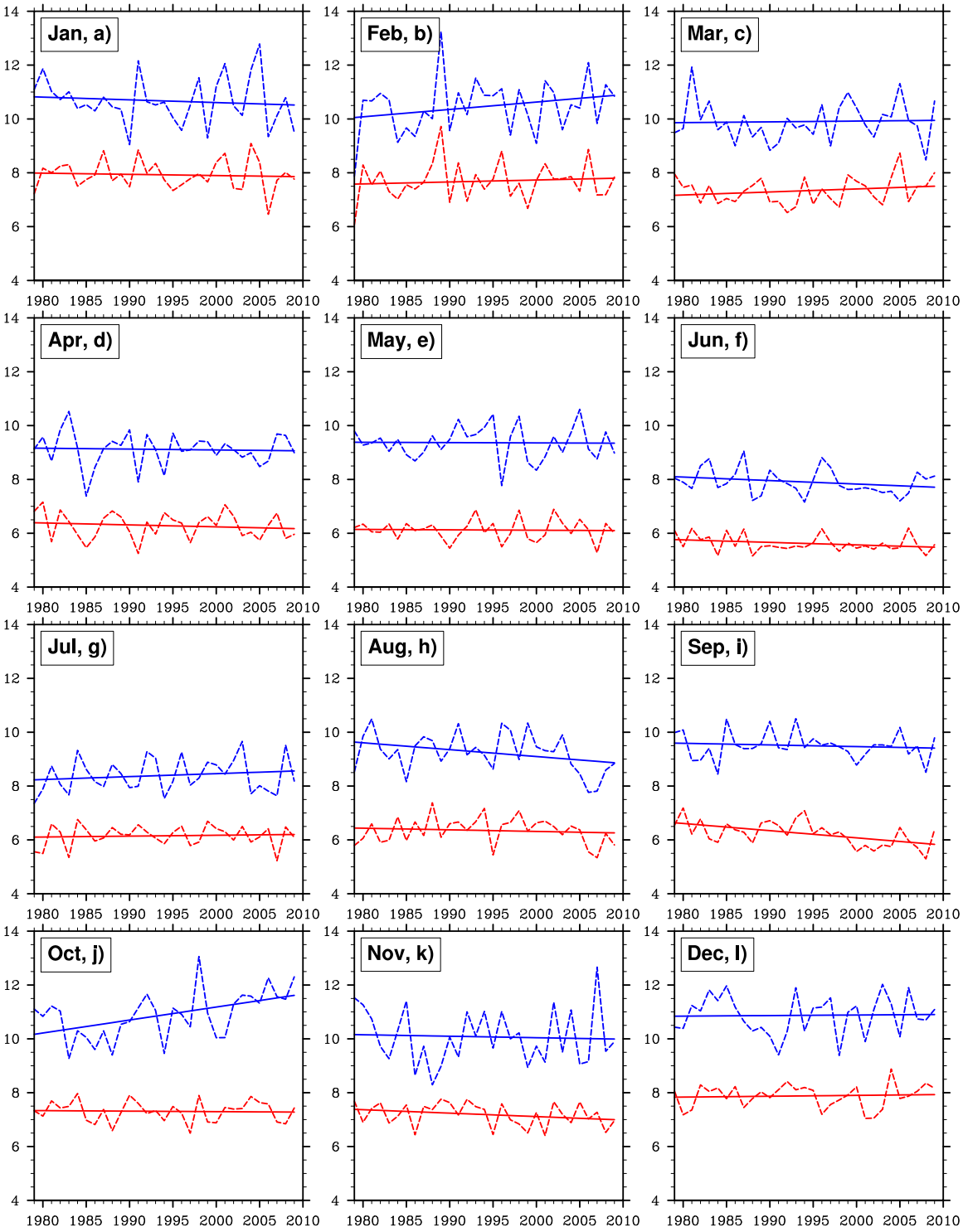

Figure 5.1.16. Monthly mean 95th-percentile wind speed (m s^{-1}) and its linear trends for 1979–2009 over ocean (blue) and land (red) in CBHAR

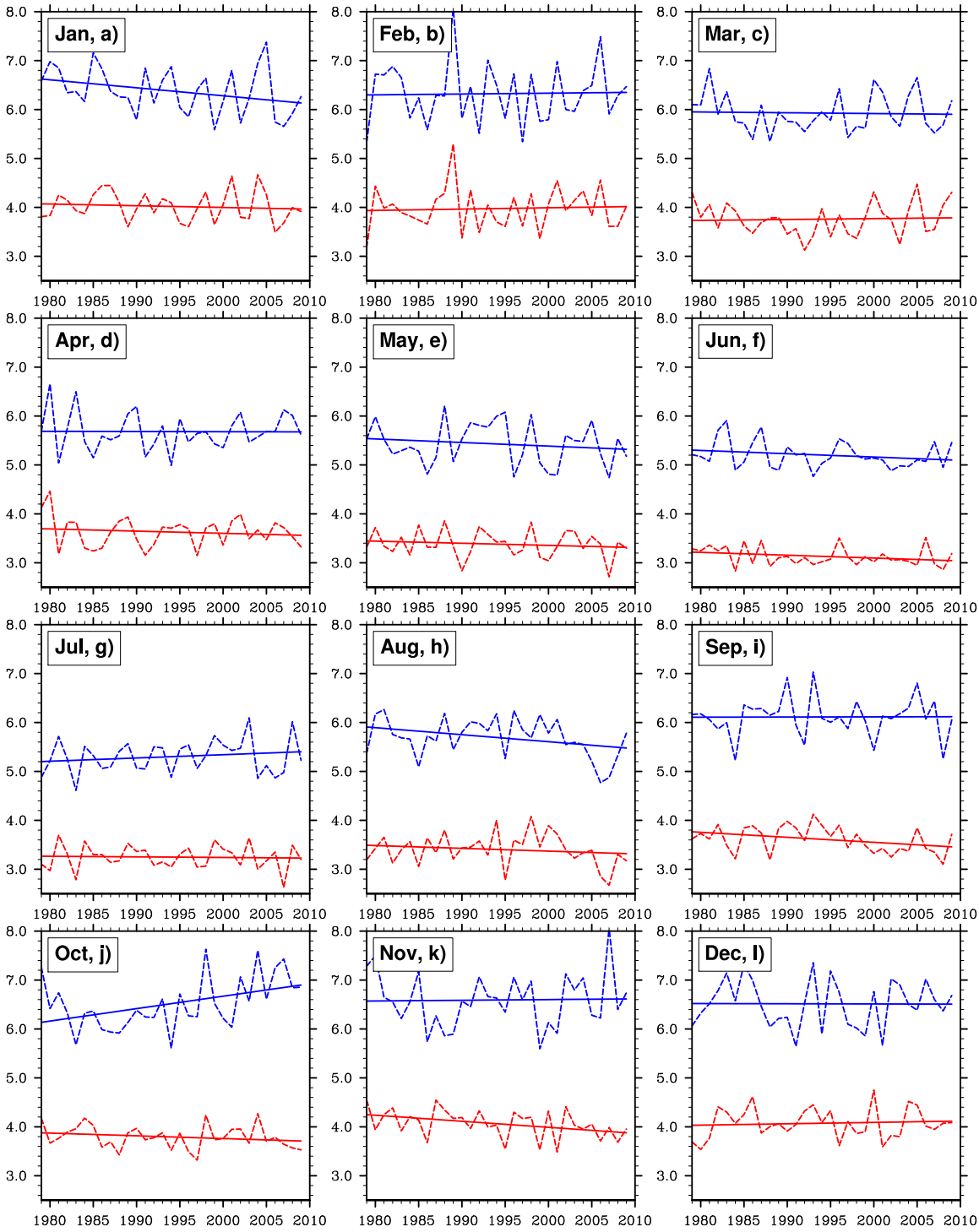

Figure 5.1.17. Monthly mean surface wind speed (m s^{-1}) and its linear trends for 1979–2009 over ocean (blue) and land (red) in ERA-Interim

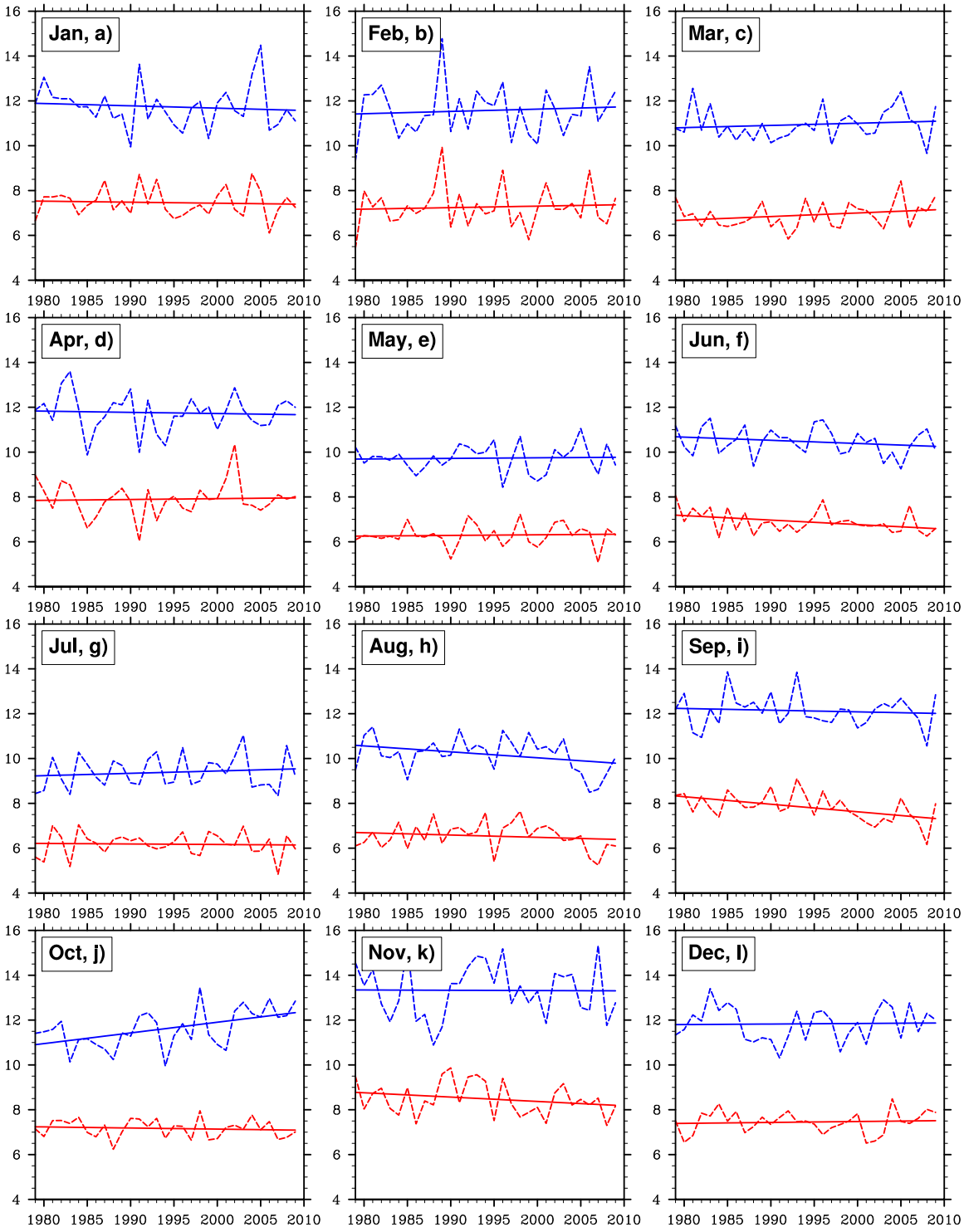

Figure 5.1.18. Monthly mean 95th-percentile wind speed (m s^{-1}) and its linear trends for 1979–2009 over ocean (blue) and land (red) in ERA-Interim

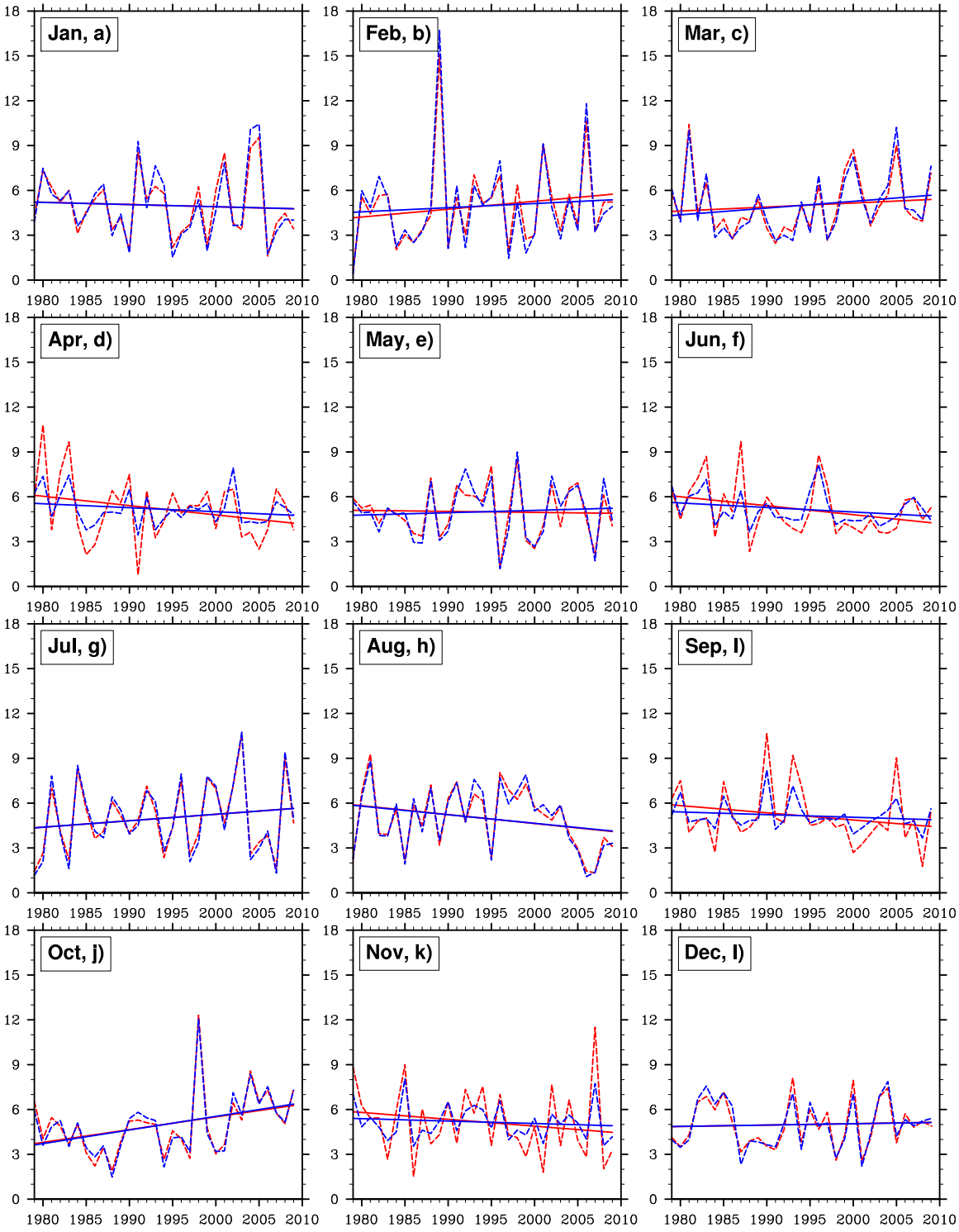

Figure 5.1.19. Frequency of extreme winds, defined as the percentage (%) of winds above the 95th-percentile wind speed, for 1979–2009 in CBHAR (red) and ERA-interim (blue)

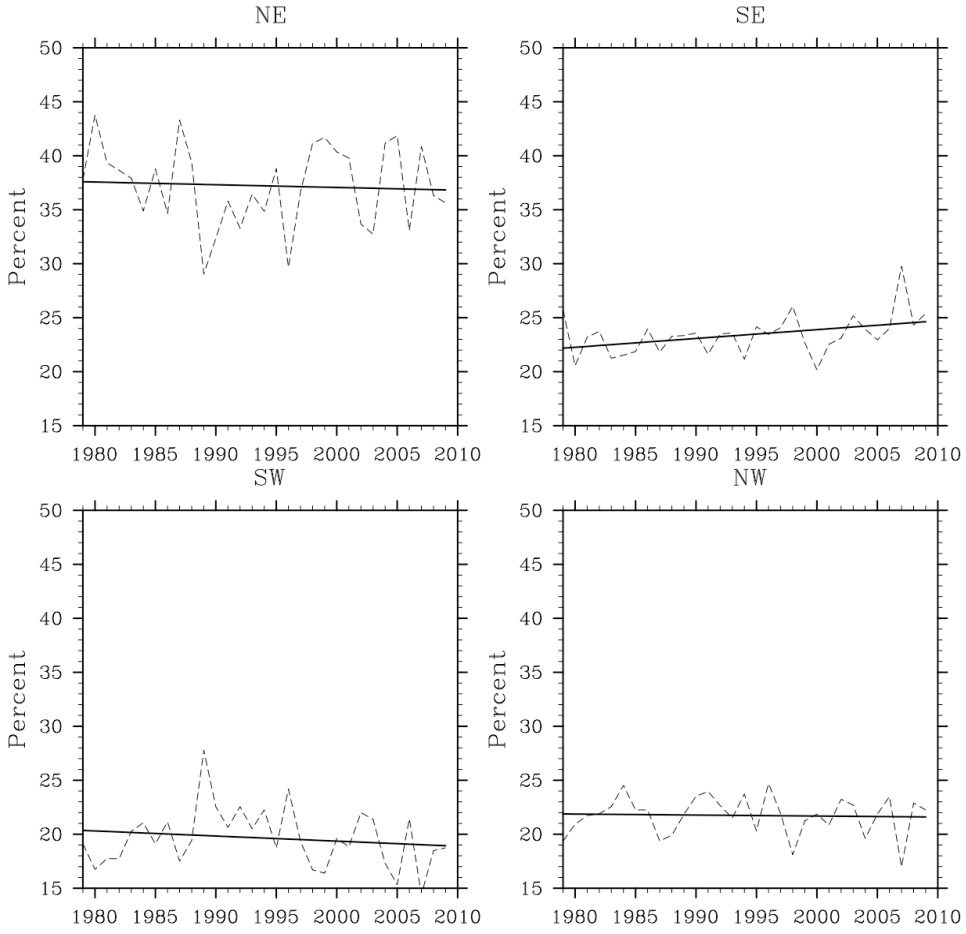

Figure 5.1.20. Frequency of surface wind directions (degrees), grouped by quadrant, for 1979–2009 in CBHAR

This analysis was extended to include wind direction by computing the frequency of winds originating from each quadrant and evaluating their interannual variability and long-term changes (Figure 5.1.20). The frequency of the wind from the northeast, northwest, and southwest directions exhibits year-to-year fluctuations, with just a slight decreasing trend. However, the frequency of the wind from the southeast has experienced a marked increase over time. Determining the reason for this increase requires further investigation into the impact of weather systems on wind direction in the region.

To further explore the geographic variability of the region, the ocean surface wind data was split into two distinct regions, the Chukchi Sea and the Beaufort Sea, separated by the 203°E meridian that passes through Point Barrow, Alaska (Figure 5.1.21). In this way the trends specific to each region can be explored separately. Figures 5.1.22 and 5.1.23 show the trends of wind speed and 95th-percentile wind speed, respectively, for each of the two zones. It is immediately apparent that the Chukchi Sea wind speeds are, on average, higher than the Beaufort Sea wind speeds for each month. Reasons for this difference could be the presence of greater storm activity over the Chukchi and/or stronger storms that first pass over the Chukchi Sea before weakening as they move over

the Beaufort. Consistent with the trend analysis discussed above, October shows the largest increase in wind speeds, with the two regions displaying similar increasing trends for this month. As with the mean wind speeds, the Chukchi Sea 95th-percentile wind speeds are consistently higher than those over the Beaufort, and October again shows the largest increasing trend. However, in this case, the Beaufort Sea winds are increasing at a faster rate than the Chukchi winds for October. Another difference between the two regions is that the Chukchi winds are increasing more in February than those over the Beaufort for both mean and 95th-percentile wind speeds. This increase in the Chukchi Sea wind speeds is also present in March and could be a result of either increased storm frequency or intensity, and may be a worthwhile topic for future exploration.

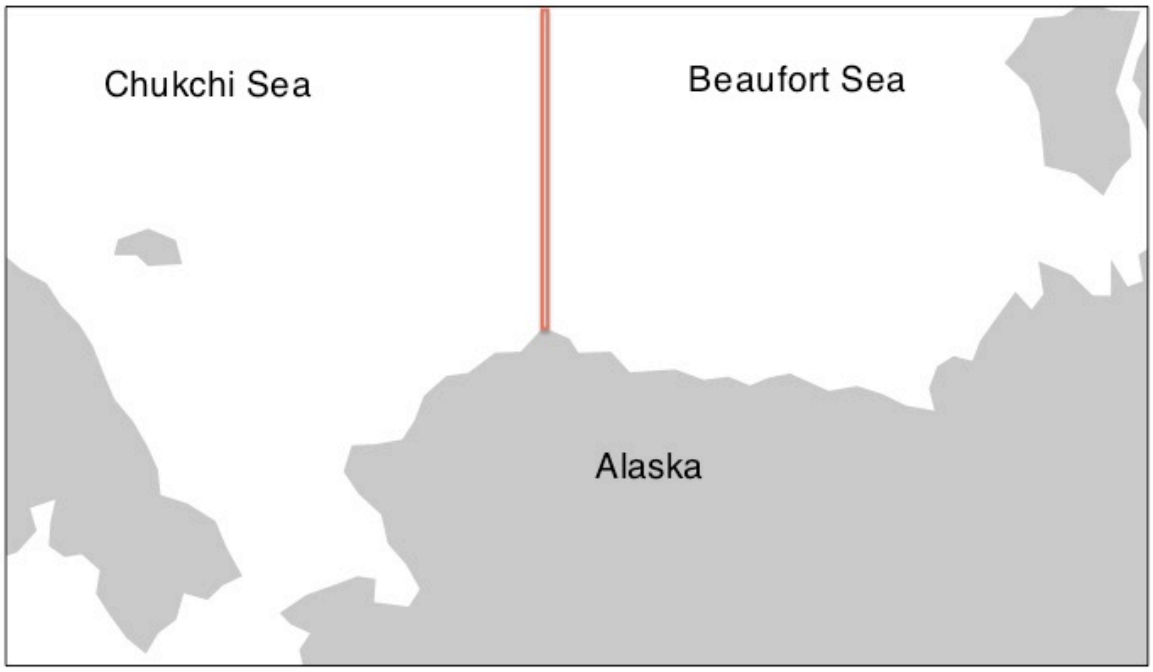

Figure 5.1.21. Illustration of the Chukchi and Beaufort Sea regions as defined here for climatological analysis of winds. The two regions are separated by the 203°E meridian extending north from Point Barrow, Alaska.

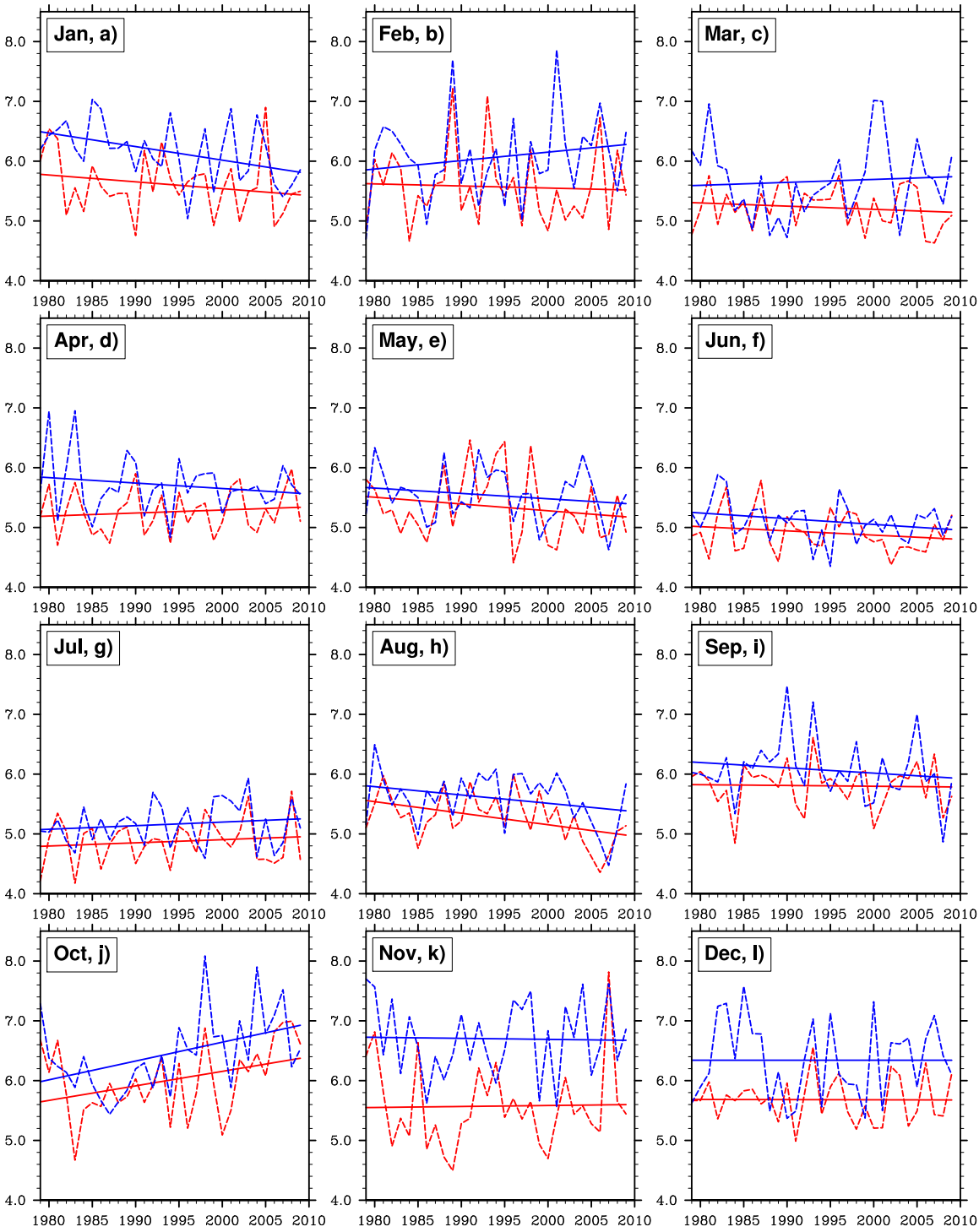

Figure 5.1.22. Monthly mean surface wind speed (m s^{-1}) and its linear trends for 1979–2009 over the Chukchi Sea (blue) and Beaufort Sea (red) in CBHAR. All data are for ocean points only.

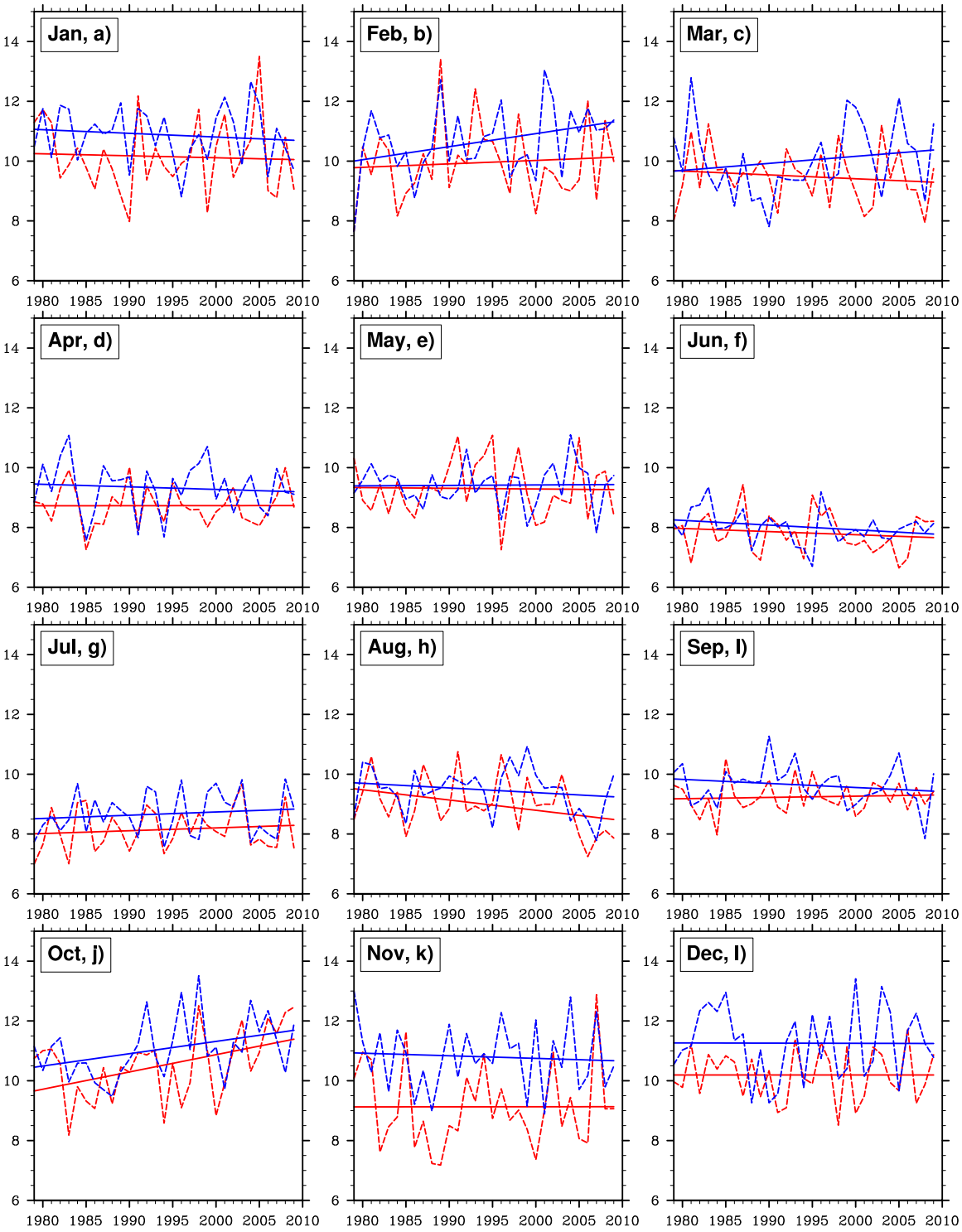

Figure 5.1.23. Monthly 95th-percentile wind speed (m s^{-1}) and its linear trends for 1979–2009 over the Chukchi Sea (blue) and Beaufort Sea (red) in CBHAR. All data are for ocean points only.

5.1.5 Spatial Structure of Changes in Surface Wind

While the domain-averaged surface wind speed demonstrates a particular long-term trend, such changes may vary dramatically at different locations in the study area. To investigate the geographic distribution of surface wind changes, their linear trends were computed at each grid point in CBHAR (Figure 5.1.24). The results indicate that the largest decrease in monthly mean wind speed has occurred over the northern Chukchi–Beaufort Sea in January, with the minimum centered near the boundary of the two seas, well north of the Bering Strait. There is at the same time, however, a noticeable increase in wind speeds near the boundary of the Chukchi and Bering Seas in January. A notable decrease also appears over ocean areas in May and August, located primarily over the Beaufort Sea and the Canada Basin. By contrast, the largest increase in monthly surface wind speed has occurred over the entirety of the Chukchi and Beaufort Seas in October. In Stegall and Zhang (2012), a similar finding was reported, and they showed a high negative correlation between sea ice retreat and higher wind speeds, i.e., less sea ice is correlated with stronger winds.

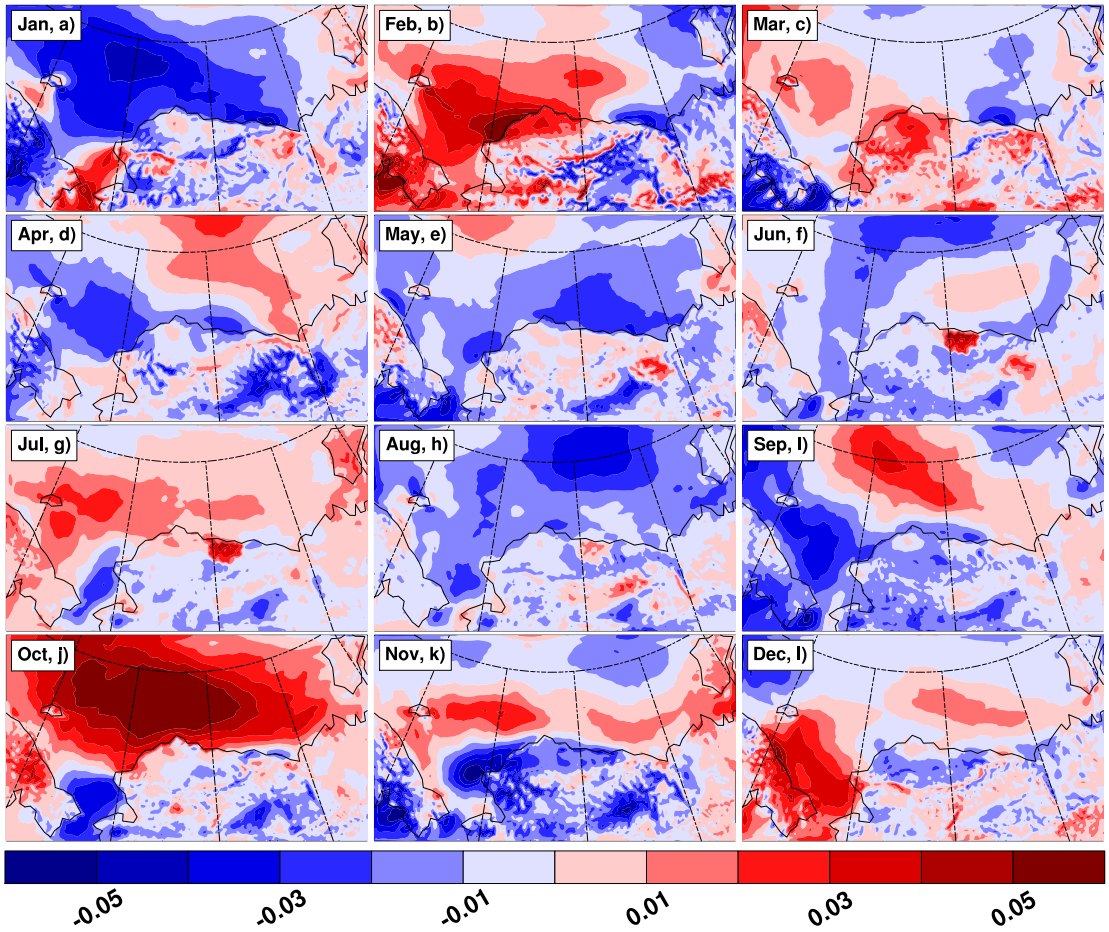

Figure 5.1.24. Linear trends in the monthly mean surface wind speed (m s^{-1} yr^{-1}) at each grid point in CBHAR. Positive values indicate an increase and negative values a decrease over the 31-year period.

A similar analysis for the 95th-percentile wind speeds (Figure 5.1.25) shows some differences from the monthly-mean analysis, even though the domain-averaged features are shown to be quite similar. Unlike the monthly means, increasing trends dominate throughout the year and the decreasing trend in January is confined to a much smaller area. Increasing trends occur over nearly the entire ocean surface in February, March, May, July, and October. As with the monthly-mean analysis, the largest trend emerges in October, with a maximum increase over the Beaufort Sea.

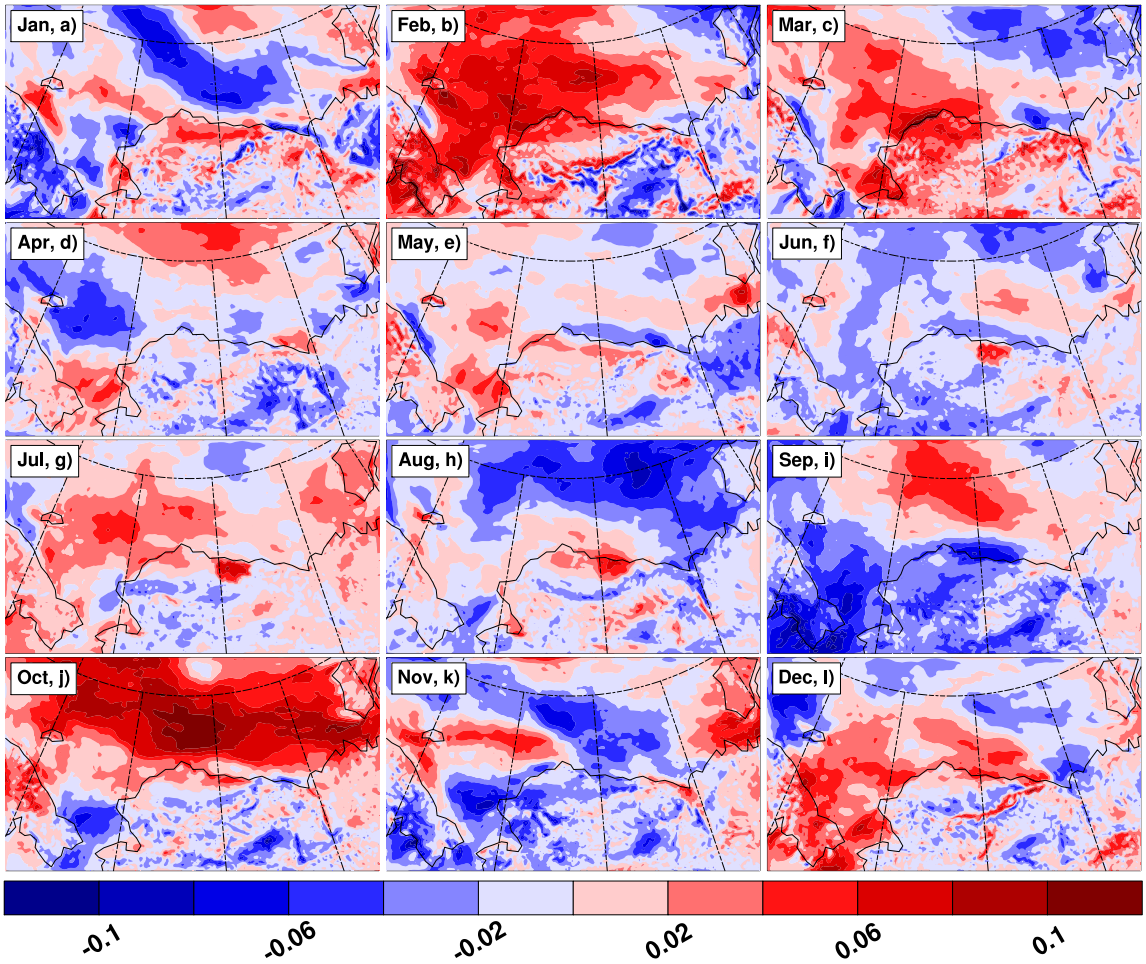

Figure 5.1.25. Linear trends in the monthly 95th-percentile surface wind speed (m s^{-1} yr^{-1}) at each grid point in CBHAR. Positive values indicate an increase over the 1979–2009 period, and negative values a decrease.

5.1.6 Trends in Sea Ice, 2-m Air Temperature, and SST

The wind field climatology (Section 5.1.2) has shown that the highest wind speeds in the study region occur during the autumn, particularly in October. This generally coincides with the time of year of the sea ice minimum and, consequently, the maximum amount of open ocean. Stegall and Zhang (2012) found that there is a high correlation between sea ice extent and wind speed. A detailed description of the sea ice concentration/extent

present in CBHAR is therefore important. It is also important to investigate the sea ice trends given that the Chukchi/Beaufort Seas region is an area that has seen dramatic sea ice loss, particularly over the last decade or so (Jahn et al. 2012).

In this section, the trends in sea ice, 2-m air temperature, and SST are analyzed for the months of July through October, when sea ice extent exhibits large fluctuations (Figure 5.1.26). The decreasing trends in ice extent shown for the study region from July through October are significant at the 95% confidence level using the t-test. The largest decreasing trend (~0.3×10^5 km^2 yr^{-1}) occurs in September, the month associated with the annual sea ice minimum. A record low extent over the entire Arctic occurred in September 2007; however, for the study region, the minimum extent occurred in September 2008. August and October also exhibit dramatic decreases in sea ice extent (~0.2×10^5 km^2 yr^{-1}). Accompanying the strong decreasing trends in sea ice during September and October, both 2-m air temperature and SST show significant increasing trends.

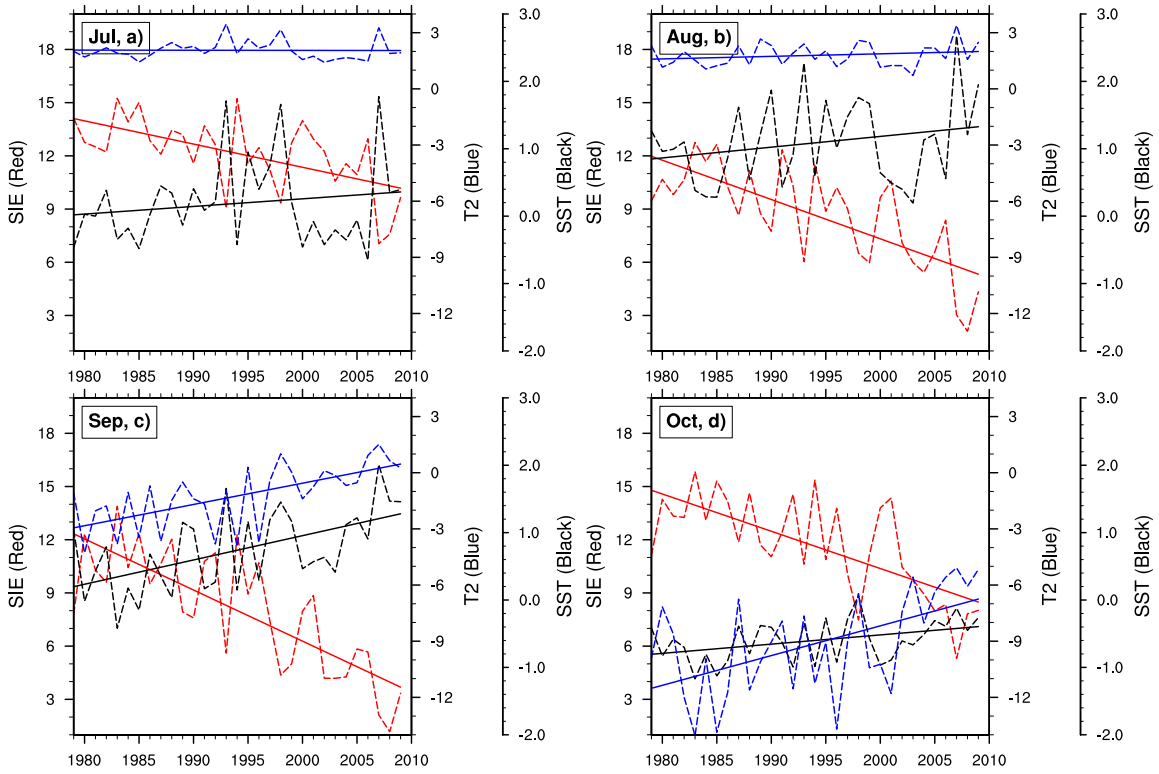

Figure 5.1.26. Monthly means and linear trends of sea ice extent (SIE, ×10^5 km^2) in red, 2-m air temperature (ocean only, °C) in blue, and SST (°C) in black for 1979–2009 in CBHAR

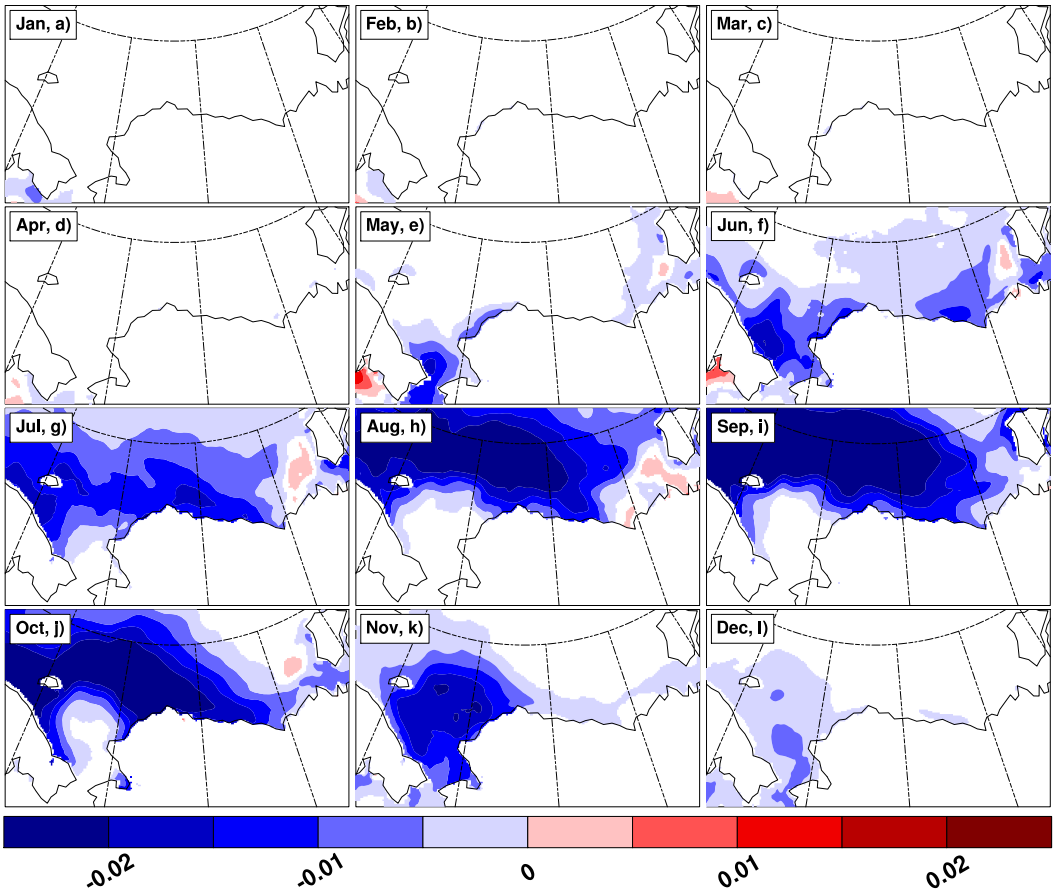

Figure 5.1.27. Linear trend of sea ice concentration (% yr^{-1}) for all months from 1979–2009 in CBHAR. Shaded colors are significant at the 95% confidence level. Positive values indicate an increase over the 1979–2009 period, and negative values a decrease.

Figure 5.1.27 shows the linear trends in sea ice concentration (% yr^{-1}) for all months; shaded colors are significant at the 95% level. The figure clearly shows that a substantial portion of the domain has experienced significant sea ice loss for July through October. For September and October most of the Chukchi/Beaufort Seas region displays a decrease in sea ice concentration. Overall, for the autumn as a whole, the study domain exhibits a negative regression in sea ice concentration, which is consistent with larger-scale trends as well as observations.

As with the wind speed analysis, the trends in sea ice extent are divided into Chukchi Sea and Beaufort Sea regions to investigate if differences exist in the trends between the two seas. Figure 5.1.28 shows these trends for July through October. Clearly, the Chukchi Sea has a larger decreasing trend than does the Beaufort for each of the four months, particularly in September and October. In September of 2007 and 2008 CBHAR shows nearly 0 km^2 in ice extent in the Chukchi, indicative of the record sea ice loss for those years. Lindsay and Zhang (2005) reported that this region is experiencing some of the

greatest sea ice thinning of anywhere in the world, along with rising 2-m air temperatures in the autumn. This supports the dramatic sea ice loss shown in the figures here.

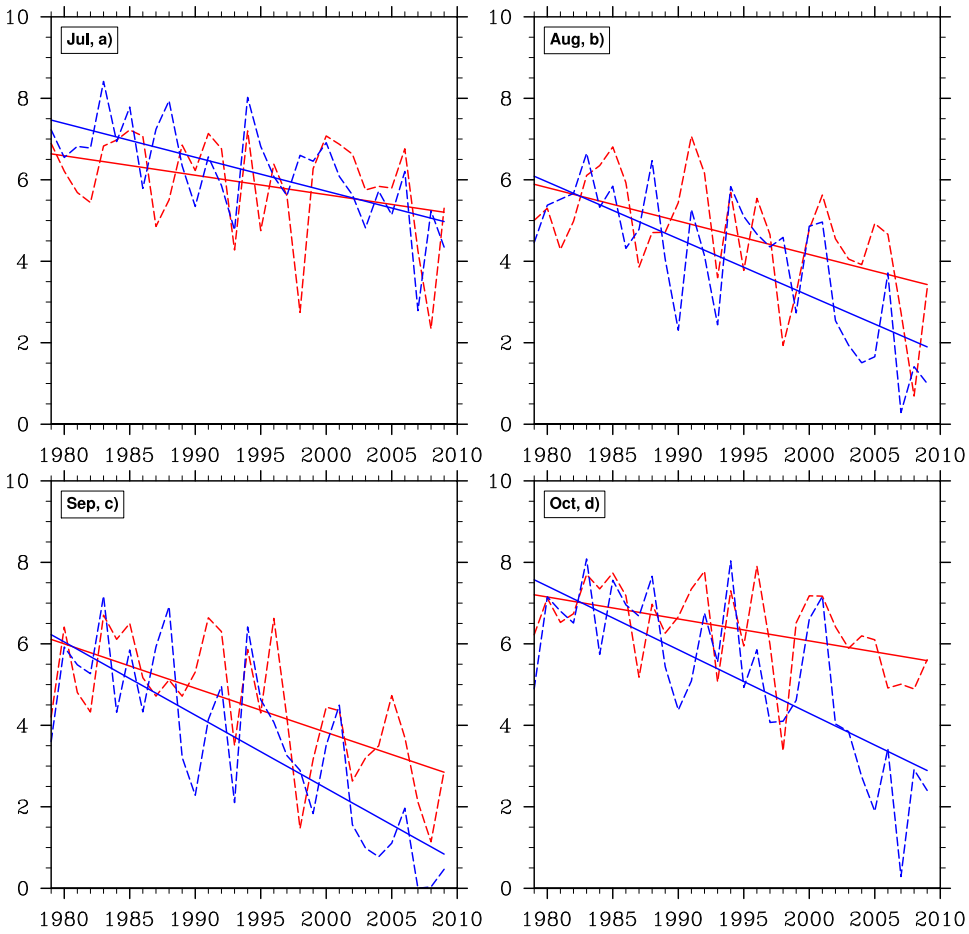

Figure 5.1.28. Monthly sea ice extent (SIE, $\times 10^5$ km^2) and its linear trends for 1979–2009 in the Chukchi Sea (blue) and Beaufort Sea (red) in CBHAR

The area-averaged 2-m air temperatures in CBHAR over ocean and land demonstrate various interannual variability and long-term trends during 1979–2009 (Figure 5.1.29). Clearly, September and October show large increases in temperature, with the greatest increase over the ocean in October. This agrees with the observed temperature increase as well as other studies showing similar results. Figure 5.1.30 displays the 2-m air temperature linear trend (°C yr^{-1}) at each grid point in CBHAR for all months of the year. Colors shown are significant at the 95% confidence level. The most obvious feature is the large area of increasing temperatures in the Chukchi–Beaufort Seas from September through December. The summer months (May–August) show little trend over most of the region. Figure 5.1.31 shows the area-averaged 2-m air temperature trends over the Chukchi and Beaufort Sea regions separately, for September through December. Overall, the Chukchi Sea shows a larger increase in temperature than does the Beaufort. Each of the Figures 5.1.29–5.1.31 indicates the presence of much warmer air in the latter part of the 31-year study period. This warmer air is one potential cause for the substantial sea ice

loss in the region. The larger increase in temperature in the Chukchi Sea should and does indicate a larger decrease in sea ice extent in that region relative to the Beaufort Sea.

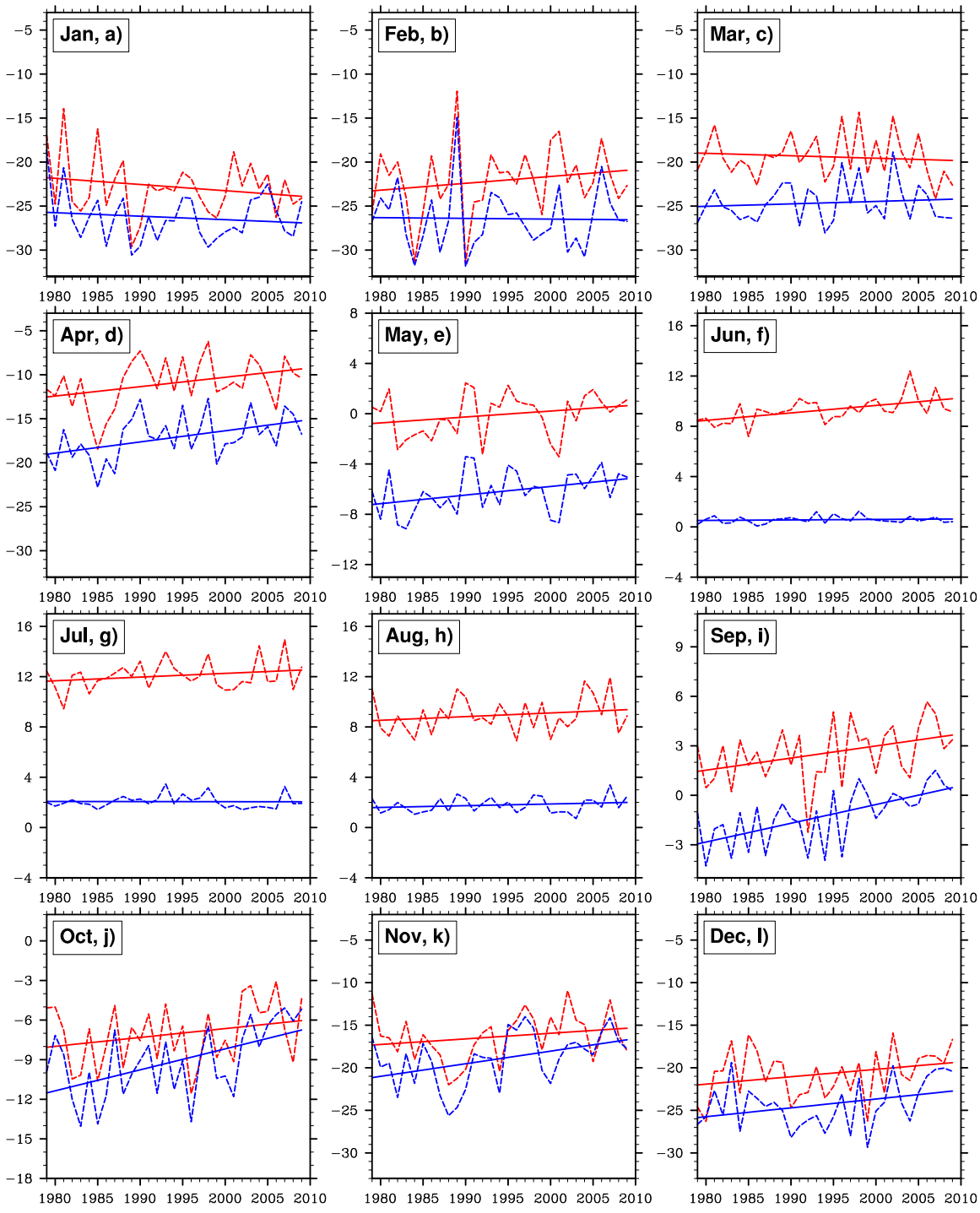

Figure 5.1.29. Monthly 2-m air temperature (°C) and its trends for 1979–2009 over ocean (blue) and land (red) in CBHAR

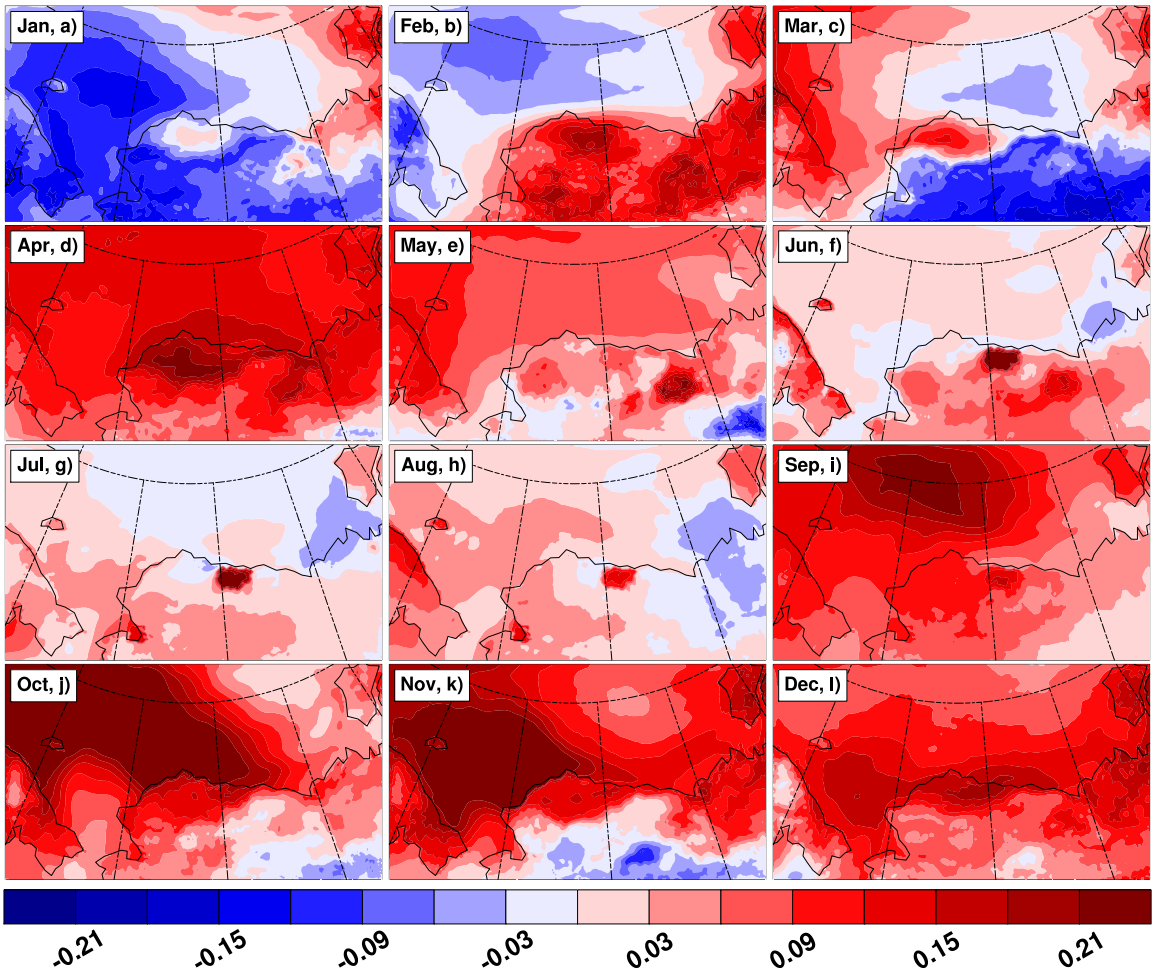

Figure 5.1.30. Linear trend of 2-m air temperature (°C yr^{-1}) for all months from 1979–2009 in CBHAR. Shaded colors are significant at the 95% confidence level. Positive values indicate an increase over the 1979–2009 period, and negative values a decrease.

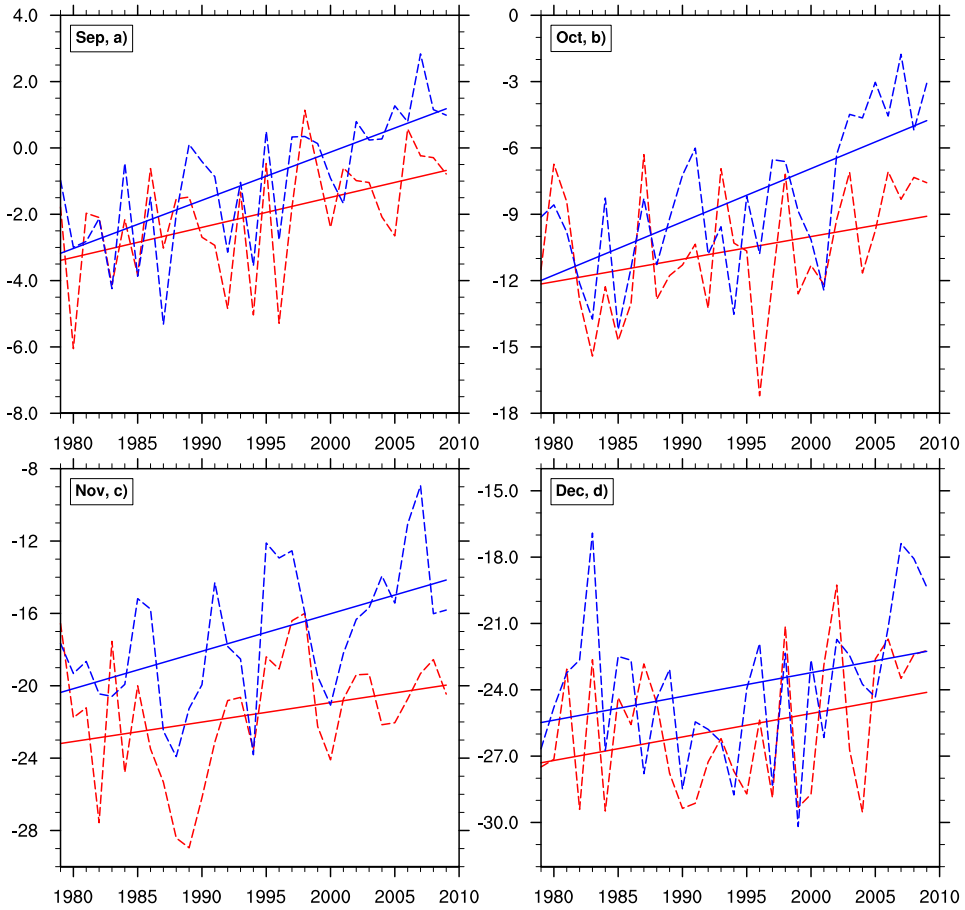

Figure 5.1.31. Monthly mean 2-m air temperature (°C) and its trends from 1979–2009 over the Chukchi Sea (blue) and Beaufort Sea (red) in CBHAR

Another important variable to analyze is the SST in areas of open, ice-free ocean. Warmer SST may contribute to sea ice loss through redistribution and mixing by ocean dynamic processes. Figure 5.1.26 above shows the long-term SST trend for the months of July through October. The largest increasing trend occurs in September, while the other three months show weaker, but still positive, trends as well. Figure 5.1.32 shows the SST linear trends at each of the ocean grid points in CBHAR. Clearly, SSTs have increased over most the study region, with the broadest area of increase occurring in September. Although there are large areas of increasing SSTs in July, August, and October, the areas of warming are not as large as the maximum area present in September. One very noticeable feature of the trends is the decreasing SST in the southeastern Beaufort Sea and off the coast of Canada. This could be related to the outflow of fresh water from the Mackenzie River/Delta and may be worth further research. Figure 5.1.33 displays the separate SST trends for the Chukchi and Beaufort Sea partitions, as was done above for the wind speed and air temperature analyses. Clearly, the Chukchi Sea experiences a much larger increasing trend for all four months, with the largest in September. The Beaufort Sea, on the other hand, only shows an increasing trend in September, with no significant trend in the other months, except for a slight decrease in July.

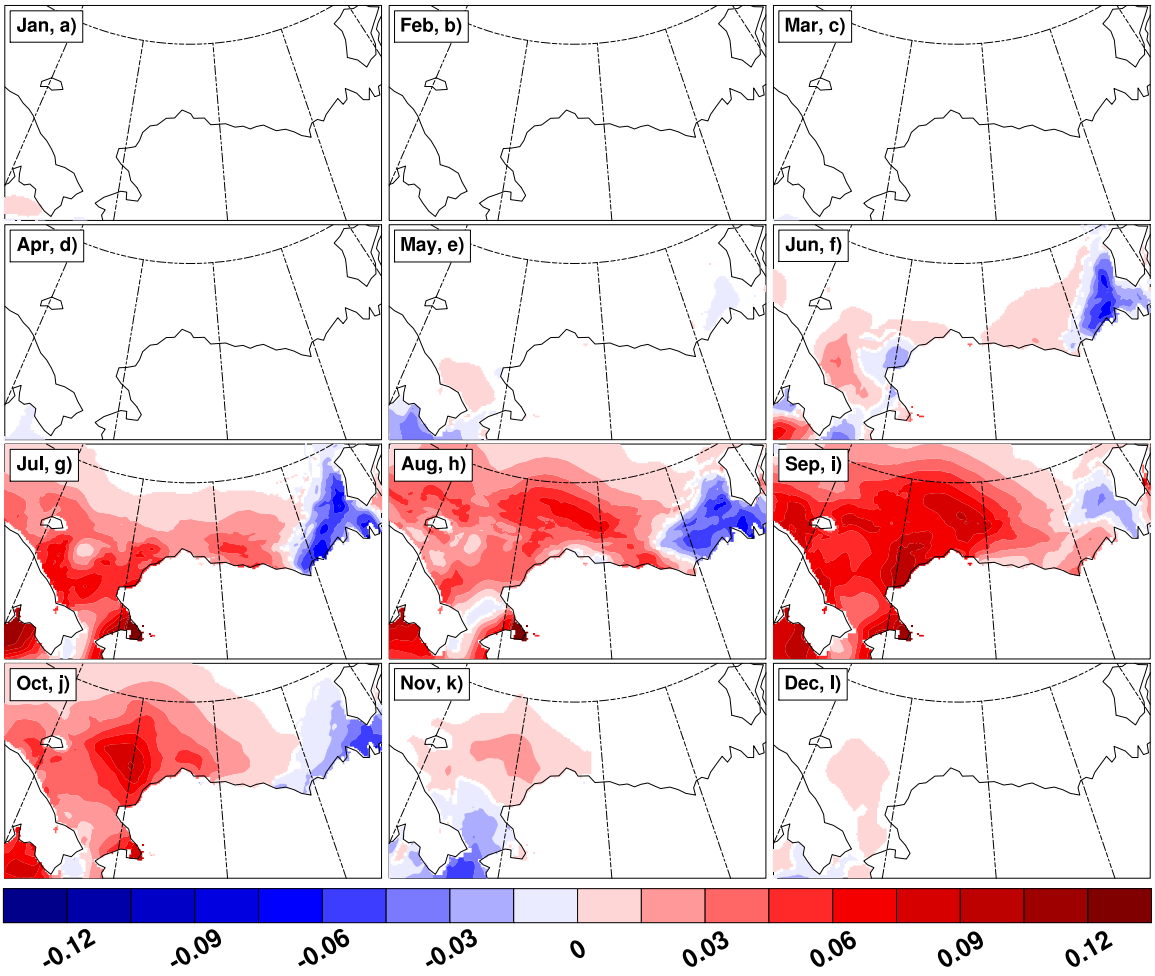

Figure 5.1.32. Linear SST trends (°C yr^{-1}) for 1979–2009 in CBHAR. Shaded colors are significant at the 95% confidence level. Positive values indicate an increase and negative values a decrease over the entire period.

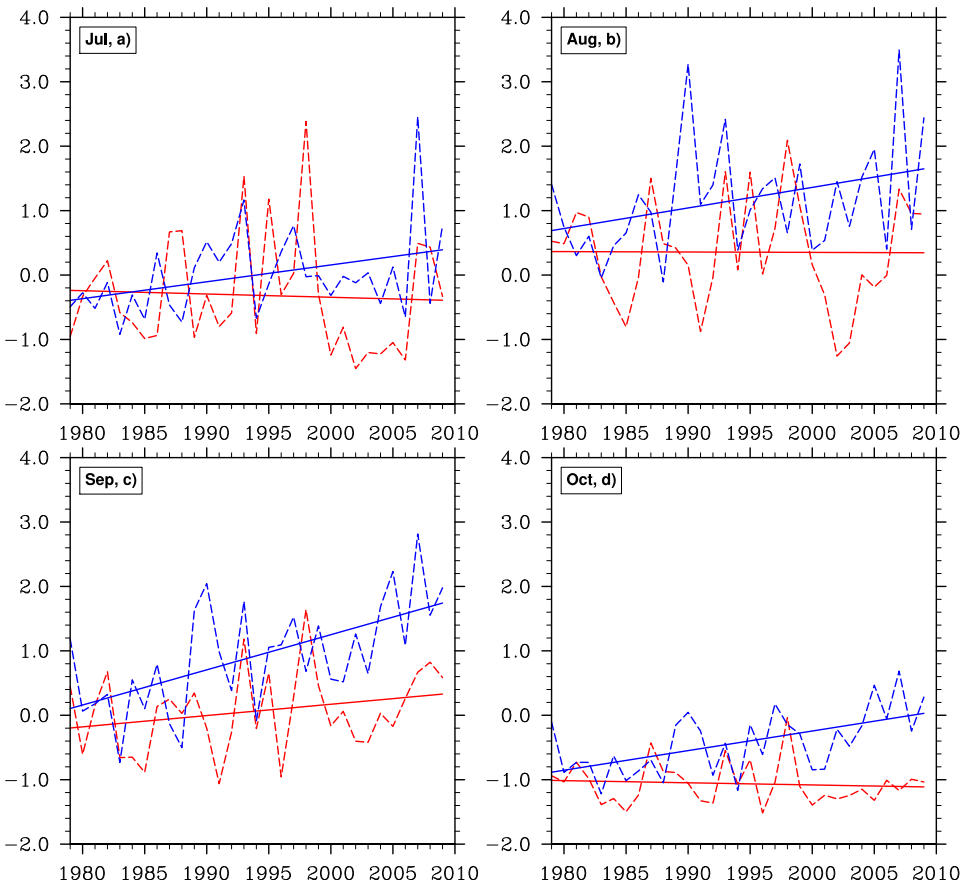

Figure 5.1.33. Monthly mean SST (°C) and its trends for 1979–2009 in the Chukchi Sea (blue) and Beaufort Sea (red) in CBHAR

5.1.7 Possible Relationships between Wind Speed, Sea Ice, SST, and Boundary Layer Stability

In order to explore the relationships between surface wind speed, sea ice, SST, and atmospheric boundary layer stability, scatterplots of binned dependent variables as a function of binned independent variables, for example, binned wind speed anomalies dependent on binned sea ice anomalies, were produced. In this way, an exceptionally large amount of data is represented with only a handful of meaningful data points. The anomalies are calculated by removing the long-term mean, thereby detrending the data. The long-term mean is removed at all times and at all grid points. In the following analysis, only the months of September and October are used since not only is this the time of year with the highest wind speeds, but it is also when the sea ice minimum occurs, thus resulting in the presence of the greatest amount of open ocean.

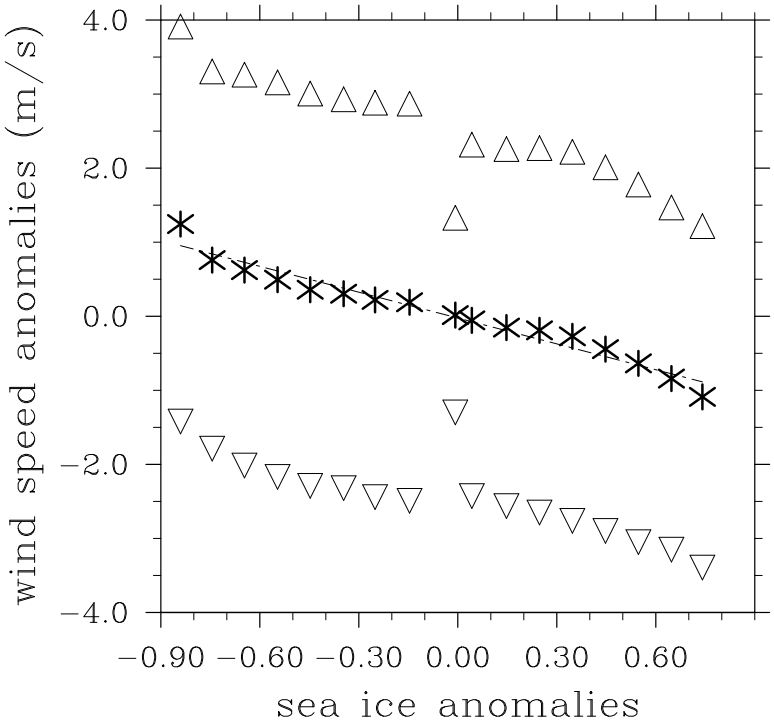

Figure 5.1.34. Binned wind speed anomalies (m s^{-1}) as a function of binned sea ice concentration anomalies in CBHAR. Triangles indicate +/– one standard deviation.

Figure 5.1.34 shows a clear relationship between wind speed and sea ice concentration. The inverse, quasi-linear relationship signifies that smaller sea ice extent is highly correlated with higher wind speed. The correlation coefficient is –0.98 and is significant at the 99% confidence level. Similarly, Stegall and Zhang (2012) also found a strong negative correlation between sea ice extent and wind speed. In other words, more open water is linked to higher wind speeds. This more than likely is the result of lower surface drag from the smoother ocean surface versus rougher sea ice. However, for the open ocean it is worth investigating the possible relationship between SST and wind speed.

The wind speed is displayed as a function of SST in Figure 5.1.35. Between open ocean (0% sea ice concentration) and about 80% concentration, an inverse linear relationship exists between wind speed and SST. The correlations for each sea ice concentration range (0%, 0–20%, 20–40%, 40–60%, and 60–80%) are –0.80, –0.86, –0.87, –0.96, and –0.86, respectively, and are significant at the 99% confidence level. The relationship for the 80–100% range is not significant.

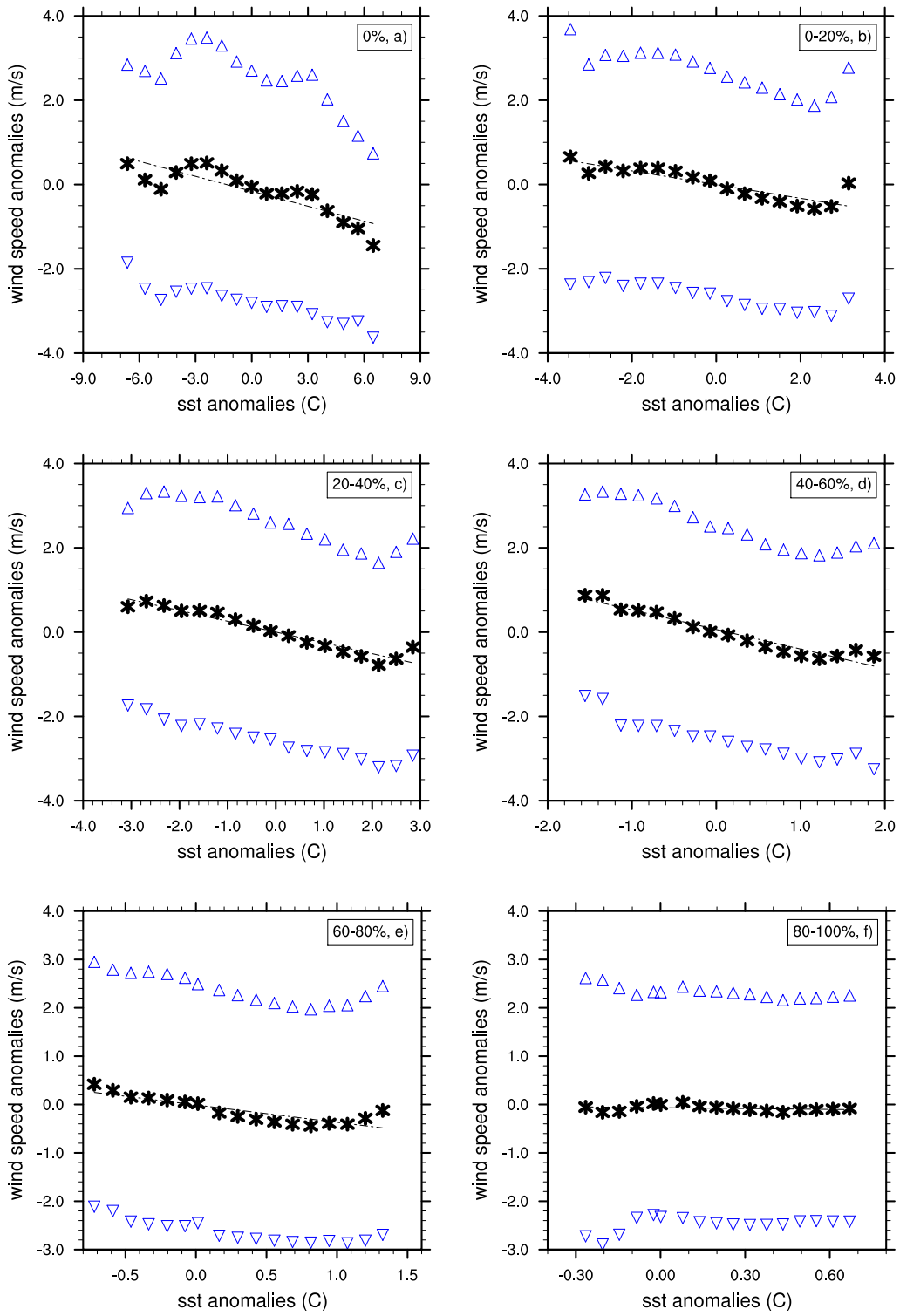

Figure 5.1.35. Binned wind speed anomalies (m s^{-1}) as a function of binned SST anomalies (°C) in CBHAR. Each plot represents a different range of sea ice concentrations as noted in the figures, i.e., 0%, 0–20%, etc. Triangles indicate +/– one standard deviation.

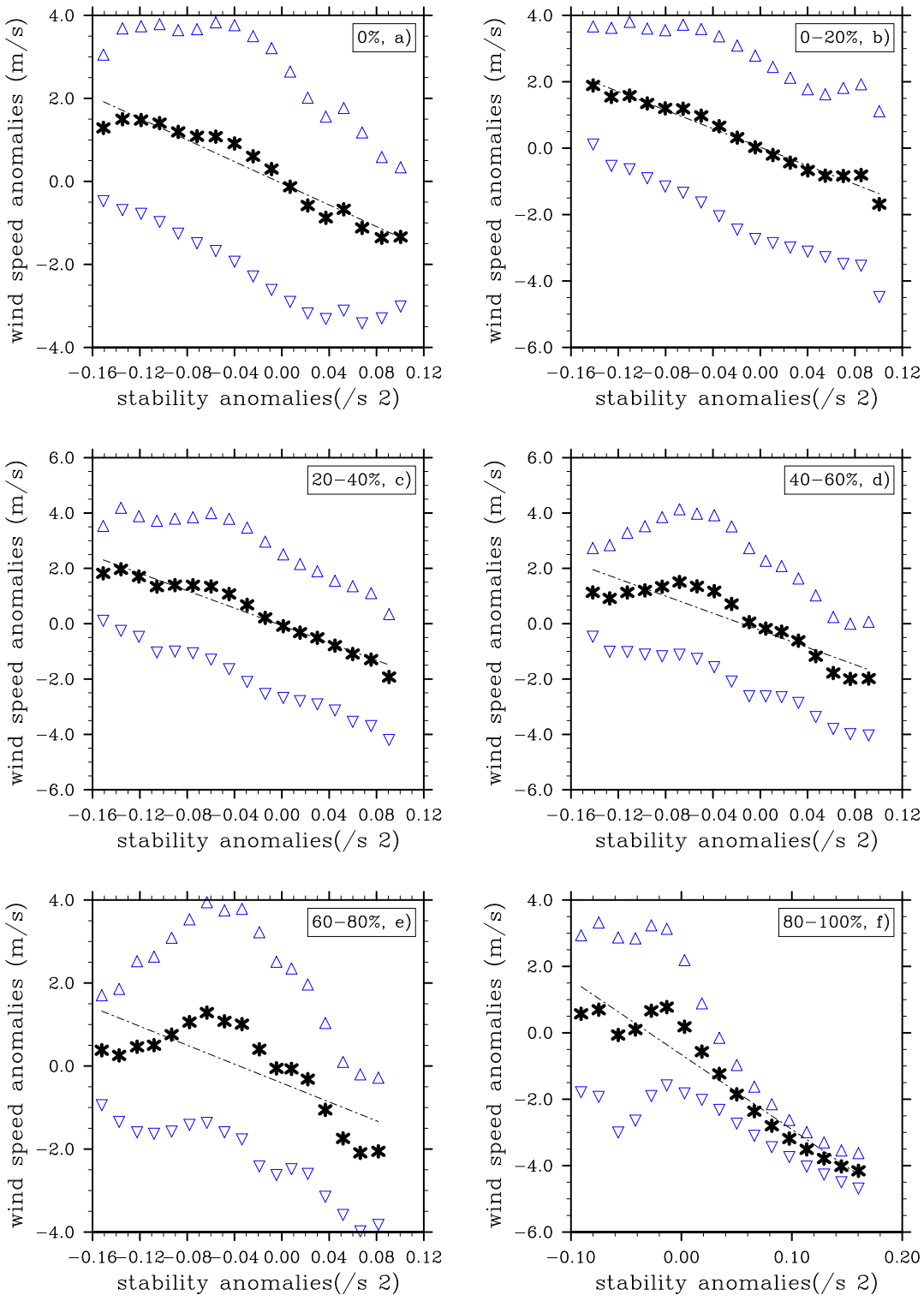

Figure 5.1.36. Same as Figure 5.1.35, except for binned wind speed anomalies (m s^{-1}) as a function of static stability anomalies (s^{-2}). Each plot represents a different range of sea ice concentrations as noted in the figures, i.e., 0%, 0–20%, etc. Triangles indicate +/– one standard deviation.

Following this, the relationship between surface wind speed and atmospheric boundary layer stability was analyzed. The near-surface stability (buoyancy) is calculated by:

$$N^2 \equiv \frac{g}{\theta}\frac{d\theta}{dz} = \frac{g}{\{\theta\}}\left(\frac{\theta_{2m} - \theta_{sst}}{dz}\right) \qquad (5.3)$$

where N is the Brunt–Väisälä frequency, θ_{sst} is the ocean-surface potential temperature, θ_{2m} is the atmospheric potential temperature at 2 m, g is gravitational acceleration, $\{\theta\}$ is the mean layer potential temperature, and dz is 2 m.

The wind speed is depicted as a function of static stability in Figure 5.1.36, shown with the same sea ice concentration ranges as in Figure 5.1.35. A strong inverse linear relationship exists here as well, particularly with increasing sea ice concentration. The correlations between wind speed and stability for each range as given in Figure 5.1.36 are –0.96, –0.99, –0.98, –0.91, –0.76, and –0.96, and all are significant at the 99% confidence level. The relationship between stability and wind speed displayed in Figure 5.1.36 is not surprising. It is expected that higher wind speed can lead to lower stability, and vice versa. The large anomalies in Figure 5.1.36 could result from the opening of leads in the sea ice and the subsequent release of latent heat to the atmosphere from the ocean water below. Changes in stability and subsequent changes in wind speeds could also result from synoptic-scale weather systems, such as low- and high-pressure systems, which would generate warm and cold air advection, thus changing the atmospheric stability and consequently the wind speeds as well.

5.1.8 Summary

The surface climate analysis using CBHAR shows that the wind speeds (monthly mean and monthly 95th percentile) exhibit a clear seasonality, with the lowest wind speeds in the spring months and the highest wind speeds in the autumn. The wind direction climatology shows that winds from the NE quadrant are the most frequent in the region, except during the summer months when the Beaufort High tends to weaken. The direction climatology also captures mesoscale features, including anomalous SW winds over the Brooks Range, anomalous NW winds over the Chukotka Mountains in eastern Siberia, and anomalous NW winds over the Mackenzie River valley in Canada, particularly during the cold season months. These anomalous winds could be the result of cold-air damming, resulting from a mesoscale force imbalance between the pressure gradient and Coriolis forces, as well as the downslope mountain breeze. The linear trend analysis of the wind speeds shows that the largest increasing trend occurs in October. These results are consistent between CBHAR and ERA-Interim, even though CBHAR employed different assimilation technology and assimilated different data. This suggests that CBHAR accurately captures changes in the large-scale surface climate. Sudden changes in trends due to a change in technology (e.g., the introduction of QuikSCAT or MODIS observations), such as discontinuities in the trend data or sudden increases or decreases in the trends are not present. Both the climatology and trends of the winds in

CBHAR agree well with ERA-I data, indicating that the assimilation of different types of data as technology changed over time was handled correctly in CBHAR.

The analysis of the relationships between sea ice and wind speed, though preliminary, yields useful information. The observed negative linear relationship supports the findings of Stegall and Zhang (2012), who similarly found a highly negative correlation between sea ice extent and wind speed. The relationship between wind speed and SST also shows a negative linear relationship. This phenomenon could be related to cold air advection, given that the primary wind direction is from the NE. There is also a strong linear relationship between near-surface stability and wind speed. This is not surprising, since higher wind speeds can cause the stability to decrease, and with decreasing stability the wind speeds can more easily increase. However, regarding the relationship between wind speed and SST, other variables such as the presence of low cloud cover need to be researched as well. The results of Section 5.1.7 are very preliminary; additional research will be conducted on these topics.

5.2 Mesoscale Wind Fields in CBHAR

5.2.1 Introduction

Both prevailing synoptic weather patterns and prominent underlying geographic features play roles in determining the surface wind climate (e.g., Schwerdtfeger 1974; Kozo 1980; Moore and Pickart 2012). In the Chukchi–Beaufort Seas region, the surface winds vary in response to the intensity and location of the Beaufort High and Aleutian Low, which are the dominant synoptic-scale weather patterns in the area, as discussed in Section 2.1 (Shulski and Wendler 2007; Overland 2009; Moore 2012). The surface winds are further modulated by local geographic features through both thermodynamic and dynamic processes (Kozo 1979, 1980; Liu et al. 2008). The geography in the area is characterized by seasonally ice-covered ocean, along with the Brooks Range in northern Alaska and the Chukotka Mountains in eastern Siberia. The land and ocean respond differently to incoming solar radiation, generating horizontal temperature gradients, which in turn cause air to flow from cool to warm areas along the surface, with a reversed compensating flow at upper levels (Figure 5.2.1a) (Kozo 1979). Land/sea breezes thus become an integral component of the surface wind regime in coastal areas during warm seasons. The same mechanism may also exist in mountainous areas, where mountain slopes are more readily heated than is the horizontally adjacent air, causing upslope winds during the day (Figure 5.2.1b). In cold seasons, the air near the terrain surface is cooled faster than the adjacent air through the loss of outgoing longwave radiation, resulting in denser surface air over the terrain and a resultant downslope wind (also referred to as gravity drainage). Topography can also impact the surface wind through other mechanisms. For example, when an air mass characterized by a low Froude number (U/NH, where U is the speed of the basic current, N is the Brunt–Väisälä frequency, and H is the mountain height) flows toward a mountain barrier, its approach will be blocked due to having insufficient kinetic energy to flow over the mountain. The accumulated air mass alters the distribution of pressure so that the flow is deflected to the left and finally

turns, becoming parallel to the mountain range. This effect is known as cold-air damming (Schwerdtfeger 1974; Kozo 1980).

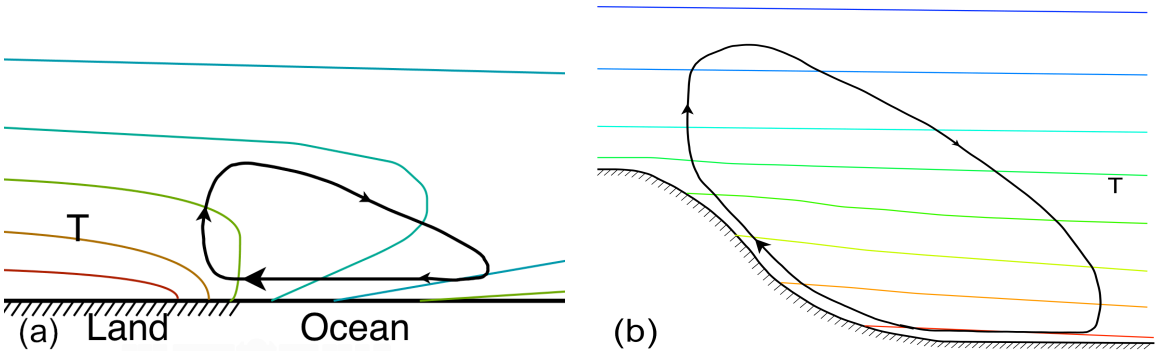

Figure 5.2.1. Schematic diagrams for (a) sea breeze and (b) upslope wind

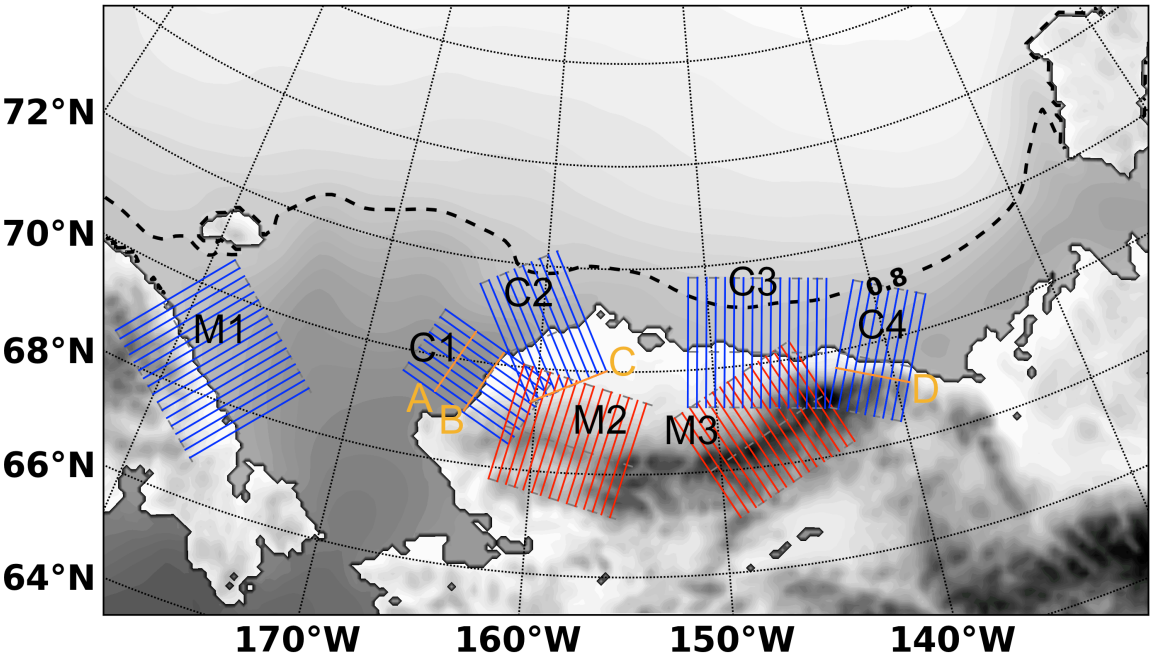

Figure 5.2.2. Vertical cross-sections used in different areas to show the vertical structure of land/sea breezes, up/downslope winds, and cold-air damming. The four locations A, B, C, and D, shown in orange, were chosen for use in displaying the land/sea breeze component at different locations in different seasons. Gray shading over the ocean represents the average sea ice concentration over the entire CBHAR period (lighter colors signify higher SIC), with the 0.8 value highlighted by the dashed line.

The CBHAR reanalysis has high spatial resolution, with a grid spacing of 10 km, and a temporal resolution of just one hour, making it able to resolve finer-scale mesoscale processes than is possible in coarser reanalyses, such as ERA-Interim. These processes

are usually generated by small-scale thermodynamic and dynamic effects, and include sea breezes, up/downslope winds, and cold-air damming, among others. To facilitate the following analysis and discussion, the model domain is again shown in Figure 5.2.2, with superimposed sea ice and geographic features, along with the vertical cross-sections used in the subsequent analysis. In order to reduce biases potentially caused by the use of a single vertical section, a series of parallel vertical cross-sections were chosen in the areas of interest and the wind fields averaged across these multiple vertical sections. In addition, the locations A, B, C, and D as shown in Figure 5.2.2, were selected in order to analyze the seasonality of both sea breezes and up/downslope winds as impacted by the nearby locations of the shoreline and mountainous terrain.

5.2.2 Sea Breeze and Up/Downslope Wind

Sea breezes and up/downslope winds are both generated by horizontal thermal contrasts at the surface, caused by the quite different thermodynamic characteristics of different geographic surfaces. For example, water has a much larger heat capacity than soil. Land is thus heated faster during the day than adjacent ocean or lake areas in the summer. For the same reason, radiative cooling also cools the land faster at night. As a result, horizontal temperature contrasts may exist both during the day and at night, driving the motion of air currents in coastal areas (Figure 5.2.1a) (Kozo 1979). A similar process occurs in the vicinity of mountain valleys, where the air over the mountain and valley surfaces experiences differential heating. Air over the warmer surface experiences increased heating and tends to ascend to upper levels. The pressure near the surface is thus decreased and correspondingly increased at higher levels, resulting in a horizontal pressure gradient both near the surface and at upper levels. This then causes cool air to flow towards the warmer surface at lower levels and warmer air to flow in the opposite direction at higher levels (Figure 5.2.1b), resulting in an up/downslope circulation pattern.

The diurnal cycle of solar radiative heating produces time-varying horizontal temperature contrasts throughout the day. As a consequence, the associated thermodynamically driven flows tend to also have a noticeable diurnal variation. Based on this fact, climatological sea breezes and up/downslope winds can be identified through the following approach. The surface wind field is first averaged over the 31-year record at each hour of the day, separated by month, in order to obtain the monthly climatological diurnal surface wind. The sea breezes and up/downslope winds in a certain month are then identified by subtracting out the climatological wind at a given reference time when the local thermodynamic effects are minimal. In this study, 0600 AKST was chosen as the reference time, based on an analysis of the variation in the climatological diurnal surface wind. The results indicate that in July, the diurnal anomalies of surface winds show significant diurnal variation in both mountainous and coastal areas (Figure 5.2.3). Along the Brooks Range, upslope winds develop when the underlying surface is heated. The maximum upslope wind occurs in the late afternoon around 1700 AKST, with maximum wind speeds of up to 2–3 m s^{-1} in the eastern Brooks Range. Along the shoreline, the surface wind field is characterized by the sea breeze, with weak onshore flow in the early morning and stronger onshore flow in the afternoon. The maximum sea breeze near the

shoreline also occurs in the late afternoon at around 1700 AKST, with a maximum wind speed of 2 to 3 m s^{-1}, though this varies in different areas. Along the Chukchi Sea coastline, the sea breeze can reach 3 m s^{-1} in July, whereas the eastern Beaufort coast experiences a relatively weak sea breeze of about 2 m s^{-1}.

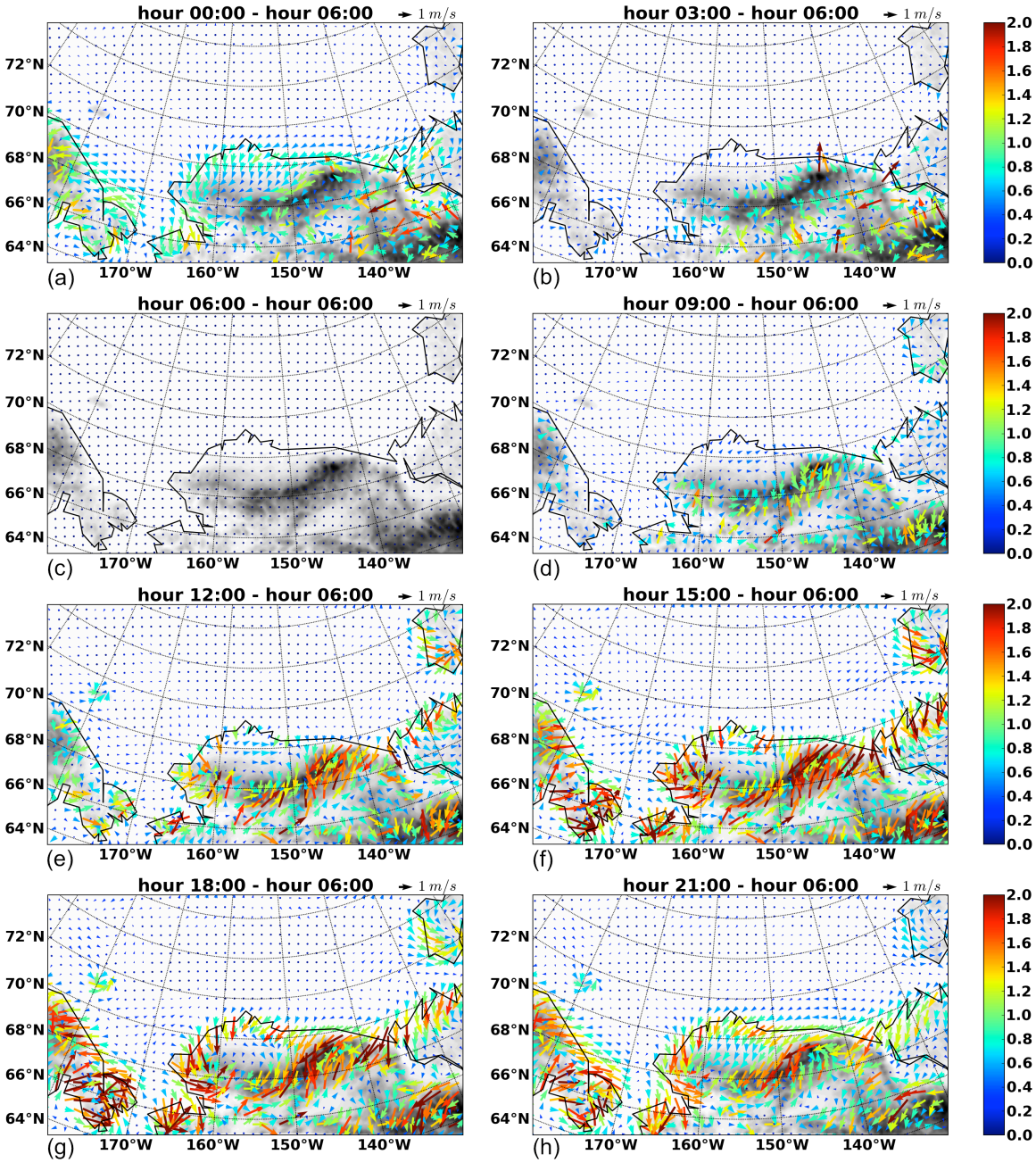

Figure 5.2.3. Climatological diurnal anomalies of surface winds (m s^{-1}) relative to winds at 0600 AKST, calculated at different hours (AKST) in July in CBHAR

To further examine the geographic dependence of the sea breeze and up/downslope wind, four particular locations were chosen for additional analysis as shown in Figure 5.2.2. Point A represents a location that is relatively far away (about 60 km) from the shoreline, where weak diurnal wind variation is expected and where the sole impact is from the sea breeze. Point B is located directly on the shoreline, experiencing the most pronounced diurnal variation in horizontal temperature contrast and, accordingly, a vigorous sea breeze. The surface wind at the inland Point C tends to show weak impacts from both the sea breeze and up/downslope winds, due to its location far away (more than 100 km) from both the shoreline and the mountain slope. The inland Point D, meanwhile, is located on the north slope of the eastern Brooks Range, where the terrain is characterized by a steep slope. The horizontal distance between Point D and the shoreline is about 60 km. By comparing the perpendicular component of the surface winds relative to the shoreline at locations A, B, C, and D, the relative impacts of the mountain and sea breezes can thus be isolated.

The mountains' topographic effects exhibit quite different impacts on the surface winds from month to month (Figure 5.2.4). At Point D, strong downslope winds occur from October through March (Figure 5.2.4d) due to the strong radiative cooling effect of the mountain slopes in the cold season, resulting in dense cold-air formation near the terrain surface. While the dense cold-air flow over the Antarctic ice sheet has been extensively studied (e.g., Parish and Cassano 2003), there have been few such studies on the Arctic Slope. The strongest downslope wind occurs during the coldest part of the year, from November to February, with a downslope wind component of 2–3 m s^{-1}. During this season, the diurnal variation of surface wind is too weak to identify due to a relative lack of solar irradiance. In October and March, the downslope flow is also present throughout the day, though with a weak diurnal variation due to surface radiative heating. In March, the downslope wind decreases from a maximum of 1.8 m s^{-1} in the early morning to about 1 m s^{-1} at around 1400 AKST. From April through September, the mountain surface receives sufficient heat during the day from solar radiation to induce an upslope wind. The diurnal variation of the wind speed is characterized by a decrease in downslope wind speed in the morning, followed by an increase in upslope wind in the afternoon. From June to August, both the daily downslope and upslope winds at Point D last roughly the same amount of time, with a maximum upslope component of about 1 m s^{-1} and a maximum downslope component of around 2 m s^{-1}.

As seen at Points A and B, the sea breeze induced by the land-sea thermal contrast does not become identifiable until June (Figure 5.2.4a,b). At the shoreline Point B, the maximum sea breeze occurs in June, with a maximum onshore wind of approximately 1 m s^{-1} in the late afternoon. The reversal from sea breeze to land breeze occurs at about 2100 AKST. The land breeze reaches its maximum after several hours and lasts for several hours more, before the wind switches back to onshore flow in the morning at around 0900 AKST. The climatological surface wind at the offshore Point A is directed offshore throughout the entire year, though like at Point B it displays a diurnal variation from June through September. At the inland Point C, the diurnal variation of the on/offshore wind component is also noticeable, which is likely primarily caused by the

thermodynamic effects of the mountains, as the point is located more than 100 km away from the shoreline.

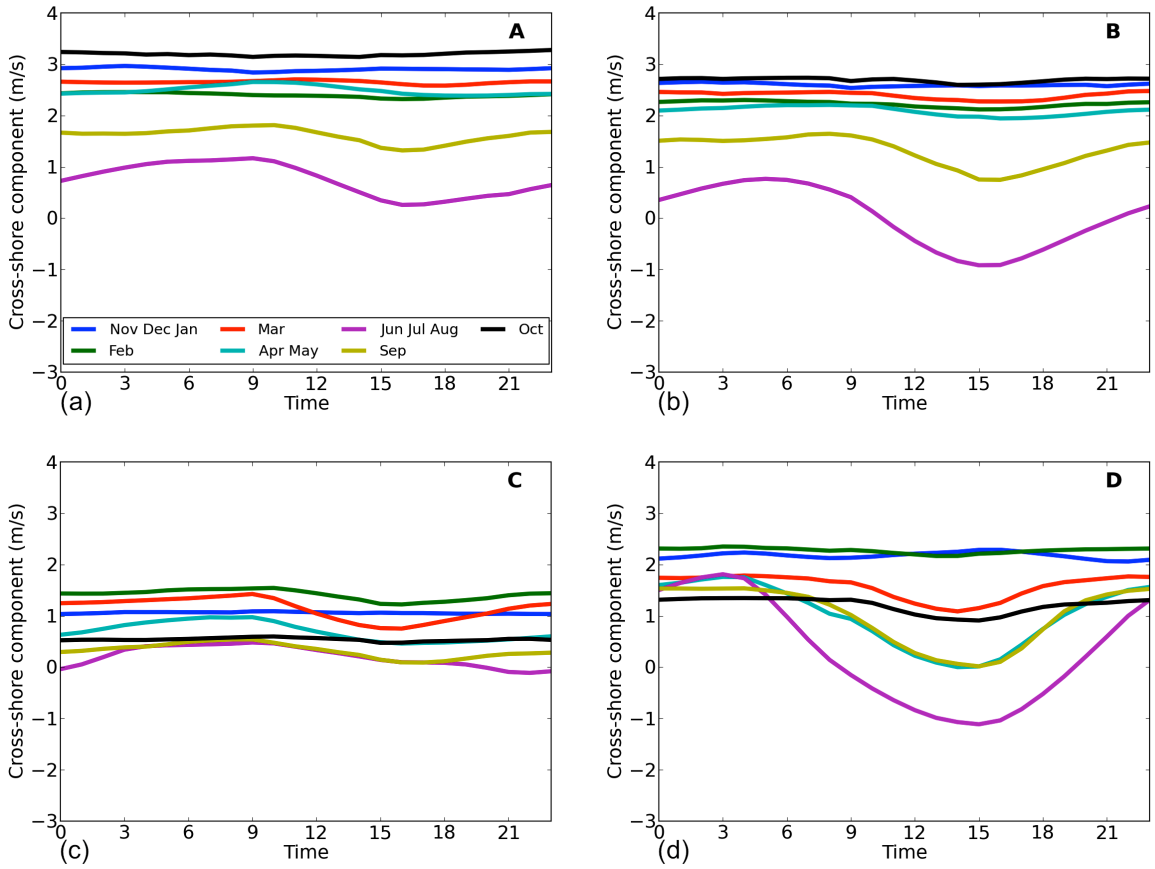

Figure 5.2.4. Climatological diurnal variation of the on/offshore surface wind component (m s^{-1}) for different months at Points A, B, C, and D in CBHAR, as shown in Figure 5.2.2. Positive values represent offshore-directed wind, and negative values onshore wind. Times are given in AKST.

A comparison of the climatological diurnal variation of the surface wind was also conducted between CBHAR and the in situ observations at Barrow, where hourly observations are available over the entire CBHAR time period (Figure 5.2.5). The impacts of the sea breeze on the surface wind can easily be identified, reflected by the obvious diurnal cycle of wind speed and direction. Due to the existence of the Beaufort High, the surface wind direction is predominantly from the east-northeast (Figure 5.2.5b). The wind direction turns toward the north during the day, when the surface is heated by solar radiation, representing a reduced offshore wind component. The comparison also indicates a consistency between CBHAR and the station observations.

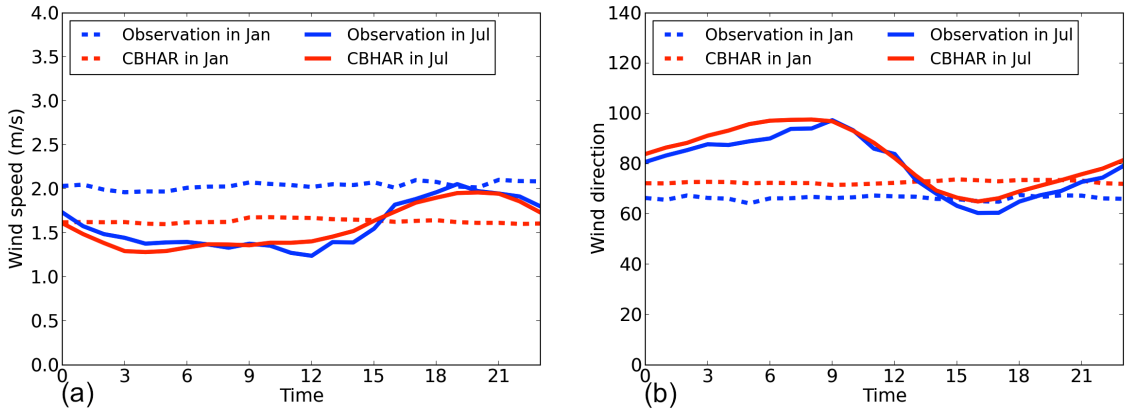

Figure 5.2.5. Climatological diurnal variation of surface wind speed (a, m s^{-1}) and direction (b, °) in January (dashed) and July (solid) at Barrow from the surface station observations (blue) and CBHAR data (red). Times are given in AKST.

The vertical structure of the sea breeze and up/downslope winds can be revealed by examining the vertical motion and on/offshore wind component along selected cross-sections. In order to reduce biases potentially caused by the use of a single vertical section, a series of parallel vertical cross-sections were instead identified in the interested areas (Figure 5.2.2) and averages of the wind fields across these vertical sections were calculated. In total, seven areas were selected for the examination of vertical wind structures, including inland areas of the Chukotka Mountains (M1) and the Brooks Range (M2 and M3), as well as four coastal areas (C1–C4). Along the vertical sections, the horizontal winds were transformed in order to define components perpendicular and parallel to the vertical section, i.e., wind components were oriented relative to the shoreline or the orientation of the mountain ranges. The climatology of the wind along the vertical sections was constructed at each hour of the day for different months.

Given that thermodynamically forced sea and land breezes become most active in June, July, and August, the climatological diurnal variation of wind in July was examined, as displayed along the vertical section C2 in Figure 5.2.6. In order to better illustrate the diurnal variation, the daily evolution of the sea breeze is also depicted in Figure 5.2.7. The sea breeze was isolated by subtracting the wind field at 0600 AKST from the wind field at each hour of the day. An important thermodynamic feature in the study domain is that the surface air temperature over land is consistently warmer than that over the ocean in July due to the long daylight hours. In July, the surface air temperature begins to increase at about 0500 AKST, when a weak offshore wind with speed less than 0.5 m s^{-1} and weak downward motion near the shoreline dominates near the surface. As the surface warms, upward motion is gradually developed inland about 20 km from the shoreline at 0900 AKST. At noon, the sea breeze circulation is initially formed, with very weak onshore wind across an expanse of just 10 km, crossing the shoreline from the shelf seas and directed inland. At the same time, the upper-air motion is oriented toward the offshore direction near the shoreline at about 200–300 meters above ground, and downward motion develops offshore within 50 km of the shoreline. The sea breeze

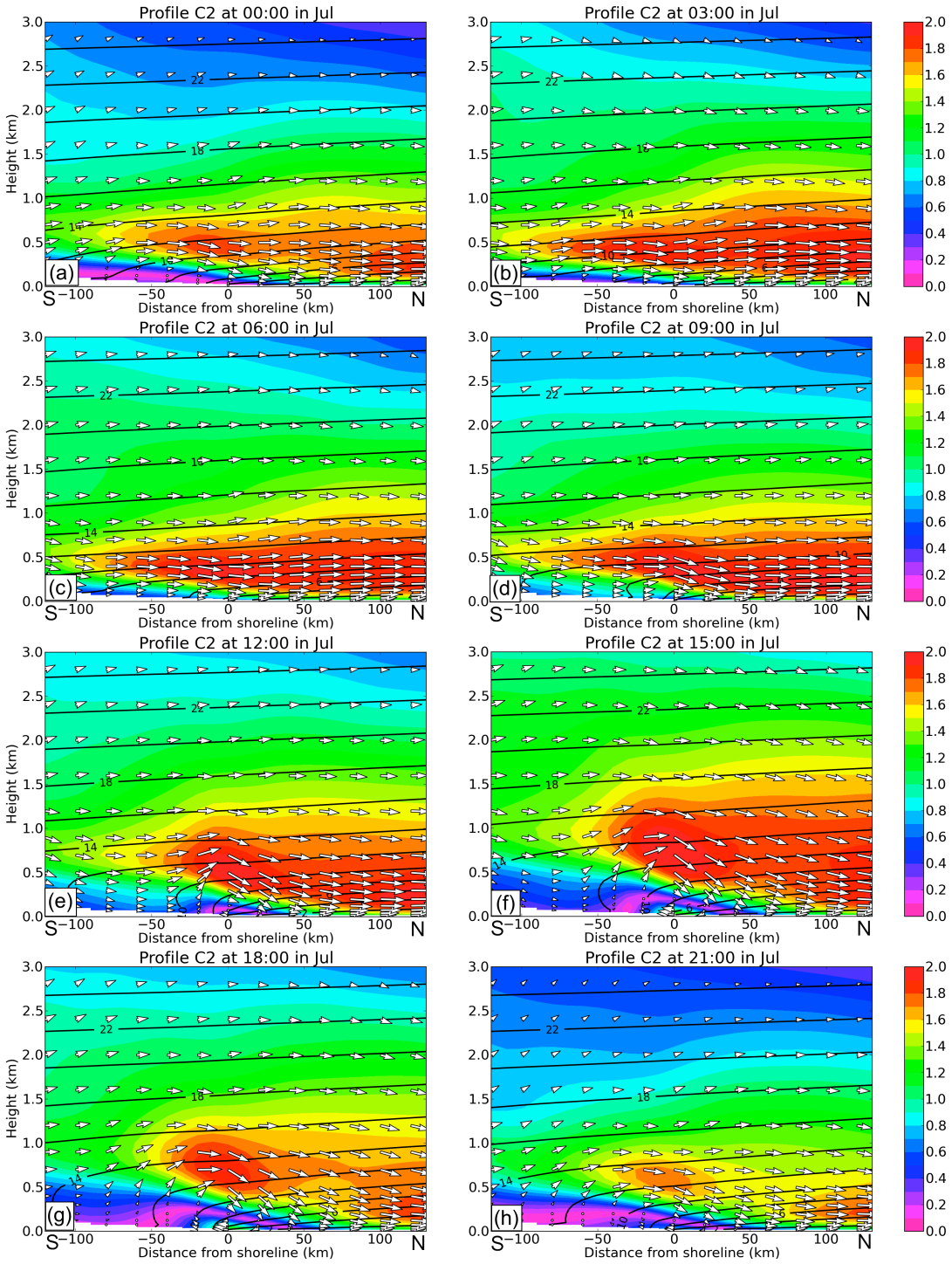

Figure 5.2.6. Diurnal variation of climatological wind in July along the vertical cross-section C2. Wind vectors include both the horizontal wind component, oriented perpendicular to the shoreline, and the vertical component. Wind speed (m s^{-1}) is indicated by colors. Solid contours indicate potential temperature (°C). The shoreline is located at 0 km, and the orientation of the cross-section is indicated by the "S" (south) and "N" (north) labels.

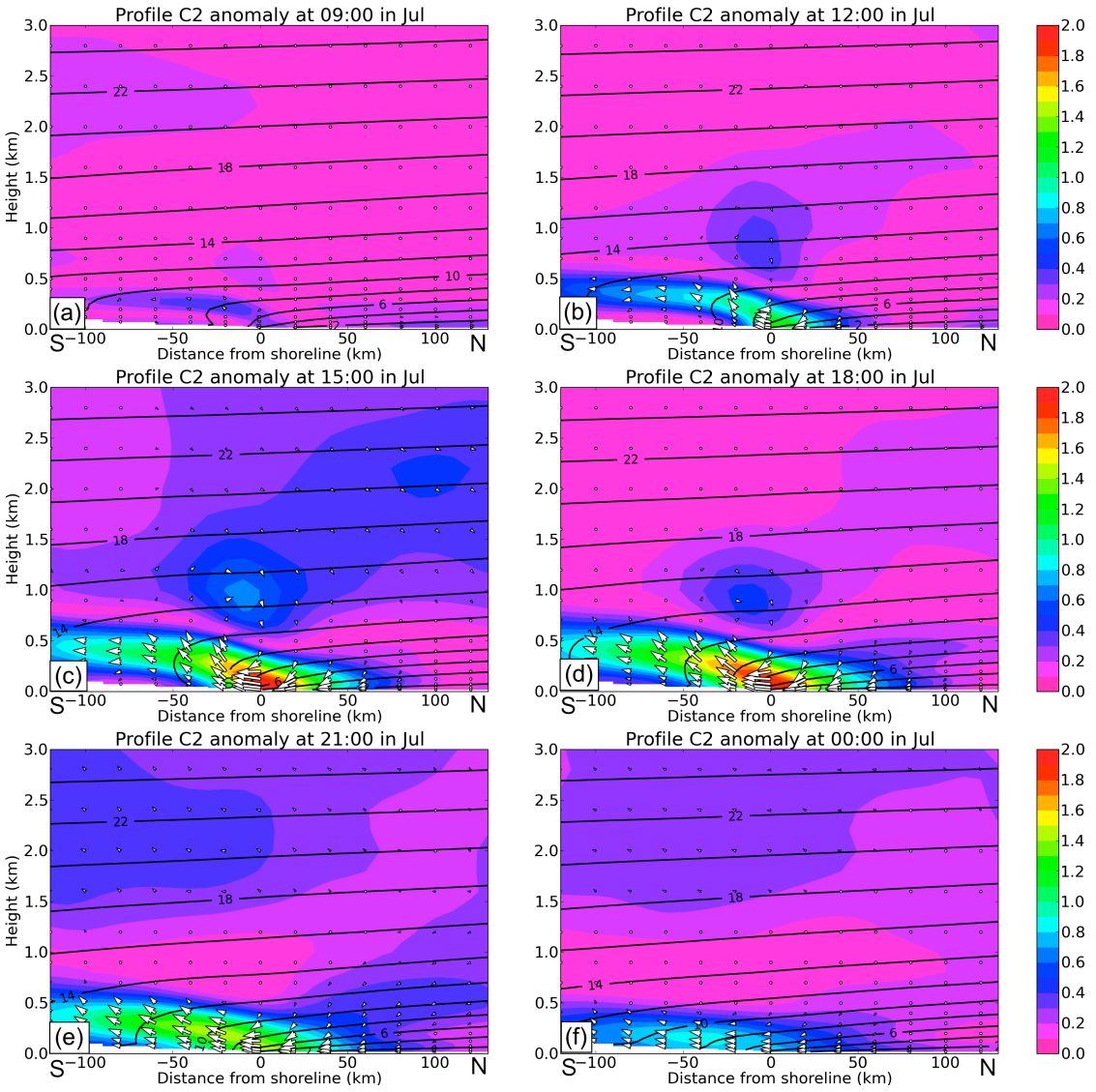

Figure 5.2.7. Same as Figure 5.2.6, but for the climatological anomalies relative to the wind at 0600 AKST, demonstrating the diurnal evolution of the sea breeze

circulation is strengthened in subsequent hours due to the increase in the surface temperature contrast, and the horizontal extent of the onshore winds gradually increases to 20 km. The strongest sea breeze occurs in the late afternoon at about 1700 AKST, with a maximum onshore wind of roughly 1.2 m s^{-1}, located around the shoreline near the surface, and a maximum return flow of about 2 m s^{-1}, located 700 meters above ground at the shoreline. The sea breeze circulation gradually weakens over the next 12 hours, with upward motion disappearing at around 2200 AKST, and offshore winds near the surface reestablished at about 0400 AKST.

Considering the seasonal and geographical dependence of the thermodynamically forced sea breeze and up/downslope winds, additional comparisons of the climatological wind profiles in January (Figure 5.2.8) and wind profile anomalies in July (Figure 5.2.9) were

conducted along different vertical sections (locations shown in Figure 5.2.2). The January wind profiles were compared due to presence of little diurnal variation at that time (see Figures 5.2.4 and 5.2.5), while the wind profile anomalies calculated between 1800 and 0600 AKST in July represent the strongest diurnal variations along the various vertical cross-sections.

In January, the surface winds are dominated by downslope winds along the north slope of the eastern Brooks Range (Figure 5.2.8c,g), where terrain height changes dramatically and the surface air is significantly cooled. Downslope winds are also a major contributor to the surface winds on the south slope of the western Brooks Range (Figure 5.2.8b). In addition, strong downward winds flowing from the top of the mountains occur in the western coastal area of Alaska (Figure 5.2.8d). This flow pattern is a combination of the mountain-slope-induced downward density flow and the background flow associated with the Beaufort High. This analysis also indicates that the surface wind along the north slope of the western Brooks Range (M2) is dominated by the mountain-parallel component (not shown). Weak downslope winds appear along the vertical sections C2 and C3 (Figure 5.2.8e,f), most likely due to more gradual mountain slopes and a weak background flow. When examining the vertical wind field in the area of the Chukotka Mountains (Figure 5.2.8a), one finds that the strong background winds flow toward the mountains, against the direction of any existing downslope winds. The mountains exert a strong barrier effect upon the approaching winds, which may lead to the formation of cold-air damming, as discussed in the following section.

In July (Figure 5.2.9), both sea breeze and upslope winds are expected to contribute to surface winds as mentioned above. The climatological sea and mountain breezes are usually well developed by 1800 AKST and relatively weak at 0600 AKST (see Figures 5.2.3–5.2.7), thus the climatological wind profile differences between 1800 and 0600 AKST are able to represent the maximum strength of the diurnal sea and mountain breezes. The sea breeze along the vertical section C1, in the presence of a relatively flat mountain slope and where mountain thermodynamic effects are very weak, extend out to about 80 km offshore and 50 km onshore, as defined by wind speed anomalies larger than 0.8 m s^{-1} (Figure 5.2.9d). On the other hand, along the vertical section C2, in the absence of any mountain slope, the sea breeze has a lesser extent offshore (60 km), but a greater extent offshore (>100 km), using the same criterion for the anomaly (Figure 5.2.9e). When examining other vertical sections where the mountain slopes are relatively steep and the mountain impacts are correspondingly greater (sections M1, C3, and C4), it is apparent that upslope winds become stronger due to reinforcement of the sea breeze and mountain thermodynamic impacts, producing a significant impact on the surface wind field. The sea breeze and upslope winds exhibit different spatial scales, extending from about 40–60 km offshore all the way to the top of the mountain onshore, again in terms of anomalies greater than 0.8 m s^{-1} (Figure 5.2.9a,f,g). Along the mountain cross-sections M2 and M3, where the distance to the shoreline is too far to receive any sea breeze impacts, the upslope winds are most likely the product of mountain thermodynamic effects, with relatively stronger upslope winds occurring along the steep eastern Brooks Range (section M3) and weaker upslope winds along the more gently sloping western

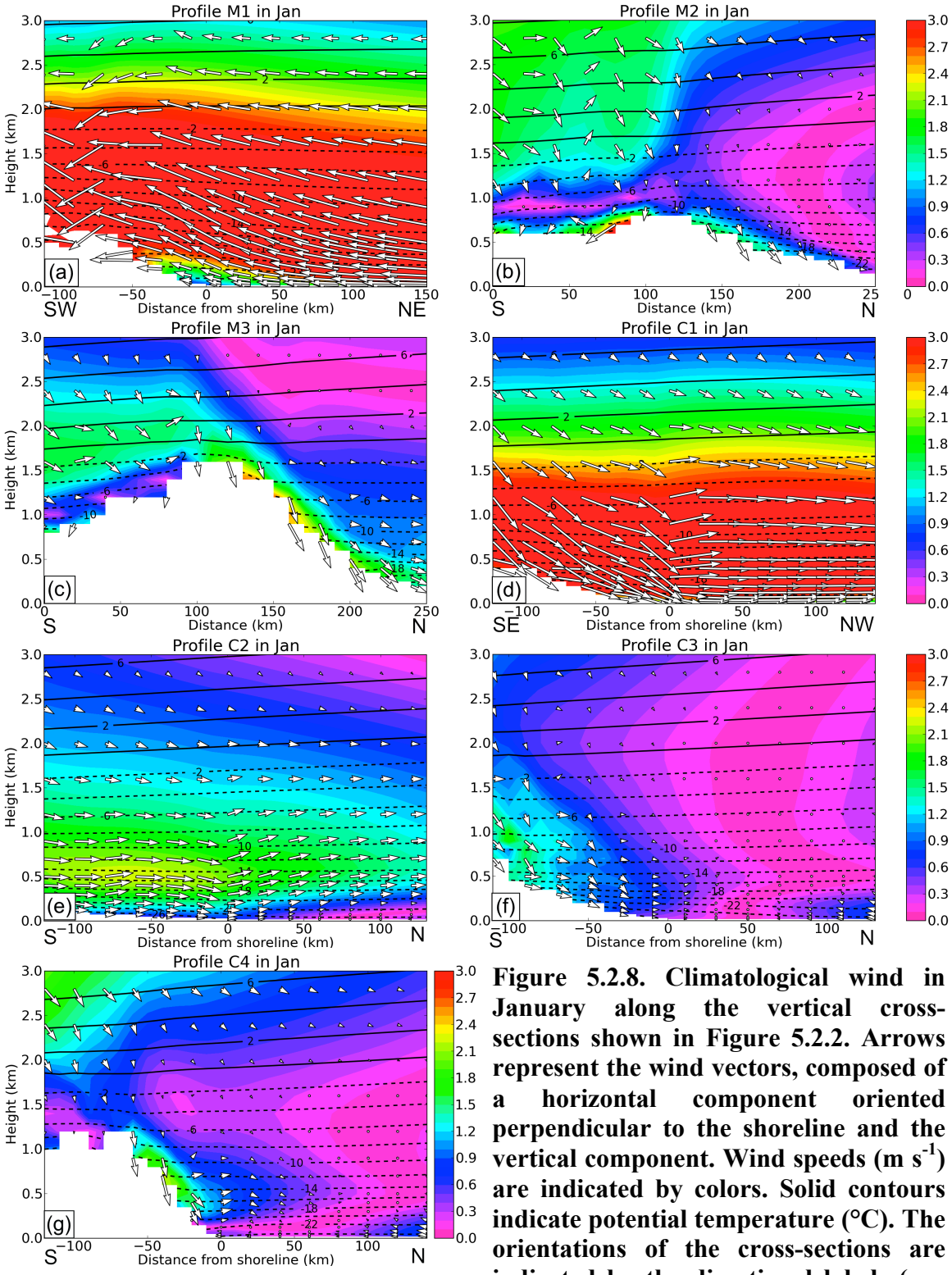

Figure 5.2.8. Climatological wind in January along the vertical cross-sections shown in Figure 5.2.2. Arrows represent the wind vectors, composed of a horizontal component oriented perpendicular to the shoreline and the vertical component. Wind speeds (m s^{-1}) are indicated by colors. Solid contours indicate potential temperature (°C). The orientations of the cross-sections are indicated by the directional labels (e.g. S, SW, NE, N).

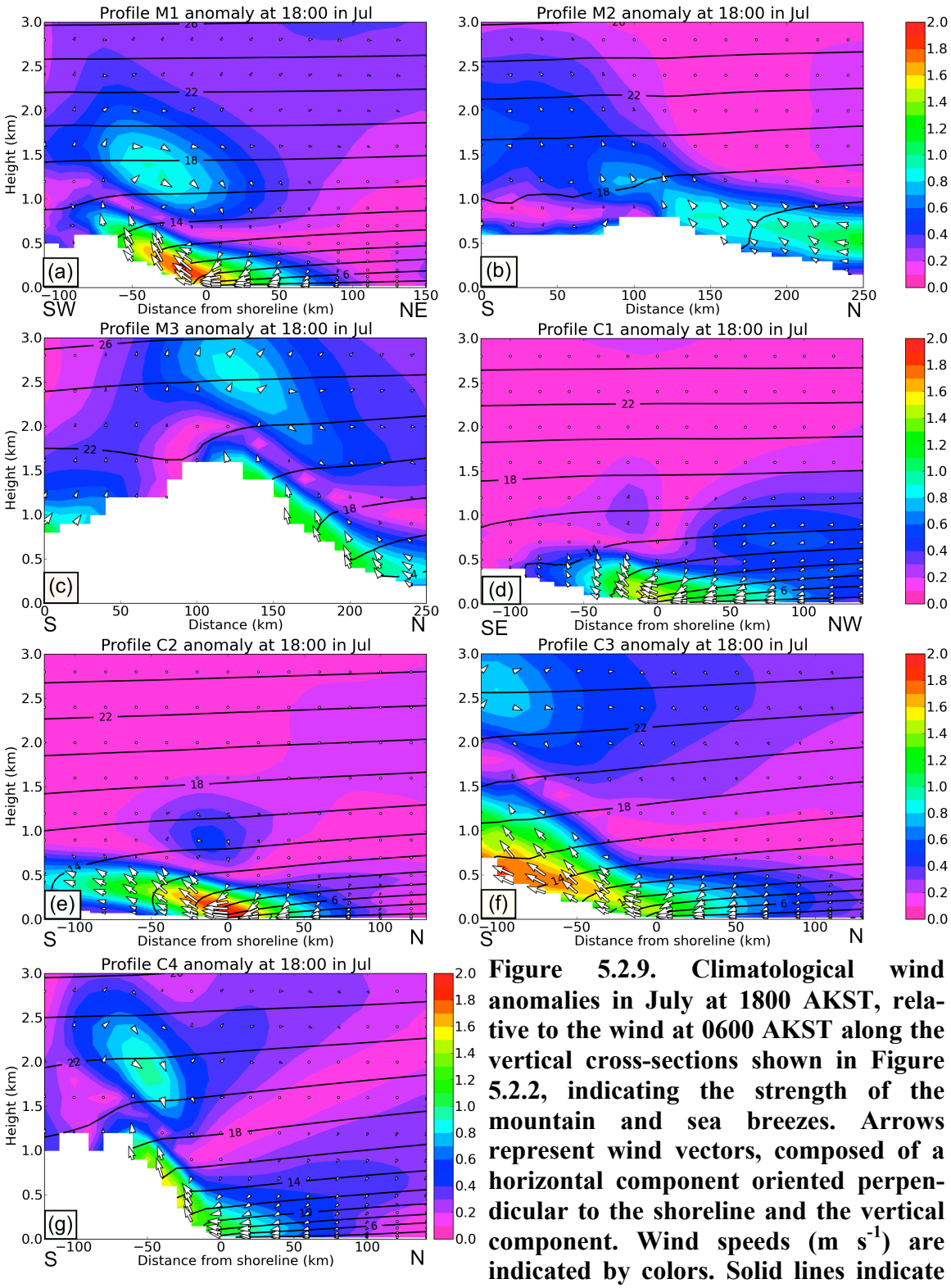

Figure 5.2.9. Climatological wind anomalies in July at 1800 AKST, relative to the wind at 0600 AKST along the vertical cross-sections shown in Figure 5.2.2, indicating the strength of the mountain and sea breezes. Arrows represent wind vectors, composed of a horizontal component oriented perpendicular to the shoreline and the vertical component. Wind speeds (m s^{-1}) are indicated by colors. Solid lines indicate potential temperature (°C). Orientations of the cross-sections are indicated by the directional labels (e.g. S, SW, NE, N).

Brooks Range (section M2). Vertically, in the absence of mountain impacts (sections C1 and C2), a weaker and shallower return flow caused by the sea breeze appears as high as 1 km above the surface. However, when mountain impacts from relatively steep slopes are present (sections M1, M3, C3, and C4), a stronger and deeper upper-air reversal flow appears around 1–1.5 km above the surface.

The spatial extent of sea breeze circulations can vary depending on season and latitude due to differences in solar radiation, geographic location, and the background wind field. To examine the distance out to which sea breezes may affect offshore locations in the study region, a simple method was employed. The distance was measured through the use of a criterion specifying that the climatological diurnal wind variation of the cross-shore wind component be greater than 0.8 m s^{-1}; exceeding this threshold was defined to indicate the presence of a sea breeze. The results show that the largest distance that the sea breeze extends offshore appears over the Chukchi Sea west of Alaska and north of the Chukotka Mountains (Figure 5.2.10). Application of this method also reveals the seasonal dependence of the sea breeze, which emerges in June with a spatial extent out to 30–80 km offshore. The affected distance decreases to about 35–50 km in August, and further to about 20 km in September.

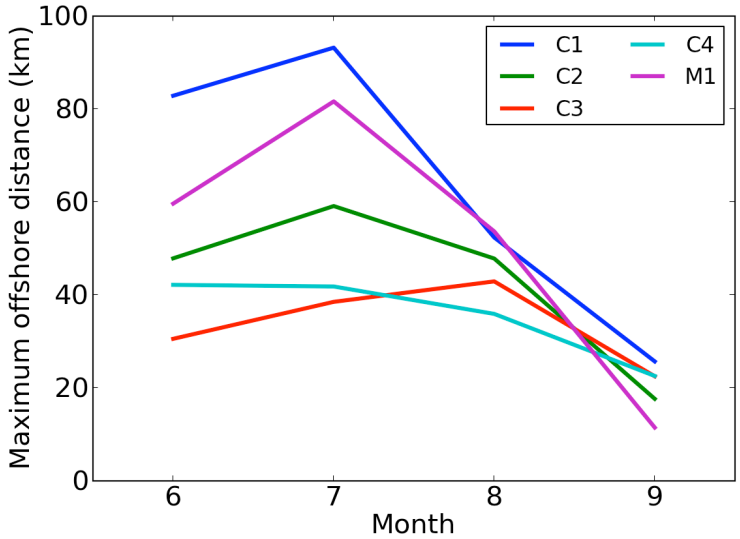

Figure 5.2.10. Maximum offshore distance (km) out to which the climatological diurnal wind variation of the cross-shore component is greater than 0.8 m s^{-1} for various cross-sections, indicating the spatial range that the sea breeze impacts different areas along the Chukchi and Beaufort coasts

5.2.3 Cold-Air Damming

Cold-air damming (Schwerdtfeger 1974; Kozo 1980) is another mesoscale process through which topography can affect the surface wind field. When air flow approaches a mountain, the air is forced to either ascend over the mountain or be blocked, depending on the properties of both the air layer and the topography as measured by a series of parameters, including the horizontal scale and slope of the mountain, the direction and speed of the large-scale flow, and the stability of the atmosphere, among others. When

the Froude number is low (U/NH<1; where U is the speed of the general flow, N is the Brunt–Väisälä frequency, and H is the mountain height), the kinetic energy of the low-level flow is insufficient for the air to pass completely over the mountain. The flow is thus blocked and decelerates as it approaches the barrier. Decelerated flow results in a decreased Coriolis force, breaking the geostrophic balance of the large-scale wind. The flow is thus deflected to the left and a mass of air accumulates near the base of the mountain, which in so doing generates a mesoscale pressure ridge. Eventually, a new balance between the large-scale pressure gradient, mesoscale pressure gradient, Coriolis force, and friction is reached. Accordingly, a low-level wind maximum is formed parallel to the mountain barrier. In the study domain, the occurrence of low Froude number flow is common, due to the orientation of the mountain ranges and the stable low-level atmosphere. Cold-air damming is therefore expected to be one of the important mechanisms affecting the surface wind field.

The climatological surface winds over the 31-year period are first examined using CBHAR in order to get an overall understanding of the occurrence of cold-air damming across the entire study domain. In this region, the surface winds are stronger in cold months (Figure 5.2.11a,d) and weaker in warm months (Figure 5.2.11c). In January, a noticeable feature is that strong surface winds occur over the Chukchi Sea, caused by the intense Beaufort High centered over its northern area. Along the Chukotka Mountains, the strong northeasterly winds are turned, flowing parallel to the mountain range with enhanced speeds, implying the possibility of the occurrence of cold-air damming. This turning of the surface winds is not identified in other areas. The vertical wind structure is thus analyzed along the Chukotka Mountains (cross-section M1 in Figure 5.2.2) in order to investigate the cold-air damming effect.

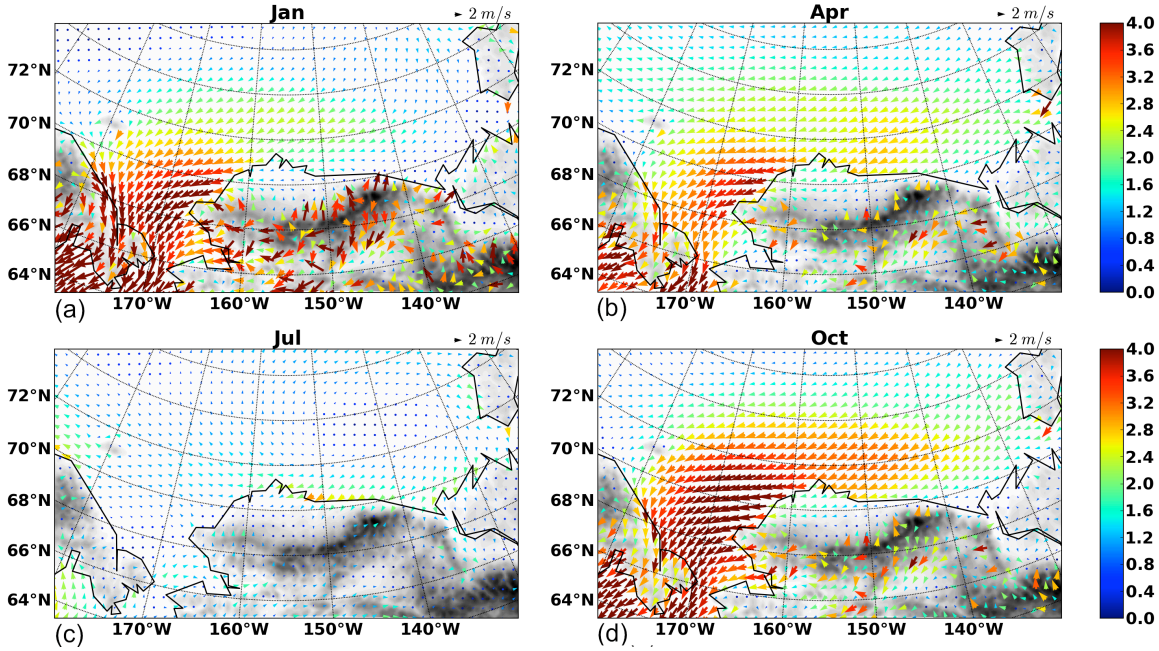

Figure 5.2.11. Climatological surface wind in (a) January, (b) April, (c) July, and (d) October in CBHAR. Wind speeds (m s^{-1}) are indicated by the vector colors.

One significant feature of climatological surface winds along the Chukotka Mountains is the existence of low-level large-scale flow directed toward the mountains from January through April and from September through December, favoring the occurrence of cold-air damming. Climatologically, a low-level wind maximum can be found in these months (Figure 5.2.12a,b,c,d,i,j,k,l). In the other months, primarily in the warm season (June–August), the wind maximum is not identifiable (Figure 5.2.12f,g,h). The maximum is larger in December and January, when the Beaufort High is strong and located over the northern Chukchi Sea, causing strong northeasterly wind to almost directly impact the Chukotka Mountains. This northeasterly wind is deflected to the left and the wind speed is also increased over the mountain slope (Figure 5.2.1b). The low-level maximum is about 6 m s^{-1} in the area 40 km inland from the shoreline, at the point where the terrain height begins to rise dramatically. The maximum also extends offshore to a fairly large distance. At the offshore location 50 km away from the shoreline, the wind component parallel to the mountain range is more than 4 m s^{-1} in January and December (Figure 5.2.12a,l). From January to April, the maximum decreases from around 6 m s^{-1} to 3.5 m s^{-1}, and reduces its extent to within 50 km of both sides of the shoreline. From September to December, the low-level wind maximum recovers its strength, following almost a reversal of the process that occurs from January to April.

A comparison between observations and CBHAR suggests that CBHAR indeed captures the cold-air damming process that impacts the surface wind field on the Chukotka Mountain slopes and in adjacent areas. For example, the observed climatological distribution of wind speed and direction for the station Mys Shmidta (Figure 5.2.13a,c), located on the shoreline near the mountains, shows that the surface is solely dominated by strong northwesterly winds in January, with a maximum wind speed of more than 7 m s^{-1}. CBHAR agrees very well with the observations (Figure 5.2.13b). In July, the dominant surface winds flow from the east-southeast, with far fewer occurrences of high wind-speed events.

Along the Brooks Range, the low-level large-scale flow has only a weak component oriented perpendicular to the mountain range; thus, the climatological vertical wind distribution does not show a similar low-level wind maximum, indicating the absence of the cold-air damming process and suggesting few impacts of cold-air damming on the surface wind field in the Brooks Range area, as compared with the Chukotka Mountains, in terms of long-term climatology. Despite this, the cold-damming process may still occasionally occur at particular times under favorable synoptic conditions and have an impact on the surface winds.

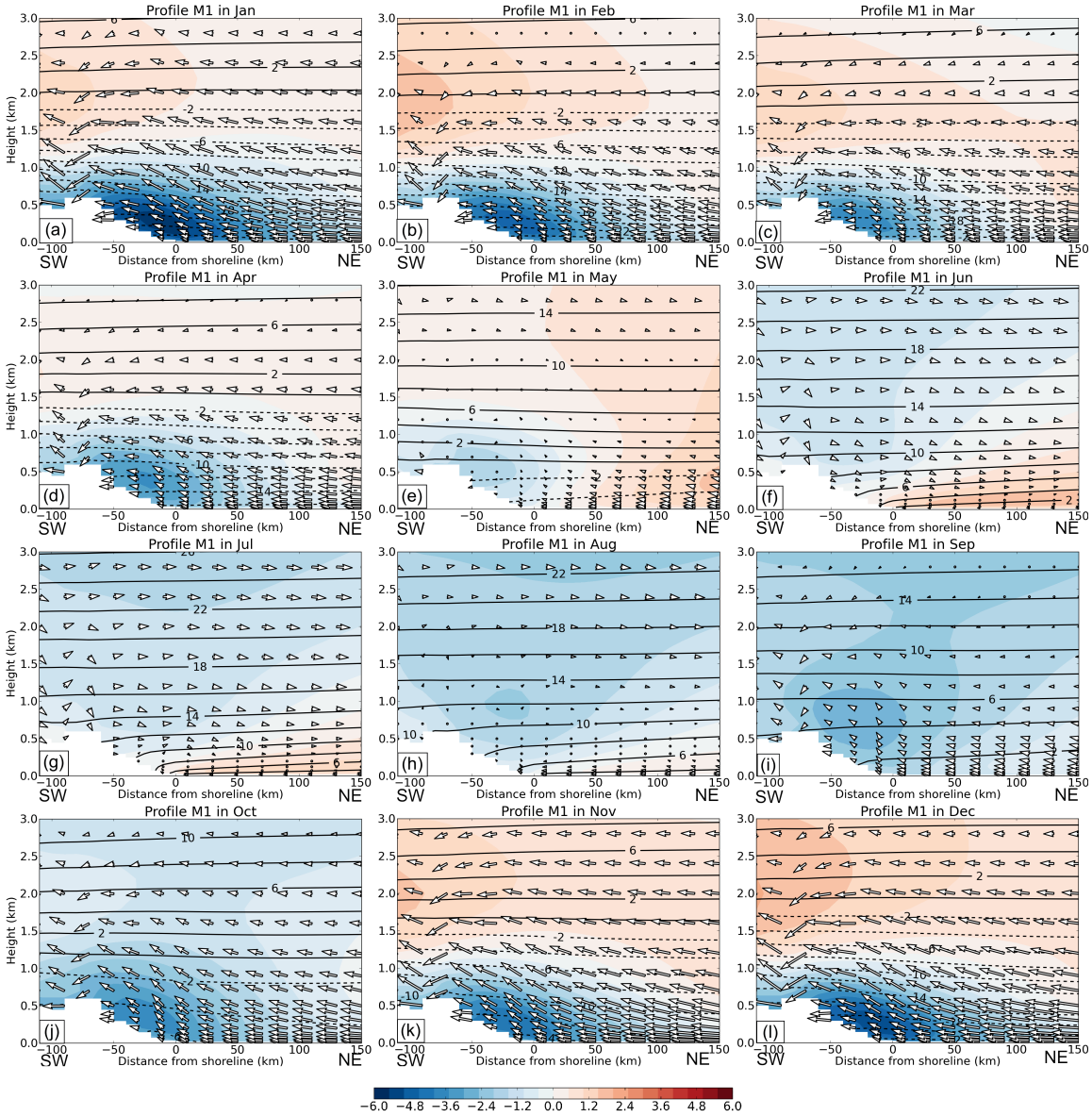

Figure 5.2.12. Climatological wind profile in different months along cross-section M1 in Figure 5.2.2. Alongshore wind is denoted by colors (m s^{-1}, negative values represent flow toward the reader), while on/offshore wind and vertical motion are indicated by vectors. The shoreline is located at 0 km, and the orientation of the cross-section is indicated by the "SW" (southwest) and "NE" (northeast) labels.

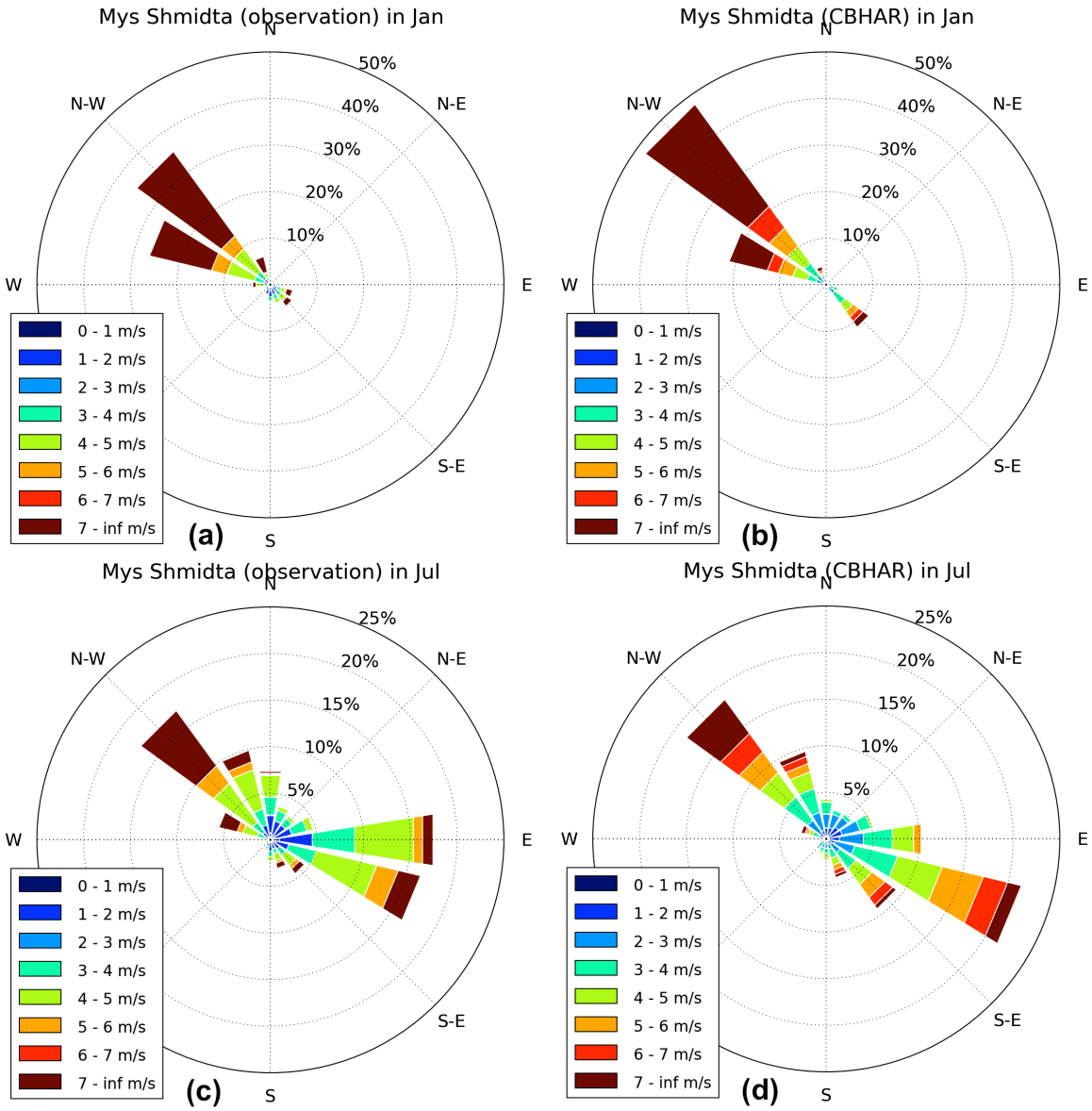

Figure 5.2.13. Wind rose at station Mys Shmidta in January (top) and July (bottom) for observations (left) and CBHAR data (right)

5.2.4 Summary

The analysis given in this section indicates that CBHAR accurately represents mesoscale sea breezes and up/downslope winds, which can play important roles in the near-surface wind field of the study region. Upslope winds are found to occur from March through September. The sea breeze begins in May, and reaches its maximum in June, July, and August. In July, the sea breeze circulation is well formed by noon and develops continuously until 1700 AKST. A corresponding compensating return flow appears about 1000 m above ground. In addition, the cold-air damming process is also represented in

CBHAR and found to be most active near the Chukotka Mountain range, as indicated by the presence of a significant low-level wind maximum along the base of the mountains.

5.3 Climatology of Storms and Their Impacts on Surface Winds in CBHAR

5.3.1 Introduction

Storms frequently invade the Chukchi–Beaufort Seas region, impacting both the regional climate and environment (e.g., Zhang et al. 2004). They play a fundamental contributing role in transporting atmospheric heat energy and moisture into both the study area and the Arctic region as a whole. Surface wind associated with these storms exerts dynamic forcing, modifying sea ice movements and ocean currents, opening sea ice leads, and redistributing sea ice cover. Furthermore, intense storms can induce extreme winds, which may give rise to high wave surges, causing flooding, coastal erosion, and property damage, particularly after the retreat of sea ice (e.g., Lynch et al. 2004). In this section, the climatology of storms in the CBHAR domain will be described, and, in particular, their impacts on the surface wind field will be analyzed.

Synoptic-scale storms are interactively steered by the atmospheric general circulation pattern. In order to better understand the storm climatology, the circulation patterns covering the Beaufort and Chukchi Seas are first documented. Regional climatological circulation patterns are generally shaped by the influence of the two semi-permanent systems in the area: the Beaufort High in the north and the Aleutian Low in the south. Therefore, climatologically, higher pressure appears in the north of the study domain and lower pressure in the south throughout the course of the year (Figure 5.3.1). Due to the presence of the Beaufort High, surface pressure increases over the Chukchi and Beaufort Seas from January to May. Lower pressure becomes more dominant in the second half of the year as the Aleutian Low gradually strengthens.

To further examine the seasonal cycle of the surface pressure as governed by the Beaufort High and Aleutian Low, the study domain was divided into northern and southern halves by the blue line shown in Figure 5.3.1. The SLP exhibits a similar increase from January to March over both the northern and southern subdomains (Figure 5.3.2). This may suggest an increased influence of the intensifying Beaufort High and a decreased influence of the weakening Aleutian Low during this time period. The intensity of the Beaufort High reaches its maximum in March and decreases afterward. In conjunction with this, SLP decreases over the study domain from March to August. In particular, the rate of SLP decrease accelerates in the northern part of the domain from May to August, ending up about 4 hPa lower in August than in May. Note that, during June–August, the difference in the areal mean of SLP between the two sub-regions declines. During this period, both the Beaufort High and the Aleutian Low are in their weaker phase. Beginning in September, both the Beaufort High and Aleutian Low start to intensify. The SLP correspondingly increases in the north, but, by contrast, remains relatively constant in the south until December. The slight southward shift of the Aleutian Low during December to January favors the increase in SLP over the study domain at this time (Figure 5.3.3).

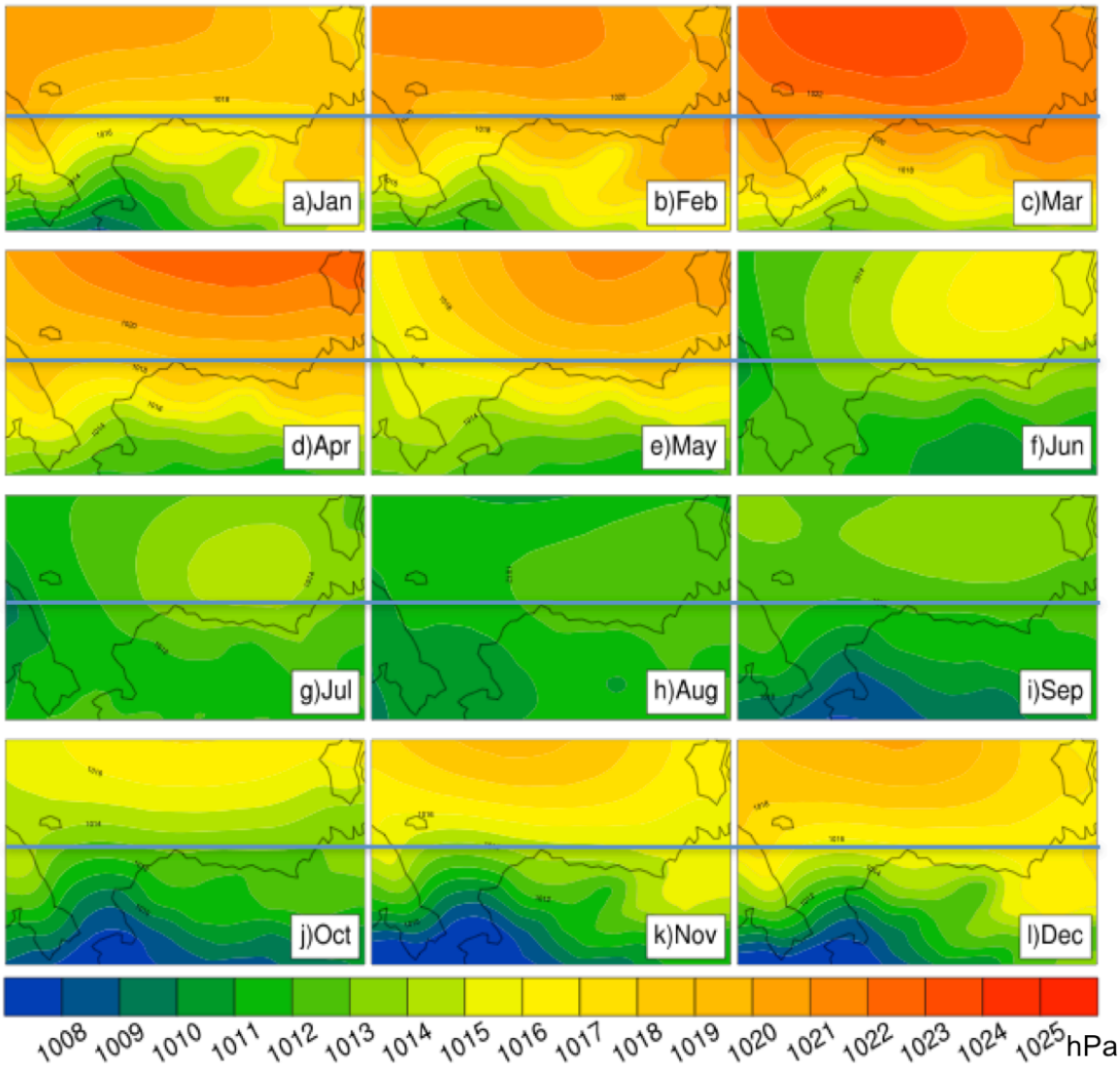

Figure 5.3.1. Climatological monthly mean sea level pressure (SLP, hPa) in CBHAR over 1979–2009. The blue line indicates the boundary between the northern and southern sub-domains used for the seasonality analysis.

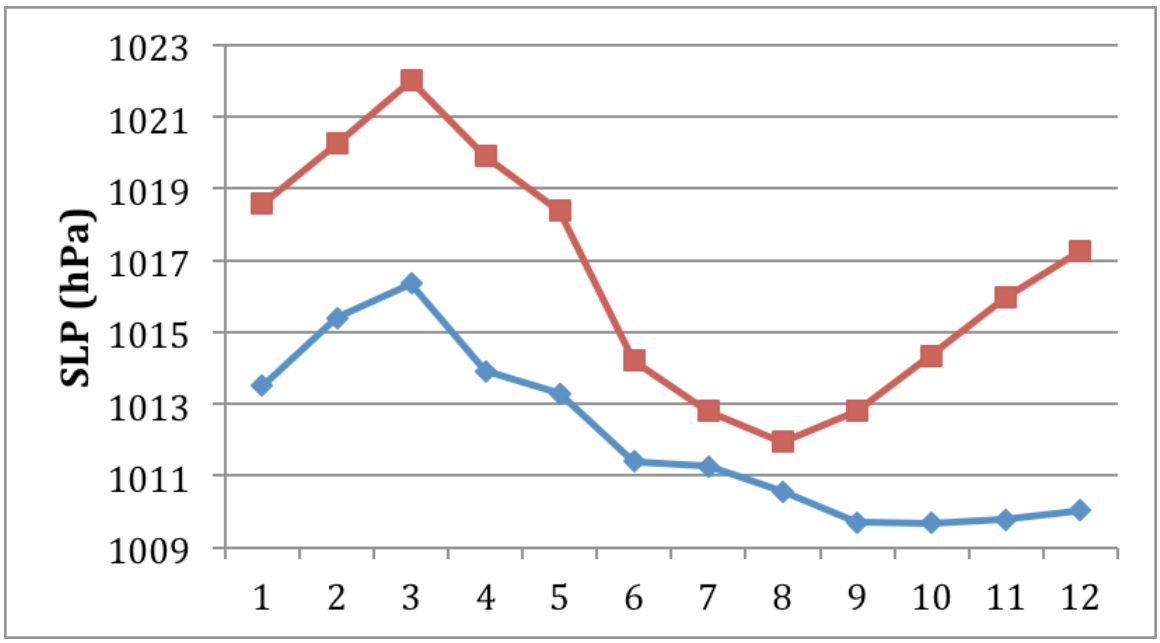

Figure 5.3.2. Climatological monthly mean SLP (hPa) over the northern (red) and southern (blue) sub-domains over 1979–2009 in CBHAR

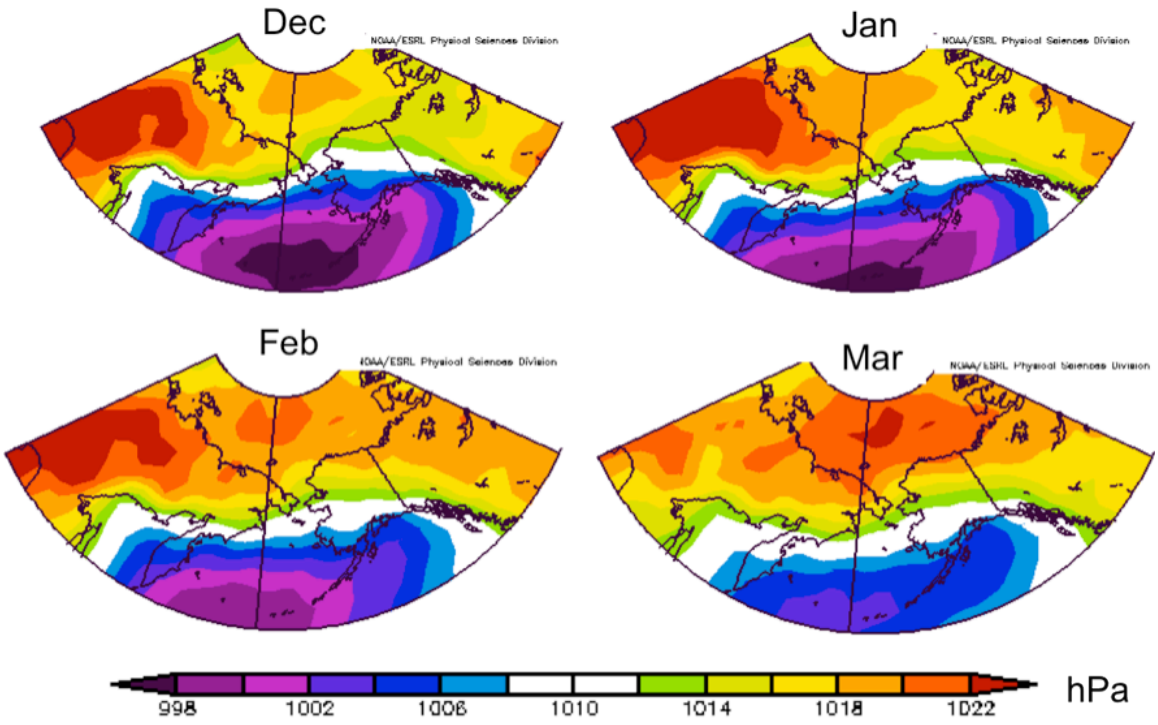

Figure 5.3.3. Climatological monthly mean SLP (hPa) over 1979–2009 in the NCEP/NCAR Reanalysis (Kalnay et al. 1996)

5.3.2 Storm Identification and Tracking Algorithm

A storm identification and tracking algorithm (Zhang et al. 2004) was employed in this study in order to investigate the climatology of storms in the study region. To accurately identify synoptic-scale storms in the high spatial and temporal resolution CBHAR data, the algorithm, originally developed for use with GCMs, was modified for its application to this analysis. The modified criteria used in this algorithm are:

1) If the SLP at one grid point is lower than at the surrounding grid points within 50 km, a cyclone candidate is identified with its center at this grid point. To minimize the impacts of thermodynamically and dynamically induced high-resolution features on the identification of synoptic-scale storms, the SLP field was initially smoothed at each grid point using the 25 surrounding grid points.
2) The minimum pressure gradient calculated between the candidate storm center and grid points 50 km away must be larger than 0.05 hPa $(100\ km)^{-1}$.
3) The SLP gradient between the central point and each of the four surrounding points both at a radius of 50 km and 100 km are compared, and at least three of them must be negative inward (i.e., the central SLP is lower than the surrounding points). The criterion requiring three of the four to be negative, not all, is created primarily to allow the inclusion of some storms that have open SLP contours directed away from the candidate center.
4) If two candidate storms simultaneously appear within 600 km of one another, they are considered to be part of the same storm system. The original algorithm set this limit to be 1200 km, but due to the region's high latitude and complex surface forcing, CBHAR has shown that two distinct storms can indeed exist within this distance. The limit was therefore reduced in order to more accurately identify dynamically separate, yet closely positioned storm centers.
5) The storm has a minimum lifetime of 12 hours. In addition, if the location of a storm is within 200 km of a storm center identified one hour earlier, the center is considered to have either moved or reformed from its previous location. Otherwise, a new storm is considered to have been generated.

In addition to the criteria of Zhang et al. (2004) that were modified for this application, the following two additional criteria were newly added specifically for the high-resolution data and complex study area used here:

6) The candidate storm's central SLP must be less than 1005 hPa.
7) The distance traversed during the storm's entire lifetime must be larger than 250 km.

These two criteria are designed to remove any dynamic and thermodynamic lows forced by the complex terrain.

5.3.3 Climatology and Variability of Storm Activity

Following Zhang et al. (2004), four parameters have been employed to describe the storm climatology, including the number, duration, and intensity of storms, as well as an integrative index, called the cyclone activity index (CAI), which measures the overall storm activity in the study region. The analysis is conducted on a monthly basis. The number of storms is defined as the number of storm trajectories located within the study domain for each month; the duration is the mean time period that all counted storms spend within the study domain for each month; and the intensity is the mean difference between the central SLP of all counted storms and the climatological monthly-mean SLP at the corresponding grid points throughout the duration of each storm for each month. The CAI is the sum of the differences between the storm's central SLP and the climatological monthly-mean SLP at the corresponding grid points for all time steps within the study domain for each month. This index thus integrates all the calculated information about the number, duration, and intensity of the storms.

A storm climatology was developed for the Chukchi–Beaufort Seas by first applying the modified storm identification and tracking algorithm described above to the CBHAR data from 1979–2009 (Figure 5.3.4). The storm activity demonstrates an obvious seasonal cycle. More numerous, but weaker storms occur in summer, and fewer, but stronger storms appear in the winter season over the study area. This climatological seasonality is precisely consistent with the previous finding for the Arctic Ocean as a whole by Zhang et al. (2004). Considering this contrast between the Arctic seasonality and that of the mid-latitudes, Serreze and Barrett (2008) conducted a follow-up and additionally found a minimum in the number of storms in March. The storm duration displays a much smaller seasonal fluctuation, characterized by a mean duration of about 30 hours throughout the year. The seasonal cycle of the CAI indicates an overall intensification in storm activity from summer to the late winter over the study domain, followed by a weakening in spring. Comparison of the four panels in Figure 5.3.4 suggests that interplay between the number and intensity of storms makes a major contribution to the seasonal variation in the CAI.

The seasonal cycle of storm activity also corresponds well to that of the regional atmospheric circulation patterns. The weakening storm activity during spring is in good agreement with the variation in the intensities of the Beaufort High and Aleutian Low. As discussed above, the Beaufort High is strongest from March through May, with its SLP reaching a maximum of 1023 hPa. At the same time, the Aleutian Low weakens noticeably from March onwards (Figure 5.3.3).

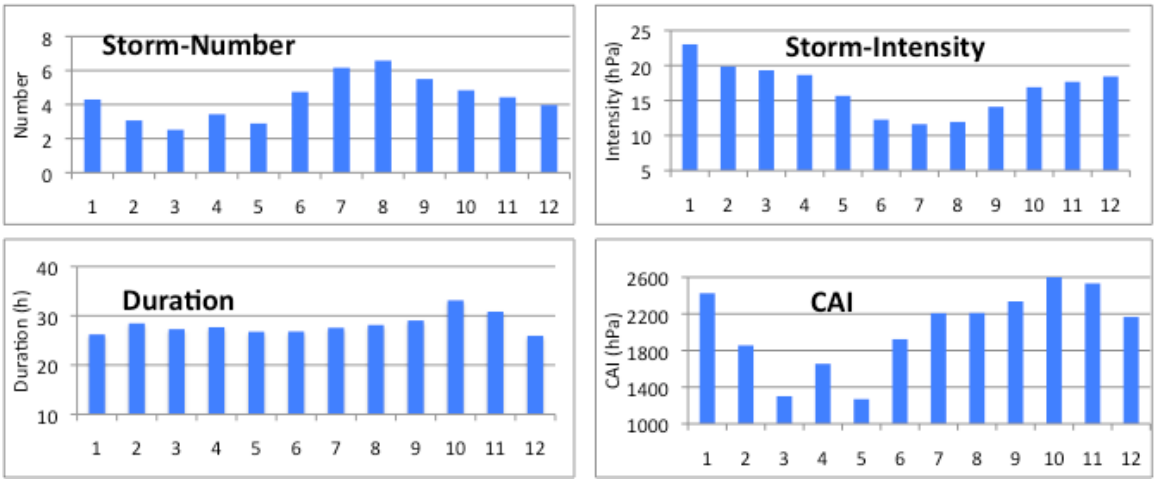

Figure 5.3.4. Climatological monthly-mean storm count, intensity (hPa), duration (hours), and CAI (hPa) for 1979–2009 over the CBHAR domain

Based on the climatological seasonal cycle of storm activity, and considering the seasonal evolution of the regional atmospheric circulation pattern as shown in Figure 5.3.1, for the next step in the analysis the year was split into four seasons to investigate the year-by-year variability and long-term changes in storm activity. The four seasons are defined as early winter (September–December, when the Aleutian Low grows strongest); late winter (January–February, when the Beaufort High intensifies and the Aleutian Low weakens); spring (March–May, when storm activity is at its weakest); and summer (June–August, when the Beaufort High is in its weakest state).

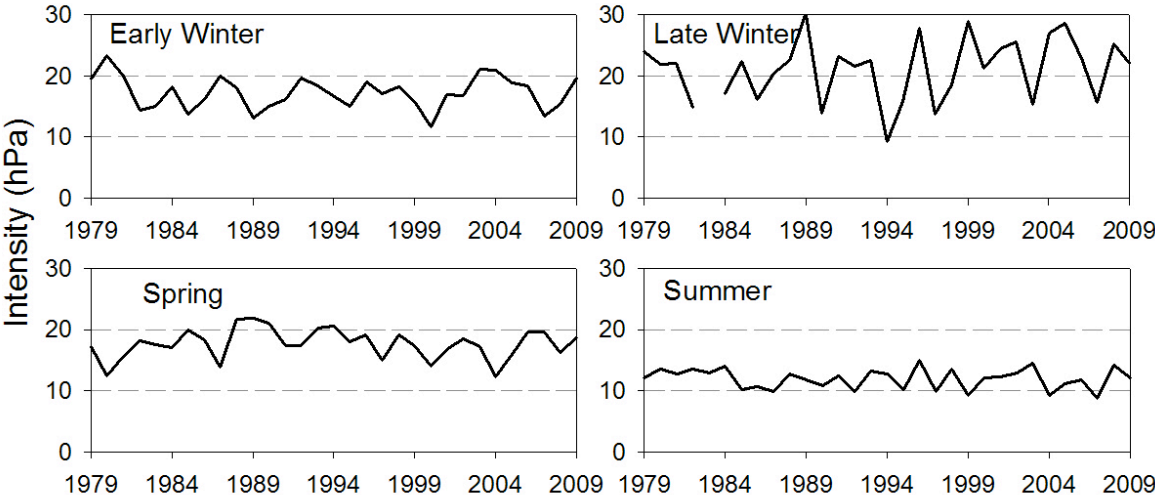

Figure 5.3.5. Seasonal storm intensity (hPa) in CBHAR during 1979–2009 (Early Winter: September–December; Late Winter: January–February; Spring: March–May; Summer: June–August)

The intensity of storms over the study domain exhibits obvious interannual variability in all four seasons from 1979–2009 (Figure 5.3.5). A slight intensification over the last 31

years appears in the late winter season, but there is no significant long-term trend. Consistent with the above climatological analysis, the interannual variability of storm intensity exhibits seasonal differences, with storms being generally stronger in the late winter than in the other seasons. The largest variability occurs in the late winter and the smallest variance in summer.

5.3.4 Impacts of Storms on Surface Wind

Strong surface winds are always associated with intense storms. To examine how the fluctuation in storm intensity impacts the surface wind field, strong winds, defined as those having speeds exceeding the 95th percentile, are identified. The computation of the 95th-percentile wind speed was introduced in Section 5.1.1. Both the intensity of storms and frequency of strong winds demonstrate large interannual variability across the four seasons (Figure 5.3.6). The two parameters are well correlated in the late winter and summer seasons, with correlation coefficients of 0.46 and 0.40, respectively, which are significant at the 95% confidence level. This suggests that the invasion or intensification of storms over the study area may contribute to an increase in surface pressure gradients, in particular when the Beaufort High is also present within the domain, and, in turn, increases the frequency of strong winds during these seasons. In contrast, insignificant, small correlations are present for the early winter and spring seasons, in particular before the mid-1990s. This could be attributable to the dominance of the stable Beaufort High. In general, storms may not be able to play a dominant role in the steering of surface winds.

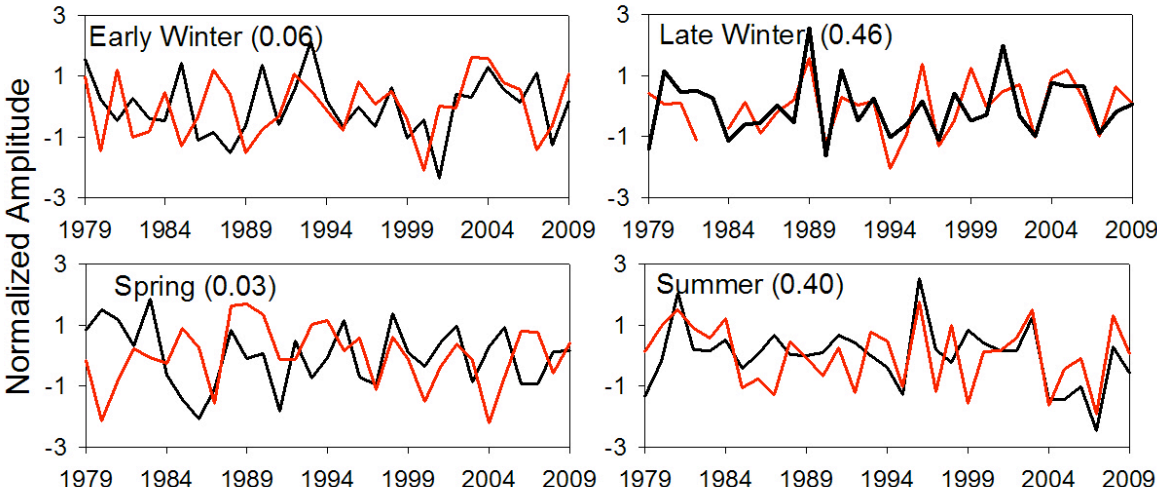

Figure 5.3.6. Standardized storm intensity (red) and frequency of strong winds (95th-percentile wind speed) (black) for each season (Early Winter: September–December; Late Winter: January–February; Spring: March–May; Summer: June–August) in CBHAR. Correlations between storm intensity and frequency of strong winds are given in parentheses.

To further examine the impacts of storms, the analysis will now focus on intense storms. In particular, a previous study has indicated that a large proportion of strong wind events

are related to strong storms (Small et al. 2011). Intense storms are defined here as those with a central SLP lower than 990 hPa. The climatological number and intensity of intense storms in each month are shown in Figure 5.3.7. The seasonal cycle of the number of intense storms exhibits differences from that of all storms. The smallest number of intense storms generally occurs from March to June, with the number increasing after June and reaching its maximum in January. The seasonal cycle of the intensity has a relatively small amplitude; it is at its strongest in January and becomes weakest in August. Based on the nature of these seasonal cycles, the focus in the following analysis will be on the early and late winter seasons.

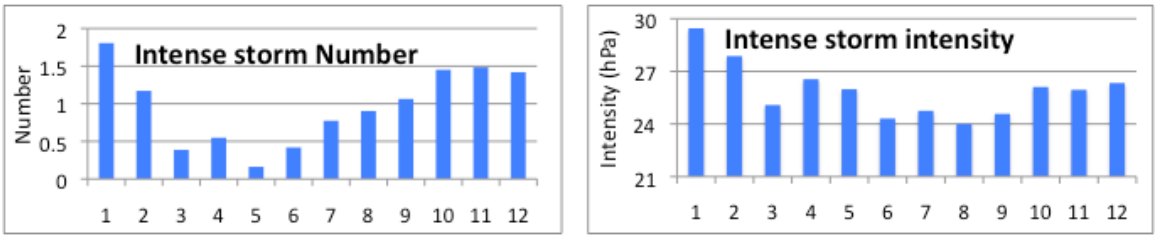

Figure 5.3.7. Climatological number and intensity (hPa) of intense storms for each month from 1979–2009 in CBHAR

The correlation between the intensity of intense storms and the frequency of strong winds is noticeably larger than the correlation calculated using all storms, in particular for the early winter, which has an increased correlation of 0.44, up from 0.06 (Figure 5.3.8a). These changes, as compared with Figure 5.3.6, suggest that intense storms are a predominant contributing factor driving the occurrence of strong surface winds. This finding has important implications for assessing the impacts of climate change. Zhang et al. (2004) found that there has been an intensifying trend of storm activity over the pan-Arctic region. If this has and will continue to occur for the current study area, the recently detected and future-projected upward trend in strong surface winds may be attributed to the changes in storm frequency that are the result of a warming climate. To examine this, the yearly frequency of intense storms over the last 31 years is shown in Figure 5.3.8. The results indeed show an increased number of intense storms in the early winter.

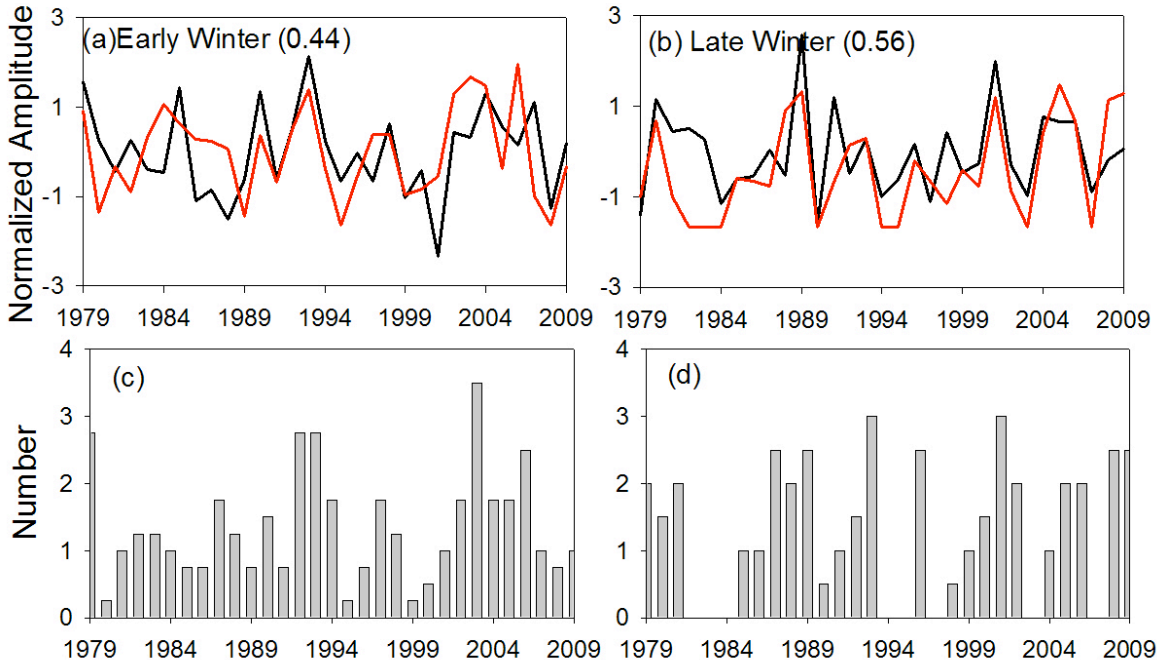

Figure 5.3.8. Standardized intensity of intense storms (red) and frequency of strong winds (95th-percentile wind speed) (black) in (a) early winter (September–December) and (b) late winter (January–February) in CBHAR. Number of intense storms in (c) early winter and (d) late winter in CBHAR. Correlations between storm intensity and frequency of strong winds are given in parentheses.

5.3.5 More Insight into the Impacts of Storms on Surface Winds: Case Studies

From the above analysis, it can be found that the variability of intense storms explains about 20–30% of the total variance of the variability in strong surface winds. Although this value suggests that intense storms have a predominant role in the long-term climate variability of surface winds, other factors can also interact with storms to impact the winds. Considering the regional atmospheric circulation patterns, the interplay between storms and the Beaufort High would be key in shaping the strong wind field, including three possible scenarios:

1) Storms themselves bring strong winds when moving into or being generated within the study domain;
2) Intensification of the Beaufort High causes strong winds; or
3) Both storms and the Beaufort High interact to generate strong winds.

To better understand how the above three scenarios shape the surface wind field, a case study has been conducted for 6–7 October 1992. During this period, an intense storm moved southeastward from Russia over the Bering Strait, reaching its minimum SLP on 6 October 1992 (Figure 5.3.9a). Strong winds occurred over the northern Chukchi and Beaufort Seas, with the maximum wind speed exceeding 18 m s^{-1} along the Alaskan coast of the southern Chukchi. Interestingly, a narrow band of strong wind extends from the

west coast of Alaska eastward along the Brooks Range, demonstrating topographic effects. The storm continued to maintain its intensity on 7 October 1992 (Figure 5.3.9b), during which time the storm center moved northward over the Chukchi Sea, bringing the associated area of strong winds along with it. At the same time, the strong winds in the extreme southern Chukchi Sea moved northward along the coast. In this case, the intense storm itself played the predominant role in causing the strong surface winds, as a well-shaped Beaufort High had not been formed.

During the late winter, it is very common that storms vigorously interact with a well-established Beaufort High. This can be exemplified by a case occurring on 21 January 1991 (Figure 5.3.9c). The storm was initially situated over the Chukchi Sea with a central SLP of 997 hPa. At the same time, the Beaufort High was located to the north with a central SLP higher than 1020 hPa. The arrangement of the storm and the Beaufort High resulted in large SLP gradients that generated 12–16 m s^{-1} winds. In this case, the intensity of the storm is moderate. In instances when the storms are stronger, more extreme winds can be expected. For example, the case occurring on 19 January 1981 shows a storm over the eastern Siberia coastal region with a central SLP of 978 hPa (Figure 5.3.9d). The obviously larger pressure gradients between the storm and the Beaufort High created strong winds with a maximum wind speed exceeding 18 m s^{-1}.

According to the regional circulation analysis given above, the Beaufort High reaches its peak strength in spring, along with the Aleutian Low, which is not a fixed feature but rather represents the time-averaged effect of storms traversing the region. Under this circumstance, the Beaufort High predominantly governs the formation of surface winds in the area. A case involving strong winds on 3 March 1981 illustrates this effect (Figure 5.3.9e). Here, the Beaufort High central SLP was higher than 1032 hPa, and the associated strong winds were around 16 m s^{-1} over the Chukchi Sea.

During summer, the Beaufort High is climatologically weak, and as such this season generally has the weakest winds, with a 95^{th}-percentile wind speed of less than 9 m s^{-1}. However, storms that either move over or are generated over the Arctic Ocean can produce relatively large winds. For example, a storm occurred over the northern Beaufort Sea on 22 July 1996 (Figure 5.3.9f). Its central SLP was 994 hPa, with associated large wind speeds of around 9–14 m s^{-1}.

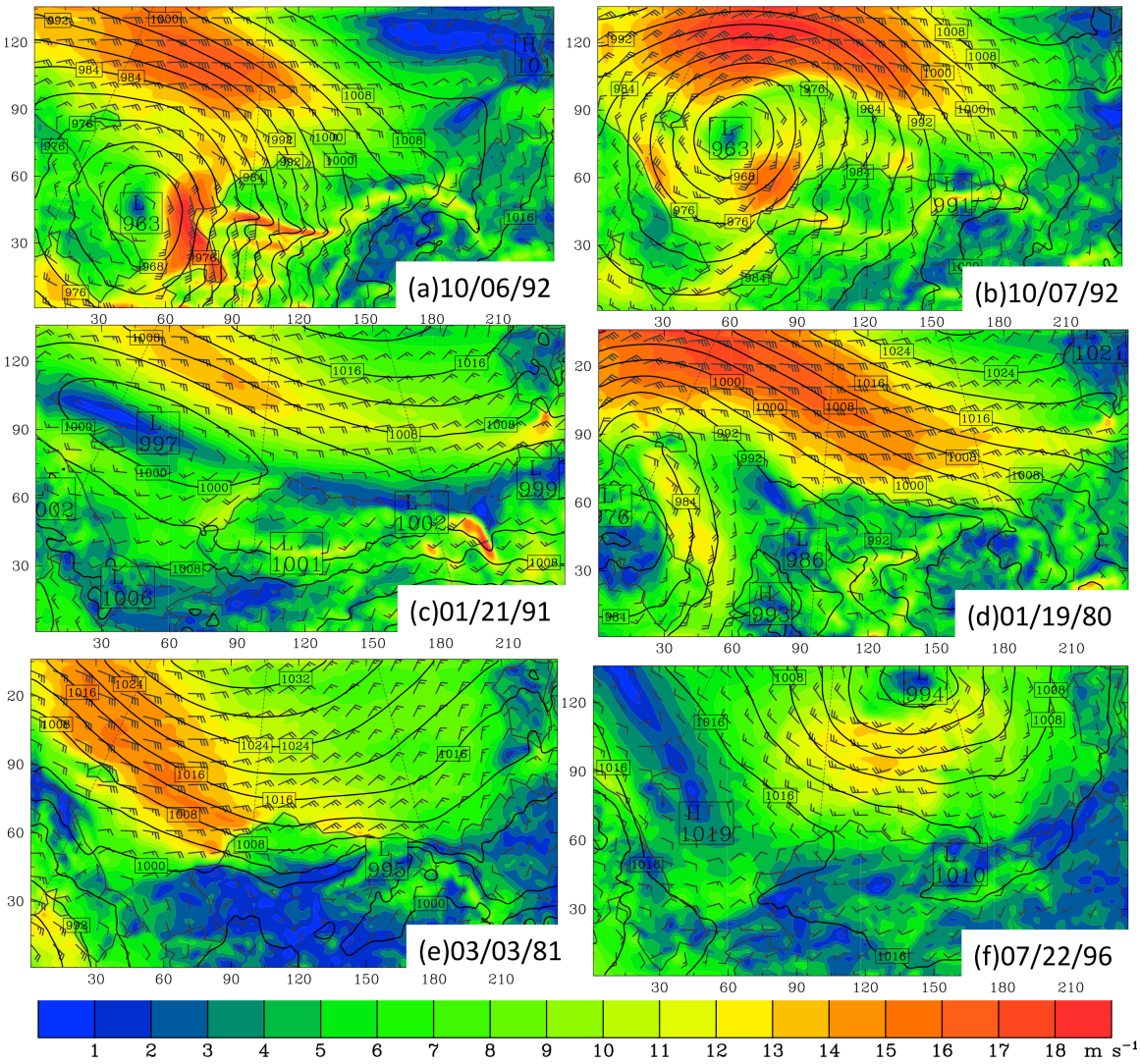

Figure 5.3.9. Sample weather charts showing the interplay between storms and the Beaufort High in generating strong surface winds. Black contours: SLP (hPa); shaded colors: 10-m wind speed (m s^{-1}); wind barbs: 10-m winds.

6 Summary

With support from BOEM/Department of the Interior (DoI) and through collaborations with national and international institutions and colleagues, the "Beaufort and Chukchi Seas Mesoscale Meteorology Modeling Study" project has hereby been conducted from September 2006 through July 2013. The research team includes Dr. Xiangdong Zhang (PI) and Mr. Jeremy Krieger from the University of Alaska Fairbanks, Dr. Jing Zhang (Co-PI) and her group from North Carolina A&T State University, and Dr. Martha Shulski (Co-PI) and her group from the University of Nebraska–Lincoln. This research has built upon the extensive experience and expertise of the team members in mesoscale meteorological modeling, data assimilation, observational data processing and quality

control, and meteorological and climatological data analysis. Mr. Warren Horowitz at the BOEM-Alaska OCS Region Office has overseen and provided management and technical guidance, and Dr. Ron Lai at BOEM Headquarters and the Scientific Review Board members Dr. Keith Hines, Dr. Peter Olsson, Dr. Igor Polyakov, and Dr. Tom Weingartner have provided scientific counsel, all of which has helped this project to proceed successfully.

The primary objective of this project was to develop a regional, high-resolution atmospheric reanalysis product, focused on surface wind over the Chukchi–Beaufort Seas and Arctic Slope. To achieve this objective, the project comprised eight components: (1) acquiring and quality controlling surface-based and satellite-retrieved observations from all available sources; (2) conducting a field program to collect additional surface observations in a selected key and data-sparse area; (3) optimizing model configurations and physical parameterizations with improved treatment of the unique Arctic environment; (4) customizing a data assimilation system for the best estimation of model errors and efficient observational assimilation; (5) constructing a high-resolution regional reanalysis for the study area through the use of the optimized modeling system and quality-controlled observational data; (6) evaluating the resulting reanalysis product against observational data and the latest generation of global reanalysis datasets; (7) analyzing the reanalysis data in order to describe the climatology, variability, changes in, and extremes of the surface wind field; and (8) disseminating the reanalysis data and scientific results to the broader community through conferences, workshops, and publications.

This project represented the first time that such a comprehensive and systematic high-resolution atmospheric modeling study has been conducted over the Chukchi–Beaufort Seas and Arctic Slope. The major resultant project outcome—the Chukchi–Beaufort High-Resolution Atmospheric Reanalysis (CBHAR)—is the first three-dimensional, thermodynamically and dynamically constrained gridded dataset to be available at such a high resolution (10 km in space and 1 hour in time) over the period 1979–2009 in the study area. These features make it possible to be used to investigate not only regional circulation and weather patterns, but also local thermodynamically and dynamically forced finer-scale processes for this remote, climatically harsh area. Major accomplishments from this project are highlighted here:

1) Developing the CBHAR reanalysis at resolutions of 10 km in space and 1 hour in time, representing a noticeably improved estimate of the regional atmospheric state as compared with observations and the new generation of global reanalysis datasets;

2) Establishing a physically optimized Weather Forecasting and Research (WRF) model and WRF-based data assimilation system, enhanced for the simulation of Arctic processes, over the Chukchi–Beaufort Seas and Arctic Slope;

3) Constructing an integrative, quality-controlled observational database comprised of all available data sources, including surface-based meteorological stations, ships, and buoys, as well as satellite remotely sensed data for the assimilation system;

4) Deploying a meteorological buoy over the highly sea-ice-dynamic Beaufort Sea and successfully acquiring continuing offshore observations of surface wind and other fundamental meteorological and ocean-surface parameters;

5) Using CBHAR to analyze surface climate over the study area, from the large scale to synoptic and mesoscales, including climatology, variability, changes, and extreme events, and describing new scientific findings;

6) Strengthening national and international collaborations between BOEM, UAF, Woods Hole Oceanographic Institution (WHOI), the industry sector including the Shell and ConocoPhillips oil companies, and JAMSTEC; and

7) Training three Ph.D. students and one master's student in mesoscale meteorological modeling, data assimilation studies, observational data processing and analysis, and Arctic climatological analysis, allowing them to participate among the next generation of Arctic scientists.

By using CBHAR data, along with the newly created observational database and the latest generation of global reanalysis datasets, this project has delivered the following specific scientific findings about the surface wind field in the study area:

1) Monthly mean and extreme (as measured by the 95th percentile) surface wind speeds over the ocean have increased markedly since 1979, with the largest increase in October, while wind speeds over most land areas have decreased.

2) Climatology of and long-term changes in the mean and extreme surface winds exhibit an obvious seasonal cycle and a variable spatial distribution, with stronger winds occurring in autumn and along the Alaskan coast.

3) Changes in wind speed are negatively correlated with changes in sea ice cover and sea surface temperature, suggesting that retreating sea ice and a warmed ocean favor the occurrence of stronger winds.

4) More strong storms occur in winter than in summer in the climatological seasonal cycle. The frequency of intense winter storms entering the Chukchi–Beaufort Seas region has increased since 1979, playing a significant role in contributing to the occurrence of strong surface winds.

5) Northeasterly wind dominates the Chukchi–Beaufort Seas region and exhibits a clear seasonal cycle, strengthening from September through May and weakening from June to August.

6) Diurnally varying sea and mountain breezes are pronounced in the summer, reaching their peak intensity in the late afternoon. Combined sea and mountain breezes along the eastern Brooks Range and Chukotka Mountains serve to intensify the onshore surface winds, the impact of which can reach out to 50–100 km offshore.

7) A strong cold-air damming process occurs on the north slope of the Chukotka Mountains in winter, producing mesoscale northwesterly winds. Radiative-cooling-induced downslope wind is the primary driver of the wintertime surface wind field in the eastern Brooks Range.

For a better understanding of the accomplishments and scientific findings described above, each of the research tasks performed during this project is briefly summarized below.

- Development of a quality-controlled observational database

Meteorological data from 262 stations in the Beaufort and Chukchi Seas region of the Arctic were gathered over the course of the project. These data represent stations from several different observational networks operating in the region, fulfilling purposes related to aviation, climate, coastal weather, fire weather, hydrology, and surface radiation. The locations of these stations accommodate land-based observations as well as offshore data from buoys, ships, exploration well sites, and an ice camp. Observed variables include: surface air temperature (°C), dew point temperature (°C), relative humidity (%), wind speed (m s^{-1}), wind direction (degrees), station pressure (hPa), sea level pressure (hPa), altimeter (in Hg), shortwave radiation (W m^{-2}), longwave radiation (W m^{-2}), 1-hr accumulated precipitation (mm), 6-hr precipitation (mm), 24-hr precipitation (mm), and snow depth (cm). In addition to the data values, any available metadata were also gathered. All available data were collected for the 1979–2009 period, with most stations reporting on an hourly or sub-hourly basis. Few stations possess data records spanning the entire 31 years; most stations have a period of record of less than 10 years.

A unified data quality control (QC) process has been applied to these data, including three primary QC evaluation procedures: identifying instances of observations falling outside of a normal range (threshold test), instances of consecutive values that are excessively different (step change test), and instances of too-high or too-low variability in the observations (persistence test). All original data are conserved in the database, and a flag is inserted after the reported data column to inform the user whether the value has passed or failed each QC check. The fraction of flagged data for the entire database is rather low (less than 5%), with the persistence test failing the highest percentage (1.34%), followed by the threshold (0.99%) and step change (0.02%) tests. When delineated by variable, wind direction and wind speed were flagged the most often, failing QC tests nearly 2% of the time. Automated checks identified the existence of problem stations (those with a high percentage of flagged data), rather than problem networks or regions. In terms of overall performance, the BOEM, buoys, CMAN, and exploration well site networks performed better than the ARM, Arctic LTER, NCDC, RAWS, Ship, and WERC stations.

- Optimization and Arctic-process enhancement of the WRF model and WRF-based data assimilation system

The WRF model includes a large number of physical parameterizations developed for various applications, primarily over the tropical and mid-latitudes, that may not perform well in an Arctic environment, including for complex air-sea-ice interactions and the seasonally varying land-sea thermal contrast and topographic effects involved. In particular, neither the WRF model nor its associated data assimilation system has before been well utilized over the Chukchi–Beaufort Seas and Arctic Slope area. An imperative exists to evaluate the capability and performance of the WRF model and its data assimilation system, and to define the model configuration capable of best representing the atmospheric state in this region. This optimization was accomplished through a thorough evaluation of the model physical parameterization schemes for the study area, including the careful selection of various in situ observations and satellite retrievals for assimilation, along with further improvement to the model physical parameterizations that require specific considerations for the unique Arctic environment.

Model physical parameterizations evaluated include those governing long- and shortwave radiation, cloud microphysics, cumulus convection, and the planetary boundary layer (PBL). Through three sets of sensitivity tests covering the periods of September 2004 (representing the seasonal transition from summer to winter), December 1997 and July 1998 (covering the unique SHEBA field experiment), and August 2009 (the warmest month of the year in the study area), the performance of different physical parameterization schemes was thoroughly compared. RRTMG (Rapid Radiative Transfer Model for GCMs) radiation (Iacono et al. 2008) and CAM (Community Atmosphere Model) radiation (Collins et al. 2004) tend to outperform other schemes in simulating both long- and shortwave irradiances, though the RRTMG shortwave performs slightly better than CAM, leading RRTMG to be selected for use in generating the CBHAR reanalysis.

Both Thom (Thompson et al. 2004) and Morr (Morisson et al. 2009) microphysics are double-moment schemes, and both performed very similarly in simulating downward irradiance, surface temperature, and wind vectors. Considering that the Morr scheme has been widely used in polar atmospheric modeling studies (Hines et al. 2011; Barton and Veron 2012; Claremar et al. 2012; Tastula et al. 2012), a decision was made to use this as the microphysics scheme in the final model configuration. When examining cumulus schemes, it was found that both the Grell–Devenyi and Grell-3D ensemble schemes (Grell and Devenyi 2002) produce smaller errors for long- and shortwave irradiances, and also contribute to a relatively small error for surface temperature. Thus, the Grell-3D ensemble cumulus parameterization was used in the production of the final CBHAR reanalysis.

The YSU (Yonsei University, Hong et al. 2006) and MYJ (Mellor–Yamada–Janjic, Mellor and Yamada 1982; Janjic 2002) PBL schemes were found to perform better than the other PBL schemes. In terms of modeling downward longwave irradiance, surface temperature, and wind vectors, YSU and MYJ perform similarly, though MYJ

outperforms YSU for the simulation of downward shortwave irradiance. Therefore, MYJ was selected for use as the PBL parameterization in the final model configuration.

In addition to the evaluation of the physical parameterizations built into WRF, the particular effects of sea ice upon the overlying atmosphere were also considered. To this end, efforts were made to implement more advanced model physical parameterizations into WRF for its application to the Arctic environment. The coupling of a thermodynamic sea ice model with WRF produces an accurate modeling of sea-ice surface albedo, resulting in an improved surface temperature, and encouraging this coupling to be applied to the final model configuration used for the production of the CBHAR reanalysis.

For an optimal WRFDA configuration in the Chukchi–Beaufort Seas region, this study concludes that the usage of customized model background error (BE) is necessary to achieve positive impacts from WRFDA assimilation in the study area. Sensitivity analyses examining the assimilation of different datasets via WRFDA demonstrate that 1) positive impacts are always seen through the assimilation of in situ surface and radiosonde measurements; 2) assimilating QuikSCAT winds improves the simulation of the surface wind field over ocean and coastal areas; 3) selectively assimilating MODIS-retrieved profiles under clear-sky and snow-free conditions is essential to avoid degradation of assimilation performance, while assimilation of COSMIC retrievals has a slight impact upon upper-air temperature alone, most likely due to limited data availability; and 4) assimilation of polar winds provides a slight benefit, though their impact on the surface fields in the kind of configuration used for this reanalysis is extremely limited. The use of three-wavenumber spectral nudging, on all vertical levels and for all variables, can effectively reduce model errors. Combining data assimilation and spectral nudging produces further improvements, encouraging the inclusion of both spectral nudging and data assimilation for generating the CBHAR reanalysis.

Forcing data required by the regional WRF model were also evaluated. WRF simulations forced by the newly developed ERA-Interim reanalysis consistently demonstrate better results for every model variable investigated. As a result, ERA-Interim was selected as the forcing data for producing the CBHAR reanalysis.

- Evaluation of CBHAR data against observations, compared with the latest global reanalysis

In order to evaluate the overall performance of CBHAR, the reanalysis data were statistically verified against the observational data collected and quality-controlled to produce the observational database also created as part of this study. Observations used for verification included surface station observations of temperature and winds, QuikSCAT ocean-surface winds, and upper-air measurements from radiosondes. To better provide an indication of the relative performance of the new reanalysis, the high-quality global reanalysis ERA-Interim, which was used to drive the production of CBHAR, was also evaluated in a similar manner. It was found that CBHAR greatly and consistently outperforms ERA-Interim in the simulation of the examined near-surface atmospheric variables in both coastal and offshore regions, as well as inland. Perhaps

counterintuitively, the largest relative gains were seen in near- and offshore areas, where the higher-resolution topography present in the WRF model was presumably less influential.

In addition to the overall verification, the reanalysis results were also verified on diurnal and seasonal time scales. Generally, errors for both surface temperatures and winds were found to be largest during the cold-season months, falling to a minimum during the climatologically less-variable warm season. While the fractional improvement in temperature error seen in CBHAR versus ERA-Interim followed a similar pattern (with larger relative decreases seen in the winter), surface winds were, notably, consistently improved throughout the course of the annual cycle, with declines in wind vector RMSE of ~15% and increases in correlation of ~8% for all months. The diurnal cycle errors in CBHAR exhibited a similar pattern to those of the annual cycle, with errors in both temperature and winds highest during the day, when boundary-layer activity is at its peak, and declining during the quieter overnight period. Relative reductions in both temperature and wind errors were found to be consistent throughout the diurnal cycle.

- Multi-scale surface climate analysis using CBHAR

By taking advantage of the high resolution of CBHAR, not only were regional-scale circulations, weather patterns, and the associated surface wind field able to be analyzed in detail, but so were the mesoscale meteorological processes forced by local thermodynamic and dynamic effects. To characterize regional climate features and describe their changes, the monthly mean and monthly 95th-percentile surface wind speeds, wind direction, 2-m air temperature, sea ice concentration, and SST were examined in particular. Wind directions were divided into quadrants—NE, SE, SW, and NW—in the analysis.

Results show that the highest wind speeds in the study region occur in November, and that northeast is the dominant wind direction. Trend analysis of the winds shows that the largest increase has occurred in October. Wind speeds and wind speed trends appear higher over the ocean than over land, including the largest increasing trend. Furthermore, CBHAR shows increasing trends in 2-m air temperature and SST, along with decreasing trends in sea ice extent, which are consistent with other findings and observations. Wind speed and sea ice extent appear to have an inverse linear relationship with one other, as do wind speed and SST; these findings will be investigated further. Comparing CBHAR with ERA-Interim data, both datasets exhibited very similar climatological features and trends, although ERA-Interim shows higher wind speeds, particularly along the coast. This is most likely due to the coarser grid spacing in ERA-Interim, which limits its capability in realistically capturing local physical processes, though this requires further investigation. CBHAR clearly captures mesoscale features in wind direction, such as the anomalous winds over the Brooks Range and the Mackenzie River valley, better than ERA-Interim.

In the mesoscale climate analysis, the primary focus was on sea and mountain breezes, up/downslope winds along mountain slopes, and cold-air damming, all of which are

prominent mesoscale meteorological processes affecting the surface wind field in the study area. There have been few studies done on these local thermodynamically and dynamically forced mesoscale wind field processes, due to a lack of both continuous and plentiful high-resolution data. However, the CBHAR data make it possible for such a mesoscale study to be conducted. The major geographic features steering the mesoscale wind processes include the seasonal variation of sea ice cover and sea surface temperature, as well as the Brooks Range in northern Alaska and the Chukotka Mountains in eastern Siberia.

Mesoscale wind processes have distinct diurnal and seasonal cycles. Thus, the climatological diurnal variation of surface winds was analyzed during different seasons. In order to understand the vertical structures of this phenomenon, a series of vertical cross-sections were constructed at different locations, in order to further investigate vertical wind profiles. These results show that sea breezes and up/downslope winds play important roles in determining the surface winds in the domain throughout different seasons of the year. The cold-air damming effect is found to dominate surface winds in the area adjacent to the Chukotka Mountains. Along the eastern Brooks Range, downslope winds, which are caused by radiative cooling in the mountains, dominate the surface winds for about half the year. Sea breezes are active in the warm months from June to August, producing significant diurnal wind variation in the coastal areas. The effects of sea breezes can extend from around 50 km offshore to about 30 km inland. In the area adjacent to the Chukotka Mountains, cold-air damming is the dominant effect in the cold months of October to April, generating enhanced surface winds (with a low-level wind maximum) in the area, oriented parallel to the mountain range. In the warm months, these surface winds are affected by both sea breezes and upslope winds.

In recent years, since the discovery of the poleward shift of storm tracks and the intensification of storm activity over the Arctic (e.g., Zhang et al. 2004), there has been increased attention paid to storms in the region. A storm identification and tracking algorithm was adapted for application to CBHAR data in the study area, and an investigation was made into how storms modulate or impact surface winds. Little research has previously been done on this topic. Specifically, all storms entering or generated within the Chukchi–Beaufort Seas region over the period 1979–2009 were identified using CBHAR data. Based on these data, the seasonal cycle and interannual changes in the number of storms and their intensity were analyzed. The relationship between storm intensity and strong-wind frequency during each season was then examined. To better understand this impact, case studies were also conducted during different seasons. The results indicate that more numerous, yet weaker storms occur in the summer, while fewer, but stronger storms exist in the winter. This is consistent with the seasonal cycle for the pan-Arctic region (Zhang et al. 2004). Intense storms produce a significant impact upon the occurrence of strong surface winds. In addition, the impact of storms on surface winds exhibits seasonality, due to its interaction with the semi-permanent Beaufort High.

7 Recommendations

Based on our experience from this project, including the evaluation of CBHAR, a preliminary climate analysis using the CBHAR data, and our interactions with the broader community and other potential users of the CBHAR data, we have summarized a list of recommendations to BOEM, given below, for planning future projects:

1) *Establish a data server and develop a user-friendly interface to disseminate the 3-D CBHAR data to the broader community.* During the project study, we have received requests for CBHAR data for various applications, including air quality modeling and assessment, the study of ocean waves and boundary currents, regional climate analysis, and hydrology and water resources research. The current project has focused on the surface wind field and does not include a platform for releasing 3-D CBHAR data. The CBHAR data has a large size (about 50 TB) and is currently stored at the Arctic Region Supercomputing Center (ARSC), which is inaccessible to the outside community. To benefit the community and allow them to fully exploit this CBHAR dataset, we recommend establishing a data server and developing a user-friendly interface to disseminate the 3-D CBHAR data to the wider community. During this process, different subsets of the data, including various layouts/formats, should be developed to meet the needs of different users in its application.

2) *Evaluate the suitability of CBHAR for various applications, such as the recently planned air quality modeling and assessment project.* Although CBHAR data has demonstrated better performance than the whole of the latest generation of global reanalysis datasets for the region including the Chukchi–Beaufort Seas and the Arctic Slope, uncertainties can still be expected to exist in CBHAR, due to model discrepancies and the limited availability of and inherent bias in the observations. We recommend a comprehensive evaluation of the suitability of CBHAR for various scientific and practical applications, including an assessment of the sensitivity of the targeted research results and an identification of where the data, including its post-processing, can be improved.

3) *Extend the CBHAR data time period to the present.* CBHAR currently covers a 31-year time period from 1979–2009. Climate and weather have changed dramatically during recent years, and the availability of observations and measurements has continually increased through the efforts of additional field campaigns since the passing of the International Polar Year. There is an imperative for the scientific community to have dynamically and thermodynamically consistent, high-resolution meteorological data covering the most recent years. We have implemented a physically optimized, WRF-model-based data assimilation system for the development of CBHAR, and we recommend using this system, along with the collection and quality control of newly available observational data, to extend CBHAR to the present time.

4) *Conduct continuing climate analysis using CBHAR, particularly for studying mesoscale climatology and climate variability and change.* We have preliminarily

analyzed regional-scale and mesoscale climatology, as well as the variability of and changes in the surface wind field and surface air temperature using CBHAR data. To better understand the recently observed dramatic climate changes and assess their environmental and societal impacts, we recommend continuing this climate analysis, which would also serve to assist the policy decision-making process. In particular, we recommend taking advantage of CBHAR's high resolution to further analyze mesoscale meteorological processes and features. We have analyzed climatological sea/mountain/valley breezes, mountain barrier effects, and cold-damming processes. We recommend a continuing analysis of the temporal variability of and changes in these mesoscale processes.

5) *Develop a new generation of CBHAR with newly available data and newly developed assimilation technology*. During the course of the current project, new observational data have become available, and new data assimilation approaches have been developed. Some applications have requested even higher spatial and temporal resolutions, as well as larger spatial coverage. Based on the physically optimized and WRF-model-based data assimilation system established over the course of the current project, we wish to recommend the development of a new generation of the CBHAR reanalysis at a higher resolution, and with additionally improved treatment of the rapidly changing Arctic sea ice and ocean, as well as cold regional land-surface processes. The development of a new generation of CBHAR is consistent with that of planned global reanalysis products.

6) *Conduct a lead-resolving modeling study for investigating coupled atmosphere-sea ice-ocean processes over the Chukchi–Beaufort Seas.* With amplified warming and thinned sea ice, leads, polynyas, and even larger open water areas are often observed even during the freezing season in the Chukchi and Beaufort Seas. In this study, we have found that the surface wind has been significantly enhanced over the last 30 years. The enhanced surface wind may further increase sea ice vulnerability, increasing the frequency of lead and polynya opening and directly agitating the opened water. The removal of ice and the associated increase in ocean mixing will enhance sensible and latent heat release, which will in turn reduce atmospheric boundary layer stratification and trigger baroclinic instability. This may result in feedbacks to the overlying weather patterns and the surface wind field. We recommend improving the representation of lead opening and polynya development and investigating feedback processes between atmosphere-leads/polynyas-ocean, including the creation of very-high-resolution atmospheric surface data sets to support such efforts.

8 References

Barker, D. M., W. Huang, Y.-R. Guo, A. J. Bourgeois, and Q. N. Xiao, 2004: A three-dimensional variational data assimilation system for MM5: Implementation and initial results. Mon. Wea. Rev., 132, 897–914.

Barker, D. M. et al., 2012: The Weather Research and Forecasting Model's Community Variational/Ensemble Data Assimilation System: WRFDA. Bull. Amer. Meteor. Soc., 93, 831–843.

Barnett, V. and T. Lewis, 1994: Outliers in statistical data. 3d ed. J. Wiley and Sons, 604 pp.

Barton, N. P. and D. E. Veron, 2012: Response of clouds and surface energy fluxes to changes in sea-ice cover over the Laptev Sea (Arctic Ocean). Clim. Res., 54, 69–84.

Bieniek, P. A., U. S. Bhatt, R. L. Thoman, H. Angeloff, J. Partain, J. Papineau, F. Fritsch, E. Holloway, J. E. Walsh, C. Daly, M. Shulski, G. Hufford, D. F. Hill, S. Calos, R. Gens, 2012: Climate divisions for Alaska based on objective methods. J. Climate, 51, 1276–1289.

Black, R. F., 1954: Precipitation at Barrow, Alaska greater than recorded. Trans. Amer. Geophys. Union, 35, 203–206.

Bougeault, P. and P. Lacarrere, 1989: Parameterization of orography-induced turbulence in a mesobeta-scale model. Mon. Wea. Rev., 1117, 1872–1890.

Bromwich, D. H., 1989: An extraordinary katabatic wind regime at Terra Nova Bay, Antarctica. Mon. Wea. Rev., 117, 688–695.

Bromwich, D. H., K. M. Hines, and L.-S. Bai, 2009: Development and testing of Polar Weather Research and Forecasting model: 2. Arctic Ocean. J. Geophys. Res., 114, D08122, doi: 10.1029/2008JD010300.

Bromwich, D. H., F. O. Otieno, K. M. Hines, K. W. Manning, and E. Shilo, 2013: Comprehensive evaluation of polar weather research and forecasting model performance in the Antarctic. J. Geophys. Res., 118, 274–292.

Cassano, J. J., M. E. Higgins, and M. W. Seefeldt, 2011: Performance of the Weather Research and Forecasting (WRF) model for month-long pan-Arctic simulations. Mon. Wea. Rev., 139, 3469–3488.

Chen, F. and J. Dudhia, 2001: Coupling an advanced land-surface hydrology model with the PSU/NCAR MM5 modeling system. Part I: Model description and implementation. Mon. Wea. Rev., 129, 569–585.

Chou, M.-D. and M. J. Suarez, 1994: An efficient thermal infrared radiation parameterization for use in general circulation models. NASA Tech. Memo. 104606, 3, 85 pp.

Claremar, B., F. Obleitner, C. Reijmer, V. Pohjola, A. Waxegard, F. Karner, and A. Rutgersson, 2012: Applying a mesoscale atmospheric model to Svalbard glaciers. Adv. Meteorol., 321649, doi: 10.1155/2012/321649.

Collins, W. D. et al., 2004: Description of the NCAR Community Atmosphere Model (CAM3.0). NCAR Technical Note, NCAR/TN-464+STR, 226 pp.

Comiso, J. C., 2003: Warming trends in the Arctic from clear sky satellite observations. J. Climate, 16, 3498–3510.

Comiso, J. C., 2012: Large decadal decline of the Arctic multiyear ice cover. J. Climate, 25, 1176–1193.

Crosby, D. S., L. C. Breaker, and W. H. Gemmill, 1993: A proposed definition for vector correlation in geophysics: Theory and application. J. Atmos. Oceanic Technol., 10, 355–367.

Dee, D. P. et al., 2011: The ERA-Interim reanalysis: Configuration and performance of the data assimilation system. Q. J. R. Meteor. Soc., 137, 553–597.

Dickey, W., 1961: A study of a topographic effect on wind in the Arctic. J. Meteor., 18, 790–803.

Doherty, S. J., S. G. Warren, T. C. Grenfell, A. D. Clarke, and R. E. Brandt, 2010: Light-absorbing impurities in Arctic snow. Atmos. Chem. Phys., 10, 11647–11680.

Doney, S. C. et al., 2012: Climate change impacts on marine ecosystems. Annu. Rev. Mar. Sci., 4, 11–37.

Dudhia, J., 1989: Numerical study of convection observed during the winter monsoon experiment using a mesoscale two-dimensional model. J. Atmos. Sci., 46, 3077–3107.

Eischeid, J. K., C. B. Baker, T. Karl, and H. F. Diaz, 1995: The quality control of long-term climatological data using objective data analysis. J. Appl. Meteor., 34, 2787–2795.

Ford, J. D. and T. Pearce, 2010: What we know, do not know, and need to know about climate change vulnerability in the western Canadian Arctic: A systematic literature review. Environ. Res. Lett., 5, 014008, doi: 10.1088/1748-9326/5/1/014008.

Gandin, L. S., 1988: Complex quality control of meteorological observations. Mon. Wea. Rev., 116, 1137–1156.

Gardner, A. S. and M. J. Sharp, 2010: A review of snow and ice albedo and the development of a new physically based broadband albedo parameterization. J. Geophys. Res., 115, F01009, doi: 10.1029/2009JF001444.

Girard, E. and J. A. Curry, 2001: Simulation of Arctic low-level clouds observed during the FIRE Arctic Clouds Experiment using a new bulk microphysics scheme. J. Geophys. Res., 106, 15139–15154.

Grell, G. A. and D. Devenyi, 2002: A generalized approach to parameterizing convection combining ensemble and data assimilation techniques. Geophys. Res. Lett., 29, 1693, doi: 10.1029/2002GL015311.

Gundlach, E. R. and M. O. Hayes, 1978: Vulnerability of coastal environments to oil spill impacts. Mar. Technol. Soc. J., 12(4), 18–27.

Guttman, N., C. Karl, T. Reek, and V. Shuler, 1988: Measuring the performance of data validators. Bull. Amer. Meteor. Soc. 69, 1448–1452.

Guttman, N. and R. G. Quayle, 1990: A review of cooperative temperature data validation. J. Atmos. Oceanic Technol., 7, 334–339.

Hamed, K. H., 2008: Trend detection in hydrologic data: The Mann–Kendall trend test under the scaling hypothesis. J. Hydrol., 349, 350–363.

Hibler III, W. D., 1979: A dynamic thermodynamic sea ice model. J. Phys. Oceanogr., 9, 815–846.

Hines, K. M. and D. H. Bromwich, 2008: Development and testing of Polar Weather Research and Forecasting (WRF) Model. Part I: Greenland ice sheet meteorology. Mon. Wea. Rev., 136, 1971–1989.

Hines, K. M., D. H. Bromwich, L.-S. Bai, M. Barlage, and A. G. Slater, 2011: Development and testing of Polar WRF. Part III: Arctic land. J. Climate, 24, 26–48.

Hinkel, K. M., F. E. Nelson, A. E. Klene, and J. H. Bell, 2003: The urban heat island in winter at Barrow, Alaska. Int. J. Climatol., 23, 1889–1905.

Hoefler Consulting Group, 2007: Study final report for the Nearshore Beaufort Sea Meteorological Monitoring and Data Synthesis Project. Minerals and Management Service, 93 pp.

Hong, S.-Y. and J.-O. J. Lim, 2006: The WRF Single-Moment 6-Class Microphysics Scheme (WSM6). J. Korean Meteor. Soc., 42, 129–151.

Hong, S.-Y., Y. Noh, and J. Dudhia, 2006: A new vertical diffusion package with an explicit treatment of entrainment processes. Mon. Wea. Rev., 134, 2318–2341.

Huang, X. et al., 2009: Four-dimensional variational data assimilation for WRF: Formulation and preliminary results. Mon. Wea. Rev., 137, 299–314.

Hubbard, K. G., S. Goddard, W. D. Sorensen, N. Wells, and T. T. Osugi, 2005: Performance of quality assurance procedures for an applied climate information system. J. Atmos. Oceanic Technol., 22, 105–112.

Iacono, M. J., J. S. Delamere, E. J. Mlawer, M. W. Shephard, S. A. Clough, and W. D. Collins, 2008: Radiative forcing by long-lived greenhouse gases: Calculations with the AER radiative transfer models. J. Geophys. Res, 113, D13103, doi: 10.1029/2008JD009944.

Jahn, A. et al., 2012: Late-twentieth-century simulation of Arctic sea ice and ocean properties in the CCSM4. J. Climate, 25, 1431–1452.

Janjic, Z. I., 1994: The step-mountain Eta coordinate model: Further developments of the convection, viscous sublayer and turbulence closure schemes. Mon. Wea. Rev., 122, 927–945.

Janjic, Z. I., 2000: Comments on "Development and evaluation of a convection scheme for use in climate models". J. Atmos. Sci., 57, 3686.

Janjic, Z. I., 2002: Nonsingular implementation of the Mellor–Yamada level 2.5 scheme in the NCEP Meso model. NCEP Office Note, No. 437, 61 pp.

Kain, J. S., 2004: The Kain–Fritsch convective parameterization: An update. J. Appl. Meteor., 43, 170–181.

Kalnay, E. et al., 1996: The NCEP/NCAR 40-Year Reanalysis Project. Bull. Amer. Meteor. Soc., 77, 437–471.

Kendall, M. G., 1975: Rank correlation methods. Griffin, London.

Kozo, T., 1979: Evidence for sea breezes on the Alaskan Beaufort Sea coast. Geophys. Res. Lett., 6, 849–852.

Kozo, T. L., 1980: Mountain barrier baroclinity effects on surface winds along the Alaskan Arctic coast. Geophys. Res. Lett., 7, 377–380.

Kozo, T. L., 1982a: An observational study of sea breezes along the Alaskan Beaufort Sea coast: Part I. J. Appl. Meteor., 21, 891–905.

Kozo, T. L., 1982b: A mathematical model of sea breezes along the Alaskan Beaufort Sea coast: Part II. J. Appl. Meteor., 21, 906–924.

Kozo, T. L. and R. Q. Robe, 1986: Modeling winds and open-water buoy drift along the eastern Beaufort Sea coast, including the effects of the Brooks Range. J. Geophys. Res., 91, 13011–13032.

Lin, Y.-L., R. D. Farley, and H. D. Orville, 1983: Bulk parameterization of the snow field in a cloud model. J. Climate Appl. Meteor., 22, 1065–1092.

Lindsay, R. W. and J. Zhang, 2005: The thinning of Arctic sea ice, 1988–2003: Have we passed a tipping point? J. Climate, 18, 4879–4894.

Liu, H., P. Q. Olsson, and K. Volz, 2008: SAR observation and modeling of gap winds in the Prince William Sound of Alaska. Sensors, 8, 4894–4914.

Liu, Z.-Q. and F. Rabier, 2002: The interaction between model resolution, observation resolution and observation density in data assimilation: A one-dimensional study. Q. J. R. Meteor. Soc., 128, 1367–1386.

Lynch, A. H., A. G. Slater, and M. Serreze, 2001: The Alaskan Arctic frontal zone: Forcing by orography, coastal contrast, and the boreal forest. J. Climate, 14, 4351–4362.

Lynch, A. H., J. A. Curry, R. D. Brunner, and J. A. Maslanik, 2004: Toward an integrated assessment of the impacts of extreme wind events on Barrow, Alaska. Bull. Amer. Meteor. Soc., 85, 209–221.

Mann, H. B., 1945: Nonparametric tests against trend. Econometrica, 13, 245–259.

Maslowski, W., J. C. Kinney, M. Higgins, and A. Roberts, 2012: The future of Arctic sea ice. Annu. Rev. Earth Planet. Sci., 40, 625–654.

Meek, D. W. and J. L. Hatfield, 1994: Data quality checking for single station meteorological databases. Agric. For. Meteorol., 69, 85–109.

Mellor, G. L. and T. Yamada, 1982: Development of a turbulence closure model for geophysical fluid problems. Rev. Geophys. Space Phys., 20, 851–875.

Mesinger, F. et al., 2006: North American Regional Reanalysis. Bull. Amer. Meteor. Soc., 87, 343–360.

Milbrandt, J. A. and M. K. Yau, 2005: A multimoment bulk microphysics parameterization. Part I: Analysis of the role of the spectral shape parameter. J. Atmos. Sci., 62, 3051–3064.

Mlawer, E. J., S. J. Taubman, P. D. Brown, M. J. Iacono, and S. A. Clough, 1997: Radiative transfer for inhomogeneous atmosphere: RRTM, a validated correlated-k model for the longwave. J. Geophys. Res., 102, 16663–16682.

Moore, G. W. K., 2012: Decadal variability and a recent amplification of the summer Beaufort Sea High. Geophys. Res. Lett., 39, L10807, doi: 10.1029/2012GL051570.

Moore, G. W. K. and R. S. Pickart, 2012: Northern Bering Sea tip jets. Geophys. Res. Lett., 39, L08807, doi: 10.1029/2012GL051537.

Morrison, H. C., M. D. Shupe, and J. A. Curry, 2003: Modeling clouds observed at SHEBA using a bulk parameterization implemented into a single-column model. J. Geophys. Res., 108, 4255, doi:10.1029/2002JD002229.

Morrison, H. C., G. Thompson, and V. Tatarskii, 2009: Impact of cloud microphysics on the development of trailing stratiform precipitation in a simulated squall line: Comparison of one- and two-moment schemes. Mon. Wea. Rev., 137, 991–1007.

Olsson, P. Q. and Harrington, J. Y., 2000: Dynamics and energetics of the cloudy boundary layer in simulations of off-ice flow in the marginal ice zone. J. Geophys. Res., 105, 11889–11899.

Onogi, K. et al., 2007: The JRA-25 Reanalysis. J. Meteor. Soc. Japan, 85, 369–432.

Overland, J. E., 2009: Meteorology of the Beaufort Sea. J. Geophys. Res., 114, C00A07, doi: 10.1029/2008JC004861.

Parish, T. R. and D. H. Bromwich, 1987: The surface windfield over the Antarctic ice sheets. Nature, 328, 51–54.

Parish, T. R. and D. H. Bromwich, 1991: Continental-scale simulation of the Antarctic katabatic wind regime. J. Climate, 4, 135–146.

Parish, T. R. and J. J. Cassano, 2003: The role of katabatic winds on the Antarctic surface wind regime. Mon. Wea. Rev., 131, 317–333.

Parkinson, C. L. and W. M. Washington, 1979: A large scale numerical model of sea ice. J. Geophys. Res., 84, 311–337.

Parrish, D. and J. Derber, 1992: The National Meteorological Center's spectral statistical-interpolation analysis system. Mon. Wea. Rev., 120, 1747–1763.

Picou, J. S. et al., 2009: Community impacts of the Exxon Valdez oil spill: A synthesis and elaboration of social science research. Synthesis: Three decades of research on socioeconomic effects related to offshore petroleum development in coastal Alaska. S. R. Braund and J. Kruse, eds. Anchorage, Alaska: Steven R. Braund & Associates, 279–310.

Pleim, J. E., 2007: A combined local and nonlocal closure model for the atmospheric boundary layer. Part I: Model description and testing. J. Appl. Meteor. Climatol., 46, 1383–1395.

Porter, D. F., J. J. Cassano, and M. C. Serreze, 2011: Analysis of the Arctic atmospheric energy budget in WRF: A comparison with reanalyses and satellite observations. J. Geophys. Res., 116, D22108, doi: 10.1029/2011JD016622.

Reed, M. et al., 1999: Oil spill modeling towards the close of the 20th century: Overview of the state of the art. Spill Sci. Technol. Bull., 5, 3–16.

Reek, T., S. R. Doty, and T. W. Owen, 1992: A deterministic approach to the validation of historical daily temperature and precipitation data from the Cooperative Network. Bull. Amer. Meteor. Soc., 73, 753–765.

Rienecker, M. M. et al., 2011: MERRA: NASA's Modern-Era Retrospective Analysis for Research and Applications. J. Climate, 24, 3624–3648.

Ryan, B. F., 1996: On the global variation of precipitating layer clouds. Bull. Amer. Meteor. Soc., 77, 53–70.

Saha, S. et al., 2010: The NCEP Climate Forecast System Reanalysis. Bull. Amer. Meteor. Soc., 91, 1015–1057.

Schwerdtfeger, W., 1974: Mountain barrier effect on the flow of stable air north of the Brooks Range. Proc. of the 24th Alaskan Science Conf., Fairbanks, 204–208.

Serreze, M. C. and A. P. Barrett, 2008: The summer cyclone maximum over the central Arctic Ocean. J. Climate, 21, 1048–1065.

Shafer, M. A., C. A. Fiebrich, D. Arndt, S. E. Fredrickson, and T. W. Hughes, 2000: Quality assurance procedures in the Oklahoma Mesonetwork. J. Atmos. Oceanic Technol., 17, 474–494.

Shupe, M. D. and J. M. Intrieri, 2004: Cloud radiative forcing of the Arctic surface: The influence of cloud properties, surface albedo, and solar zenith angle. J. Climate, 17, 616–628.

Shulski, M. D. and G. Wendler, 2007: The climate of Alaska. University of Alaska Press, 216 pp.

Skamarock, W. C., J. B. Klemp, J. Dudhia, D. O. Gill, D. M. Barker, M. G. Duda, X.-Y. Huang, W. Wang, and J. G. Powers, 2008: A description of the Advanced Research WRF Version 3. NCAR Tech Note, NCAR/TN–475+STR, 113 pp.

Small, D., E. Atallah, and J. Gyakum, 2011: Wind regimes along the Beaufort Sea coast favorable for strong wind events at Tuktoyaktuk. J. Appl. Meteor. Climatol., 50, 1291–1306.

Stegall, S. T. and J. Zhang, 2012: Wind field climatology, changes, and extremes in the Chukchi–Beaufort Seas and Alaska North Slope during 1979–2009. J. Climate, 25, 8075–8089.

Stroeve, J. C., M. C. Serreze, M. M. Holland, J. E. Kay, J. Malanik, and A. P. Barrett, 2012: The Arctic's rapidly shrinking sea ice cover: A research synthesis. Clim. Change, 110, 1005–1027.

Sukoriansky, S., B. Galperin, and V. Perov, 2006: A quasi-normal scale elimination model of turbulence and its application to stably stratified flows. Nonlinear Process. Geophys., 13, 9–22.

Tao, W.-K., J. Simpson, and M. McCumber, 1989: An ice-water saturation adjustment. Mon. Wea. Rev., 117, 231–235.

Tao, W.-K. and J. Simpson, 1993: The Goddard cumulus ensemble model. Part I: Model description. Terr. Atmos. Ocean. Sci., 4, 35–72.

Tastula, E.-M., T. Vihma, and E. L. Andreas, 2012: Evaluation of Polar WRF from modeling the atmospheric boundary layer over Antarctic sea ice in autumn and winter. Mon. Wea. Rev., 140, 3919–3935.

Thompson, G., R. M. Rasmussen, and K. Manning, 2004: Explicit forecasts of winter precipitation using an improved bulk microphysics scheme. Part I: Description and sensitivity analysis. Mon. Wea. Rev., 132, 519–542.

Thompson, G., P. R. Field, R. M. Rasmussen, and W. D. Hall, 2008: Explicit forecasts of winter precipitation using an improved bulk microphysics scheme. Part II: Implementation of a new snow parameterization. Mon. Wea. Rev., 136, 5095–5115.

Trenberth, K. E., D. P. Stepaniak, J. W. Hurrell, and M. Fiorino, 2001: Quality of reanalyses in the tropics. J. Climate, 14, 1499–1510.

Uppala, S. M. et al., 2005: The ERA-40 re-analysis. Q. J. R. Meteorol. Soc., 131, 2961–3012.

Wade, C. G., 1987: A quality control program for surface mesometeorological data. J. Atmos. Oceanic Technol., 4, 435–453.

Webler, T. and F. Lord, 2010: Planning for the human dimensions of oil spills and spill response. Environ. Manage., 45, 723–738.

Wilks, D. S., 2006: Statistical methods in the atmospheric sciences. 2nd ed. Academic Press, 627 pp.

Wilson, A. B., D. H. Bromwich, and K. M. Hines, 2011: Evaluation of Polar WRF forecasts on the Arctic System Reanalysis domain: Surface and upper air analysis. J. Geophys. Res., 116, D11112, doi: 10.1029/2010JD015013.

Yue, S., P. Pilon, B. Phinney, and G. Cavadias, 2002: The influence of autocorrelation on the ability to detect trend in hydrological series. Hydrol. Processes, 16, 1807–1829.

Zhang, C., Y. Wang, and K. Hamilton, 2011: Improved representation of boundary layer clouds over the southeast Pacific in ARW-WRF using a modified Tiedtke cumulus parameterization scheme. Mon. Wea. Rev., 139, 3489–3513.

Zhang, X. and J. Zhang, 2001: Heat and freshwater budgets and pathways in the Arctic Mediterranean in a coupled ocean/sea-ice model. J. Oceanogr., 57, 207–237.

Zhang, X., J. E. Walsh, J. Zhang, U. S. Bhatt, and M. Ikeda, 2004: Climatology and interannual variability of arctic cyclone activity: 1948–2002. J. Climate, 17, 2300–2317.

Appendix A: Structure of the Chukchi–Beaufort Region Meteorological Database

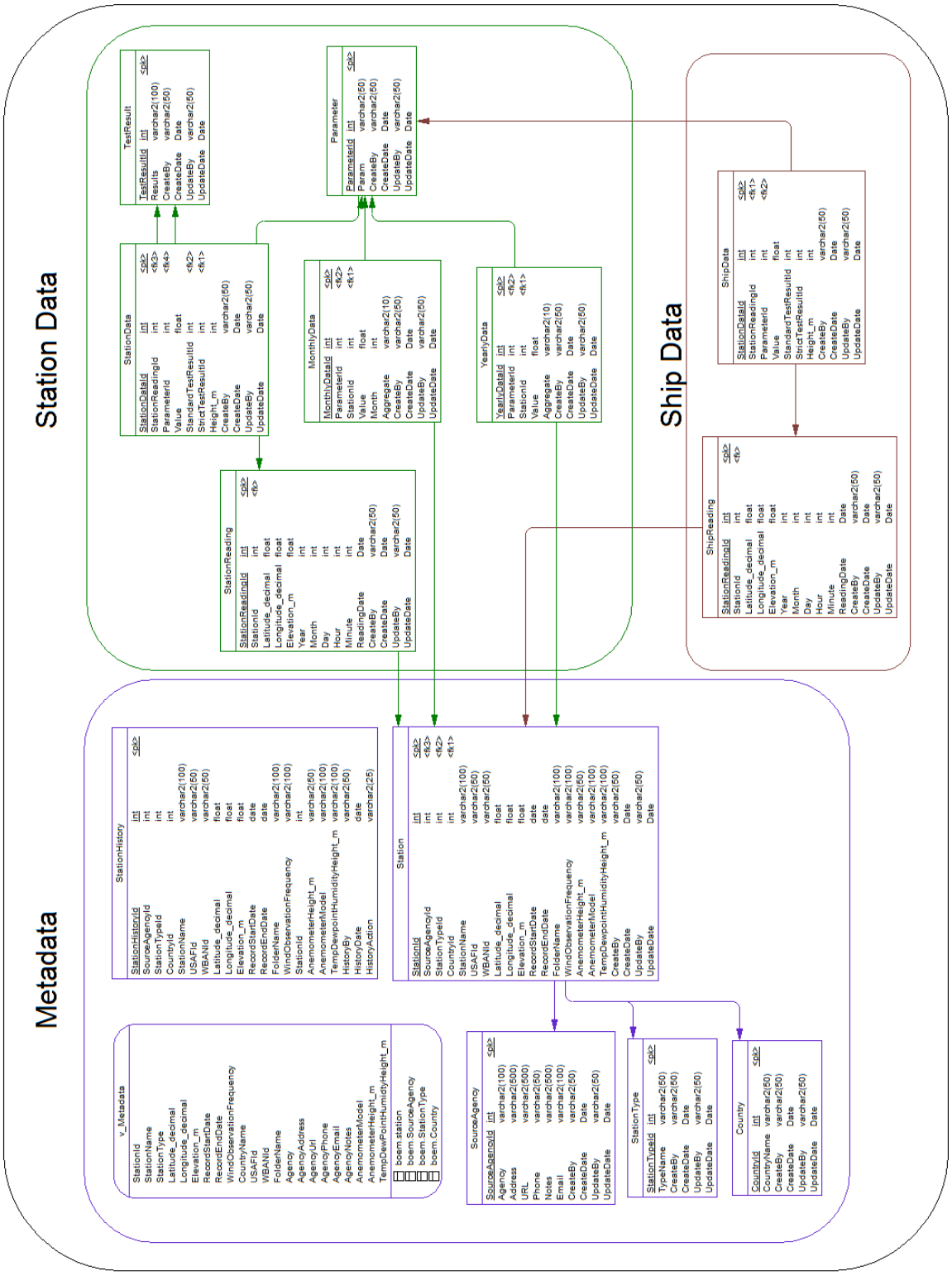

Entity Relationship Diagram (ERD)

Table Descriptions

STATION	Information related to the individual data collection sources. Contains the unique STATIONID along with sensor and operational information.
STATIONHISTORY	Keeps a history of changes made to the STATION table. Needed to query the full range of available dates for a particular station without querying the actual data. Invalid entries should be removed from this table in order to maintain a clean history. It is designed to keep track of changes such as those to a WBANID or sensor.
STATIONTYPE	Lookup table for the available station types such as buoy, land, well site, etc.
SOURCEAGENCY	Lookup table for the contact information of each data source
COUNTRY	Lookup table for the country where data was recorded
PARAMETER	Lookup table of available data parameters (e.g., temperature, wind speed)
TESTRESULT	Lookup table for the quality-control flag definitions
STATIONREADING	Relational table containing unique location/temporal station-based events
STATIONDATA	Contains the data collected for each station-reading event
MONTHLYDATA	Monthly summary statistics (min,max,avg,stdev) for standard climatology stations
YEARLYDATA	Summary statistics (min,max,avg,stdev) for standard climatology stations aggregated by all available data
SHIPREADING	Relational table containing location/temporal events for ships
SHIPDATA	Contains the data collected for each ship-reading event
QUIKSCATREADING	Contains the unique location/temporal events for the QuikSCAT dataset
QUIKSCATDATA	Contains the values (wind speed and direction) for each QuikSCAT reading
WRFREADING	Contains the unique grid points, location, and time instances of each WRF-model event
WRFDATA	Contains the data values associated with each WRF reading

Appendix B: Statistical Evaluation Metrics

In the discussion of the statistical performance of modeling results throughout this report, a number of evaluation metrics are employed. Though these are standard parameters frequently used in verification analyses of atmospheric model data, a summary is presented here for the sake of completeness. The statistical quantities primarily discussed are root-mean-square error (RMSE), mean bias, and correlation. Definitions of these metrics are presented below; further discussion can be found in Wilks (2006). All other statistical quantities used in the report are defined in the sections in which they are introduced.

Root-mean-square error (RMSE)

RMSE is a statistic commonly used to measure the overall accuracy of a modeled field through direct comparison with observed values. The deviations of the modeled values from their observed counterparts are squared and averaged, before calculating the square root of the mean, like so:

$$RMSE = \sqrt{\frac{1}{N}\sum_{k=1}^{N}(x_k - o_k)^2}$$

Both here and below, N is the total number of observations, x is the modeled value, and o is the observed value. Due to the squaring of the deviations, this statistic is sensitive to outliers and thus penalizes large modeled errors. Taking the square root allows the statistic to retain the same units as the variable being evaluated.

Mean bias

In contrast to RMSE, which evaluates the accuracy of a modeled field at individual observational locations, mean bias is a measure of the field as a whole through the calculation of the average deviation of the modeled field:

$$BIAS = \frac{1}{N}\sum_{k=1}^{N}(x_k - o_k)$$

Since the deviations are not squared before being summed, a deviation at one station location can be offset by the deviation at another. Thus, this quantity is used to present the overall bias of a modeled field, but gives no information about the accuracy at individual locations.

Correlation

Correlation, as used here, is a statistical metric used to indicate the accuracy of the "shape" of the modeled field, while disregarding any inherent model bias. The standard Pearson product-moment correlation coefficient is used here for scalar variables:

$$CORR = \frac{\sum_{k=1}^{N}(x_k - \overline{x})(o_k - \overline{o})}{\sqrt{\sum_{k=1}^{N}(x_k - \overline{x})^2 \sum_{k=1}^{N}(o_k - \overline{o})^2}}$$

Correlation is a unitless quantity that varies from 0 to 1, with 1 representing a modeled field that is perfectly correlated to the observations (i.e., they have an identical "shape"). Because the standard correlation can only be used for scalar variables, the correlation of the vector wind field is calculated using the technique described in Crosby et al. (1993), in which it is computed using the zonal and meridional components of the wind vector (U and V, respectively). The vector correlation represents a generalization of the standard scalar correlation, and thus has the same properties.

The Department of the Interior Mission

As the Nation's principal conservation agency, the Department of the Interior has responsibility for most of our nationally owned public lands and natural resources. This includes fostering the sound use of our land and water resources, protecting our fish, wildlife and biological diversity; preserving the environmental and cultural values of our national parks and historical places; and providing for the enjoyment of life through outdoor recreation. The Department assesses our energy and mineral resources and works to ensure that their development is in the best interests of all our people by encouraging stewardship and citizen participation in their care. The Department also has a major responsibility for American Indian reservation communities and for people who live in island communities.

The Bureau of Ocean Energy Management

The Bureau of Ocean Energy Management (BOEM) works to manage the exploration and development of the nation's offshore resources in a way that appropriately balances economic development, energy independence, and environmental protection through oil and gas leases, renewable energy development and environmental reviews and studies.

www.boem.gov